Feasibility Study on Logitudinal Phase Space Measurements at GSI UNILAC using Particle Detectors

Vom Fachbereich Physik
der Technischen Universität Darmstadt

zur Erlangung des Grades
eines Doktors der Naturwissenschaften
(Dr. rer. nat.)

vorgelegte Dissertation von
Dipl.-Phys. Timo Milosic
aus Darmstadt

TECHNISCHE
UNIVERSITÄT
DARMSTADT

Darmstadt 2012
D17

Referent:	Prof. Dr. J. Enders
Korreferent:	Prof. Dr. Dr. h.c./RUS D.H.H. Hoffmann

Tag der Einreichung:	November 14, 2012
Tag der Prüfung:	November 14, 2012

Zusammenfassung

Summary

Contents

List of Figures

List of Tables

Abbreviations

ADC	Analog-to-digital converter
_A_keV	Kinetic energy given in keV per nucleon
_A_MeV	Kinetic energy given in MeV per nucleon
_A_GeV	Kinetic energy given in GeV per nucleon
ASIC	Application specific integrated circuit
BIF	Beam-induced fluorescence
BNC	Bayonet Neill Concelman (coaxial RF connector type)
CHORDIS	Cold or hot reflex discharge ion source
CVD	Chemical vapour deposition
CCE	Charge-collection efficiency
DAQ	Data acquisition
DLC	Diamond-like carbon
DTL	Drift-tube linear accelerator
ECR	Electron cyclotron resonance source
ESR	Experimental storage ring
FAIR	Facility for Antiproton and Ion Research
FRS	Fragment separator
FSE	First-shot ellipse
FWHM	Full width at half maximum
GSI	GSI Helmholtzzentrum für Schwerionenforschung GmbH
IH	Interdigital H-mode
HIPPI	High intensity pulsed proton injector
HLI	High charge injector (German: Hochladungsinjektor)
HSI	High current injector (German: Hochstrominjektor)
KONUS	Combined zero-degree structure (German: Kombinierte Null-Grad Struktur)
LEBT	Low energy beam transfer
LINAC	Linear accelerator
LSB	Least significant bit
MC	Mono crystalline
MCD	Minimum covariance determinant
MCP	Microchannel plate (also multi-channel plate)
MEVVA	Metal vapour vacuum arc ion source
MUCIS	Multi cusp ion source
MVE	Minimum volume ellipsoid
NIM	Nuclear instrumentation module
PC	Poly crystalline
PEEK	Polyether ether ketone
PHD	Pulse-height distribution

POSIX	Portable operating system interface based on UNIX
RF	Radio frequency
RFQ	Radio frequency quadrupole
RMS	Root mean square
ROI	Region of interest
SCUBEEx	Self-consistent, unbiased elliptical exclusion method
SFSE	Scaled first-shot ellipse
SHE	Super heavy elements
SIS	Heavy ion synchrotron (German: Schwerionen-Synchrotron)
SMA	SubMiniature version A (coaxial RF connector type)
SNR	Signal-to-noise ratio
SRIM	Stopping and range of ions in matter
TDC	Time-to-digital converter
TOF	Time-of-flight
UNILAC	Universal linear accelerator
USB	Universal serial bus
VARIS	Vacuum arc ion source
VME	Versa module eurocard (bus)

Chapter 1

Introduction

The goal of beam diagnostics is the precise measurement of all relevant beam parameters of particle or heavy-ion accelerators. During commissioning and operating of accelerator facilities, beam diagnostics plays a crucial role. Beam diagnostics is not only an important tool for an optimised configuration of the beam-line settings, but also serves to provide feedback in case of erroneous accelerator settings or to provide important information for further theoretical calculations or simulations. The ideal situation, from a beam-diagnostics perspective, would be the direct access to the six-dimensional phase-space density at an arbitrary location at all times for a large energy range. This contains the maximum information and allows to derive all parameters of interest. Unfortunately, this situation is not realistic. In fact, beam diagnostics devices only access a certain subset of parameters, such as projections of the particle distribution, and are available only at dedicated locations of the beam line. Furthermore, depending on the type of accelerated particles, energy and intensity, access to parameters might be a technical challenge.

The GSI accelerator facility belongs to the class of pulsed, RF-driven accelerators. Soon after emission from the ion sources, the beam is compressed into little segments and is accelerated in so-called “bunches”, the regular micro structure of the beam. Through cascading and reuse of cavities in ring accelerators, RF acceleration allows for higher effective field gradients than static-gradient accelerators which comes at the price of a significantly more complicated beam dynamics. For a proper operating of the accelerator, a delicate synchronised setup is required to reach high beam transmission and beam quality. In particular, this includes the settings of the cavity structure which relies on the knowledge of the input phase space and must accordingly be operated at a matching phase and voltage level. Being a versatile facility able to accelerate all ion species, this is a special issue at GSI. Due to the various modes of operation with different beam parameters, dedicated setups for experiments at GSI can often be considered as recommissioning parts of the beam line, where the knowledge of the phase space is an important piece of information. At a certain location along the beam line, the phase space is given by the particle distribution and the corresponding momentum per particle.

While several established methods exist to access the four-dimensional transverse degree of freedom at low-energy sections of heavy-ion facilities, there are no standard methods available to access the longitudinal phase space. This is the topic of this work.

The measurement of longitudinal phase-space distributions of low energy heavy particles proves difficult, compared to the transverse case, which is typically provided by the well-established slit-grid technique [1]. At low energies of heavy particles, common longitudinal measurement techniques, based on the electric field distribution, fail due to the large longitudinal field component. Measurement techniques relying on the electric-field distribution, like capacitive pick-ups [2], consequently produce significantly convolved output signals, rendering the determination of the bunch structure impossible. A rarely used approach is based on a horizontal dispersive dipole section, for spatial momenta separation, followed by a RF-synchronised vertical deflecting system [3]. Eventually, the beam is sampled by a slit-grid setup, thereby mapping the longitudinal phase-space distribution to a two-dimensional transverse profile distribution. Besides the high costs, in general this device is not feasible to be inserted inside existing beam lines, due to its large dimension of several meters. At low energies, most accelerator facilities omit longitudinal phase-space diagnostics where altogether possible.

In this work, a new type of device is studied which aims to determine the longitudinal phase space of low and high-intensity heavy-ion beams at low energy. The measuring device has been developed by P. Forck et al. in 1999 to support commissioning of the new high-current injector line at GSI UNILAC. At present, the device is installed inside the charge-separation chicane of the UNILAC gas-stripper section. The first design targeted the measurement of longitudinal particle distribution only, also called “bunch structure” [4]. An iteration of the design [5] in 2000 allowed, in principle, the measurement of the particle momentum by means of time-of-flight and, hence, the full two-dimensional longitudinal phase space.

With the emerging upgrade of the accelerator facility, FAIR, certain design values have to be met by the existing GSI accelerator infrastructure which will serve as injector to FAIR. To reach the FAIR design values of the UNILAC high-current injector, optimisation of the matching into the Alvarez linear accelerator is one important task. Hence, the knowledge of the six-dimensional phase space near the first Alvarez tank is desirable. This work studies the feasibility of longitudinal phase-space measurements with the mentioned device. Additionally, a single-detector direct-calorimetric approach is investigated. In particular, this comprises the achievable timing resolution and the study of systematic contributions. Parts of the original data acquisition have been rewritten for the TOF system and build from scratch for the calorimetric measurement. The data analysis of the phase spaces aims for a consistent description of statistical moments by means of robust estimators.

Emphasis of this work lies on consistent analysis of a rather small amount of data which is due to the fact that the TOF-measurement setup requires single-user operation of the full accelerator facility. Thus, beam time for the experiment presented here was restricted to an absolute minimum.

The Program

Chapter 2 presents the fundamentals, the definitions of relevant terms related to phase space and emittance. Further, technical principles and details of accelerating structures.

Chapter 3

Presents experimental setup, describes experimental area and particle detectors involved, principles of coulomb scattering for beam attenuation.

Chapter 4

Shows treatment of measurement data, algorithms for post-processing for TOF and calorimetric measurements provides the background for minimum covariance determinant estimator.

Chapter 5

Test measurements with TOF and calorimetric setup.

Chapter 6

Treats the study of the limited resolution. Systematic errors, boundary conditions originating from foil imperfections and detector characteristics as well as accelerator settings and influences of the detectors.

Chapter 7

Shows the influence of the device limitations on the measurable phase space.

Chapter 8

Summarises the findings and gives an outlook for future strategies for precision phase-space measurements.

Chapter 2

Fundamentals

2.1 Macroscopic Time Structure

Depending on the type of particle accelerator, the section under consideration or the runtime configuration of the accelerator section, the time structure of the beam may be described by different characteristic parameters. Usually, linear accelerators, such as the GSI UNILAC, providing particle energies above several *MeV per nucleon* (*A*MeV), feature a macroscopic and microscopic time structure as schematically depicted in Fig. 2.1. The *macro pulse* consists of multiple *bunches* (sometimes also referred to as *micro pulses*) which are a direct result of particle acceleration using an alternating electric field (radio frequency RF). The macro-pulse structure has a different origin. Ion sources can deliver high beam intensities only for short time intervals which are typically in the order of hundreds of microseconds up to a few milliseconds at GSI [6]. Furthermore, at high beam energies and intensities, the RF power consumption of more than 1 MW and consequently the required cooling does not allow for a cw (continuous-wave) operation at reasonable expenditure. The ability to accelerate multiple ion species in an interleaved mode, sharing up to 14 distinct accelerator configurations (*virtual accelerators*) presumes a beam concept based on macro pulses. The dashed thick red line in Fig. 2.1 depicts the effective macro pulse current I_m of a single virtual accelerator. It is usually measured using beam-current transformers and represents a smoothed, averaged current of the underlying bunch train of length τ. The *repetition rate* ν_r of the macro pulses is given by the period time separating them

$$\nu_r = T_m^{-1} , \tag{2.1}$$

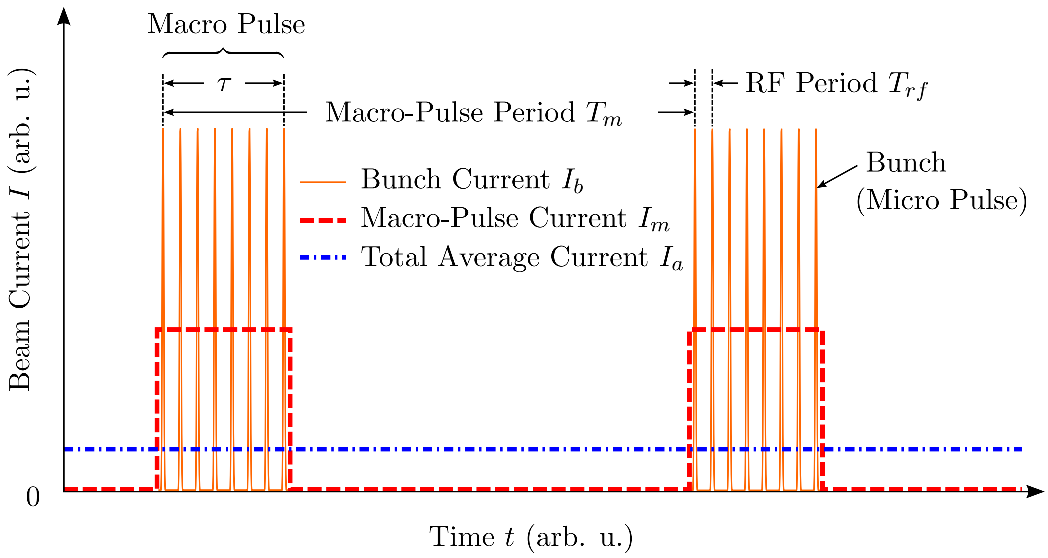

Fig. 2.1: Schematic representation of macro-pulse current I_m and bunch (micro-pulse) current I_b. The macro-pulse current I_m is typically measured using fast beam-current transformers which can resolve pulses down to several microseconds, but are incapable of resolving the time structure of the bunch current with a typical length of about a few nanoseconds (RMS).

whereas the *duty cycle* f_d is given by

$$f_d = \frac{\tau}{T_m} = \tau\,\nu_r\,. \tag{2.2}$$

Repetition rates at the GSI injector facility are based on a 50 Hz pulse to pulse time reference. They typically range from the sub-Hz regime up to 50 Hz and strongly depend on the ion source and the targeted experimental area (UNILAC or synchrotron injection). Also the requested pulse length τ and the intensity may limit the maximum repetition rate for a given source.

As denoted on Fig. 2.1 by the thin orange line, the macro pulse consists of many single bunches occurring at the frequency ν_{rf} of the accelerating RF. In total a macro pulse contains about n_τ bunches with

$$n_\tau = \frac{\tau}{T_{rf}} = \tau\,\nu_{rf}\,. \tag{2.3}$$

For a better visibility only a few bunches have been depicted in Fig. 2.1, whereas a typical macro pulse at the GSI UNILAC contains several thousands of bunches.

The important particle dynamics is related to the bunches which are described in a six-dimensional phase space. All bunches, within a virtual accelerator, are expected to be described by the same phase space distribution. The goal of this work is to present and qualify a measurement setup for determination of the longitudinal subspace.

2.2 Phase Space

For many physical systems, the *phase space* is a mathematical way to define the state of a dynamic system by the parameters of the underlying model. This concept is also applied in accelerator physics. Especially particle distributions of the actual beam are represented in the appropriate phase-space parameterisation. *Phase portraits*, on the other hand, visualise the phase-space trajectories of single particles under different boundary conditions. Taking heavy ions as reference, the beam configuration is commonly considered to be sufficiently abstracted from the position and momentum along the three spatial degrees of freedom of each ion. Thus, the ions themselves are considered as macroscopic systems, sometimes including the net charge distribution if space-charge effects are taken into account. Further degrees of freedom such as the constituents of the nucleus, the spin or the residual electronic configuration are not of relevance. The two spatial transverse degrees of freedom $\{x, y\}$ and the longitudinal degree of freedom $\{z\}$ span a six-dimensional phase space P_{6D}

$$P_{6D} = \underbrace{(x, p_x) \otimes (y, p_y)}_{\text{transverse}} \otimes \underbrace{(z, p_z)}_{\text{longitudinal}} \ , \tag{2.4}$$

by the so-called conjugate variables of the Hamiltonian theory.

During conception of accelerator sections, crucial distributions in phase space at several locations can be deduced by sophisticated simulations which help, in an iterative process, to meet the design goals. Nevertheless, real phase-space distributions of the beam may differ significantly from theoretical predictions making the measurement of the phase space indispensable during commissioning, optimisation and, to some extent, daily operation. Dedicated measurement systems are required for the transverse and longitudinal degrees of freedom. An universal approach does not exist. The availability of a feasible measurement device strongly depends on the type of particle, the desired subset of parameters to measure and the energy range at the location of measurement. The intensity of the beam as well as the required accuracy are relevant too. Other design criteria, for example if a non-interceptive device is targeted or the required performance of the data acquisition (DAQ), may represent strong limitations that cannot not be resolved. Finally, the total cost of design, construction and maintenance effort may affect availability of access to certain beam parameters.

Transverse Degree of Freedom. A common representation of the transverse subspace is given by the spatial displacement from the design beam axis $\{x, y\}$, usually based on a right-handed coordinate system, and the tangent of the corresponding divergence angle θ_x and θ_y. Thus, the momentum information is contained in the values $\{x', y'\}$ by the ratio of the transverse momentum components p_x and p_y with respect to the longitudinal momentum p_s of the reference particle (synchronous particle) or the local longitudinal central momentum $\langle p \rangle$, typically in units of mrad (since $p_{\{x,y\}} \ll p_z$):

$$\{x', y'\} = \frac{p_{\{x,y\}}}{p_s} = \tan \theta_{\{x,y\}} \tag{2.5}$$

This pragmatic choice of coordinate system for the transverse plane is mainly motivated by the direct measurement of position and divergence angle via the well established *slit-grid* method. It is a common method for measuring the transverse phase-space distribution at linear accelerators and transfer sections where the range in matter is short enough to fully stop the beam within the micrometer or millimeter regime and still be able to cool the absorbing geometry. A slit-grid measurement is a beam-destructive approach which cuts out a narrow area at certain position using a slit. After a free drift section the distribution is sampled with a wire grid, integrated over many bunches and directly provides the momentum distribution by the corresponding $\tan\theta$. To measure the full transverse phase space, the horizontal and vertical degree of freedom require a separate slit-grid module. Another beam-destructive method for measuring the full four-dimensional transverse phase space immediately with a single bunch (single shot) is the *pepperpot* device [7]. Non-interceptive methods, such as *beam induced fluorescence* (BIF [8]), allow to measure transverse density profiles.

Longitudinal Degree of Freedom. As given in Eq. (2.4), the longitudinal subspace of the phase space is spanned by the spatial location z along the beam line and the corresponding momentum p_z. However, the longitudinal subspace is often parameterised relative to a reference particle, the so-called *synchronous particle s*. The synchronous particle marks the design particle of expected behaviour along the accelerating structure or sometimes, with a lower stringency, another distinguished property such as the particle that corresponds to the first central moments of the beam under consideration. Moreover, measurements of the longitudinal plane at a certain position z_0, for example when recording the arrival time distribution of ions, suggests the use of a time equivalent parameterisation instead of the spatial distribution *at a certain time* t_0. Therefore, the arrival time Δt_i of particle i relative to the synchronous particle is chosen as

$$\Delta t_i = t_i - t_s \,. \tag{2.6}$$

The same information is contained in the phase difference

$$\Delta\phi_i = \phi_i - \phi_s \,, \tag{2.7}$$

the difference between the phase of particle i with respect to the phase of the synchronous particle s and depends on the accelerating RF. Early particles, which have smaller arrival times with respect to the synchronous particle, have larger phases. Hence, the proportionality between $\Delta\phi_i$ and Δt_i is given by

$$\Delta\phi_i \propto -\Delta t_i \,. \tag{2.8}$$

The exact relation relies on the frequency ν_{rf} of the accelerating RF

$$\Delta\phi_i = -c_{sc}\,\nu_{rf}\,\Delta t_i \qquad \text{with } c_{sc} = \begin{cases} 360^\circ & (deg) \\ 2\pi & (rad) \end{cases} \,, \tag{2.9}$$

where the coefficient c_{sc} depends on the unit *deg* or *rad*, respectively.

In addition to the plain value of the longitudinal momentum p_z, other representations are common. Apart from the absolute energy, relative fractions are given with respect to the synchronous particle for the momentum (omitting the z index)

$$\frac{\Delta p_i}{p_s} = \frac{p_i - p_s}{p_s} \tag{2.10}$$

as well as for the kinetic energy

$$\frac{\Delta E_i}{E_s} = \frac{E_i - E_s}{E_s}\,. \tag{2.11}$$

As mentioned before, the theoretical synchronous particle quantities p_s and E_s are often replaced by the mean values of the corresponding distribution, $\langle p \rangle$ and $\langle E \rangle$, for practical purposes.

2.3 Emittance

The bunch of ions, being a many-body system, can be described by the ensemble of states which represents the individual particles. While such a representation is advantageous for beam simulations of ensembles of single-particle trajectories, for example, it is not always optimal for characterisation of the beam in terms of beam diagnostics. Instead, a reduction of the phase-space distribution, as an ensemble of single particles into few characteristic parameters, is often desirable. As an analogous example, one could think of a classic ideal gas that is macroscopically characterised by its pressure, volume and temperature. Characterisation as a microscopic model, by means of the single gas particles, would be ill-suited for the majority of practical cases.

Concerning the particle distribution inside a particle accelerator, an important information is contained within the volume of the phase space which the particle distribution covers. Only a certain region of the phase space is accelerated in such a way that particles are not lost or beam quality degrades. Typically, it is possible to simulate which region of the phase space complies with stable acceleration, at a certain position along the beam line. This fraction of the six-dimensional phase-space volume is called the *acceptance* of the accelerator which depends on the operating values and the location along the beam line. For example, the longitudinal acceptance at an accelerating RF section is given by the corresponding area inside the *separatrix* (see Sec. 2.6.3).

As the acceptance represents a volume (or an area) of the phase space, it is reasonable to characterise the phase-space distribution by its extension. This quantity is called *emittance* and is a measure of the beam quality. A general aim is to reduce overall emittances by optimisations of the accelerator chain to improve on the beam quality. The emittance ε_h of a non-realistic *homogeneous* longitudinal density distribution is given trivially by the integral of the covered phase space area A

$$\varepsilon_h = \int_A \mathrm{d}\phi\,\mathrm{d}p\,, \tag{2.12}$$

where A is the smallest possible area that contains all particles. Realistic phase space densities, in contrast, are of different structure depending on the history of the bunch. This includes the initial particle emission from the ion source, further complex beam dynamics and various dissipative effects. Nevertheless, assuming a Gaussian phase-space density distribution as a model space is commonly considered to be a good approximation of the bunch. The bivariate Gaussian distribution $\{x, y\}_G$[1] is uniquely parameterised by the location of its centre and the determinant $|C|$ variance-covariance matrix

$$C = \begin{pmatrix} \sigma_{xx} & \sigma_{xy} \\ \sigma_{xy} & \sigma_{yy} \end{pmatrix} = \begin{pmatrix} \sigma_x^2 & \sigma_{xy} \\ \sigma_{xy} & \sigma_y^2 \end{pmatrix} . \tag{2.13}$$

In this nomenclature σ_{xx} and σ_{yy} are the variances of x and y whereas σ_{xy} denotes the covariance between x and y. Using the exemplary set of coordinates $\vec{v} = (\phi, p)$, denoting phase and momentum equivalents in the subscript, the centred Gaussian density distribution G_ρ is parameterised by

$$G_\rho(\phi, p; C) = \frac{1}{2\pi\sqrt{|C|}} \mathrm{e}^{-\frac{1}{2}\vec{v}\, C^{-1}\, \vec{v}^{\mathrm{T}}} = \frac{1}{2\pi\sqrt{\sigma_\phi^2\,\sigma_p^2 - \sigma_{\phi p}^2}} \,\mathrm{e}^{-\frac{\sigma_p^2\,\phi^2 - 2\,\sigma_\phi\,\sigma_p\,\sigma_{\phi p}\,\phi\, p + \sigma_\phi^2\, p^2}{2\left(\sigma_\phi^2\,\sigma_p^2 - \sigma_{\phi p}^2\right)}} . \tag{2.14}$$

By definition, while fading out quickly with increasing distance from the centre, this model density distribution covers the infinite phase space without boundary. This, of course, represents an obvious deficiency of the model space as realistic bunch distributions are always confined in phase space. On the other hand, realistic bunch distributions also contain populated phase space cells far from the core region. Therefore, using an approach as Eq. (2.12) to evaluate the phase-space extension on a Gaussian-like distribution is inappropriate. The effectively covered phase-space area would be overestimated by a large amount since a small fraction of particles has a major impact on the calculated emittance. Thus, a more reasonable and general definition of the emittance, suitable for realistic, long-ranged distributions, is the characterisation by means of the standard deviation and covariance, as implicitly provided by the covariance matrix Eq. (2.13). With the parameterisation of Eq. (2.14) this elliptical phase space area is of size

$$A_{rms} = \pi\sqrt{\sigma_\phi^2\sigma_p^2 - \sigma_{\phi p}^2} \tag{2.15}$$

and contains about 39 % of all particles provided the underlying particle distribution is indeed of Gaussian type. It should be noted, that for arbitrary particle distributions this is not generally true and might differ significantly. As proposed by Lapostolle [9] and according to Eq. (2.15) the RMS emittance is defined by the square root of the determinant of the covariance matrix

$$\varepsilon_{rms} = \sqrt{\sigma_\phi^2\sigma_p^2 - \sigma_{\phi p}^2}\,, \tag{2.16}$$

usually omitting the π.[2] This phase space area contains about 15 % of all particles in

---

[1] x and y label the degrees of freedom within one of the transversal or the longitudinal subspaces.

[2] See Chapter 3, page 91, "Charged Particle Beams" by Stanley Humphries Jr. [10] for an introduction to

case of a Gaussian density distribution. Figure 2.2 depicts the ellipse corresponding to the RMS-contour level of Eq. (2.14)

$$\sigma_p^2\,\phi^2 - 2\sigma_{\phi p}\,\phi\,p + \sigma_\phi^2\,p^2 = \varepsilon_{rms}^2\,. \tag{2.17}$$

This parametrisation directly follows from the contour line satisfying $G_\rho(\phi,p) = \sqrt{\mathrm{e}}\;G_\rho(0,0)$.

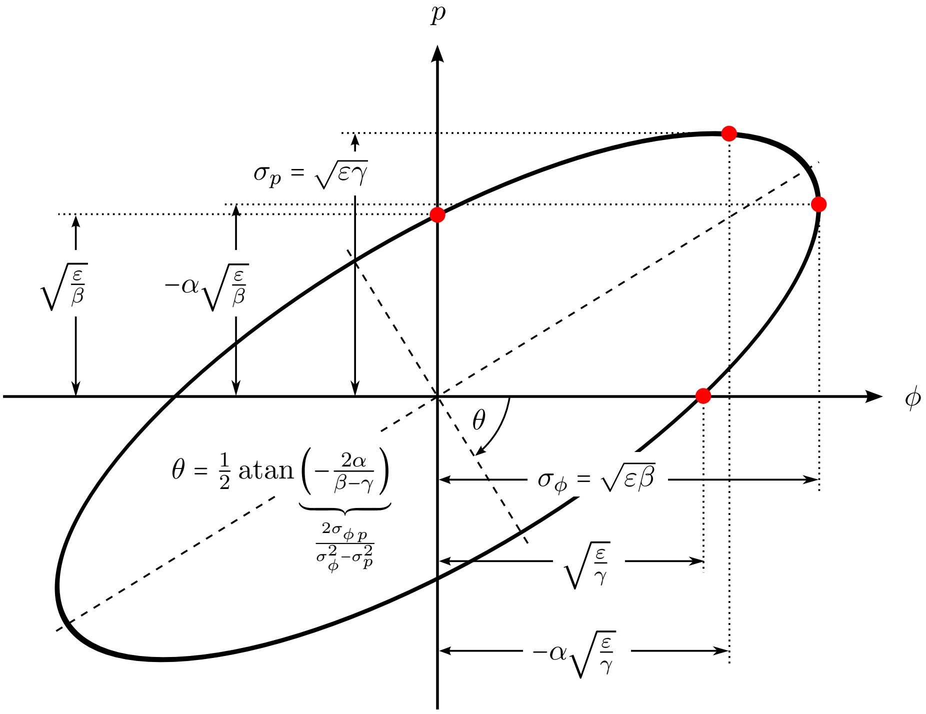

Fig. 2.2: RMS contour of elliptic phase-space density. The corresponding characteristic points are given by the standard deviations σ_ϕ, σ_p and covariance $\sigma_{\phi p}$ or, alternatively, by the emittance ε_{rms} and *Twiss parameters* α, β, γ (Sec. 2.4). Assuming a Gaussian particle density, about 39 % of all particles are covered by the area of the RMS ellipse.

Assuming no mismatch along the beam line and treating the particle distribution as a free ensemble, the emittance shrinks with increasing normalised particle velocity β_s. This *adiabatic damping* affects the transverse as well as the longitudinal emittance in the same way. More precisely, scaling of the emittance by $\beta_s\gamma_s$

$$\varepsilon_{rms}^n = \beta_s\gamma_s\varepsilon_{rms} \tag{2.18}$$

allows comparison of the emittance at different sections of the beam line at different β_s. The quantity ε_{rms}^n is called *normalised emittance* (RMS).

According to *Liouville's Theorem*, the particle density in the vicinity of a particle trajectory is conserved when the particle dynamics can be described by conservative forces within the

---

the concept of emittance plus the explanation of units which are normally used in a confusing way.

Hamilton Formalism. Then, for conservative forces only, the normalised emittance is a constant of motion. The real situation is different. Dissipative contributions are numerous and contribute to an increasing emittance or, in other words, heating of the beam. These are, for example, intra-beam scattering, space-charge forces, electronic stopping and straggling at gas or foil targets. Another effect, the so-called *filamentation*, which is not of dissipative origin, leads to a pseudo-increase of the emittance although Liouville's Theorem still holds. This is possible at acceleration sections when acceleration is carried out at the non-linear regime of the sinusoidal RF, i. e. the phase stabilising force (see Sec. 2.6.2) is not perfectly linear. Then, instead of a rigid rotation of the phase space in case of perfect focusing, particles rotate with a different velocity (in phase space) depending on the distance from the centre of the phase space and consequently impose a spiral-like structure on the phase space which eventually smoothes out over a large area. While the actual area covered by the phase space has not increased, this effect does indeed degrade the quality of the beam and is treated like a real growth of emittance. Non-linear contributions at quadrupole focusing sections show the same phenomenon for the transverse subspace, which usually results in an s-shaped phase space distribution in the x and y plane.

The emittance can be related to the entropy of the bunch distribution [11]. According to the second law of thermodynamics, the entropy of an isolated system cannot decrease with time. Equally, the normalised emittance along the beam line, parameterised by the spatial parameter s, cannot get smaller within an isolated system

$$\varepsilon^n_{rms}(s) \le \varepsilon^n_{rms}(s + \Delta s)\,. \tag{2.19}$$

The isolated system considers no particle loss and the cooling effect of beam acceleration is excluded by means of the normalised emittance. While the definition of a strictly isolated system is problematic in case of an accelerator, Eq. (2.19) still holds true. This means, in particular, that the quality of the beam is limited by the initial emittance provided by the ion source. Thus, exact determination of beam emittance ε_{rms} is crucial for accelerator optimisations.

2.4 Twiss Parameters

An alternative parameterisation of the Gaussian particle distribution is given by the *Twiss parameters* α, β and γ (see Fig. 2.2), the variances normalised by the RMS emittance $\varepsilon_{(rms)}$:

$$(-)\alpha = \frac{\sigma_{xy}}{\varepsilon} \qquad \textit{correlation} \tag{2.20}$$

$$\beta = \frac{\sigma_x^2}{\varepsilon} \qquad \gamma = \frac{\sigma_y^2}{\varepsilon} \tag{2.21}$$

The sign of α is a matter of definition and varies among different authors. In this work $\alpha = -\sigma_{xy}/\varepsilon$ is used consistently. The density distribution Eq. (2.14) expressed by the Twiss parameters and RMS emittance writes

$$G_\rho(\phi, p;\, C) \to G(\phi, p;\, \alpha, \beta, \gamma\,\varepsilon) = \frac{1}{2\pi\,\varepsilon}\,\mathrm{e}^{-\frac{1}{2\varepsilon}\left(\gamma\,\phi^2 + 2\,\alpha\,\phi\,p + \beta\,p^2\right)}\,. \tag{2.22}$$

Originally, the Twiss parameters have been introduced to describe the stable transverse motion inside periodic lattices of synchrotons by means of the so-called *machine ellipse*s and, ideally, conserved emittance. The actual shapes of the ellipses depend on the location s along the beam line parameterised by $\alpha(s)$, $\beta(s)$, $\gamma(s)$ and mark the boundary of stable transverse motion. Particle distributions that are not well matched against the machine ellipse suffer filamentation or particle loss.

While a similar concept can be extended to the longitudinal phase-space plane in case of synchrotrons, by means of longitudinal machine ellipses, this is obviously not possible at linear accelerators. Machine ellipses are only meaningful in periodic lattices. Nevertheless, Twiss parameters are widely used in the LINAC community, typically in order to reuse existing software originally tailored for transverse phase-space analysis.

If uncertainties of the standard deviations and the covariance are accessible, they can be directly mapped to the uncertainties of the RMS emittance and Twiss parameters via

$$\Delta\varepsilon \approx \varepsilon\beta\gamma\sqrt{\left(\frac{\Delta\sigma_x}{\sigma_x}\right)^2 + \left(\frac{\Delta\sigma_y}{\sigma_y}\right)^2 + \left(\frac{\alpha^2}{1+\alpha^2}\right)^2\left(\frac{\Delta\sigma_{xy}}{\sigma_{xy}}\right)^2}\,, \tag{2.23}$$

$$\Delta\alpha \approx \alpha\beta\gamma\sqrt{\left(\frac{\Delta\sigma_x}{\sigma_x}\right)^2 + \left(\frac{\Delta\sigma_y}{\sigma_y}\right)^2 + \left(\frac{\Delta\sigma_{xy}}{\sigma_{xy}}\right)^2}\,, \tag{2.24}$$

$$\Delta\beta \approx \beta\sqrt{(1-\alpha^2)^2\left(\frac{\Delta\sigma_x}{\sigma_x}\right)^2 + (1+\alpha^2)^2\left(\frac{\Delta\sigma_y}{\sigma_y}\right)^2 + \alpha^4\left(\frac{\Delta\sigma_{xy}}{\sigma_{xy}}\right)^2}\,, \tag{2.25}$$

$$\Delta\gamma \approx \gamma\sqrt{(1+\alpha^2)^2\left(\frac{\Delta\sigma_x}{\sigma_x}\right)^2 + (1-\alpha^2)^2\left(\frac{\Delta\sigma_y}{\sigma_y}\right)^2 + \alpha^4\left(\frac{\Delta\sigma_{xy}}{\sigma_{xy}}\right)^2}\,. \tag{2.26}$$

2.5 Linear Accelerators

Acceleration of charged particles using static electric fields is limited by a specific breakdown voltage, usually several hundreds of kilovolts, depending on dielectric strength, surface properties and geometry of the acceleration structure. At the top end there are *Van-de-Graaff*-type accelerators which can even provide an effective voltage of about 10 MV.

This limitation can be overcome by a regular setup of shielding drift tubes with a time-varying electric field applied between the gaps. This RF power is commonly fed into a cavity in an appropriate way, usually inductively or via waveguides, whereas the geometry determines the preferred resonant mode. Since the net energy transfer to a charged particle in a harmonically oscillating electric field is zero, shielding of the particles has to be accomplished during the decelerating half cycle of the local RF voltage using appropriate drift-tube geometries. Between the drift tubes (gaps), the beam particles are consequently exposed to an accelerating voltage and thus a synchronised and coherent net energy transfer is provided. Depending on the particle velocity, the drift tubes therefore have to be designed in such a way, that their axial lengths scale linearly with increasing average normalised particle velocity $\langle\beta\rangle = \frac{\langle v\rangle}{c}$.

2.5.1 Wideröe Structures

In 1928 Rolf Wideröe suggested the first practicable concept of such a *drift-tube linear accelerator* structure (DTL [12]). As depicted in the upper half of Fig. 2.3, a schematic Wideröe structure, the drift tubes of increasing length are directly fed by the ac power with successive electrodes being of opposite electric potential. Coherent acceleration of particles requires the time-dependent longitudinal electric field

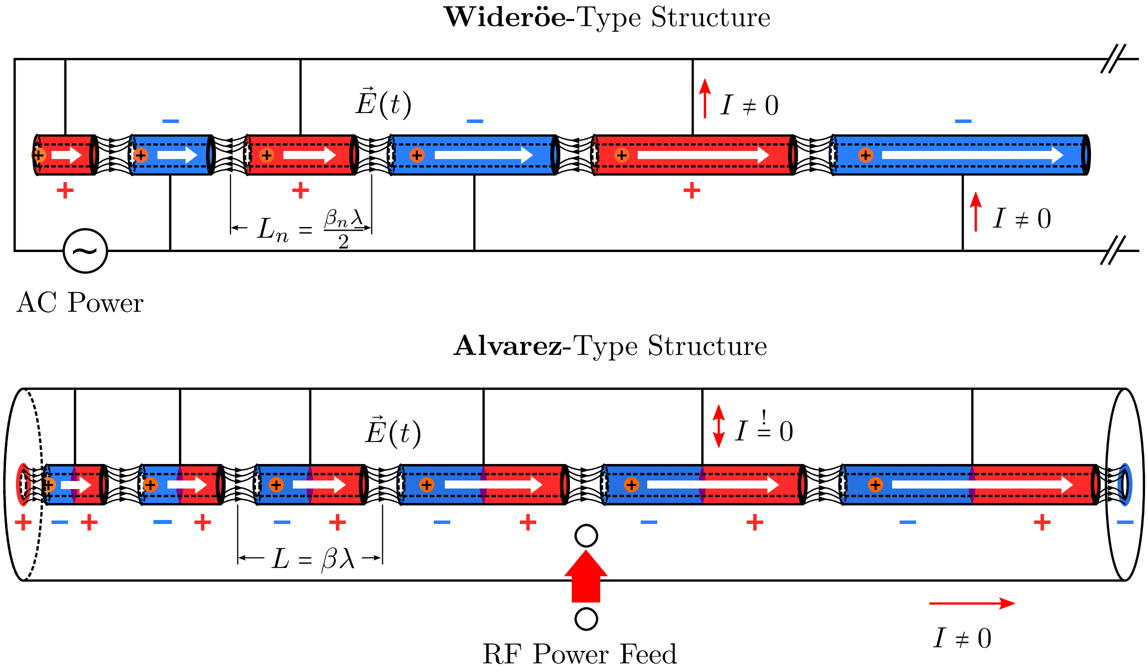

Fig. 2.3: Schematic linear accelerator structures of Wideröe (top) and Alvarez (bottom) type. The improved Alvarez cavity in comparison to the Wideröe includes transverse focusing cells inside the drift tubes to accommodate for the net defocusing effect (transverse) at the gap.

$$E_z(t,z) = E_0 \cos\left(\phi_{\omega,k_z}(t,z)\right) \qquad (\text{with } \phi_{\omega,k_z}(t,z) = \omega_{rf} \cdot t - k_z \cdot z) \tag{2.27}$$

to have the same phase velocity $v_{ph} = \frac{\omega_{rf}}{k_z}$ as the current centre velocity βc of the particle at the drift section under consideration. Contiguous gaps between Wideröe drift tubes have a phase advance $\Delta\phi_{\omega,k_z,n}$ of 180° which means successive gaps contain oppositely oriented, longitudinal electric field components at all times. With n labeling the n-th drift section under consideration, the corresponding length of the drift tube is therefore implicitly given by

$$\Delta\phi_{\omega,k_z,n+1}\big|_t = \phi_{\omega,k_z}(t,z) - \phi_{\omega,k_z}(t,z+L_n) = k_z\,L_n \overset{!}{=} \pi\,. \tag{2.28}$$

As mentioned above, the phase velocity v_{ph} of the electric field has to be about the same as the mean longitudinal velocity βc of the particle distributions (the *bunches*) traversing the drift tube. It follows from Eq. (2.28) with $v_{ph} = \frac{\omega_{rf}}{k_z} \overset{!}{=} \beta c$ that the length L_n of the Wideröe drift tubes scales with increasing β_n as

$$L_n = \frac{\pi}{k_{z,n}} = \frac{\pi}{\omega_{rf}} \beta_n c = \frac{\beta_n \lambda}{2} . \tag{2.29}$$

Drift tube LINACs generally come with the inherent issue, that the dynamic electric field between the tubes is not perfectly homogeneous as shown in Fig. 2.3. At gap entrances, the field lines have transverse focusing properties whereas at gap exit a transverse defocusing characteristic is present. As a consequence, the overall net defocusing effect causes an additional transverse beam spread which limits the performance of the accelerating structure. The Wideröe LINAC marks an archaic approach by today's standards. At GSI the first UNILAC design featured a Wideröe structure which served as the full prestripper section after the so-called LEBT (Low Energy Beam Transfer). As of 1999 it was replaced by a modern two stage design, consisting of a RFQ and two H-mode KONUS IH structures (see Sec. 2.5.3), to allow for higher beam intensities [13].

2.5.2 Alvarez Structures

With the iteration of the DTL concept by W. L. Alvarez [14], the *Alvarez structure*, drift tubes are housed in a circular cavity. Instead of a direct AC feed of the drift tube electrodes, a cavity is driven in resonance by the TM_{010} mode which provides the matching electric fields for particle acceleration. Contrary to the empty cavity resonating on a E-mode (or TM-mode) which features no transverse electric field component by definition, the boundary conditions of the support and drift-tube geometry impose a non-vanishing transverse electric field component nearby the gap region which, together with the RF, has an overall transverse defocusing effect. This is counteracted by the inclusion of adequate quadrupole layouts inside the drift tube geometry. Active transverse focusing together with the cavity approach confining the RF power, a much higher efficiency is accomplished compared to the Wideröe structure. According to the TM-mode characteristics, charges flow along the cavity wall and the electrode geometry only (there is no current along the stems). Concerning the length of the drift tubes, the phase advance between successive gaps is 2π and, thus, the length L_n of the n-th drift tube is given by

$$L_n = \frac{2\pi}{k_{z,n}} = \beta_n \lambda . \tag{2.30}$$

The lower half of Fig. 2.3 depicts a schematic Alvarez structure with the typical circular cavity profile and drift tubes of increasing length. An *Alvarez period* consists of a drift tube including the aforementioned transverse focusing elements along with appropriate cooling and an acceleration gap between them. Acceleration is carried out using the TM_{010} mode of the empty cavity. By insertion of the drift tube cell structure a dominant longitudinal electric field component along the beam axis is conserved due to symmetry considerations and is even increased locally.

Alvarez structures are still used while more sophisticated accelerating structures with a higher effective field gradient exist. On the other hand maintenance effort is low and the design is well understood due to its simplicity. A 4-stage Alvarez structure and several single gap resonators serve as final accelerating structure of the UNILAC complex.

2.5.3 H-mode Structures

More efficient, modern heavy ion linear accelerating structures than the Alvarez approach are the so-called *H-mode LINAC Structures*, also referred to as *H-type LINAC Structures* [15]. Contrary to the Wideröe (if driven by a cavity) or the Alvarez structure, the H-mode (TE-mode) has no longitudinal electric field component in the empty cavity by definition. Only due to sophisticated boundary conditions by the geometry of the stems and drift tubes (or crossbars respectively), longitudinal acceleration is accomplished with the advantage of a significantly enhanced effective field gradient compared to Alvarez-type DTLs. Although all H-Type cavities are based on H_{n10}-modes, one can differentiate between two major cavity designs: The 'Interdigital H-Type Structure' (IH) using the H_{110}-mode and the 'Crossbar H-Type Structure' (CH) used in the high β range resonating on the H_{210}-mode. As there are no relevant longitudinal wall currents present, since the electric field mode is fully transverse at least in the empty cavity, power losses are significantly lower compared to the Alvarez design.

KONUS Beam Acceleration. H-mode structures have been suggested already in the 70s to improve the power efficiency per unit length. Further improvements on the effective gradient can be accomplished by the concept of 'Combined Zero-Degree Structure' ('**KO**mbinierte **NU**ll-Grad **S**truktur', KONUS, [16]). A *KONUS period* consists of a 0° synchronous particle structure at which the beam is injected above synchronous particle energy, a separate transverse focusing section by a quadrupole triplet or a solenoid and a longitudinal focusing section at typically $\phi_s = -35°$, usually referred to as *rebunching section*. Instead of transverse focusing elements being housed in each drift tube, the separate focusing section allows a compact LINAC design with an enhanced number of accelerating gaps per unit length compared to the Alvarez design. At the same time, the apertures of the drift tubes can be significantly reduced which further improves the shunt impedance and, thus, the power efficiency of the LINAC structure. Also the plain acceleration section at crest voltage alone provides about 15 % improvement in efficiency (regarding the same amplitude) of the synchronous particle gradient per acceleration gap compared to Alvarez structures.

From a beam dynamics point of view, KONUS is a delicate challenge. A H-mode cavity design using KONUS is an intuitive approach based on experience with no straightforward design recipe available. This effectively ends up in a trial and error approach using simulated dynamic field distributions and particle tracking codes at hand. Most efficient acceleration at 0° phase comes at the cost of unstable, i. e. defocusing particle trajectories with respect to the synchronous particle. While the longitudinal broadening of the bunch length is counteracted by the separate rebuncher section, the influence of the strong nonlinearity of voltage around 0° cannot be fully compensated and may have an influence on the longitudinal phase space distribution by filamentation. Although filamentation is not a process that causes an increase of the emittance, since it cannot be classified as a dissipative effect which leads to an increase of the covered phase-space area, it does indeed increase

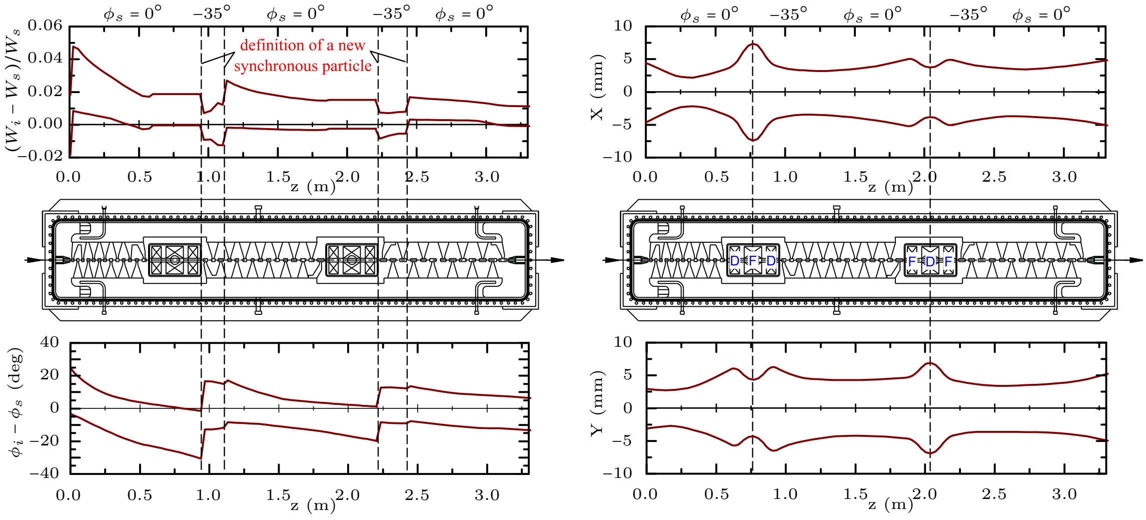

(Calculations and graphics *Rudolf Tiede*, IAP, Frankfurt)

Fig. 2.4: KONUS driven H-Type (IH) structure cell at GSI High Charge Injector (HLI). **Left**: The relative energy deviation (top) and deviation from synchronous phase (bottom), along the accelerating structure, for two different start conditions. **Right**: The transverse envelopes for two different start conditions.

the boundaries of a phase space distribution and, thus, introduces higher requirements on the acceptance.

The first KONUS driven cavity has been installed at GSI at the UNILAC as part of the *high current injector* in 1999 and partial replacement for the Wideröe LINAC. A KONUS cavity has been also the predestined choice of design for the *high charge injector* (HLI) due to its high effective gradient. As an exemplary tracking simulation of KONUS, Fig. 2.4 shows the new GSI HLI structure. Apart from the aforementioned KONUS period, the complicated beam dynamics compared to the Alvarez design can be seen by the required redefinition of the synchronous particle during acceleration. This manifests itself by unsteady jumps of the tracked particle observables in the left graphics, showing the relative energy deviation and the relative phase. Design, commissioning and operating of KONUS structures can be challenging, but is considered worthwhile if highest requirements of effective gradient and beam intensity have to be met. To that end, reliable beam diagnostics of transverse and in particular longitudinal degree of freedom is mandatory which is the goal of the measurement setup studied in this work.

2.6 Longitudinal Beam Dynamics

To get a glimpse on the importance of longitudinal beam diagnostics targeted in this work it is helpful to outline basic theoretical concepts of drift-tube LINACs used at the GSI injector line. Wideröe and Alvarez structures (see Sec. 2.5.2) follow a common acceleration scheme. Along the beam axis, at the gap between the shielding drift tubes, a quasi-harmonic oscillating potential provided by the TM_{010} mode accelerates the transiting charged particles. Similarly, H-mode LINACs in turn use H_{n10} modes to accelerate the beam as described in Sec. 2.5.3 and the following explanation can be applied likewise. Due to the specific geometries and significant beam effects such as inter-particle space-charges, the design and optimization of modern linear accelerator structures require the use of sophisticated *tracking codes*, e. g. LORASR [17], DYNAMION [18] or PARMILA [19]. Nevertheless, it is possible to analytically model major properties of linear accelerators qualitatively. In the following, the energy gain and the longitudinal equation of motion will be described under simplified boundary conditions.

2.6.1 Energy Gain during Gap Transition

Acceleration of charged particles takes place at the gaps between the drift tubes. While the space inside the drift tube is assumed to be field-free, the electric field still reaches inside to a small extent. The relevant longitudinal electric field component amplitude $E_z(r, z)$ is depicted in Fig. 2.5 for the axial case $r = 0$. To account for the electric field reaching inside the tube volume, the effective gap length g_{eff} is taken into consideration. Since the exact electric field distribution depends on the specific accelerator geometry, an exemplary on-axis amplitude distribution is shown. Several numerical frameworks exist to calculate static and dynamic electro-magnetic field properties from the actual geometry of the accelerator cavity. Usually it is legitimate to consider $E_z(r, z)$ to be symmetric with respect to the centre of the gap. In the following the energy is denoted by W to avoid confusing with the electric field E. Using the time-dependent longitudinal electric field E_z as given by Eq. (2.27), we can write the energy gain ΔW_i of a particle i transiting the gap as

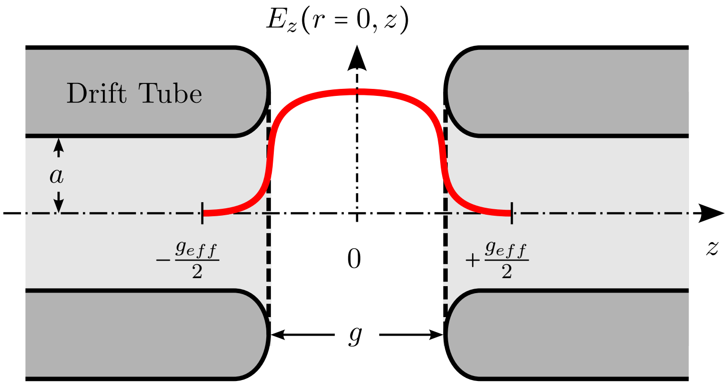

Fig. 2.5: Schematic longitudinal electric field amplitude at an acceleration gap. The electric field is not perfectly shielded inside the drift tubes which is taken into account by the effective bounds $\pm g_{eff}/2$.

$$\Delta W_i = q \cdot \int_{-g_{eff}/2}^{+g_{eff}/2} \mathrm{d}z \; E_z(0,z) \cos\left(\omega_{rf} \cdot t + \phi_i\right) = q \cdot \int_{-g_{eff}/2}^{+g_{eff}/2} \mathrm{d}z \; E_z(0,z) \cos\left(\frac{\omega_{rf}}{\beta_i c} z + \phi_i\right) , \qquad (2.31)$$

where g_{eff} denotes the effective gap length and accounts for the incomplete shielding of the field inside the drift tubes. The maximum potential difference U_0 exposed to a theoretical particle with an infinite velocity is therefore given by

$$U_0 = \int_{-g_{eff}/2}^{+g_{eff}/2} \mathrm{d}z \; E_z(0,z)\,, \tag{2.32}$$

whereas an actual particle i would see an effective potential difference $U_{eff,i}$ of

$$U_{eff,i} = \int_{-g_{eff}/2}^{+g_{eff}/2} \mathrm{d}z \; E_z(0,z) \cos\left(\frac{\omega_{rf}}{\beta_i c}\, z + \phi_i\right)\,, \tag{2.33}$$

by assuming a constant velocity approximately at the gap under consideration for simplicity. Furthermore, with the assumed mirror symmetry of $E_z(r,z)$ with respect to $z = 0$ and the symmetric integral limits, Eq. (2.33) is identical to

$$U_{eff,i} = \cos\phi_i \cdot \int_{-g_{eff}/2}^{+g_{eff}/2} \mathrm{d}z \; E_z(0,z) \cos\left(\frac{\omega_{rf}}{\beta_i c}\, z\right)\,. \tag{2.34}$$

A common approach to account for the effective gradient and thus the effective energy gain of the particle is to introduce the so-called *transit time factor*

$$T = \frac{\left|U_{eff,s}\right|}{U_0} = \frac{\left| \int_{-g_{eff}/2}^{+g_{eff}/2} \mathrm{d}z \; E_z(0,z) \cos\left(\frac{\omega_{rf}}{\langle\beta\rangle c}\, z\right) \right|}{\int_{-g_{eff}/2}^{+g_{eff}/2} \mathrm{d}z \; E_z(0,z)} \cos\phi_s \le 1\,. \tag{2.35}$$

Characteristically, the actual value of T scales inversely with the ratio of the effective gap length g_{eff} versus the RF wavelength. Time transit factors range from 0.8 to 0.9, with shorter gaps usually reaching higher values depending on the actual gap geometry. The energy gain Eq. (2.31) for the synchronous particle at gap transition can be rewritten as

$$\Delta W_s = q\, U_0\, T\, cos\,\phi_s\,. \tag{2.36}$$

Introducing the effective mean electric field amplitude

$$E_{z,0} = \frac{U_0}{g_{eff}} = \frac{1}{g_{eff}} \int_{-g_{eff}/2}^{+g_{eff}/2} \mathrm{d}z \; E_z(0,z)\,, \tag{2.37}$$

the energy gain for any particle i, but especially the synchronous particle s can finally be expressed as

$$\Delta W_s = q\, E_{z,0}\, g_{eff}\, T\, \cos\phi_s = q\, U_{eff,s}\, \cos\phi_s \tag{2.38}$$

by means of the effective voltage U_{eff} and the synchronous phase ϕ_s.

2.6.2 Longitudinal Phase Stability

Real particle distributions inside a linear accelerator have a finite second moment attached to all degrees of freedom. In other words this means a finite phase space volume or, in the terminology commonly referred to in accelerator physics, emittance. The initial particle distribution provided by the ion source usually already comes with a pronounced emittance. According to Sec. 2.6.1, the energy gain depends on the relative phase ϕ_i of the particle with respect to the RF voltage. Based on the fact that the longitudinal (as well as the transverse) particle distribution is neither a sharp distribution in phase nor momentum, the principle of acceleration must be chosen in a way, that it can provide a stabilised motion. This means stabilised in the sense of phase stability and therefore the quest to keep the particles as localised as possible during acceleration. In the following, phase stability is discussed taking the relative phase ϕ_i with respect to the RF as the free parameter.

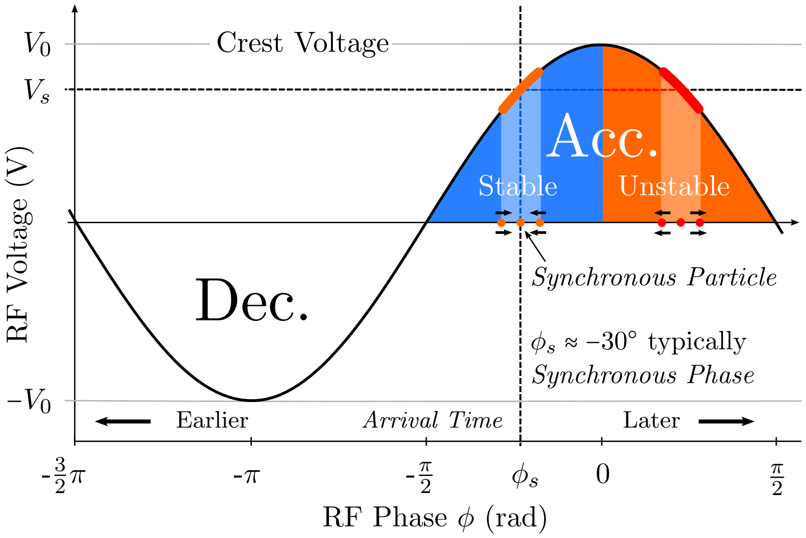

Fig. 2.6: Schematic RF voltage between drift tubes for negatively-charged particle. In this picture particles to the left of the synchronous particle are advanced, whereas particles to right are retarded. For a stable longitudinal motion at linear accelerators only the region (marked as *stable*) is useful for acceleration.

Fig. 2.6 shows the schematic RF voltage applied between the drift tubes. With the phase origin usually located at crest voltage, the stable acceleration region at $[-\frac{\pi}{2}, 0] + n\cdot 2\pi$ (blue section), where n numbers a unique period, is commonly referred to as a *bucket* with the corresponding confined, stable phase space distribution referred to as a *bunch* or *micro pulse*. A more precise definition of a *bucket* will be given in Sec. 2.6.3, when a simplified longitudinal equation of motion is explicitly solved. The operation value of the *synchronous phase* ϕ_s, which is the reference phase of the design particle (*synchronous particle*) with respect to the RF, is typically set at around −30°. For typical Gaussian-like particle distributions, most particles with a surplus of energy compared to the *synchronous particle* i_s arrive at an earlier time/phase and as such undergo less acceleration. Together with the fact, that particles of a lower energy than i_s get accelerated by a larger effective voltage, this illustrates the longitudinal focusing effect with respect to the synchronous particle. On the other hand, the phase range $[0, \frac{\pi}{2}] + n \cdot 2\pi$, while also accelerating, has an intrinsic, longitudinally defocusing tendency as depicted in Fig. 2.6 and is labeled as *unstable* region. It should be noted that the design decisions for the location of the synchronous phase mainly depend on the bunch length. Shorter bunch lengths allow for a more efficient synchronous phase nearer to the crest voltage without losing many particles to the unstable region and thus a more effective acceleration. Nevertheless, following the sinusoidal schematic from Fig. 2.6 it is obvious that approaching 0° phase comes with increasing nonlinear force and therefore increasing size of the phase space.

Unfortunately, longitudinal and transverse focusing at the same time is impossible using a drift tube acceleration. At sections that have a net *longitudinal focusing* effect they contribute to a net *transverse defocusing* effect. From a qualitative point of view this is evident by the topology of the electric field inside the accelerating gap as depicted schematically in Fig. 2.3. At gap entrance the transverse field components possess focusing properties, and they are defocusing the second half of the gap. Since the field amplitude is ramped while the bunch is transiting the acceleration gap, the defocusing effect at the second half is dominating, assuming a constant normalised particle velocity β for simplification. A more elaborate discussion of the topic was published first by E.M. McMillan in 1950 [20]. Usually the inherent effect of transverse defocusing needs to be compensated by separate focusing elements, i. e. magnetic quadrupole or solenoidal lenses.

2.6.3 Longitudinal Equation of Motion

For a better understanding of the characteristics of common DTL beam dynamics, this section provides the derivation of a simplified equation of motion of the longitudinal degree of freedom. Furthermore, it highlights the advantage if access to the longitudinal degree of freedom is available by beam diagnostics which allows monitoring and optimisation of the beam line. For instance the knowledge of a longitudinal phase-space distribution can either serve as feedback to see if a LINAC is well adjusted or to pin down the starting condition for the setup of the following structures to provide optimal matching conditions.

This section will outline the derivation of the equation of longitudinal particle dynamics under simplified boundary conditions roughly following T. P. Wangler [21]. The discrete acceleration structure is approximated as a continuous differential equation under the assumption of a space-charge free, paraxially approximated system. Furthermore, the rate of acceleration is assumed to be sufficiently small to consider the terms $\frac{\mathrm{d}}{\mathrm{d}z}\beta$ and $\frac{\mathrm{d}}{\mathrm{d}z}\gamma$ negligible with respect to other terms. By switching over to a continuous description, the accelerating fields will be replaced by effective mean fields.

In the following, the separation between two contiguous gap centres is labeled by L_n for the n-th acceleration cell, at which the normalised velocity β_n and the energy W_n are treated as constant. Additionally, within the *thin gap approximation* the energy is instantaneously transferred to the particle at the gap centre by the effective voltage $U_{eff,n}$ after the $(n-1)$-th drift section. Thus, the kinetic energy gain[3] $\Delta W_{n,i}$ between the $(n-1)$-th and n-th drift section for an *arbitrary particle* i is given by

$$\Delta W_{n,i} = W_{n,i} - W_{n-1,i} = q\, U_{eff,n} \cos\phi_{n,i} \tag{2.39}$$

using Eq. (2.38). Taking the *synchronous particle* s as reference, the difference in energy gain therefore writes as

$$\Delta(W_i - W_s)_n = \Delta W_{n,i} - \Delta W_{n,s} = q\, U_{eff,n} \left(\cos\phi_{n,i} - \cos\phi_{n,s}\right) . \tag{2.40}$$

By design, the phase advance $\Delta\phi_{n,s}$ for the synchronous particle is

$$\Delta\phi_{n,s} = N \cdot 2\pi \qquad N = \begin{cases} \frac{1}{2}, & \text{Wideröe, IH} \\ 1, & \text{Alvarez} \end{cases} . \tag{2.41}$$

On the other hand, the fraction of phase advance between an arbitrary and synchronous particle at the $(n-1)$-th cell equals the fraction of their transit times

$$\frac{\Delta\phi_{n,i}}{\Delta\phi_{n,s}} = \frac{\Delta\phi_{n,i}}{N\, 2\pi} \overset{!}{=} \frac{T_{n-1,i}}{T_{n-1,s}} = \frac{\beta_{n-1,s}\,\lambda}{\beta_{n-1,i}\,\lambda} = \frac{1}{N} \frac{L_{n-1}}{\beta_{n-1,i}\,\lambda} , \tag{2.42}$$

recalling the length L_n of the n-th cell is $N \cdot \beta_{n,s}\,\lambda$. Consequently, an arbitrary particle has its phase changed by

$$\Delta\phi_{n,i} = 2\pi \frac{L_{n-1}}{\beta_{n-1,i}\,\lambda} \tag{2.43}$$

between gap $n-1$ and gap n. This allows to calculate the difference in phase advance between an arbitrary and the synchronous particle accumulated after transit of the $(n-1)$-th cell with

$$\begin{aligned} \Delta(\phi_i - \phi_s)_n &\overset{!}{=} \Delta\phi_{n,i} - \Delta\phi_{n,s} = 2\pi \frac{L_{n-1}}{\lambda} \left(\frac{1}{\beta_{n-1,i}} - \frac{1}{\beta_{n-1,s}} \right) \\ &= 2\pi \frac{L_{n-1}}{\lambda} \left(\frac{1}{\beta_{n-1,s} + \underbrace{\beta_{n-1,i} - \beta_{n-1,s}}_{=:\Delta\beta}} - \frac{1}{\beta_{n-1,s}} \right) = 2\pi \frac{L_{n-1}}{\lambda} \left(\frac{1}{\beta_{n-1,s} + \Delta\beta} - \frac{1}{\beta_{n-1,s}} \right) , \end{aligned} \tag{2.44}$$

which can be further simplified by exploiting that $\frac{\Delta\beta}{\beta_{n-1,s}} \ll 1$ and thus

$$\Delta(\phi_i - \phi_s)_n \approx -2\pi \frac{\Delta\beta}{\beta_{n-1,s}^2} = -2\pi \frac{\beta_{n-1,i} - \beta_{n-1,s}}{\beta_{n-1,s}^2} . \tag{2.45}$$

---

[3] As in Sec. 2.6.1, the energy is denoted by W to avoid confusion with the electric field E.

The work ΔW required to change the normalised velocity by the amount of $\Delta\beta$ taking into account the linear term only

$$\Delta W = \Delta\left(E - E_0\right) = \Delta E \approx \frac{\mathrm{d}E}{\mathrm{d}\beta}\Delta\beta = \left(\frac{\mathrm{d}}{\mathrm{d}\beta}m_0\gamma c^2\right)\Delta\beta = E_0\,\frac{\mathrm{d}\gamma}{\mathrm{d}\beta}\,\Delta\beta = E_0\,\gamma^3\,\beta\,\Delta\beta \tag{2.46}$$

and Eq. (2.45) provides the relationship between the change in phase deviation and energy deviation with respect to the synchronous particle at the n-th cell

$$\Delta(\phi_i - \phi_s)_n = -2\pi\frac{W_{n-1,i} - W_{n-1,s}}{m_0\,c^2\,\gamma^3_{n-1,s}\,\beta^2_{n-1,s}}\,. \tag{2.47}$$

As mentioned before, the discrete model based on the real cell structure is replaced by a continuous model treating the electric fields as general mean field along the beam axis with $E_{z,0} = \frac{V_0}{L_{n-1}}$. By formally going from $\frac{\Delta}{L_{n-1}}$ to $\frac{\mathrm{d}}{\mathrm{d}z}$ and dropping the discrete index n, the relative energy deviation Eq. (2.40) writes as

$$\frac{\Delta\left(W_i - W_s\right)}{L_{n-1}} \quad\longrightarrow\quad \frac{\mathrm{d}}{\mathrm{d}z}\left(W_i - W_s\right) = q\,E_{z,0}\,T\,\left(\cos\phi_i - \cos\phi_s\right)\,. \tag{2.48}$$

In the same way the relative phase deviation $\Delta(\phi_i - \phi_s)_n$ transforms into a continuous representation

$$\frac{\mathrm{d}}{\mathrm{d}z}\left(\phi_i - \phi_s\right) = \frac{\Delta(\phi_i - \phi_s)}{L_{n-1}} = \frac{\Delta(\phi_i - \phi_s)}{\beta_{n-1}\lambda} \tag{2.49}$$

and is connected to the change in relative energy deviation by Eq. (2.47)

$$\frac{\mathrm{d}}{\mathrm{d}z}\left(\phi_i - \phi_s\right) = -2\pi\frac{W_i - W_s}{m_0\,c^2\,\gamma_s^3\,\beta_s^3\,\lambda}\,. \tag{2.50}$$

Derivation by $\frac{\mathrm{d}}{\mathrm{d}z}$ and inserting Eq. (2.48)

$$\frac{\mathrm{d}}{\mathrm{d}z}\left\{\gamma_s^3\,\beta_s^3\frac{\mathrm{d}}{\mathrm{d}z}\left(\phi_i - \phi_s\right)\right\} = -\frac{2\pi\,q\,E_{z,0}\,T}{m_0\,c^2\,\lambda}\left(\cos\phi_i - \cos\phi_s\right) \tag{2.51}$$

provides a second order differential equation from two coupled first order differential equations. Furthermore, the rates of change $\frac{\mathrm{d}\beta_s}{\mathrm{d}z}$ and $\frac{\mathrm{d}\gamma_s}{\mathrm{d}z}$ at the acceleration gap are usually small compared to their value. Neglecting those terms, the final problem reads as

$$\frac{\mathrm{d}^2}{\mathrm{d}z^2}\left(\phi_i - \phi_s\right) = -\frac{2\pi\,q\,E_{z,0}\,T}{m_0\,c^2\,\gamma_s^3\,\beta_s^3\,\lambda}\left(\cos\phi_i - \cos\phi_s\right)\,. \tag{2.52}$$

Fortunately, given by the approximations used, this differential equation can be solved analytically. Multiplication with $\frac{\mathrm{d}}{\mathrm{d}z}\left(\phi_i - \phi_s\right)$, which is identical to $\frac{\mathrm{d}\phi_i}{\mathrm{d}z}$, and applying the inverse product rule on the left side

$$\mathrm{d}\left\{\frac{1}{2}\left(\frac{\mathrm{d}}{\mathrm{d}z}\left(\phi_i - \phi_s\right)\right)^2\right\} = -\frac{2\pi\,q\,E_{z,0}\,T}{m_0\,c^2\,\gamma_s^3\,\beta_s^3\,\lambda}\left(\cos\phi_i - \cos\phi_s\right)\,\mathrm{d}\phi_i \tag{2.53}$$

simplifies the problem significantly as Eq. (2.50) can replace $\left(\frac{\mathrm{d}}{\mathrm{d}z}\left(\phi_i - \phi_s\right)\right)^2$. This in turn provides a trivial way to integrate both sides. In doing so, the boundary condition is contained within the constant of integration C

$$\frac{\pi\,\left(W_i - W_s\right)^2}{m_0\,c^2\,\gamma_s^3\,\beta_s^3\,\lambda} = -q\,E_{z,0}\,T\,\left(\sin\phi_i - \phi_i\,\cos\phi_s + C\right) \tag{2.54}$$

and finally rearranged the kinetic energy deviation $W_i - W_s$ is given by

$$W_i - W_s = \pm\sqrt{\frac{1}{\pi} m_0\,c^2\,\gamma_s^3\,\beta_s^3\,\lambda\,q\,E_{z,0}\,T\,\left(\phi_i\,\cos\phi_s - \sin\phi_i - C\right)}\,. \tag{2.55}$$

For different start conditions, imposed by C, Eq. (2.55) provides the corresponding phase space trajectories. The *separatrix* is a special trajectory which marks the boundary of stable particle motion with the corresponding integration constant C_s

$$C_s = -\left(\phi_s\cos\phi_s - \sin\phi_s\right)\,. \tag{2.56}$$

It is now possible to refine the definition of a *bucket* (section 2.6.2) as the phase space area enclosed by the separatrix bound. At the same time this represents the acceptance of the LINAC section as stated in Sec. 2.3.

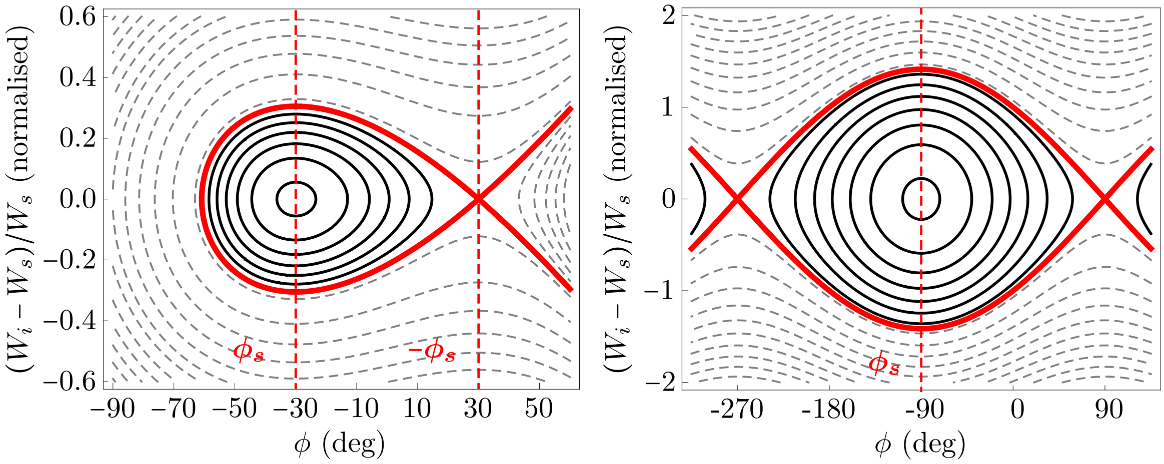

Fig. 2.7: Left: Longitudinal phase portrait for acceleration with a synchronous particle at $\phi_s = -30°$. The *separatrix* (red, thick curve) marks the boundary for the stable and confined phase space area. **Right**: Longitudinal phase portrait for a synchronous phase of $\phi_s = -90°$. The phase space area covered by the separatrix is maximal, but the beam undergoes no net acceleration with the accelerator acting as a buncher at optimum linearity. This phase portrait is well known from the classical harmonic oscillator.

Figure 2.7 shows the phase portrait for a synchronous phase $\phi_s = -30°$ on the left, which is typically used in Alvarez structures or rebunching sections at KONUS structures. The right of Fig. 2.7 depicts the phase portrait with a synchronous phase of $\phi_s = -90°$, which means operation in pure bunching mode and no net acceleration. The energy axis is displayed in the commonly used representation of the relative energy deviation [4]

$$\frac{W_i - W_s}{W_s} = \pm\sqrt{\underbrace{\frac{\gamma_s^3\,\beta_s^3\,\lambda\,q\,E_{z,0}\,T}{\pi\,m_0\,c^2\,\left(\gamma_s - 1\right)^2}}_{\xi}\left(\phi_i\,\cos\phi_s - \sin\phi_i - C\right)}\,. \tag{2.57}$$

Both portraits show the separatrix as a thick line with the stable orbits enclosed as continuous lines, the unstable trajectories are marked by dashed lines. Around the synchronous phase ϕ_s, for small amplitudes $\Delta\phi$, the orbits are of elliptic shape. Furthermore, the enclosed areas differ significantly. Thus, the acceptance during acceleration at $\phi_s \approx -30°$ is much smaller compared to pure bunching at $\phi_s = 0°$. It should be noted that in reality, due to the acceleration and thus a shrinking phase space, the stable orbits are not closed in the $\phi_s = -30°$ case.

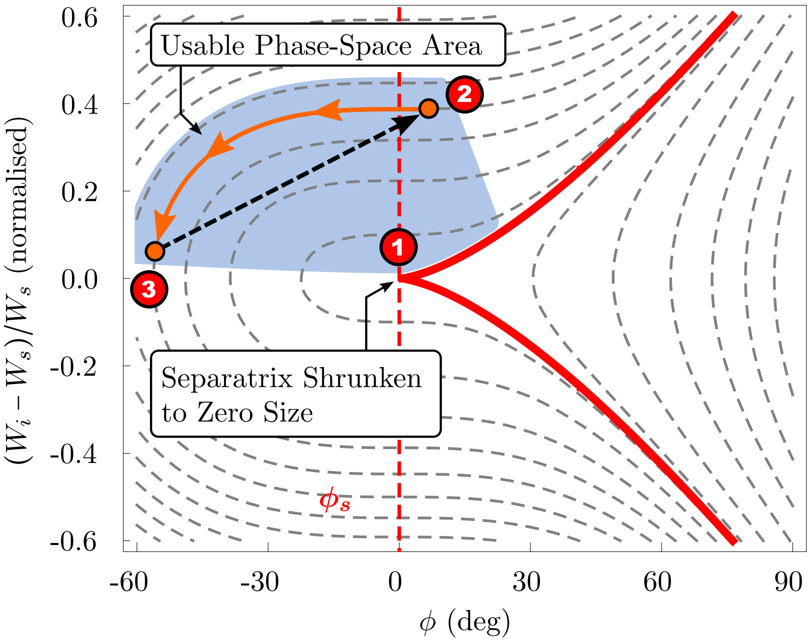

Fig. 2.8: Acceleration with a synchronous phase of $\phi_s = 0°$, i. e. at crest voltage. With the size of the phase space covered by the separatrix shrunken to zero at $(0, 0)$, no per se stable motion is possible. While the KONUS principle relies on the most efficient acceleration at $\phi_s = 0°$ it also includes rebunching sections at $\phi_s \approx -30°$ to counteract the resulting longitudinal debunching. For the marked points in the diagramme, see text.

Most efficient acceleration would be carried out by setting the synchronous phase ϕ_s at crest voltage. As described in Sec. 2.5.3, this is done at certain sections of KONUS dynamics based H-mode accelerating structures. The corresponding phase portrait is depicted at

---

[4] The factor ξ is set to 1 as a normalisation since specific accelerator and particle parameters do not lead to a qualitatively different result.

Fig. 2.8. Obviously the (formal) separatrix at ① has shrunken to zero and does not enclose any area of the phase space, which means it does not provide stable orbits. By definition of the axes, the phase space cell of the synchronous particle is located at the centre at ①. Now, in case of KONUS beam dynamics, the reference particle and synchronous particle are not the same. At ② the reference particle is injected with an energy above synchronous particle energy located close to the synchronous phase $\phi_s = 0^\circ$. This means at crest voltage particles in the vicinity of the reference particle experience neither longitudinal nor transverse focusing. When the bunch further advances through the 0°-structure, the reference particle follows the denoted phase space trajectory and finally approaches near synchronous particle energy ③, which is the reason for injection of the beam at greater than synchronous particle energy. During this process all particles in the environment of the reference particle are accelerated and experience longitudinal focusing due to the increasingly negative phase of the reference particle. Once the reference particle approaches quadrant II, defocusing of the bunch sets in as a particle arriving early would again see a higher accelerating field. This is avoided by resetting the KONUS section (③→②), thus, confining the motion mainly to quadrant II. Usually, the KONUS section is followed by a dedicated transverse focusing section, consisting of a quadrupole triplet and a rebunching section, with a synchronous phase of about $\phi_s \approx -30^\circ$, which, as an ensemble, is called a *KONUS period*.

2.7 GSI Overview

Founded in 1969 to serve as a research institution for heavy ion studies, GSI underwent several upgrades. Initially, the setup consisted of a linear accelerator only, based on a Wideröe structure (Sec. 2.5.1) and an Alvarez structure (Sec. 2.5.2) as final stage. In 1990 the first major upgrade was accomplished, when the existing facility has been extended by a synchrotron (SIS18) and a storage ring (ESR). As of today, the GSI accelerator facility comprises the *linear accelerator* UNILAC, the *heavy ion synchrotron* SIS18 and the *experimental storage ring* ESR. The UNILAC consists of two different upstream injectors, the *high current injector* (HSI) and the *high charge injector* (HLI) feeding the Alvarez poststripper section. Those can provide all ion species from hydrogen to uranium. Before the beam is injected into the synchrotron at an energy of usually 11.4 AMeV, the ions are stripped at the transfer channel (TK), and a higher charge state is selected, e. g. $\mathrm{U}^{28+}\rightarrow\mathrm{U}^{73+}$. The synchrotron SIS18 (bending power $B\cdot\rho = 18$ Tm) accelerates the ions to energies between 50 to 2000 AMeV. Finally, beams are either delivered to the high energy target area or the ESR (10 Tm) for storage and electron cooling using fast or slow extraction. For production of radioactive nuclei, a fragmentation target with a magnetic *fragment separator* (FRS) provides isotope selection for injection into the ESR or transport to the target area, where experimental setups are located.

2.8 The UNILAC Facility

The GSI **UNI**versal **L**inear **AC**celerator (UNILAC) features two different prestripper injectors feeding the final Alvarez stage (see Fig. 2.9) also referred to as poststripper section. The HLI (High Charge Injector), which is equipped with an ECR ion source, is mainly

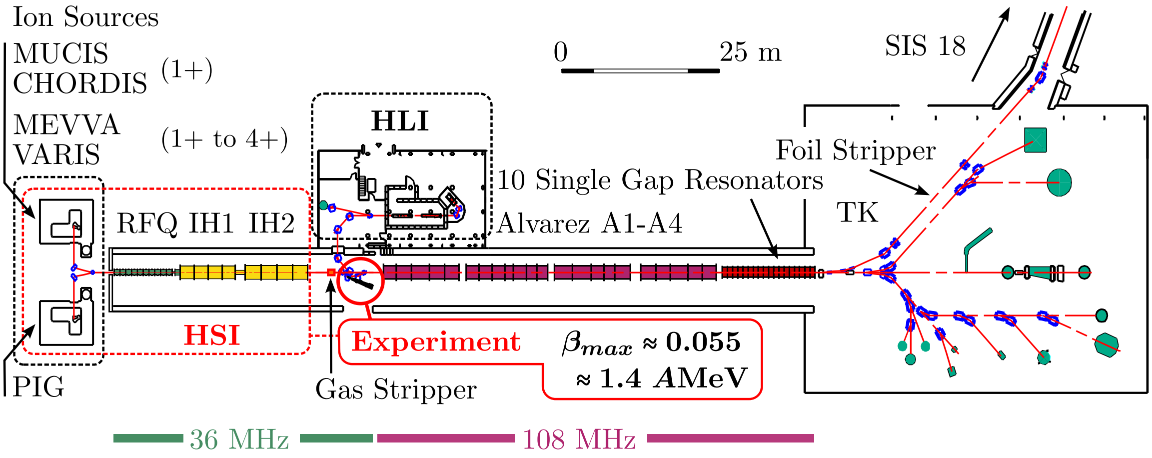

Fig. 2.9: UNILAC site overview from ion source to experiments (bottom right) and the transfer line (TK) injecting into the SIS18.

used in *super heavy element synthesis* (SHE) at the SHIP/SHIPTRAP [22, 23] and TASCA experiments [24]. It injects behind the first stripper section and is not accessible by the experimental setup presented in this work.

HSI - High Current Injector. Originally featuring a Wideröe structure, a major upgrade of the HSI has been performed in 1999 [25]. Prior to the upgrade, Penning sources fed the HSI to provide high initial charge states required by the relatively low effective gradient of the Wideröe structure (34 MV max.). As a consequence, mass numbers higher than 150 could not fill the SIS18 to its space-charge limit since the ion sources were not able to provide sufficient current for those charge states. Therefore, the Wideröe structure was removed in favour of a H-mode RFQ (further upgrade in 2004 and redesigned electrodes in 2009) and two IH cavities with a maximum effective gradient of about 91 MV. Additionally, a short 11-cell RFQ buncher, the so-called *Super Lens*, has been installed after the main RFQ for an improved matching into the first IH structure. All structures of the HSI, i. e. the RFQ, Super Lens and the IH structures, operate at a frequency of 36.136 MHz. The upgrade allows the acceleration of ions with a mass(number) to charge ratio up to $A/q = 65$. For instance, the typical charge state of uranium at the HSI after the upgrade could be lowered from U^{10+} to U^{4+}, fed by a high current ion source of MEVVA-type (see below) for SIS18 injection. At the same time, the lower charge state reduces the non-conservative space-charge effect which benefits the maximum beam intensity of the HSI.

Different ion species can be accelerated interleaved at the same time with individual accelerator settings, in particular different energies and even different charge states of the same ion species. Macro pulse operation works on a 50 Hz time base, i. e. at maximum 50 macro pulses per second can be delivered to the post-stripper section. The UNILAC facility can run up to 14 *virtual accelerators* which represent distinct accelerator settings on a pulse-to-pulse base.

Two ion source terminals are available at the HSI. Each terminal can only run one ion source at a time and thus the HSI can request pulses from two different ion sources interleaved.

High-current ion beams are available from the *northern terminal* (see Fig. 2.9), from where short pulses of high intensity usually can be extracted only at a low duty cycle of a few Hz or even less.

The following ion sources are available:

- MUCIS - **MU**lti **C**usp **I**on **S**ource
- MEVVA - **ME**tal **V**apour **V**acuum **A**rc ion source
- CHORDIS - **C**old or **HO**t **R**eflex **D**ischarge **I**on **S**ource
- VARIS - **V**acuum **AR**c **I**on **S**ource

The *southern terminal* houses a Penning ion source (PIG - **P**enning **I**on **G**auge) applicable for almost all elements at a high duty cycle with broad charge-state spectra. On the other hand only low to medium currents are available from a Penning ion source. A recent and complete summary of all ion sources in use at GSI and their performances can be found in [6].

The LEBT (*low energy beam transfer*) delivers ions from the ion source terminals with a sharp energy of about 2.2 AkeV ($\Delta E/E \leq 1 \times 10^{-4}$). Subsequently the ions are bunched and accelerated inside the RFQ structure up to an end energy of 120 AkeV. The *Super Lens*, a short RFQ working in bunching mode ($\phi_s = -90°$), prepares the bunches for an improved matching into the first IH structure. Inside the two IH structures the bunches are accelerated up to an energy of about 1.4 AMeV, which corresponds to a normalised velocity of $\beta \approx 0.055$.

From there the bunches reach the first stripping section. The gas stripper which has been installed in 1999 [26] and received an upgrade in 2006 [27] is a gas target, realised as a stationary, supersonic, differential nitrogen gas jet. The pressure at the nozzle can be adjusted from several bar down to 50 mbar, usually ranging around 4 bar. Interaction of the beam with the gas target results in a broad charge state distribution depending on ion species and stripper pressure. A typical charge spectrum for uranium is shown in Fig. 2.10 at a nozzle pressure of about 2 bar. The stripping efficiency is about 12 %, which is the fraction of particles with a certain charge state after stripping (here 27+). Charge separation and selection is accomplished by a chicane acting as dispersive section with fast kicker dipoles and two horizontal actively cooled high-current slits. A technical drawing of the cooled slits can be found in the Appendix, Fig. A.3.

Alvarez A1-A4. The final acceleration section of the UNILAC, the poststripper, is provided by the four Alvarez structures with design energies of 3.6, 5.9, 8.6 and 11.4 AMeV and 10 single gap resonators for energies up to 17.7 AMeV ($^{20}\mathrm{Ne}^{7+}$) and beam powers of more than 1 MW. Injection into the SIS18 is usually performed at 11.4 AMeV at a higher charge state stripped at the transfer channel (TK). An overview over the HSI design goal parameters at uranium are given in Tab. 2.1. Those values have not been reached so far. Furthermore, required values for SIS18, acting as a booster ring for the future fast-ramped super-conducting synchrotron SIS100 of the FAIR project are listed on the right. Improvement to the existing UNILAC facility by optimisations is a major task towards the future FAIR project.

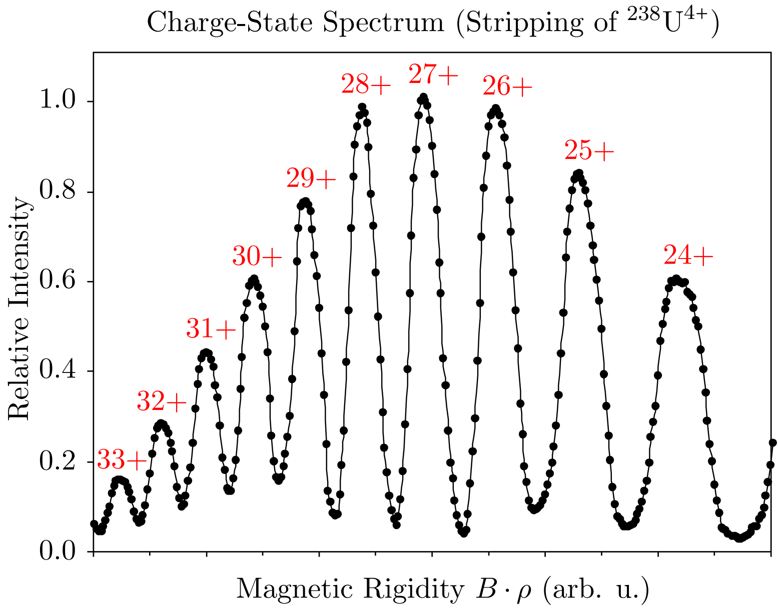

Fig. 2.10: Typical charge-state distribution of ^{238}U after stripping at an incoming energy of 1.4 *A*MeV and charge of 4+ [26]. The intensity has been normalised to the U^{27+} amplitude.

Tab. 2.1: Specified design parameters of the UNILAC HSI (design ion - uranium 238) to deliver 4×10^{10} of $^{238}U^{73+}$ ions within 100 µs to the SIS18 as reported in [28].

	HSI entrance	**HSI** exit	**Alvarez** entrance	**SIS18**	**FAIR**
Ion species	$^{238}U^{4+}$	$^{238}U^{4+}$	$^{238}U^{28+}$	$^{238}U^{73+}$	$^{238}U^{28+}$
El. current (mA)	16.5	15	12.5	4.6	15
Part./100 µs pulse	2.6×10^{12}	2.3×10^{12}	2.8×10^{11}	4.2×10^{10}	3.3×10^{11}
Energy (*A*MeV)	2.2×10^{-3}	1.4	1.4	11.4	11.4
ΔE/E RMS	n/a	4×10^{-3}	1×10^{-2}	2×10^{-3}	2×10^{-3}
$\varepsilon_{n,x}$ (mm·mrad)	0.3	0.5	0.75	0.8	0.8
$\varepsilon_{n,y}$ (mm·mrad)	0.3	0.5	0.75	2.5	2.5

Chapter 3

Experimental Setup

3.1 Principle of Measurement

Compared to available standard methods of measurement for the transverse degree of freedom, straightforward approaches for the longitudinal phase space of heavy ions do not exist. The short range in matter, about 10 µm for heavy ions with an energy of 1.4 AMeV, must be considered carefully in case of interceptive measurements. Also, the low velocity at the location of measurement after the prestripper sections, limits the possibility to access the longitudinal particle distribution by means of the electric field distribution, such as provided by capacitive pick-ups [2].

This is obvious from Fig. 3.1 which depicts the free longitudinal and transverse electric fields of a singly-charged particle at different velocities, neglecting the boundary condition of the pick-up geometry. The field components for three exemplary normalised velocities β are shown: 1.4 AMeV at location of measurement (stripper section), 11.4 AMeV at the transfer channel and a β of 0.9 corresponding to a kinetic energy of about 1.2 AGeV. Pronounced advanced and retarded tails are evident at lower velocities. Thus, the measured longitudinal particle distribution would be smeared out by the convolution of the electric field contribution and the long-range tails at the given velocity $\beta \approx 0.055$. A typical pick-up signal and the corresponding recorded bunch structure with the device investigated in this work is depicted in [5]. It shows a measured bunch length of 0.7 ns (FWHM) which is represented by a pick-up signal with an extension of about 10 ns.

At the first stripper section, where the measurement setup is located, particle distributions have a typical arrival time distribution of 0.5 to 2 ns (RMS). Hence, a determination of the bunch length or even detailed structures of the bunch is not possible by means of its electric field distribution. Other methods such as direct spectrometers [29] by a dispersive section

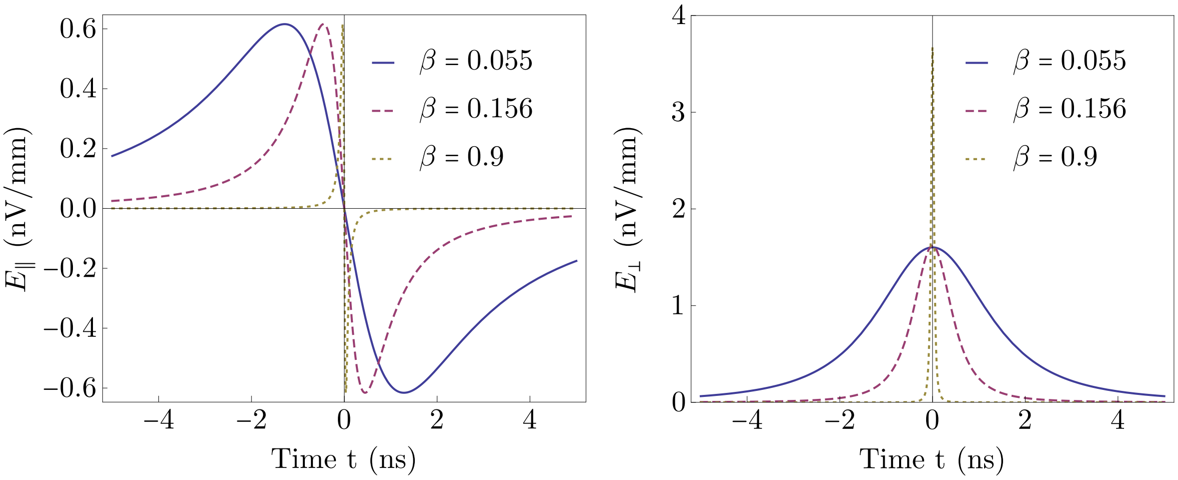

Fig. 3.1: Free longitudinal and transverse electric fields of a singly-charged particle, depicted for different values of β. The measurement setup is located at a $\beta \approx 0.055$ ($E_{kin} \approx$ 1.4 AMeV), whereas the maximum velocity behind the Alvarez structure is $\beta \approx 0.156$ ($E_{kin} \approx$ 11.4 AMeV).

and vertical deflectors are large, expensive and must be considered already during the design phase of an accelerator section. Moreover, this approach, as well as the method presented in this work, requires a prepared collimated beam in front of the dispersive section. This is usually provided by transversal and horizontal slit configurations after the first dipole.

A different approach to access the longitudinal phase space is investigated in this work. The bunch ensemble is transferred into a *single-particle measurement* by which the momentum/energy information is extracted via time-of-flight (TOF). Additionally, the *relative* phase information is recorded by the arrival time with respect to a fixed RF master oscillator reference. This allows, in principle, to reconstruct the longitudinal phase space by histogramming the recorded single-particle events. As an alternative approach, a direct calorimetric measurement based on a mono-crystalline diamond detector of high purity was investigated.

3.1.1 Time-of-Flight Measurement

The design of the time-of-flight (TOF) measurement setup by Forck et al. [4,5] is based on three essential components:

- **Particle-number attenuation** via *Coulomb scattering* into a small solid angle ω.
- **Timing signal** at *MCP module* (indirect measurement via secondary electrons).
- **Timing signal** at a *poly-crystalline diamond* detector after a drift of about 800 mm.

The essential components will be covered in the following sections.

A schematic representation of the TOF setup is depicted in Fig. 3.2. Incoming bunches, entering the device at the bottom left, have been already pre-attenuated to several microamperes and undergo Coulomb scattering at a thin tantalum foil of 210 µg/cm^2 thickness

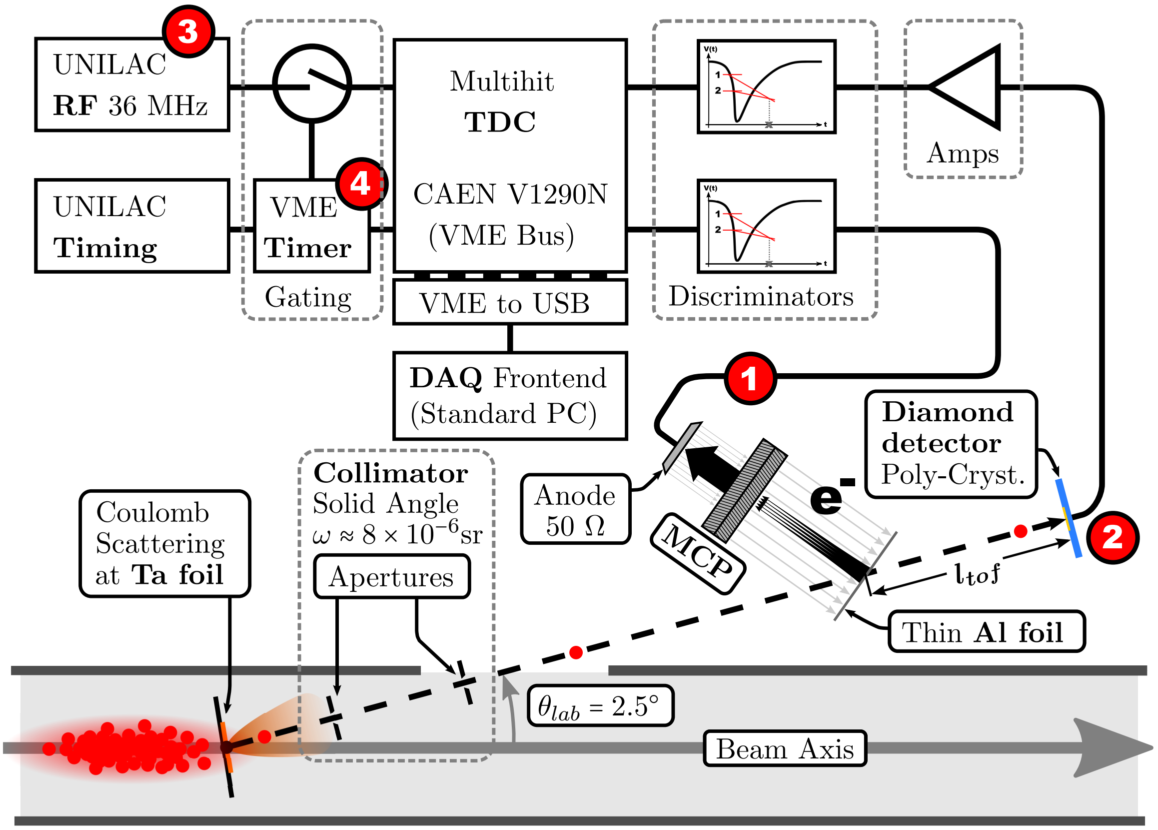

Fig. 3.2: Schematic TOF measurement setup. A simplified bunch distribution is depicted at the lower left of the figure. It enters the attenuation section consisting of the tantalum foil and the collimator as described in the text. The longitudinal phase space is reconstructed from *three timing signals* by histogramming. The timing at the PC-diamond detector t_{dia} ② with respect to a fixed reference of the RF master oscillator t_{rf} ③ is a measure of the relative phase of the incident particle, whereas the momentum/energy information is contained within the TOF between the timing at the MCP module t_{mcp} ① and the PC-diamond detector t_{dia} ② separated by the distance l_{tof}. Furthermore, the macro-pulse start timing t_{macro} ④ is recorded.

(about 126 nm) mounted behind an aperture with diameter 2 mm. Subsequently, under a small solid angle ω of about 8×10^{-6} sr and at an angle θ of 2.5° in the laboratory frame, ions are stochastically selected and registered by the MCP and poly-crystalline diamond detectors, thereby generating two timing signals. Choosing appropriate collimator dimensions, i. e. a small scattering probability into ω, most of the bunches (micro pulses) scatter no or only a single ion into the sensitive area following Poisson statistics. A negligible fraction of bunches scatter two or more ions into ω as will be discussed in Sec. 3.4.5. This is a strict requirement since the measurement relies on detector events which can be unambiguously related to a single ion.

As for the first timing signal t_{mcp} ①, it is important to generate the appropriate timing pulse at a negligible amount of interaction with the measurement apparatus compared to the true energy spread of the actual ion distribution. Otherwise the measured distribution is falsified. The idea is to provide the time reference by means of an indirect measurement of secondary electrons registered with a microchannel plate (MCP). On passage of an ion, liberated secondary electrons from a thin 10 µg/cm^2 (about 37 nm) aluminium foil are accelerated towards the MCP front by an electric field of about 1 kV/cm. A significant gain of the net electron yield is provided by the cascading characteristic of the MCP at an applied voltage of about 2 kV. The amplified stream of electrons is collected at a conical anode (50 Ω geometry) at the backside of the MCP. From the acquired pulse the logic timing is generated by a so-called double-threshold discriminator (see Sec. 4.1.1) and eventually registered in a fast time-to-digital converter (TDC, see Sec. 4.1.3 for a detailed description). When the TDC registers the timing pulse (NIM) it internally dumps the timing information from a global clock and thus provides a fixed relationship between different input channels.

After the drift $l_{tof}(\approx 800$ mm) a poly-crystalline diamond detector (thickness 185 µm) fully stops the ion. The detector signal is processed by a two-stage amplifier while the logic timing is again generated by a double-threshold discriminator. Finally, the timing signal is registered by the TDC providing the second timing signal t_{dia} ❷. Furthermore, the timing from the accelerating RF is recorded in equidistant, prescaled intervals of ten RF periods ($\approx$ 277 ns) to reduce the overhead of the regular data. This represents a fixed timing reference which allows to reconstruct the RF timing reference t_{rf} ❸ for each single bunch (micro pulse). Together with the arrival time of a particle at the diamond detector t_{dia} ❷ the longitudinal arrival time distribution is evaluated as a measure of the so-called longitudinal bunch structure. To account for the macro-pulse start reference, a dedicated timing signal is provided by a custom-made VME UNILAC timing module [30]. The reference timing of the macro-pulse start t_{macro} ❹ allows to compare events between different macro pulses. For example, it is possible to introduce time cuts and compare the phase space distribution between the first and second half of the macro-pulse ensemble.

The longitudinal phase space is consequently reconstructed as a 2-dimensional histogram by means of the single particle (i) event timing $(t_{dia} - t_{rf})_i$, representing the phase information, versus $(t_{dia} - t_{mcp})_i$ which is a measure of the momentum information. Chapter 4 covers the process in detail.

3.1.2 Direct Calorimetric Measurement

An alternative measurement to the time-of-flight approach has been investigated using a diamond detector with calorimetric properties. Poly-crystalline diamond semiconductor materials, as used in the TOF setup, cannot be used for direct energy measurements. Due to their large fluctuations of pulse heights for fully stopped, monochromatic particles, they are typically considered as timing detectors or within tracker geometries only. On the other hand, new diamond detector materials of high purity and improved electrode treatment, so-called mono-crystalline or single-crystalline diamonds, are able to provide a significantly more stable and enhanced linear signal response with respect to the deposited energy. Hence, this type of detector allows extraction of the energy information by calibration of the mere pulse height or integral liberated charge. These materials are still subject to research and undergo steady improvement [31].

The mono-crystalline diamond detector mounted on a pneumatic feed-through is housed in the same diagnostics chamber as the TOF setup introduced earlier. As the calorimetric measurement also requires unambiguous single-particle events, the mechanism of particle-number attenuation from the TOF approach is reused. Generated diamond pulses are amplified, digitally sampled and recorded. At the same time, the RF reference acquired from the master oscillator is sampled and recorded to provide a *relative* phase reference. Hence, after measurement, the phase space is reconstructed by post-processing the dataset consisting of an ensemble of digitised traces which are pairwise related. The procedure is presented in detail and discussed in Chapter 4.

3.2 Experimental Site

3.2.1 UNILAC Stripper Section

The experimental setup is located inside the UNILAC stripper section. Figure 3.3 shows the stripper section at the UNILAC which connects the HSI (left) and the Alvarez A1 structure (right). The measurement setup can access the beam from the UNILAC High Current Injector (HSI, see Sec. 2.8) and is located inside the dipole chicane upstream from the gas stripper. Due to the length of the diagnostics chamber, a straight-through installation in front or behind the chicane is not possible. Hence, no alternative location to the installation inside the dispersive section is available. Also, the restricted space at the given accelerator site imposes a limit on the practicable separation of the TOF detectors.

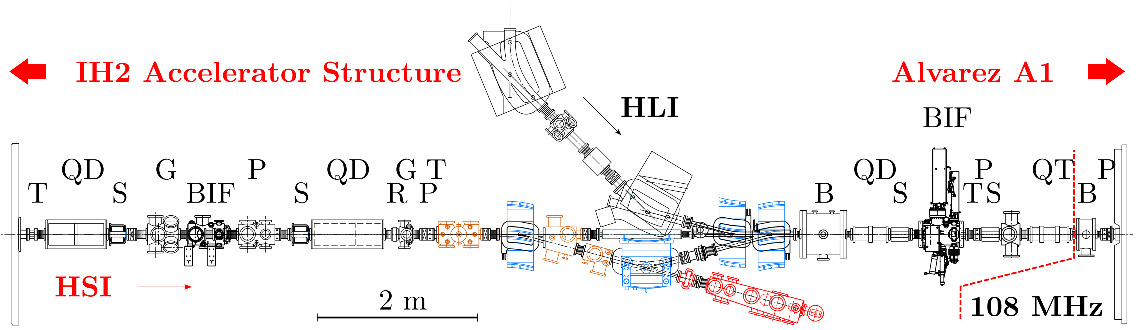

Fig. 3.3: Stripper section (as of **end of 2010**) between IH structures and Alvarez DTL tanks where the setup for longitudinal measurements is located. Apart from the charge separator section the available modules are denoted as follows: Current Transformer (**T**), Quadrupole Doublet (**QD**), Quadrupole Triplet (**QT**), Steerer Hor./Ver. (**S**), Profile Grid (**G**), Beam Induced Fluorescence Monitor (**BIF**), Resonance Probe (**R**), Phase Probe (**P**), Buncher (**B**).

A beam from the HSI enters the stripper section (see Fig. 3.3) and can be transversally adjusted by two quadrupole doublets and two steerers until it reaches the gas stripper. Depending on energy, pressure of gas jet nozzle and ion species, a characteristic charge state spectrum results. An exemplary charge state distribution is shown in Fig. 2.10 for ^{238}U. Subsequently, a dispersive dipole chicane, which is depicted in Fig. 3.4, spatially separates the charge states on the horizontal plane. Two high-current slits (US3DS4/5, [32]) allow to select the desired charge state. During usual delivery, the beam is deflected back towards the LINAC beam axis by a −30° dipole kicker magnet (US3MK2). Finally, dipole kicker magnet US4MK3 guides the beam back on the axis of the tank structures. Until the beam is eventually injected into the Alvarez A1 structure, the beam undergoes further preparation. Apart from transversal focusing quadrupole doublet/triplets and two steerers, longitudinal focusing is accomplished by two dedicated bunchers. A buncher, as explained in Sec. 2.6.3, provides no net acceleration at a synchronous phase $\phi = -90°$ with a maximum possible acceptance and allows to minimise the phase extension by effectively rotating the longitudinal phase space ellipse. One buncher is located right after the dipole chicane and is driven by the 36.136 MHz of the prestripper section. Another buncher is placed next to the entrance of the Alvarez structure, as can be seen from Fig. 3.3, and operates at about 108.4 MHz. This is three times the prestripper frequency in accordance with the Alvarez base frequency. The matching procedure from the prestripper section into the Alvarez structure represents a delicate challenge. As described in Sec. 2.3, the six-dimensional acceptance of the accelerator section under consideration determines the phase space volume which is transported properly. Hence, to obtain high transmissions and, thus, high efficiencies the six-dimensional phase space of an incoming beam must have a large overlap with the accelerator acceptance. In case of Alvarez matching, the task is to find a good configuration of the transversal focusing and the bunchers for an improved injection. In particular, for a good choice of the bunching RF phase and RF voltage, the knowledge of the longitudinal phase space is advantageous.

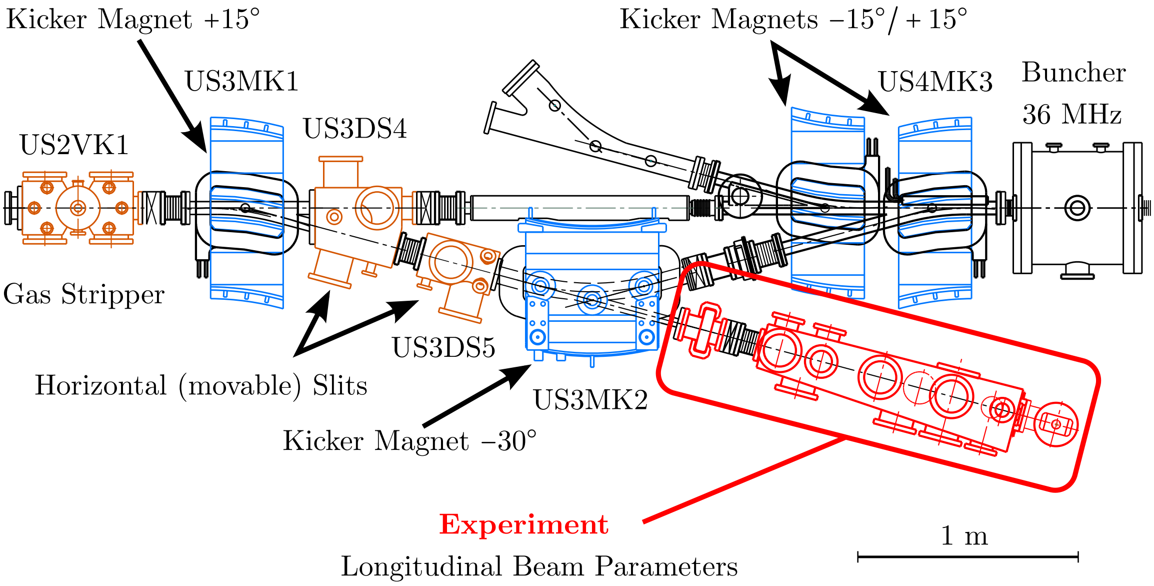

Fig. 3.4: Detailed drawing of the dipole chicane at the stripper section between HSI and Alvarez structure. The measurement setup is located the high-current slits US3DS4/5 on the common beam axis. In case of a measurement the 30° kicker magnet US3MK2 is not in operation.

The measurement setup is located behind the high-current slits inside the chicane as depicted in Fig. 3.4. During measurement, the dipole magnet US3MK2 is not in operation. In high current mode it is of major interest to keep the space charge unmodified as long as possible. Otherwise, the measured phase-space distribution would not reflect well the situation of normal operation. Therefore, two possibilities are available to attenuate a beam of several milliamperes to only several microamperes:

- Selection of a charge state far from the equilibrium charge state.
- Use of a very narrow slit setup through which only a small fraction of the beam passes.

The method of attenuation strongly depends on the beam parameters. While it is sometimes helpful to select a different charge state *and* geometrically shadow certain fractions of the beam via the high-current slits, the charge state which is used in ordinary beam operation is favourable for consistency.

3.2.2 Diagnostics Chamber

The diagnostics chamber houses the dedicated modules required for the experiment, i. e. the collimator which is responsible for particle-number attenuation and detectors of various kind. Designed by Forck et al., the chamber in TOF configuration has been already extensively in use during commissioning of the revised UNILAC pre-stripper section (see

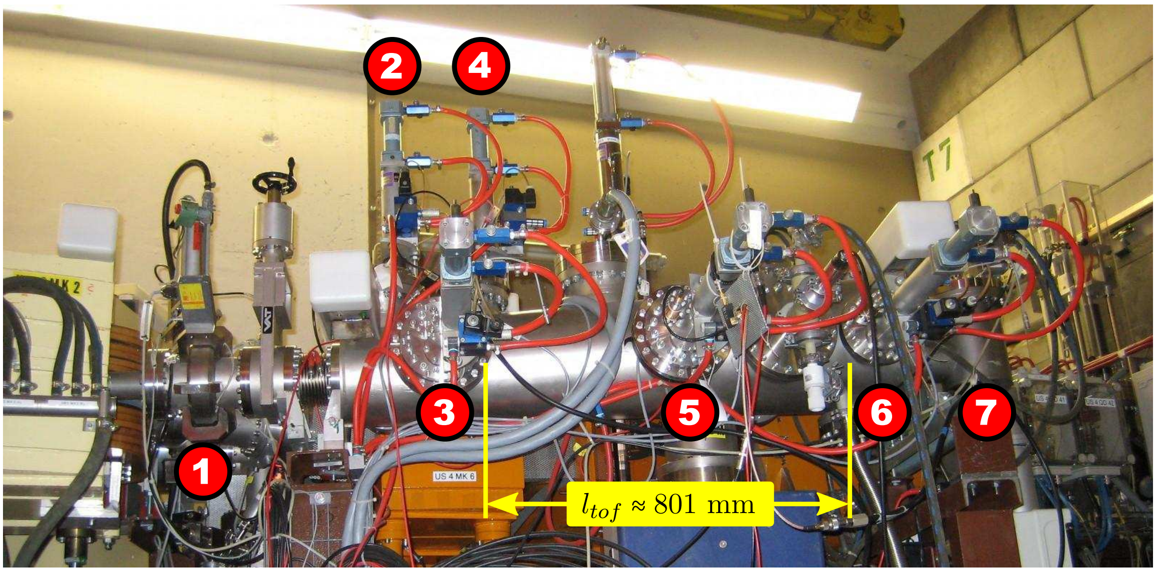

Fig. 3.5: Photograph of the experimental setup including: Current transformer (beam current) ①, first collimator aperture including the tantalum foil ②, second collimator aperture ③, MCP module including the aluminium foil ④, mono-crystalline diamond detector investigated as a direct calorimetric method ⑤, poly-crystalline diamond detector used in TOF measurement delivers second timing signal ⑥, Faraday Cup beam-current measurement ⑦. For a detailed technical drawing see Fig. 3.6.

Sec. 2.8). Figure 3.5 shows a recent photograph of the measurement setup. All crucial modules are labeled and explained accordingly in the following sections of this chapter. The corresponding technical drawing (top view) of the diagnostics chamber in Fig. 3.6 preserves the numbering scheme given in Fig. 3.5. A pre-attenuated beam enters on the left where the macro-pulse current (see Sec. 2.1) can be recorded with the current transformer US3DT6 [33], labeled with ①. Knowing the incoming beam current is important to prevent the primary foil from melting. Pneumatic feed-throughs carry the tantalum foil and apertures, labeled with ② and ③, which constitutes the collimator configuration responsible for particle number attenuation. The MCP module ④ follows closely the exit of the collimator as depicted in Fig. 3.6 (for a detailed technical view see Appendix, Fig. A.1). After the drift l_{tof} of about 800 mm with respect to the MCP aluminium foil, the poly-crystalline diamond detector ⑦ is installed. In between the aforementioned TOF detectors, a mono-crystalline diamond detector ⑤ has been installed. All detectors are mounted on a pneumatic feed-through. Depending on the measurement method, i. e. TOF or direct calorimetric, either the MCP together with the poly-crystalline diamond detector or the mono-crystalline diamond detector are exposed to the scattered beam particles. Finally, a Faraday cup ⑦ can be used as a complimentary measurement for adjustment of the beam current (macro-pulse current) before collimator and detectors are exposed to the beam.

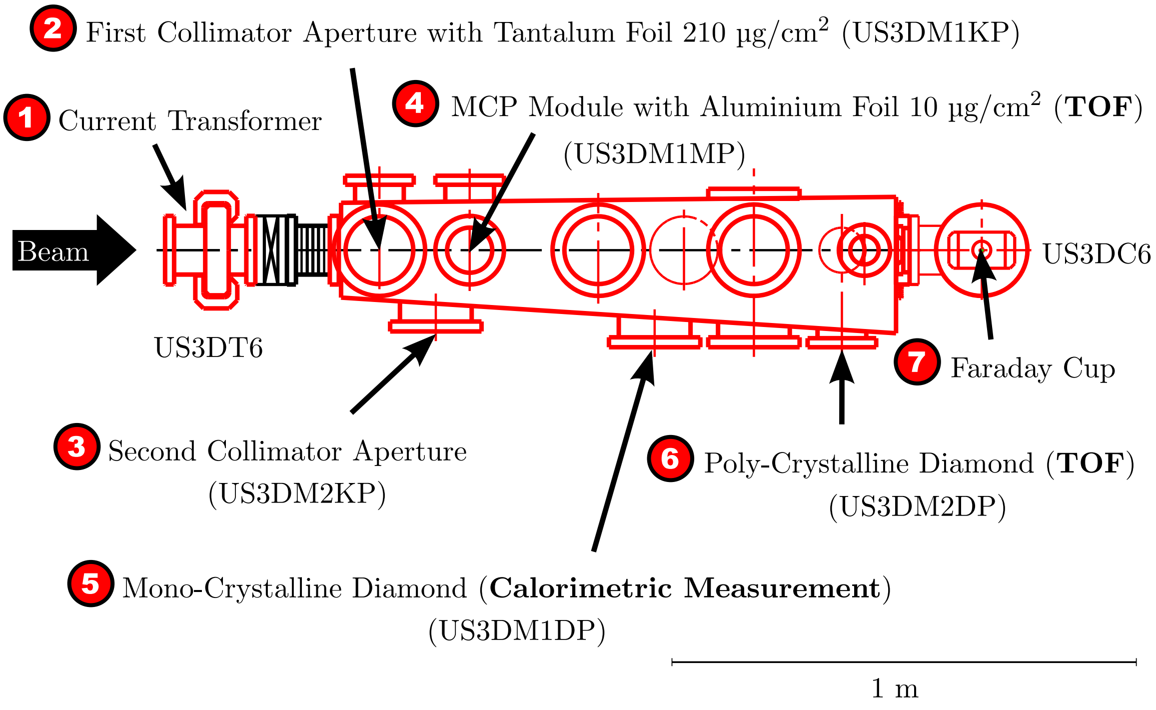

Fig. 3.6: Schematic measurement setup in detail (top view). The numbering scheme of the components matches the one present in Fig. 3.5.

3.3 Particle Detectors

3.3.1 Microchannel-Plate Module

The first timing of the time-of-flight (TOF) measurement is generated using a so-called microchannel plate (MCP), sometimes also referred to as multi-channel plate. Since the TOF requires two timing references at a well defined separation, it is obvious that the beam-device interaction at the evaluation of the first time reference must be sufficiently low, in order to preserve the phase space information of the original beam. Otherwise the TOF is falsified as the measured phase space would have been significantly altered.

Manufacturing and Properties. An MCP consists of a parallel assembly of very thin tubes (typically about 10 µm diameter), usually made of lead glass and biased by a certain angle with respect to the front normal (typically about 10°). The fabrication process is derived from fiber glass production. Lead glass fibres with an etchable core are drawn-out and assembled in a hexagonal configuration. Those packets of fibres are drawn-out again and put together in an iterative procedure until the targeted channel size and the diameter of the MCP are met. Slices are cut from the final packet, taking care of the bias angle. The core is removed in an etching process which reveals the single channels. Subsequently, the channel surface is treated with a semiconductor material, while evaporated metallic layers on both sides of the MCP serve as electric contact. As a result of the high-ohmic coating of the channel walls, the electric resistance between the electrodes on front and back side typically ranges from 10-100 MΩ. The electrode layer reaches into the channels, in such a way that the special diffused junction allows fast charge recovery after ignition to minimise the dead time per channel while the high-ohmic surface is maintained.

Working Principle. The single channels of MCPs can be compared to photo multipliers but with a cylindric continuous-dynode geometry. In contrast to separate dynodes, connected by a voltage divider circuit, the high-ohmic surface represents a continuous resistor chain which allows to sustain the high field gradient at a very small leakage current as described by Wiza [34]. In principle, MCPs are sensitive to all kinds of ionising primary irradiation, such as electrons, heavy ions and electro-magnetic radiation.

Figure 3.7 schematically depicts the working principle, taking electrons as primary particles. The liberated secondary electrons are accelerated by the electric field inside the MCP channels and follow parabolic lines, while the voltage applied per MCP is typically about 1 kV. The electrons again collide with the channel wall and knock out further electrons, starting a cascade of generated electrons. This eventually ends in an intense electron shower emitted at the back of the MCP. If the MCP output is extracted with an anode, the pulse-height distribution (PHD) typically follows a negative exponential at lower gains, while it approaches a Gaussian distribution for high gains near saturation [35]. Saturation occurs at very high space-charge densities near the channel exit when liberated electrons cannot gain any kinetic energy. Also, at high gains the probability of ionising residual gas atoms is enhanced. The positively charged gas atoms in the vicinity of the channel are accelerated in the reverse direction. When the ion eventually hits the channel wall unwanted retarded

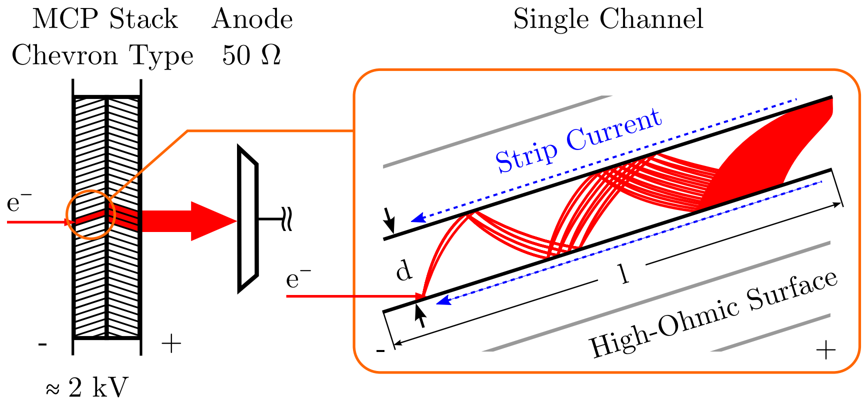

Fig. 3.7: Electrons of sufficient kinetic energy will knock out several secondary electrons when they enter the thin channels of the MCP. The voltage applied to the MCP accelerates the liberated electrons which in turn knock out secondary electrons as well. Finally an electron shower is generated with a minimum gain of 10^6.

pulses occur. This effect is called *ion-feedback* and can lead to significant damage to the MCP at insufficient vacuum pressures. Therefore, MCPs must not be operated above a certain vacuum level, typically 10^{-4} Pa. It is worth noting that the performance characteristics of an MCP only depend on the fraction l/d, i.e. the effective *channel length* l and the *channel diameter* d in good approximation [34]. The longer the channels and the smaller their diameter the more collisions on the channel occur for a given MCP. On the other hand, the number of collisions decreases with increasing voltage applied and the number of liberated electrons per hit increases. When it comes to the response time which limits the time resolution, short channels with small diameters are favourable as they decrease the path length and allow for MCP configurations with rise times below 500 ps. At the same time, the time jitter is damped and a faster recovery time results from the increased channel density [35].

Application Area. MCPs are used for different purposes, originally targeted as image intensifier for night vision devices. In beam diagnostics, several devices feature an MCP of large diameter working as a preamplifier of spatial intensity distributions, where the primary particles are usually either photons or electrons [36]. While MCPs are sufficiently sensitive to photons within the ultraviolet and soft X-ray domain, visible light usually requires an additional photocathode as a first stage. The two-dimensional spatial density profile of generated electrons are mapped to the optical region by phosphor screens of various kinds. A combination of optical filters and cameras finally provide the raw data information. In the special geometry used in this work only the time resolution is of importance.

MCP Specifics (Hamamatsu F4655-13). The MCP used in the TOF setup is a commercially available compound module by Hamamatsu Photonics K.K. and has been specifically designed for TOF measurements with high timing requirements in the sub-nanosecond

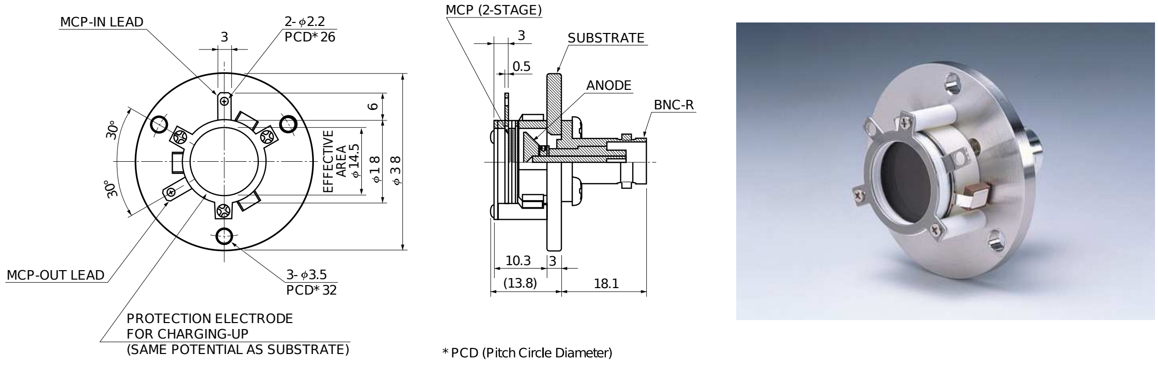

Fig. 3.8: MCP module (Hamamatsu F4655-13) used in the TOF setup. Technical drawings and the picture were taken from the corresponding specification sheet [37]. Courtesy of Hamamatsu Photonics Deutschland GmbH.

regime. Figure 3.8 shows the technical drawings and a photo of the module. The MCP features an effective circular area of 1.65 cm^2, a thickness l of 0.41 mm, a small channel diameter d of 4 µm ($l/d \approx 100$) and an electrical resistivity of about 50 MΩ each. Per MCP a maximum voltage of 1 kV must not be exceeded. Two identical MCPs are stacked in a so-called chevron configuration, i. e. the orientation of the channels of both MCP are aligned against each other to form a “\/-shape” as denoted in Fig. 3.7. Together with the channel bias angle of 12°, the chevron configuration damps the occurrence of ion feedback while delivering an enhanced gain at the same time. In case of the module at hand the gain ranges between 10^6 to 10^7. On the other hand, the unavoidable gap between the MCPs in the chevron configuration gives rise to a broad pulse-height distribution. This is a direct cause of the lateral spread of the electron stream between the two MCP stages and activates several channels at the second MCP stage. Apart from the number of activated channels and their input intensity, this process results in a fluctuating final intensity as not all of those channels are driven into saturation. The MCP configuration at hand is specified with a PHD of 120 % (FWHM with respect to the distribution maximum) [38]. As only the timing information is of interest, a conical anode is installed behind the MCP chevron configuration. The anode signal is extracted from a BNC connector (50 Ω geometry) and is immediately adapted to SMA connections and cabling of high bandwidth. The specification of the MCP promises rise times of less than 300 ps at fall times of less than 600 ps and pulse-length of 455 ps (FWHM) [37].

Construction and Electric Layout. As mentioned earlier, the generation of the first time reference, during the TOF measurement, is an indirect measurement. Liberated secondary electrons from a thin aluminium foil are accelerated in an homogeneous electric field and amplified by a fast MCP (Hamamatsu F4655-13). The electric field between aluminium foil and MCP which accelerates the electrons towards the MCP front is supported by three metallic guide rings and an appropriate voltage divider circuit to guarantee a homogeneous field distribution. All components, the foil, guide rings, voltage divider circuit and MCP, are mounted inside a PEEK construction on a pneumatic feed-through. A corresponding simulation of the field distribution [39] is given in the Appendix, Fig. A.2. The simulation illustrates a good homogeneity inside the guide ring section and only minor non-axial deviations near the foil area. Particles cross the foil at an angle of 46.5° with respect to the foil normal. A copper housing which is connected to ground prevents accumulation of charges and, consequently, discharges that may destroy the MCP. The electric schematics of the MCP setup is depicted in Fig. 3.9. In this typical configuration the aluminum foil is

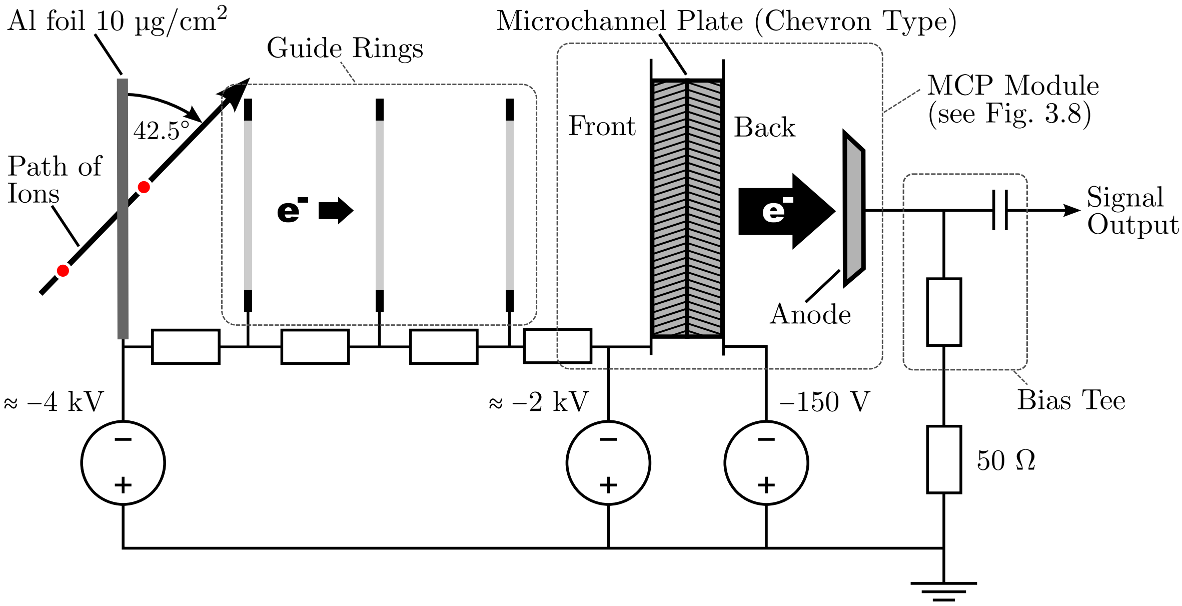

Fig. 3.9: Electric layout of the MCP compound module.

biased by -2 kV with respect to the MCP front. The anode signal is collected with a bias tee connected to ground without further amplification. Pulses are converted to logic timing pulses and registered in the TDC electronics.

3.3.2 Poly-Crystalline Diamond Detector

After particles have passed the aluminium foil of the MCP module, the second timing in the TOF setup is generated in a so-called poly-crystalline (PC) diamond detector. The diamond semiconducting material has a band gap of 5.47 eV, which allows the detector to be used at room temperature without cooling. It is sensitive to any kinds of ionising radiation providing enough energy to produce energy-hole pairs (average energy of 13.1 eV). As a drawback, this relatively high energy results in small signal amplitudes compared to other semiconductor materials. Despite the broad pulse-height distribution for monochromatic particles, the high mobility of free charges provides fast, short pulses with a uniform rise time. While this does not allow for a direct calorimetric measurement of the deposited energy, it provides excellent timing properties with rise times below 300 ps and a pulse width of about 1 ns which allows for count rates of more than 10^8 ions per second [40]. According to E. Berdermann et al. [40] the reason for the poor pulse-height resolution lies in the granular texture of PC-diamonds. The charge-collection efficiency (CCE) is significantly enhanced inside the region of big grains. Hence, major fluctuations of the total collected charge result from the inhomogeneity of the poly-crystalline structure. On average the CCE for PC-diamond material is less than 60 %. Typically, PC-diamond detectors are used as trackers for high energy particles where the deposited energy ΔE is much smaller than the average particle energy $\langle E \rangle$. In this work particle distributions are studied with a maximum energy of 1.4 AMeV. Hence, due to the short range in matter of about 10 µm, the total energy is deposited in the diamond material close to the surface. Significant degradation of the pulse-height distribution and leakage current has not been observed for 5×10^{10} ions/cm^2 traversing uranium ions with a high energy of 1 AGeV [41] as reported in [40] (both Berdermann et al.). The same authors report on test runs with carbon ions of 5.9 AMeV which are fully stopped within a thin layer around a depth of 57 µm [40]. There, at high fluences, the pulse-height resolution even improved by a factor of 5 between irradiation with 10^8 ions/cm^2 and 10^{10} ions/cm^2 (*priming*). Disadvantageous irradiation effects are not expected in the current work due to the minimal amount of implanted particles. The diamond detectors are only exposed to the attenuated single-particle beam. A measurement typically comprises about 10^4 events.

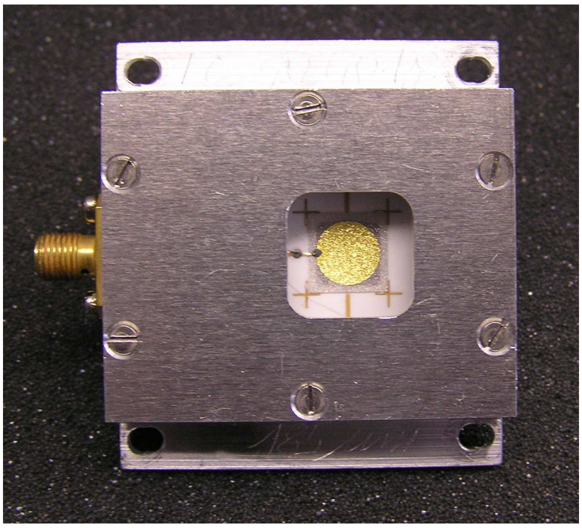

Fig. 3.10: Poly-crystalline diamond detector module used in the TOF measurement to provide the stop timing signal. Particles are fully stopped inside the diamond material of 185 µm thickness.

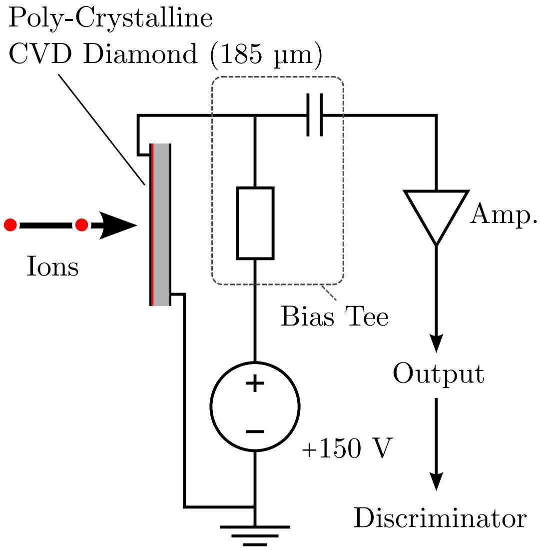

Fig. 3.11: Electrical interface to the poly-crystalline diamond detector. Extracted signals are amplified and converted to logic timing.

The semiconducting diamond material, with a large band gap of 5.47 eV, is synthesised in a process called *chemical vapour deposition* (CVD) which is suited for the fabrication of thin films. Especially the challenge to synthesise improved single-crystalline structures of high-purity is still ongoing research. The detector used in the TOF configuration has been assembled by the GSI detector laboratory and features a thickness of 185 µm. An identical detector module is depicted in Fig. 3.10. The golden, circular electrode has a diameter of 8 mm and marks the sensitive diamond area. Figure 3.11 shows the schematic electrical interface. The detector voltage is applied using a bias tee which allows extraction of the signals at the same time. Subsequently, a 50 Ω low noise two-stage amplifier chain is attached with a Mini-Circuits ZFL-1000LN (100 kHz - 1 GHz, 20 dB typ.) and a Mini-Circuits ZFL-1000VH2 (10 MHz - 1 GHz, 28 dB typ.) as final stage.

3.3.3 Mono-Crystalline Diamond Detector

Apart from the time-of-flight measurement, based on an MCP module and a poly-crystalline CVD diamond detector, a direct calorimetric detector, as a variation of the measurement setup, has been implemented. With the advancement of the CVD process over the last decade, which allows to produce synthetic mono-crystalline diamond materials of high purity, calorimetric measurements using diamond detectors became possible. Mono-crystalline CVD diamonds (sometimes also referred to as *single-crystal* diamonds) feature an enhanced carrier mobility (J. Isberg et al. [42]) and, thus, very fast response times shorter than the typical rise times of PC-diamond detectors. Of course, this may be limited by the DAQ electronics and the time constant given by the capacity of the detector and the impedance of the readout chain of 50 Ω. At typical detector capacities of 3-5 pF, a time constant of 150-250 ps marks the lower limit of the measured rise time. Although the conversion factor for electron-hole creation of 13.1 eV is high compared to other semiconductor detector materials, and thus results in relatively small signal amplitudes, readout noise is very low. This is a direct result of the extremely low leakage current at room temperature. New electrode techniques come with steady damping of the leakage current at high electric fields. The so-called diamond-like carbon (DLC) fabrication process of the electrical contact, gives rise to leakage currents of less than 0.5 pA at electric field strengths of 2 V/µm [43]. Furthermore, compared to PC-diamond detectors, the mono-crystalline diamond structure is able to provide a charge collection efficiency up to 100 % for low electric fields. This significantly improves the pulse-height resolution and allows for direct calorimetric measurements to some extent. For the detector model in use, an energy resolution of about 1 % for α particles (5.5 MeV) is claimed by the manufacturer [43]. Ongoing efforts target improvements of the CVD process to produce mono-crystalline diamond materials of higher purity which further reduces polarisation due to charge trapping.

The mono-crystalline diamond has been installed behind the collimator setup on a pneumatic feed-trough. A photo of the module by *Diamond Detector LTD* is depicted in Fig. 3.12 together with the corresponding plain data of specification sheet. The electrical interface is similar to the one used at the PC-diamond, see Fig. 3.11. At a thickness of 100 µm a positive bias of 100 V is used throughout the experiments. According to Pomorski et al. [44] a negative bias leads to electron trapping. The polarisation of the detector results in a reduced resistivity and, hence, may lead to breakdowns, rendering the detector unusable. Additionally, the lower drift velocity of electrons, compared to electron holes (at positive bias), produces pulse shapes of inferior quality. Together with the advantage of a positive bias voltage, an electric field of 1 V/µm has been used to avoid spontaneous breakdowns for electric fields above 1.4 V/µm observed by Pomorski et al. [44]. While the heavy ion radiation hardness of mono-crystalline diamonds is considered to be very good [45], this is not a strict requirement in the setup at hand. The detector is only exposed to the beam in conjunction with the collimator setup and, thus, is only irradiated by a very small number of ions. A single measurement typically comprises in the order of 10^4 events only.

Diamond Detector LTD 09-003

- Thickness 100 µm
- Active diamond area $4.5 \times 4.5\ \text{mm}^2$
- Circular electrode of $4.4\ \text{mm}^2$ diameter
- Electrode configuration:
  3 nm DLC, 16 nm Pt, 200 nm Au
- Energy resolution about 1 % for α particles
- Leakage current < 0.1 nA

Fig. 3.12: Mono-crystalline diamond detector used for the direct calorimetric measurement and the specification as provided by the manufacturer *Diamond Detectors LTD.*

3.4 Single-Particle Detection via Coulomb Scattering

This section covers the particle-number attenuation mechanism which allows single-particle detection and is partly based on ideas by P. Forck and P. Strehl [46].

Reconstructing the full longitudinal phase space by histogramming single-particle events requires unambiguous detection signals as a prerequisite. Strictly speaking, an unambiguous event means only one particle event occurs per bunch (micro pulse) at most. As we will see in Sec. 3.4.5, the probability to have a certain number of particles inside a bunch (micro pulse) follows a Poissonian distribution. Therefore, it is not possible to perfectly rule out multiple particles being scattered into the collimator acceptance during a single bunch. Still, a significant suppression of multi particles is possible as described in Sec. 3.4.5. As the typical bunch lengths range between 1-3 ns (RMS) and detector pulses have characteristic widths larger than 1 ns, a large fraction of the multiple-particle events would end in disadvantageous pile-up configurations. Pile-up signals lead to distorted pulse-shapes and, thus, to an increased time jitter.

The pre-attenuated beam of several µA contains about $n_\tau \approx 10^9$ ions per macro pulse, depending on charge state q and macro pulse length τ

$$n_\tau = \frac{I}{q\,\mathrm{e}}\tau, \tag{3.1}$$

with typical parameters $I = 25\ \mu\text{A}$, $\tau = 200\ \mu\text{s}$ and $q \approx (10-30)$. Taking theses value for an exemplary Ar^{10+} beam, a total number n_τ of 3.1×10^9 ions are contained in macro pulse. Hence, within a bunch, $n_b \approx 4.3 \times 10^5$ ions are delivered on average.

An additional mechanism is therefore required to have a suitable environment for single-particle detection within the drift space between the MCP and the diamond detector. At the device entrance a collimator setup (see Fig. 3.2 and Fig. A.1) houses a thin tantalum foil of $\kappa = 210\ \mu\text{g/cm}^2$, tilted by an angle of 1.25° with respect to the incoming beam axis. It is accompanied by two apertures with diameters of 0.5 mm and a distance of 160 mm. The already attenuated beam traverses the Ta foil and undergoes Coulomb scattering. Scattered particles are selected at an angle of $\theta = 2.5°$ with a resulting solid angle of $\omega = 7.7 \times 10^{-6}$ sr, given by the geometry of the collimator setup[1]. Thus, only a small fraction of the particles of the incoming beam scatters into the TOF section. The goal of the following sections is to calculate an estimation of the attenuation achieved using the classical Rutherford scattering cross-section in non-relativistic limit ($\beta \approx 5.5\%$). Additionally, a complementary SRIM simulation has been performed and both results are compared for consistency.

3.4.1 Probability for Scattering into Solid Angle $\{\theta, \omega\}$

In general, at a given process p with the related cross-section σ_p, the reaction rate $j_p \cdot A$ is given by

$$j_p\,A = j\,n\,A\,d_f\,\sigma_p, \tag{3.2}$$

where j denotes the incoming particle flux, n denotes the target atomic density, while A is the geometric area affected by the incoming beam [47] and d_f the thickness of the target. Consequently, the probability for a particle to undergo process p is given by

$$P_{\sigma_p} = n\,d_f\,\sigma_p = \kappa\left(\frac{N_A}{A_t}\frac{\text{mole}}{\text{gram}}\right)\sigma_p \qquad \text{with} \quad A_t: \text{ mass number of the target.} \tag{3.3}$$

To determine the relevant cross-section σ for particles passing the collimator, the differential Rutherford scattering cross-section is a good starting point

$$\frac{\mathrm{d}\sigma_{lab}}{\mathrm{d}\omega}(\theta) = \left(\frac{e^2}{4\pi\epsilon_0}\right)^2\left(\frac{Z_pZ_t}{4\,m_pv^2}\right)^2\frac{1}{\sin^4(\theta/2)} \qquad \text{with} \quad \frac{e^2}{4\pi\epsilon_0} = \alpha\hbar c \approx \frac{197}{137}\,\text{MeV fm}\,. \tag{3.4}$$

Transformation into the centre of mass frame allows straight forward incorporation of the finite mass of the scatterer by introduction of the reduced mass $A_{red} \cdot m_u$

$$\frac{\mathrm{d}\sigma_{cms}}{\mathrm{d}\Omega}(\Theta) = (\alpha\hbar c)^2\left(\frac{Z_pZ_t}{A_{red}\,m_uc^2}\right)^2\frac{1}{\beta^4\,\sin^4(\Theta/2)} \qquad \text{with} \quad A_{red} = \frac{A_p\,A_t}{A_p + A_t}\,. \tag{3.5}$$

The finite cross-section σ for particles scattered into the solid angle ω and scattering angle θ in the laboratory frame is received by back transformation $\{\Theta, \mathrm{d}\Omega\}_{cms} \leftrightarrow \{\theta, \mathrm{d}\omega\}_{lab}$ from the centre of mass frame [48] using

$$\frac{\mathrm{d}\Omega}{\mathrm{d}\omega} = \frac{\sin^3\Theta}{\sin^3\theta}\left(1 + \frac{A_p}{A_t}\cos\Theta\right)^{-1} \qquad \text{and} \qquad \tan\theta = \frac{\sin\Theta}{\frac{A_p}{A_t} + \cos\Theta}\,. \tag{3.6}$$

Figure 3.13 shows the transformation of the scattering angle from centre-of-mass to laboratory frame for different projectiles, assuming a tantalum target. It should be noted that for

---

[1] Lower case letters ω and θ refer to the laboratory frame, while upper case letters Ω and Θ refer to the centre-of-mass frame.

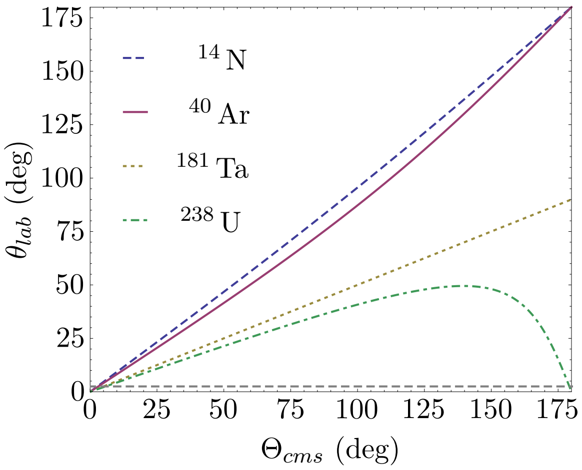

Fig. 3.13: Transformations of projectile scattering angle from centre-of-mass to laboratory frame for different projectile masses and a Ta target.

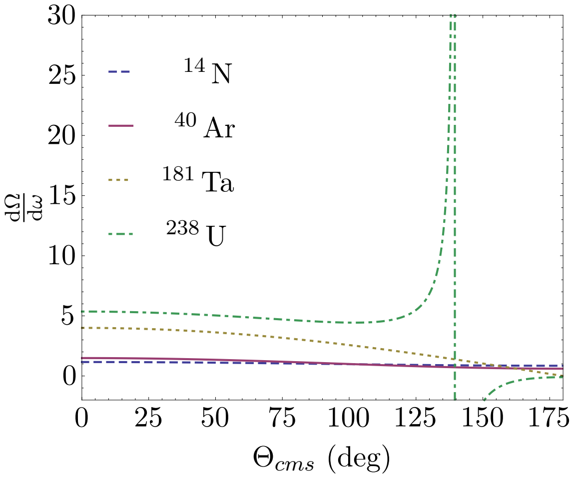

Fig. 3.14: Transformation of differential solid angles $\frac{d\Omega}{d\omega}(\Theta)$. Uranium has a noticeable pole at $\cos\Theta = -\frac{A_t}{A_p}$ due to $A_p > A_t$.

projectiles with $A_p > A_t$, as is the case for an uranium ion impinging on the tantalum foil, small angles occur in pairs. These angles are connected to peripheral collisions with minor impact on the projectile, but also head-on collisions with a major energy transfer to the target. The latter is of minor relevance since the diamond detector electronics together with the discriminator settings adjusted for the 1.4 AMeV particles will not register those low-energy events. The transformation of the differential solid angles between centre-of-mass Ω and laboratory system ω is plotted in Fig. 3.14. This allows to calculate the cross-section in the laboratory system σ_{lab}, since

$$\sigma_{lab}(\theta, \omega) = \frac{d\sigma_{cms}}{d\Omega}\frac{d\Omega}{d\omega}\,\omega\,. \tag{3.7}$$

Together with Eq. (3.3) the probability for a particle to be scattered into $\{\theta, \omega\}$ is finally calculated to be

$$P_{sc}(\theta, \omega) = \kappa\left(\frac{N_A}{A_t}\frac{\text{mole}}{\text{gram}}\right)\sigma_{lab}(\theta, \omega) = \kappa\left(\frac{N_A}{A_t}\frac{\text{mole}}{\text{gram}}\right)\frac{d\sigma_{cms}}{d\Omega}\frac{d\Omega}{d\omega}\,\omega\,. \tag{3.8}$$

As Fig. 3.15 shows, the probabilities magnitude is about $1.6 \times 10^{-5} \pm 30\,\%$ and differs only by a factor of less than two between nitrogen with $P_{sc}(\theta = 2.5°, \omega = 7.7 \times 10^{-6}) \approx 2.1 \times 10^{-5}$ and uranium with $P_{sc}(\theta = 2.5°, \omega = 7.7 \times 10^{-6}) \approx 1.2 \times 10^{-5}$.

3.4.2 Energy Transfer to Target Nucleus

In the picture of classical Rutherford scattering, momentum is only transfered from the projectile to the target nucleus at rest. After elastic collision, i. e. the kinetic energy of the projectile and target nucleus are the only degrees of freedom, the energy of the projectile

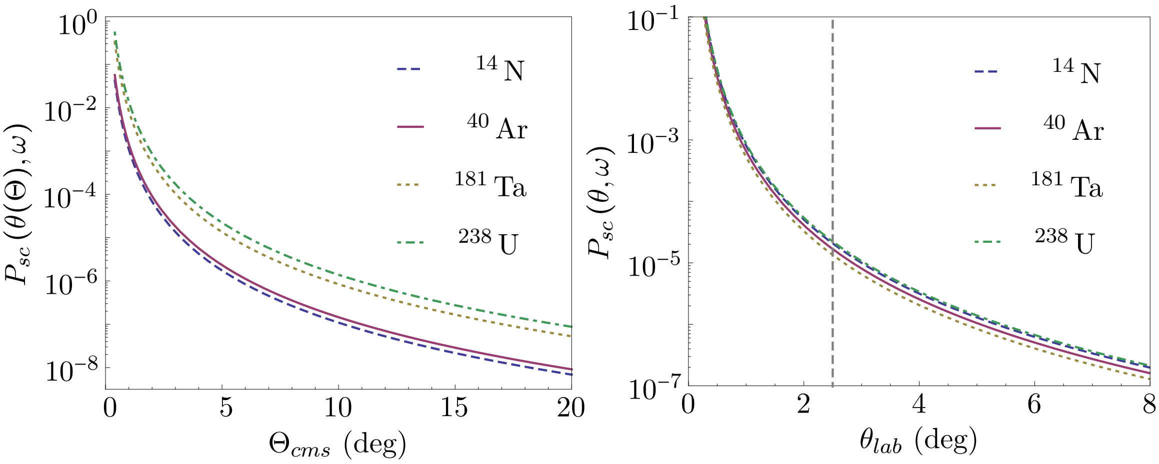

Fig. 3.15: Dependence on angle $\{\Theta, \theta\}$ for the fraction of particles scattered into a solid angle $\omega \approx 7.7 \times 10^{-6}$ sr given in centre of mass (left) and laboratory frame (right). The dashed vertical line marks the angle $\theta = 2.5°$ between the beam axis and the collimator setup housing the tantalum foil.

in the centre-of-mass frame is given by

$$E(\Theta; A_p, A_t) = E_0 \left\{ 1 - 4 \sin^2(\Theta/2) \frac{A_{red}}{A_p + A_t} \right\} \tag{3.9}$$

according to energy and momentum conservation. For the laboratory frame, Fig. 3.16 shows

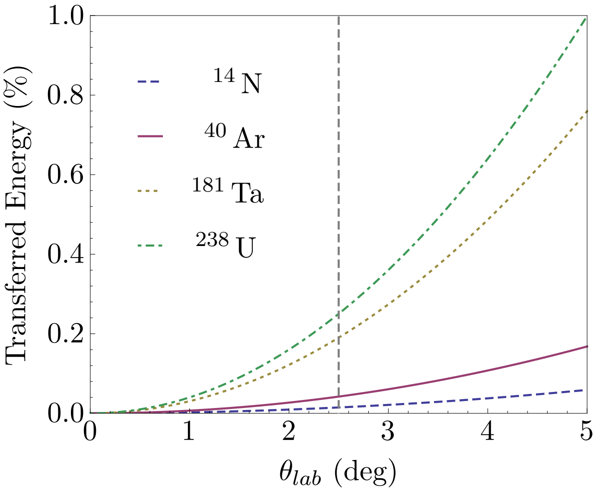

Fig. 3.16: Energy transferred to the target nucleus by the projectile given as fraction of the initial energy.

the transferred energy to the target, whereas the vertical, dashed line marks the angle of the collimator axis with respect to the incoming beam. The energy transfer to the target nucleus is below 0.3 % for all projectiles up to uranium. While a mean shift of energy is not a major issue for the determination of the phase-space distribution, the energy spread due to the finite solid angle has to be small. Both contributions will be discussed in Chapter 7.

3.4.3 Complementary SRIM Calculation

Apart from the analytical estimation of the attenuation factor $P_{sc}(\theta, \omega)$ (Eq. (3.8)), a SRIM simulation has been carried out for consistency. SRIM is a commonly used semi-empirical approach to simulate the kinematics of ions in matter [49]. In contrast to the considerations in Sec. 3.4 the effect of the electronic configuration of the target is taken into account. A large pool of experimental data of stopping powers for projectile-target combinations and energies is used by the authors to continuously improve the semi-empirical Monte-Carlo simulation in addition to new theoretical understandings. SRIM only takes geometries of parallel, layered target materials with customisable thickness into account and further allows to specify the incident angle of the monochromatic, unidirectional projectiles. Since the output data contains the directional cosine information, it is possible to take the collimator acceptance $\{\theta, \omega\}$ into account.

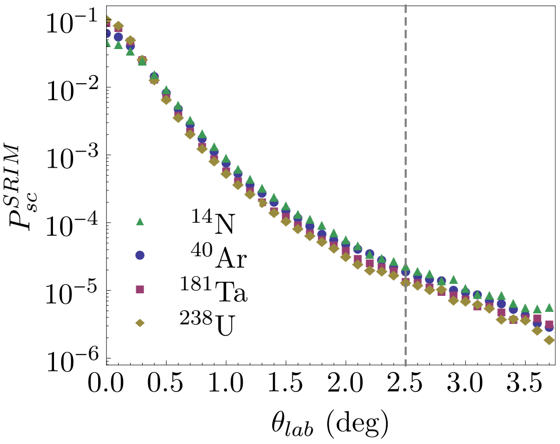

Fig. 3.17: Particle attenuation for N, Ar, Ta, and U projectiles using SRIM under consideration of $\theta = \{0°, 3.7°; \Delta\theta = 0.1°\}$ and solid angle $\omega = 7.7 \times 10^{-6}$.

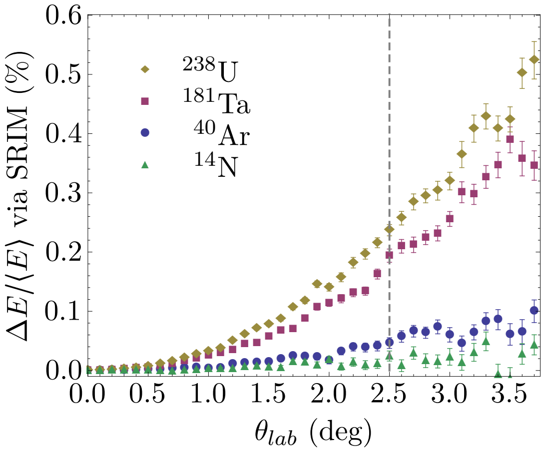

Fig. 3.18: Energy transfer for peripheral collisions using SRIM. Contributions from electronic stopping have been subtracted to be comparable to Fig. 3.16.

Simulation runs have been performed with typical projectiles $\left(^{14}\text{N}, ^{40}\text{Ar}, ^{181}\text{Ta}, ^{238}\text{U}\right)$ at a monochromatic kinetic particle energy of 1.4 AMeV. The unidirectional stream of particles with no lateral extension enters the tantalum foil of 210 µg/cm^2 under an angle of 1.25°. Subsequently, only particles are considered which have been scattered into the collimator acceptance. Emission point angles θ from the foil to the collimator are sampled from 0° to 3.7° at a constant solid angle $\omega = 7.7 \times 10^{-6}$. Obviously, due to the low probability for a particle to pass the collimator, a large number of about 10^7 initial particles is required. In Fig. 3.17 the fraction of particles scattered into solid angle ω is plotted for different angles of the collimator setup (corresponding to Fig. 3.15). The dashed vertical line marks the actual experimental configuration of 2.5°. For comparison, the values at $\theta_{lab} = 2.5°$ are listed in Tab. 3.1 together with the those calculated in Sec. 3.4.1 showing a very good agreement within 10%. Additionally, the momentum transfer to the target nucleus is shown in Fig. 3.18, by means of the transferred energy. To account for the momentum transfer, the collisional straggling contribution at 0° has been subtracted as a constant offset from the data. Hence, it can be compared to the values calculated from Eq. 3.9 and Fig. 3.16. The corresponding values are listed in Tab. 3.1 and also show a very good agreement within the statistical error of the SRIM data.

Tab. 3.1: Comparison of attenuation numbers derived from classical Coulomb scattering and via the SRIM Monte-Carlo suite. The transferred energy computed by SRIM is corrected by the straggling offset at 0° for comparison.

Proj. → Ta Foil (210 μg/cm^2)	^{14}N	^{40}Ar	^{181}Ta	^{238}U
Attenuation factor via classical Coulomb scattering	2.07×10^{-5}	1.67×10^{-5}	1.34×10^{-5}	1.24×10^{-5}
Attenuation factor via SRIM	2.23×10^{-5}	1.75×10^{-5}	1.46×10^{-5}	1.34×10^{-5}
Statistical uncertainty (%)	1.5×10^{-6}	1.4×10^{-6}	1.2×10^{-6}	1.1×10^{-6}
Energy transfer (%) via classical Coulomb scattering	0.015	0.042	0.19	0.25
Energy transfer (%) via SRIM	0.024	0.046	0.19	0.24
Statistical uncertainty (%)	8.5×10^{-3}	9.0×10^{-3}	1.1×10^{-2}	1.0×10^{-2}

Results of the SRIM Monte-Carlo simulation support the analytical calculations using the classical Rutherford cross-section, which includes the probability for ions to scatter in solid angle ω and the momentum transfer to the target nucleus. In general, an attenuation factor for this setup is in the order of 1.5×10^{-5}.

3.4.4 Estimate of Total Attenuation Factor

With Eq. (3.8) we now have an estimate $P_{sc}(\theta,\omega)$ on the fraction of particles being effectively detected based on the incoming flux j. What has not been accounted for so far is the effect of the first aperture on the particle attenuation. Figure 3.19 (left) shows a typical transverse density distribution (in approximation of a Gaussian distribution) of an argon beam with the dimension of the aperture as a relatively small, black disk compared to the beam extension. On the right of Fig. 3.19 the projections onto the transversal axes are plotted. Since the beam widths in horizontal and vertical σ_x and σ_y fulfill the condition $\sigma_x \gg r_a$ and $\sigma_y \gg r_a$, the *maximum* fraction that transits the aperture $P_{ap}(r_a\,;\sigma_x,\sigma_y)$ can be calculated approximately by

$$P_{ap}(r_a\,;\sigma_x,\sigma_y) \approx \frac{1}{2\pi\sigma_x\sigma_y}\underbrace{\mathrm{e}^{-\frac{1}{2}\left\{\left(\frac{x=0}{\sigma_x}\right)^2+\left(\frac{y=0}{\sigma_y}\right)^2\right\}}}_{=1}\cdot\pi r_a^2 = \frac{r_a^2}{2\sigma_x\sigma_y} \approx 7.7\times10^{-4}. \tag{3.10}$$

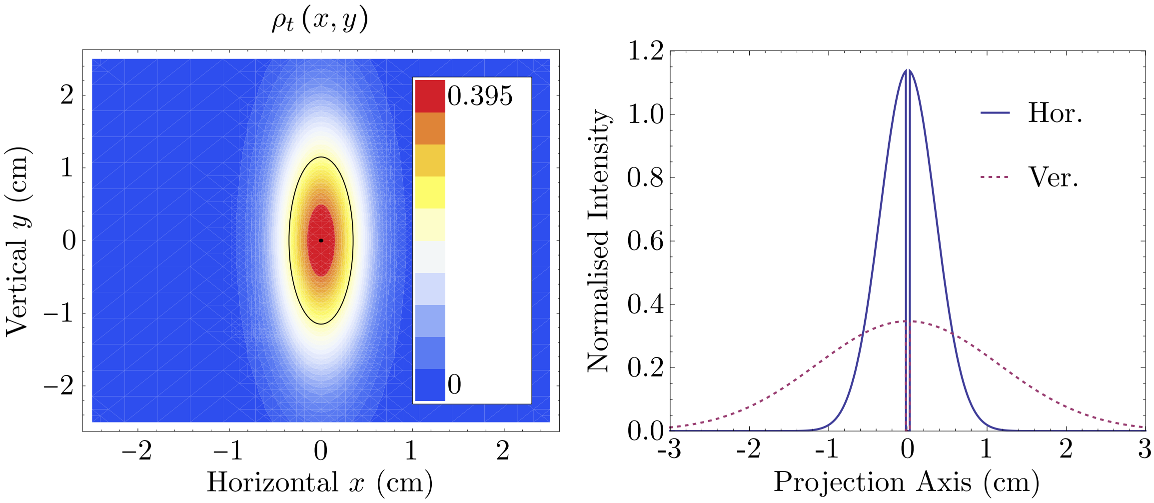

Fig. 3.19: Typical transverse particle density distribution $\rho_t\,(x,y)$ in Gaussian model space (normalised) during measurements (left) with $\sigma_x \approx 3.5$ mm and $\sigma_y \approx 11.5$ mm. The black dot in the centre shows the dimension of the first aperture of $r_a = 0.25$ mm with respect to the transverse beam extension. Within the black ellipse with semi-axes $\{\sigma_x, \sigma_y\} \approx 39\,\%$ of all particles are located. A projection onto both axes with a simplified shadowed cut of the aperture is shown on the right figure.

Together with $P_{sc}(\theta,\omega)$ the estimated effective attenuation factor

$$P_{eff}(\theta,\omega,r_a\,;\sigma_x,\sigma_y) = P_{sc}(\theta,\omega)\cdot P_{ap}(r_a\,;\sigma_x,\sigma_y) \tag{3.11}$$

is on the order of 10^{-8}. Consequently, the estimated *mean* rate of particles $\lambda_b\,(\text{bunch}^{-1})$ entering the experiment setup is given by

$$\lambda_b = P_{eff}(\theta,\omega,r_a\,;\sigma_x,\sigma_y)\cdot n_\tau\cdot\frac{\tau}{T_{rf}}, \tag{3.12}$$

with τ being the macro pulse length, n_τ the number of ions per macro pulse and T_{rf} the period length of the UNILAC prestripper RF of about 36.136 MHz as given in Tab. 3.2.

Tab. 3.2: Mean event rate per bunch λ_b registered at typical parameters; number of particles inside macro pulse n_τ, mean scattering angle θ, solid angle ω, radius of the first aperture r_a, transversal horizontal and vertical spreads σ_x and σ_y, macro-pulse length τ and RF period length T_{rf}.

$\boldsymbol{\lambda_b}$ (per bunch)	$\boldsymbol{n_\tau}$	$\boldsymbol{\theta}$ (°)	$\boldsymbol{\omega}$ (sr)	$\boldsymbol{r_a}$ (mm)	$\boldsymbol{\sigma_x}$ (mm)	$\boldsymbol{\sigma_y}$ (mm)	$\boldsymbol{\tau}$ (µs)	$\boldsymbol{T_{rf}}$ (ns)
1.4×10^{-3}	10^9	2.5	7.7×10^{-6}	0.25	3.5	11.5	200	27.7

3.4.5 Poisson Process

From a statistic point of view, very low probabilities $P_{eff} \ll 1$, for a particle to be scattered into solid-angle acceptance ω of the collimator, mean that the particle attenuation is described by a Poissonian process, which is characterised by its mean value λ_b only[2]. Here, the Poisson distribution

$$P_{\lambda_b}(k) = \frac{\lambda_b^k}{k!} \mathrm{e}^{-\lambda_b} \tag{3.13}$$

delivers the probability to measure k particles of a certain bunch at a mean rate of λ_b measured particles per bunch. The probability distribution is plotted in Fig. 3.20 with the mean event rate per bunch of $\lambda_b \approx 1.4 \times 10^{-3}$ (see Tab. 3.2). Since λ_b is very small on the bunch time-scale, the most probable situation is that no event occurs at a certain bunch. While the probability for no event to occur during bunch delivery $P_{\lambda_b}(0)$ is about 1 (0.9986), it is significantly suppressed for a single event to occur $P_{\lambda_b}(1)$, which is 1.398×10^{-3} ($\approx \lambda_b$, since $\lambda_b \ll 1$). Measuring exactly two events is suppressed by more than three orders of magnitude as $P_{\lambda_b}(1) \approx 1 \times 10^{-6}$.

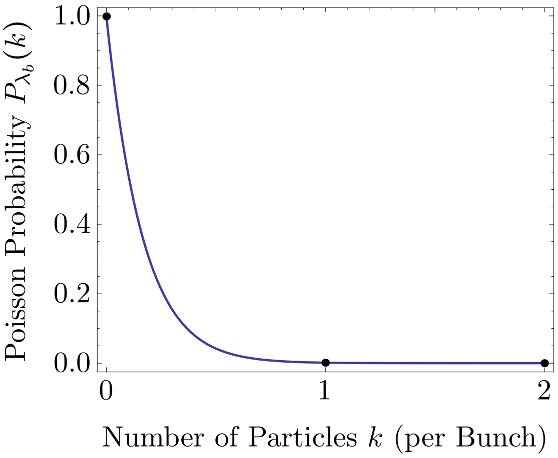

Fig. 3.20: Poisson probability for k events to occur inside a single bunch at an expectation value of $\lambda_b = 1.4 \times 10^{-3}$.

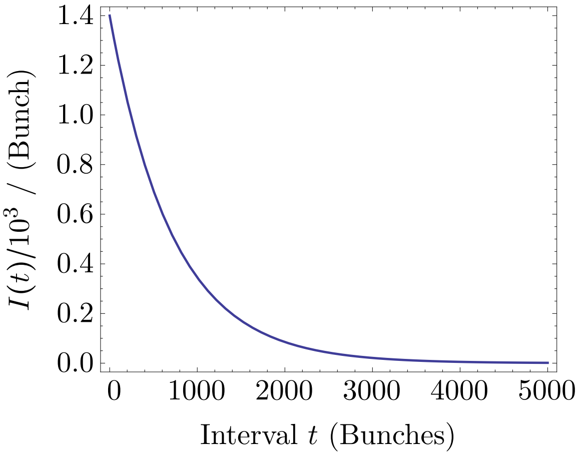

Fig. 3.21: Distribution of intervals between adjacent events. The most probable situation is that the next event occurs in the same bunch.

Moreover, the interval distribution of adjacent events

$$I(t; \lambda_b) = \lambda_b \, \mathrm{e}^{-\lambda_b t} \tag{3.14}$$

as described in [50], is shown in Fig. 3.21. The distribution is normalised,

$$\int_0^\infty \mathrm{d}t \, I(t; \lambda_b) = 1 \,, \tag{3.15}$$

---

[2] Subscript "b" highlights the reference period of occurrence which is a bunch (micro pulse) here.

and the fraction of multiple events per bunch $P^{me}_{\lambda_b}$ can therefore be estimated by

$$P^{me}_{\lambda_b} = \int_0^1 \mathrm{d}t\, I(t;\lambda_b) = \sum_{k=2}^{\infty} P_{\lambda_b}(k)\,. \tag{3.16}$$

Since the rate of scattered particles is very small on the bunch time scale, Eq. (3.16) is approximately given by

$$P^{me}_{\lambda_b} = \sum_{k=2}^{\infty} P_{\lambda_b}(k) = 1 - \sum_{k=0}^{1} P_{\lambda_b}(k) \approx 1 - P_{\lambda_b}(0) \tag{3.17}$$

using the fact that $P_{\lambda_b}(0)/P_{\lambda_b}(1) = \lambda_b \ll 1$. Further simplification gives

$$P^{me}_{\lambda_b} \approx 1 - \frac{\lambda_b^0}{0!}\mathrm{e}^{-\lambda_d} \overset{\lambda_b \ll 1}{\approx} 1 - (1 - \lambda_b) = \lambda_b. \tag{3.18}$$

Taking into account that at a given attenuation ratio it is not possible to completely avoid multiple hits, with a probability $P^{me}_{\lambda_b} < 2 \times 10^{-3}$ for multiple particles entering the TOF section within a certain bunch, we can safely neglected them in the present configuration.

Thus it is shown that in the present TOF setup multiple hits do not significantly contaminate the data.

Chapter 4

Data Acquisition and Data Analysis

The following chapter describes the signal handling downstream the detectors of the TOF setup and the direct calorimetric approach. After the data acquisition has been introduced, the full post-processing chain of the raw data is described. This includes the reconstruction of the phase space and further treatment of the data.

4.1 Time-of-Flight Setup

4.1.1 Double-Threshold Discriminator

Before detector signals can be reasonably registered at the TDC module, the pulse signals must carefully be processed by discriminators. As outlined in Sec. 3.1.1, signals from the MCP detector and poly-crystalline diamond detector reflect an event at two ends of a drift section of known separation. This TOF relies on the precise timing information when the particle has crossed the reference points. Therefore, the pulse shapes of nanosecond duration have to be associated with a logic timing signal. On the technical side, the generation of the logic timing is done by so-called discriminators. Discriminators are available with different working principles. For signals of identical shape, a so-called leading edge discriminator is sufficient. It generates the timing signal from a tunable threshold value which determines the logical timing once the detector signal crosses the threshold value. As long as the rise time is smaller than the required time resolution, a leading edge discriminator is generally well suited for the task. Otherwise, for high timing requirements, as it is required in this work, the leading edge discriminator is obviously an insufficient approach if pulse shapes from a detector exhibit a broad pulse-height distribution. The introduced undesired systematic time jitter of leading edge discriminators is called *time walk* or simply *walk*. Constant-fraction discriminators [51] provide time walk correction for signals with a broad pulse-height distribution of pulse shapes that only differ by a scaling factor. If the pulse shapes vary beyond a scaling factor, a discrimination approach that solely relies on the rising edge is favourable. A method which implements the sensitivity on the slope of the rising edge only is the *double-threshold discriminator* which has been proposed by Frolov et al. [52] and has been considered for certain TOF modules [53] of the CERN ALICE experiment. The working principle takes into account two tunable thresholds at the rising edge as schematically depicted in Fig. 4.1. It assumes a linear characteristics of the pulse shape ensemble between the two thresholds. When the signal reaches a threshold $thr_{\{1,2\}}$ a linear voltage ramp is started. The slope $a_{\{1,2\}}$ of the ramps are generated internally to comply with

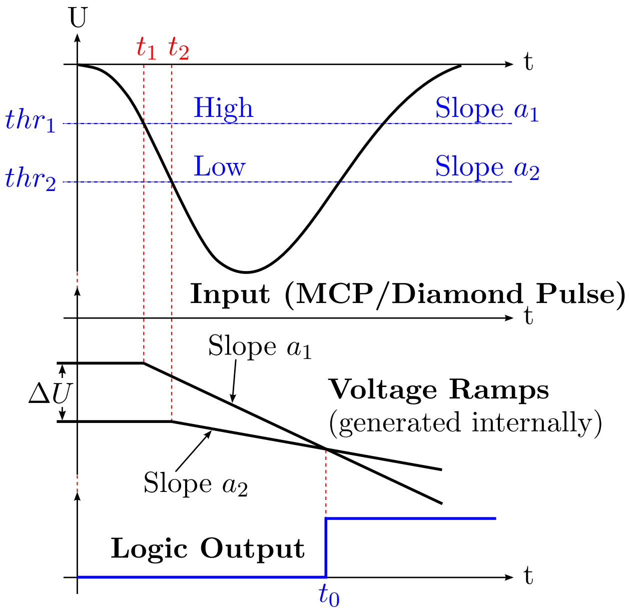

Fig. 4.1: Working principle of the *double-threshold discriminator* used for timing generation of the MCP and diamond pulses.

$$\frac{thr_1}{thr_2} = \frac{a_1}{a_2}\,. \tag{4.1}$$

A low-walk timing pulse is triggered at the intersection of both ramps at

$$t_0 = \frac{\Delta U}{a_1 - a_2}\,. \tag{4.2}$$

According to Frolov et al. [52] a walk of only 10 ps could be obtained at a pulse-height distribution ranging from 0.2 to 1.5 V. The discriminator used in the work is based on an ASIC designed at GSI experiment electronics department [54].

4.1.2 NIM Electronics Setup

The information to reconstruct the phase space distribution (see Sec. 4.1.5) recorded using the TOF setup is based on three input timings.

- UNILAC RF timing reference (from master oscillator)
- MCP timing
- Diamond timing (Poly-crystalline diamond)

MCP and diamond timings are used to determine the TOF, whereas the UNILAC RF serves as a relative arrival time measure for the bunch structure. A NIM setup prepares all timing signals fed into the TDC module as depicted in Fig. 4.2. In the following, the numbering scheme of the signal sources and NIM modules is kept constant.

RF Reference. ① The RF reference from the UNILAC master oscillator is assigned to a slope-sensitive zero-crossing timing at discriminator module ⑤. As the RF reference would contribute to an excessive amount of data, at a regular time period of $T_{rf} \approx 27.7$ ns, overhead reduction is considered and RF timings are restricted to macro-pulse delivery by a safe margin (see Sec. 4.1.4). The amount of data is further significantly reduced by prescaling at a ratio of 1:10. Leading-edge discriminator ⑤ generates the RF timing pulse and provides the aforementioned prescaling by suppressing the output for nine following periods. This is accomplished using one logical output with an adjusted pulse width of about $9 \times T_{rf}$ as veto trigger. Finally, module ⑥ provides gating of the RF timing with respect to the macro-pulse delivery, while a timing module ② generates the appropriate macro-pulse/cycle gate.

Macro-Pulse/Frame Gate.[1] ② A UNILAC-event-timing module generates a gate pulse according to a cycle defined between two events. To enclose the actual macro pulse by a safe margin, UNILAC-timing events 4 and 8 have been chosen. This includes a RF preparation-time of at least 50 µs advancing and 40 µs after real macro-pulse delivery. For a detailed documentation of the UNILAC-timing interface and event structure see [55] (german only).

MCP Timing. ③ Detector pulses from the MCP are processed by the double-threshold discriminator ⑧. To omit distinct dark counts, the detector timings are only registered during macro-pulse delivery. The corresponding gating is provided by module ⑦ before the timing is fed to the TDC.

Diamond Timing. ④ Since the diamond detector, contrary to the MCP, features no dark counts, the detector pulse is only processed by the double-threshold discriminator ⑧ and fed to the TDC.

---

[1] Depending on the context, this time interval is referred to as *macro-pulse gate*, *cycle* or *frame*. The term “macro pulse” is used whenever the fact of the macro pulse being enclosed during the gate is highlighted (although the gate time is not sharply clipped to the macro pulse). Furthermore, the term “cycle” is connected to the corresponding UNILAC events. The term “frame” is used in conjunction with recorded timing signals and consists of all data registered within a cycle.

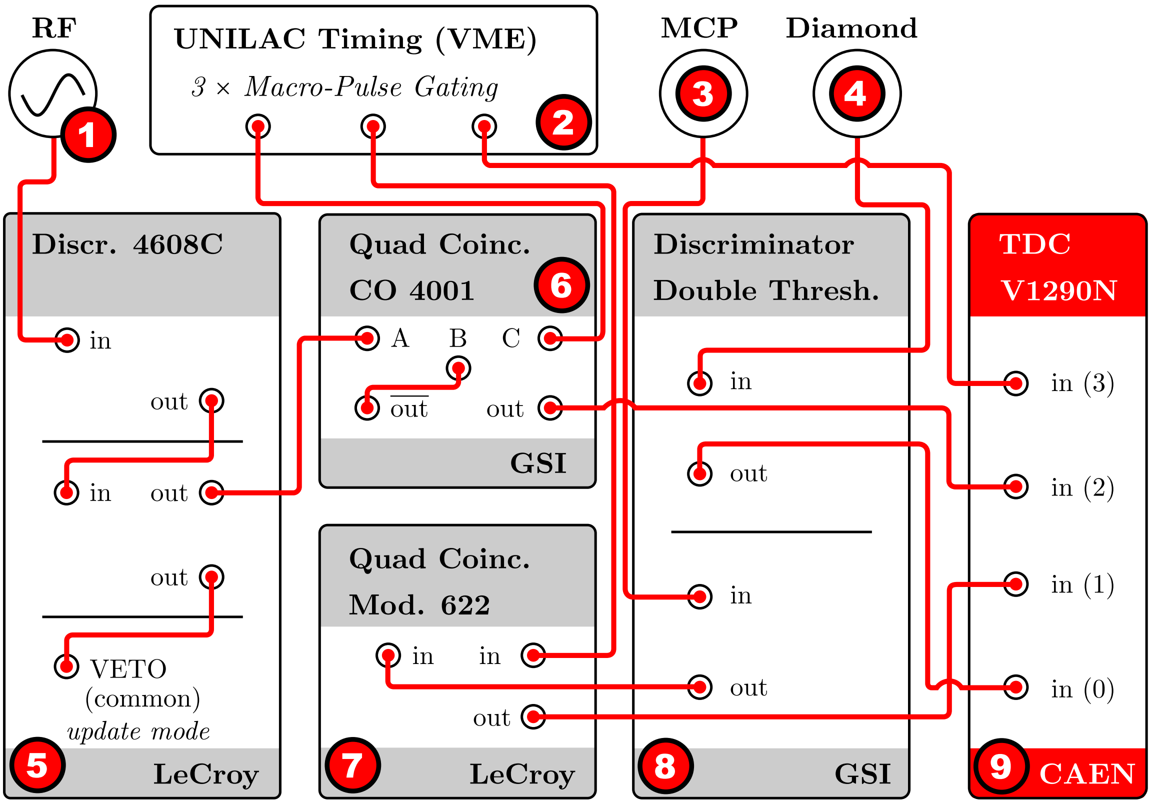

Fig. 4.2: Schematic signal processing network for the *time-of-flight* measurement. Labels ① to ④ reference the signal sources consisting of: the UNILAC RF signal ① provided by the master oscillator (36.136 MHz), the macro-pulse/cycle gate ② generated by the custom-made GSI timing board (D. Liakin [30]), the anode at the back of the MCP ③ and the poly-crystalline diamond detector ④. NIM modules ⑤ and ⑥ are used as prescaler (1:10) of the generated logical RF reference to damp the incoming data rate and blocks RF output not within the time window of the macro pulse. Similarly, module ⑦ limits the logical MCP output to the macro pulse only, to avoid distinct dark pulses. In advance, the MCP pulses are processed by the *double threshold discriminators* ⑧. Eventually, processed signal sources ① to ④ are registered by a fast TDC ⑨.

4.1.3 Time-to-Digital Converter

After the timing signals of the TOF setup have been generated and processed by the NIM chain, as described in Sec. 4.1.2, a low time-jitter TDC registers the timing data. The TDC, a CAEN V1290N VME module [56], features a nominal resolution of better than 35 ps (RMS). Per input channel a double-hit resolution of 5 ns allows to record events that are at least 5 ns separated. Once a NIM pulse is registered, the internal global clock state is dumped to the appropriate channel output buffer.

A timing data structure, as schematically depicted in Fig. 4.3, is represented by a 4-byte vector alignment. It consists of a header field denoting the input channel and the 21-bit clock dump. With a channel width corresponding to about 24.4 ps, this data field overflows

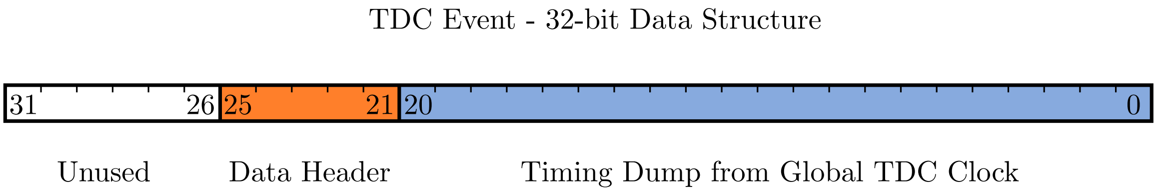

Fig. 4.3: TDC timing represented as a 4-Byte vector. The lower 21-bits contain the actual dump from the internal global clock of the TDC. Given the LSB equivalent of about 24.4 ps, overflowing occurs every 51.2 µs

every 51.2 µs. The raw clock information is stored and the overflow-corrected values are put into relation to the preceding macro-pulse-start timing. Moreover, as the macro-pulse number is recorded, timing values are globally connected throughout the measurement.

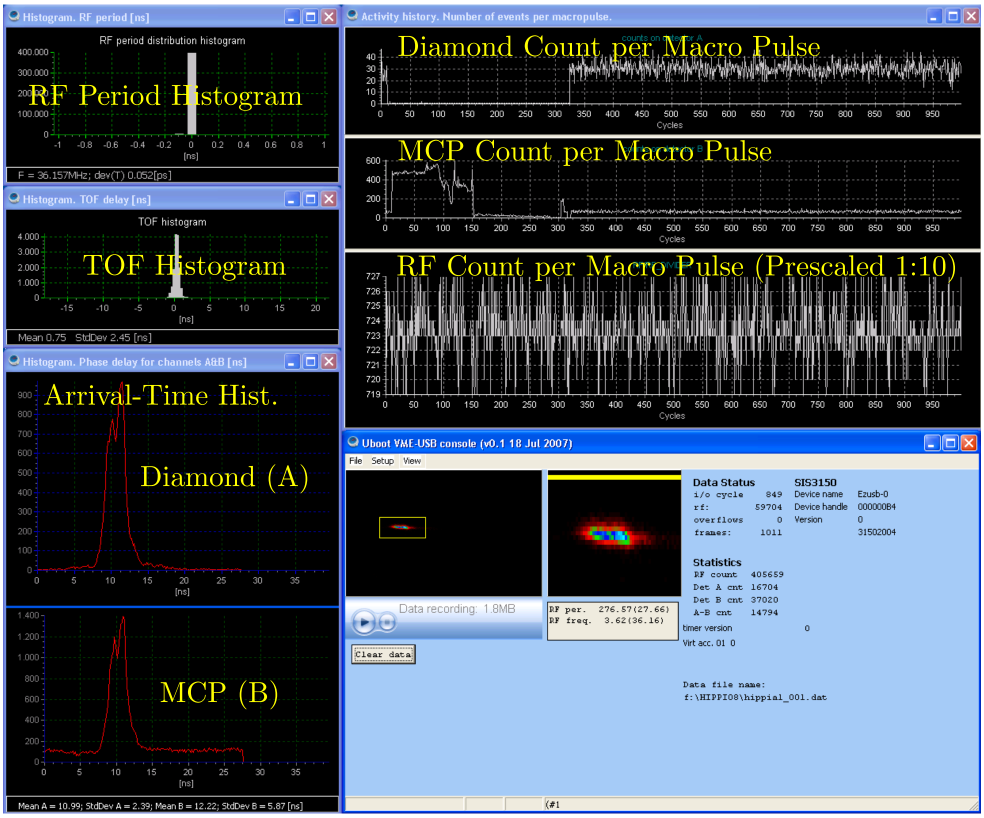

```
F = 36.157MHz; dev(T) 0.052[ps]
Mean 0.75   StdDev 2.45 [ns]
Mean A = 10.99; StdDev A = 2.39; Mean B = 12.22; StdDev B = 5.87 [ns]

Data recording:  1.8MB

RF per.   276.57(27.66)
RF freq.   3.62(36.16)

Data Status              SIS3150
i/o cycle      849       Device name     Ezusb-0
rf:          59704       Device handle   000000B4
overflows        0       Version         0
frames:       1011                       31502004

Statistics
RF count    405659
Det A cnt   16704
Det B cnt   37020
A-B cnt     14794
timer version               0
Virt acc. 01  0

Data file name:
f:\HIPPI08\hippial_001.dat
(#1
```

Fig. 4.4: GUI frontend by Dmitry Liakin (2006). The DAQ frontend runs on a regular PC and communicates with a USB 2.0 to VME interface (Struck SIS3150). Apart from providing an on-line display of all incoming timings and statistics, the high-voltage supplies can be controlled from within the program.

A Struck SIS 3150 VME controller [57] acts as VME bus master to the TDC and timing module and is interfaced by a commercial PC via USB 2.0. During a measurement, a set of timing data, according to Fig. 4.3, is accumulated in a single file of linear data. The actual phase space distribution is reconstructed via off-line post processing developed in this work along with data analysis. Apart from the aforementioned timing signals, the macro-pulse start timing is directly recorded via the macro-pulse gate from module ❷. While it is not strictly necessary for the plain phase space distribution, it allows to relate bunches with respect to the macro-pulse start. This becomes necessary when time cuts of the phase space are compared, e. g. the phase-space distribution of the first and second half of the macro pulses.

Figure 4.4 shows the main view of the data acquisition GUI frontend. During recording of the raw data, statistics of the timing signals are provided on-line, in particularly, the preliminary phase space distribution (bottom right window). Histograms of the raw detector timings are shown on the bottom left. A noteworthy comparison of the poly-crystalline diamond **(A)** and MCP **(B)** histograms shows a flat background of dark counts of the MCP detector which is not present at the diamond detector.

4.1.4 Post-Processing of Raw Data

During a measurement, using the TOF setup, the TDC channel buffers are continuously dumped from a linear data stream. A TDC event is represented by the 4-byte data structure as depicted in Fig. 4.3. The four recorded events are characterised as follows:

- **Diamond detector** (Poly-crystalline)
    - Timing signals from the poly-crystalline diamond detector provided by a double-threshold discriminator
    - Features no dark counts
- **MCP detector**
    - Timing signals from the micro-channel plate, provided by a double-threshold discriminator
    - Dark counts occur
- **UNILAC RF**
    - Slope-sensitive zero-crossing of the UNILAC RF master oscillator signal
    - Regular data, prescaled (1:10) to reduce overhead
- **Frame start**
    - Start timing provided by the macro-pulse gate reference

Post-processing of the raw data aims for the extraction of the actual plain particle events forming the phase-space distribution. This comprises the determination of the correlated MCP and diamond events, the corresponding RF reference, the bunch (micro pulse) at which the particle event occurs and the macro pulse number.

Calibration of the TDC is performed using the RF signal of 36.136 MHz provided by the UNILAC master oscillator. With the knowledge of the RF period time, a TDC channel is determined to 24.414 ± 0.0002 ps by linear regression of the recorded RF timing.[2] TDC-clock dumps are represented by 21 bits. This means that overflowing occurs about every

---

[2] In this work 'channels' always refers to channels of the TDC in context with the TOF DAQ.

51.2 µs per input channel and must be considered consistently. Overflow correction of the RF data is straightforward as the prescaled RF frequency is higher by about a factor of 200. Diamond and MCP timings, in contrast, are overflow corrected in accordance with the regular RF timing. Multiple particle events per bunch, which are unavoidable (see Sec. 3.4.5), will be detected and discarded as long as they are separated by more than 5 ns, given the double-hit resolution limit of the TDC.

The regular RF timing is prescaled (1:10) by the NIM setup, as described in Sec. 4.1.2, to prevent excessive data overhead. Hence, with an RF period time of about 27.7 ns, an RF timing signal is registered every 277 ns. Restoration of the skipped RF events is accomplished by linear regression. At the same time, the effective RF timing precision is slightly enhanced. To characterise the stability of the linear regression, a measurement from the HIPPI [58] campaign in December 2008, with a large number of events, is taken as reference. The measured data comprises 2428 macro pulses with a gate length of 200 µs, which corresponds to ≈ 720 supporting points. Each macro pulse is connected to a separate fit of the raw RF timing data. The corresponding distribution, shown in Fig. 4.5, features a mean slope of ≈ 11334.8981 channels per ten RF periods with a standard deviation of $\approx 3.5 \times 10^{-4}$ channels per ten RF periods. This results in an RMS width, with respect to the mean value, of $\frac{\sigma}{\mu} \approx 3.1 \times 10^{-8}$ and highlights a very narrow distribution supported by the low integral-non-linearity of the TDC of less than 2.5 LSB (corresponding to 61 ps) [56] and the large amount of supporting points. Typically, the fit comprises several hundreds of supporting points, depending on the macro-pulse length. Recorded RF timings preceding the actual beam delivery are skipped, as will be explained in the following paragraph.

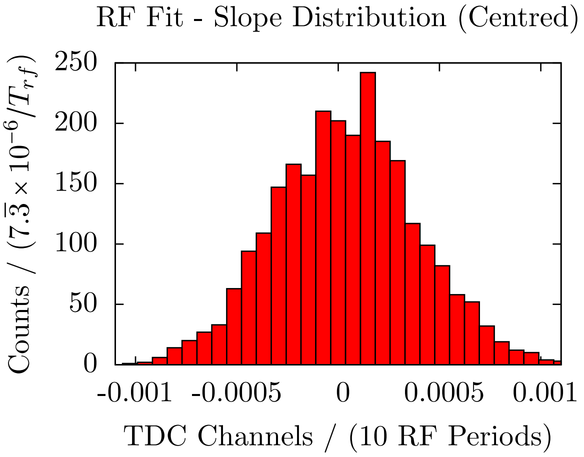

Fig. 4.5: Centred slope distribution from RF fit for RF reconstruction. Fits from all 2428 macro pulses were used, each incorporating RF timings from beam delivery start onwards.

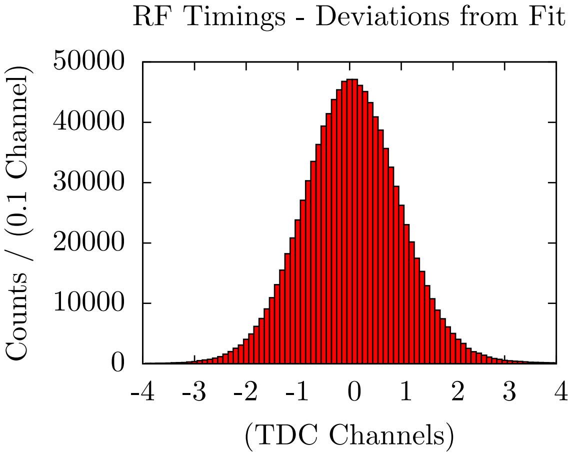

Fig. 4.6: Deviation of prescaled RF timings from the corresponding linear RF fit. Includes RF timings from all 2428 macro pulses. RF timings from beam delivery start onwards are taken into account.

The expected stable regularity of the RF is not sustained over the full frame. Based on the same dataset as the previous slope distribution, Fig. 4.7 shows the deviation of registered

RF data with respect to the corresponding linear regression, represented by the grey data points, along a random frame. Most data points scatter around the fit reference about less

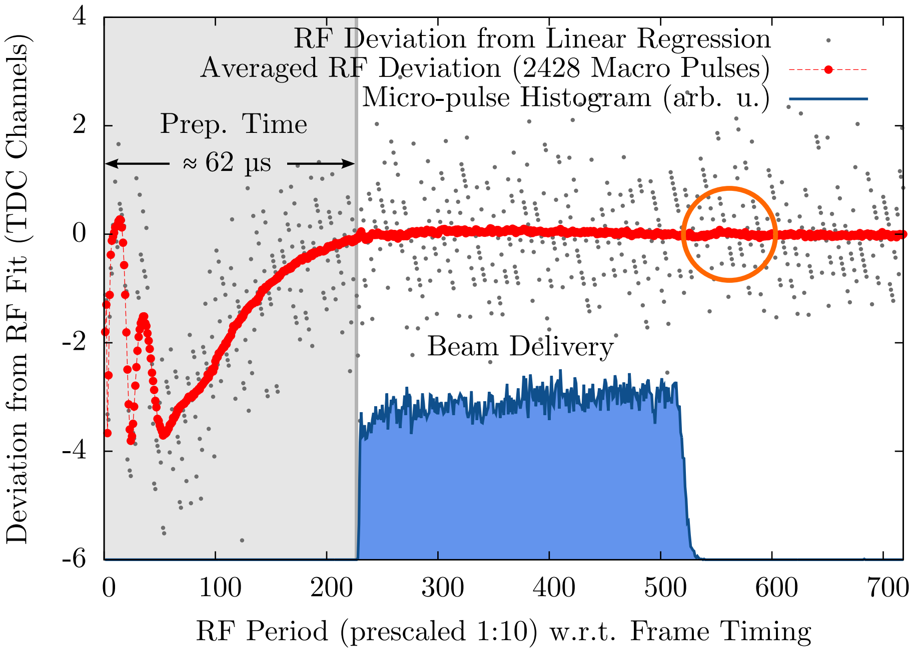

Fig. 4.7: Typical deviation of measured, prescaled RF timings from the linear regression. An avarage over all 2428 acquired cycles is shown by the red data points. The grey-shaded area marks the region which is affected by transient oscillation between UNILAC-timing event 4 and 6 [55]. For completeness, the corresponding macro-pulse-current equivalent, by means of the micro-pulse histogram, is given by the blue line. The data is taken from a measurement during the HIPPI [58] campaign 2008 which features a high count of $\approx 6 \times 10^4$ events.

than ±1 TDC channels which is in accordance with the TDC specification [56], claiming an input jitter of less than 35 ps (RMS). The red line marks the deviation averaged over all 2428 acquired frames. At the beginning of the macro-pulse gate, prescaled RF timings up to about period 230, the grey-shaded area, feature a clear deviation from a uniform behaviour along the frame. In terms of the global UNILAC event timing [55] this interval is defined between event 4 and 6. Although the UNILAC master oscillator is expected to provide a constant stable RF, the fluctuations in measured RF period length most likely origin from pick-up effects of transient oscillations during high-power RF switching. Regardless of the small impact of the fluctuations, with a relative deviation of less than 0.4 ‰ per RF period at maximum, it is taken care of by excluding the "preparation time interval" when performing the linear regression. The blue line in Fig. 4.7 shows the micro-pulse occupancy, taking all recorded frames into account. This provides information of the macro-pulse current represented at the given RF time base. It is clearly visible that the initial distortions, during "preparation time", virtually do not affect the interval of actual beam delivery. Furthermore, an additional bump is present, denoted by the orange circle. Since it is correlated with the final edge of the macro-pulse current, the bump can also be attributed to power switching processes. Taking only RF events into account starting with beam delivery after the preparation time, the jitter distribution with respect to the linear RF fit is shown in Fig. 4.6. The histogram comprises prescaled RF data from all 2428 macro pulses with a total of $\approx 10^6$ events and, thus, results in an almost perfect Gaussian distribution. A standard deviation of only 0.968 channels, which corresponds to ≈ 23.6 ps, highlights a very good performance of the RF DAQ chain described earlier in this chapter. The present characteristic were reproducible in all measurements with only minor variations.

Detector Timings. With the reconstructed RF events it is straightforward to properly align the registered MCP and diamond detector timings. Subsequently, coincidences are determined using an appropriate time window. Ambiguous events are taken care of where possible, but detection is limited by the double-hit resolution of the TDC. Multiple-ion events per bunch give rise to ambiguous coincidences within the time window. In contrast to the diamond detector, the MCP features a mean dark-pulse rate, typically in the order of $1-10\ \mathrm{s}^{-1}\,\mathrm{cm}^{-2}$. Hence, in rare cases, those may also add to ambiguous event configurations which cannot be resolved and must be discarded.[3] Unfortunately, it turned out that time windows cannot be limited to a single bunch interval. In fact, large-range low-energy tails may require time windows of three to four RF periods, which will be discussed in Chapter 5. Obviously, with larger time windows ambiguous event configurations become more likely. Concerning the MCP geometry, we can assume a flat distribution of dark pulses at a mean rate of $\approx 10\,\mathrm{s}^{-1}$. This gives rise to a probability of 10^{-7} to register a *random* dark event within four RF periods which can safely be neglected. Multiple-ion events, in turn, have a bigger impact. The interval-length distribution of consecutive ions scattered into the acceptance of the collimator setup is given by Eq. 3.14. Consequently, the mean fraction $\langle p_n \rangle$ of ambiguous configurations within the first n RF periods after an ion is registered, is estimated by

$$\langle p_n \rangle = \int_0^n \mathrm{d}t\, I(t;\lambda_b) = \lambda_b \int_0^n \mathrm{d}t\, e^{-\lambda_b t} \overset{\lambda_b \ll \frac{1}{n}}{\approx} n\,\lambda_b\,. \tag{4.3}$$

Incoming mean rates λ_b typically range between 10^{-4} and 10^{-3} ions per bunch depending on the ion species. This means, for a time window spanning four bunches and using Eq. 4.3, the fraction of ambiguous event configurations is less or equal than $4\,‰$. These ambiguities are detected and discarded as long the separation of the events is larger than the double-hit resolution of the TDC. With a double-hit resolution of 5 ns of the TDC (per input channel), we can assume only those configurations to cause potential spurious events which arrive within a single bunch. This estimate is supported by typical bunch lengths of 1 to 3 ns (RMS) and entails a fraction of potentially flawed events between 0.1 and $1\,‰$.

---

[3] MCP pulses, which originate from dark emission of the MCP channels, posses a different characteristic shape. Compared to the biased secondary electrons emitted from the aluminium foil, those pulses have significantly lower amplitudes. Nevertheless, it is not possible to exploit this as a decision criteria; Pulse heights are not directly accessible in the TOF setup as threshold settings need to be low to reach higher timing resolutions.

4.1.5 Reconstruction of the Phase Space

As outlined in the previous section, the TOF setup presented in this work, registers timing data from the MCP and Diamond detector. In the following, for *particle i*, $t_{mcp,i}$ refers to the MCP timing, $t_{dia,i}$ refers to the diamond-detector timing and $t_{rf,i}$ refers to the preceding RF zero-crossing reference. Transformation from the registered timing information into phase-space coordinates is straightforward but a few remarks are indicated. The measurement does not provide absolute access to phase and energy and focuses on the particle distribution. Instead, the typical approach is to use a linear approximation to reconstruct the momentum/energy information. This allows for a translational invariant description with respect to the relative cable delays. Systematic contributions originating from the related approximations are discussed in Chapter 7. Measurement of the absolute phase and energy of the bunch centre can be performed by the phase-probe TOF sections available at different locations along the UNILAC.

Phase Information. The phase information is directly contained in the arrival time of the incoming ion at the diamond detector. As explained in Chapter 2 and Eq. 2.6, the arrival time $\Delta t_{phase,i}$ is often evaluated with respect to the synchronous particle. This is the common approach in theoretical models of beam transport or within tracking codes. Since access to the synchronous particle is not available, the preceding RF timing is considered a fixed reference as explained earlier in this chapter

$$\Delta t_{phase,i} = t_{dia,i} - t_{rf,i}\,. \tag{4.4}$$

An additional, relative cable delay is not taken into account, since evaluation of the phase space data, in terms of *Twiss parameters* and *emittance*, only covers central moments. It should be noted that, of course, the inter-particle phase relation is not affected by this method. Hence, the difference in phase between two random particles is accessed precisely within the timing resolution, which is important for the distribution characteristics.

On the other hand, the RF reference limits a non-ambiguous determination of the phase to the RF period time. As it turned out, slow particle contributions occur which may span over several RF periods. To some extent it is possible to reconstruct the overflow in phase by the energy phase correlation, i.e. the assumption that slow particles arrive later. This is a legitimate approach as bunches drift several meters after last accelerating IH2 structure, and thus, are expected to show a significant phase-energy correlation. Commonly, the arrival time is provided in nanoseconds. For transformation to the RF phase equivalent rad and degree, see Chapter 2 and Eq. 2.9.

Momentum/Energy Information. The expected mean energy $\langle E\rangle \approx 1.4\ A\mathrm{MeV}$ is derived from the design value of the normalised velocity $\langle\beta\rangle \approx 5.5\,\%$. Hence, the kinematics can be restricted to the classical energy-momentum relation, with mass number A and atomic mass $\approx A \cdot m_u$:

$$E\left(\overset{def.}{=} E_{kin}/A\right) \approx \frac{m_u}{2} c^2 \beta^2\,. \tag{4.5}$$

In terms of detector separation l_{tof} and time of flight $t_{tof,i}$ of *particle i*, between MCP foil and poly-crystalline diamond detector, the kinetic energy trivially writes

$$E_i = E\left(t_{tof,i}\right) = \frac{m_u}{2}\left(\frac{l_{tof}}{t_{tof,i}}\right)^2 . \tag{4.6}$$

By separating out the mean energy $\langle E\rangle$,

$$E_i = \langle E\rangle + \Delta E_i = E\left(t_{\langle E\rangle}\right) + \Delta E_i\left(t_{tof,i} - t_{\langle E\rangle}\right) , \tag{4.7}$$

and considering the linear correction term of the Taylor series of the expansion about $t_{\langle E\rangle}$,[4]

$$\Delta E_i \overset{\frac{\Delta t_i}{t_{\langle E\rangle}} \ll 1}{\approx} \frac{\mathrm{d}}{\mathrm{d}t}E(t)\bigg|_{t_{\langle E\rangle}} \Delta t_i = -2\langle E\rangle\frac{\Delta t_i}{t_{\langle E\rangle}} \quad \text{with} \quad \Delta t_i := t_{tof,i} - t_{\langle E\rangle} , \tag{4.8}$$

the relative energy deviation is approximately given by

$$\frac{\Delta E_i}{\langle E\rangle} \approx -2\frac{\Delta t_i}{t_{\langle E\rangle}} \approx -2\frac{\Delta t_i}{t_{\langle p\rangle}} = -2\frac{c\,\langle\beta\rangle}{l_{tof}}\Delta t_i . \tag{4.9}$$

Several assumptions have been made. Trivially, the linearisation is only valid in the vicinity of the expansion point $t_{\langle E\rangle}$. Furthermore, the last approximation in Eq. 4.9 relies on the assumption that $t_{\langle p\rangle}$ is sufficiently close to $t_{\langle E\rangle}$. This will be discussed in detail in Sec. 7.7. The relative momentum deviation in linear approximation writes accordingly as

$$\frac{\Delta p_i}{\langle p\rangle} \approx -\frac{\Delta t_i}{t_{\langle p\rangle}} = -\frac{c\,\langle\beta\rangle}{l_{tof}}\Delta t_i . \tag{4.10}$$

The mean velocity of bunches registered at the device is provided manually and a deviation from the real situation affects the expansion point of the Taylor series. The mentioned systematic contributions are not of major negative impact and are discussed in detail in Sec. 7.7.1.

Histogramming. Recorded ion events, which have been transformed into appropriate phase-space coordinates, are accumulated in 2-dimensional histograms. A measurement, with a duration of typically several tens of minutes, relies on stable phase-space conditions. Measurements usually require exclusive access to the whole pre-stripper section of the UNILAC due to global settings. This in turn ensures stable beam delivery, from an operating point of view, with constant accelerator settings throughout the whole pre-stripper facility. Stability of beam delivery also varies between different types of ion sources and their operating time with respect to the expected life time. The access to the macro-pulse start timing, using the TOF setup, allows to select certain classes of events and compare the corresponding phase-space distributions. For instance, phase spaces consisting of macro-pulses of the beginning of a measurement can be compared to later ones. This can reveal issues of the ion source and accelerator settings. Also, phase-space distributions of a certain bunch

---

[4] $t_{\langle E\rangle}$ and $t_{\langle p\rangle}$ refer to the TOF of particles of mean energy $\langle E\rangle$ and mean momentum $\langle p\rangle$.

range within the macro pulses can be compared to others. Concerning statistics, this, of course, requires the total event count to be sufficiently large.

4.2 Mono-Crystalline Diamond Setup

The experimental setup, based on a mono-crystalline diamond detector, relies on a single detector only. Instead of a TOF measurement, a semi-conducting detector with calorimetric properties (see Sec. 3.3.3) is used. The particle attenuation mechanism is identical to the TOF approach described in Sec. 3.1.1 and Sec. 3.4. Particles of an attenuated beam, that scatter into the solid-angle acceptance of the collimator setup, will be detected at the mono-crystalline diamond. To recapitulate the experimental site, see Fig. 3.6 for an overview of the diagnostics chamber. Voltage pulse signals from the detector provide a measure of the deposited energy, if the functional dependency on the total accumulated charge from with the projectiles' kinetic energy is known. In principle an injective functional behaviour is obligatory, for the sake of a distinct mapping of a certain pulse information to the kinetic energy. Ideally, a linear dependency is sustained over a large range.

Schematics. Schematics of the electric interface to the detector and the DAQ are depicted in Fig. 4.8. The detector pulses are extracted at the bias tee and amplified by a one- or two-stage Mini-Circuits ZX60-33LN-S+ (50 MHz - 3 GHz, 17.5 dB typ.) amplifier. A positive bias of 100 V, which corresponds to a field strength of 1 V/µm, has been applied to the

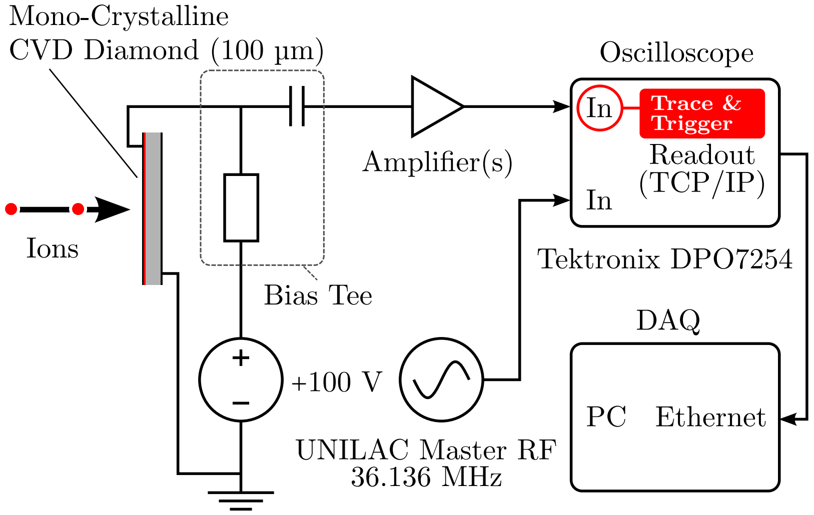

Fig. 4.8: Schematic data acquisition chain for the calorimetric measurement using a single crystalline diamond (Fig. 3.12). The diamond is fed by bias tee at a supply voltage. After amplification of the signal a fast oscilloscope is used as ADC module. The detector signal as well as the UNILAC RF from the master oscillator are streamed to a PC setup via Ethernet.

diamond detector. As explained in Sec. 3.3.3, the detection of electron holes is considered favourable.

4.2.1 Data Acquisition

The data acquisition is performed with a fast oscilloscope. DAQ, post-processing to reconstruct the phase space and data analysis software have been purpose-built developed. For the setup at hand, preamplified pulse shaping is unfavourable with typical integration times of several µs. Hence, an approach where detector signals are amplified and sampled directly at a high sample rate has been chosen. At the same time, the UNILAC master oscillator signal is recorded as a fixed arrival-time reference. This allows to extract the relative phase information between events, as done in the TOF setup.

The oscilloscope used is a Tektronix DPO 7254 [59] which features an 8-bit ADC and a real sample rate of 20 GS/s[5] in two-channel mode. The ADC data is transfered in floating point mode, but the actual scaling of the raw data is irrelevant due to the required energy calibration. As the amplified diamond readout and the RF reference needs to be recorded simultaneously, a sample period of 50 ps is available. During measurement, the data is streamed to a PC via Ethernet and recorded with a custom program.[6] Data traces of the diamond pulse and RF are recorded simultaneously, using the internal trigger of the oscilloscope on the diamond pulse. The threshold is set manually with a safe margin above noise level. Currently, data acquisition is limited to one acquisition per macro pulse. A higher efficiency is targeted with a later version of the program. The actual phase space is reconstructed off-line.

4.2.2 Post-Processing of Raw Data

Typical examples of acquired data for a single event are shown in Fig. 4.9, recorded with an Ar^{14+} beam of ≈ 1.4 AMeV. The diamond-pulse trace is given by the red line with linear interpolation and contains 2000 samples at 20 GS/s, i.e. the recording window corresponds to 100 ns at a sample period of 50 ps. The low noise figure of the amplifiers give rise to a comfortable SNR of ≈ 23 dB[7]. An impedance mismatch at the amplifier input seem to cause reflections at a characteristic cable length of 1 m and could not be sorted out at the time of measurements. Nevertheless, the reflection is separated well enough from the primary pulse without overlapping signal contributions. The lower parts of each plot in Fig. 4.9 show the harmonic RF data samples from the UNILAC master oscillator. Simultaneous acquisition of the diamond trace and the UNILAC RF reference allows to extract energy and RF reference. Reconstruction of the phase space requires to post-process the raw data stream from the oscilloscope. The corresponding software has been developed in this work. In the following, the necessary steps are outlined.

---

[5] A real sample rate of 40 GS/s can only be achieved in single-channel acquisition mode.

[6] The source of the command-line tool is available on request and should run on any POSIX compliant system without further modification.

[7] Pulse-to-noise amplitude ratio for a typical pulse at phase-space centre at ≈ 1.4 AMeV. The standard deviation of the noise amplitude, after baseline restoration, has been determined to be ≈ 200 in the vertical scale of Fig. 4.9.

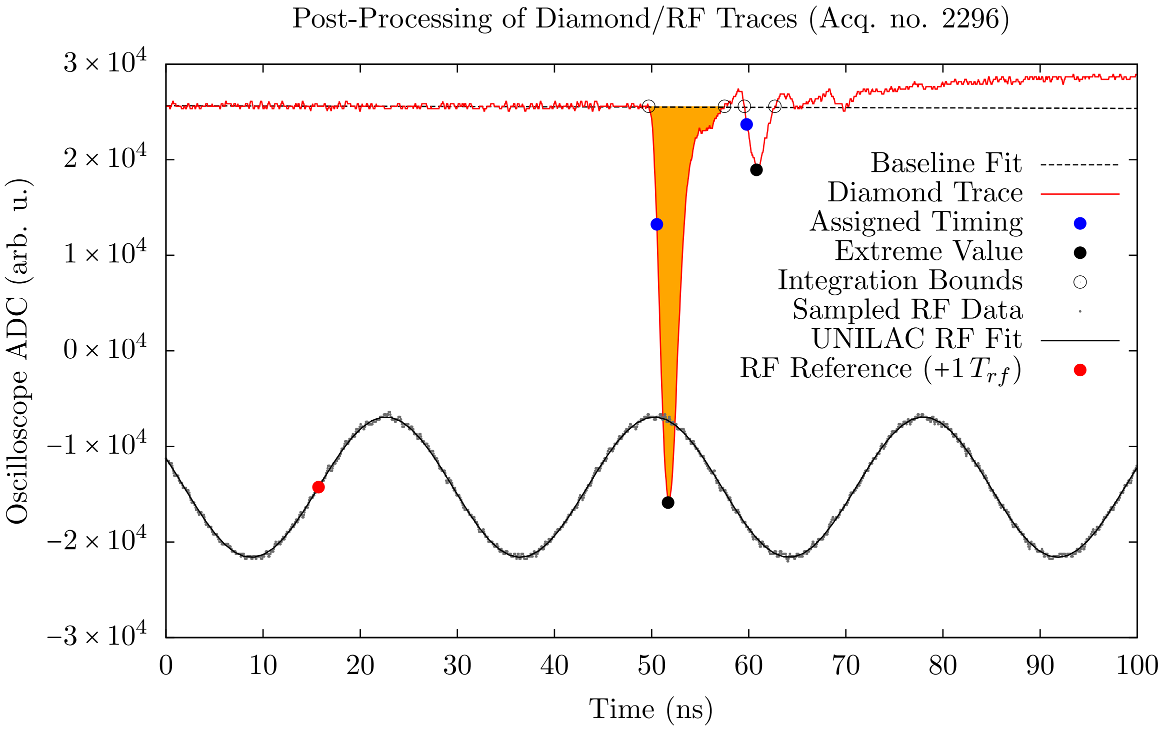

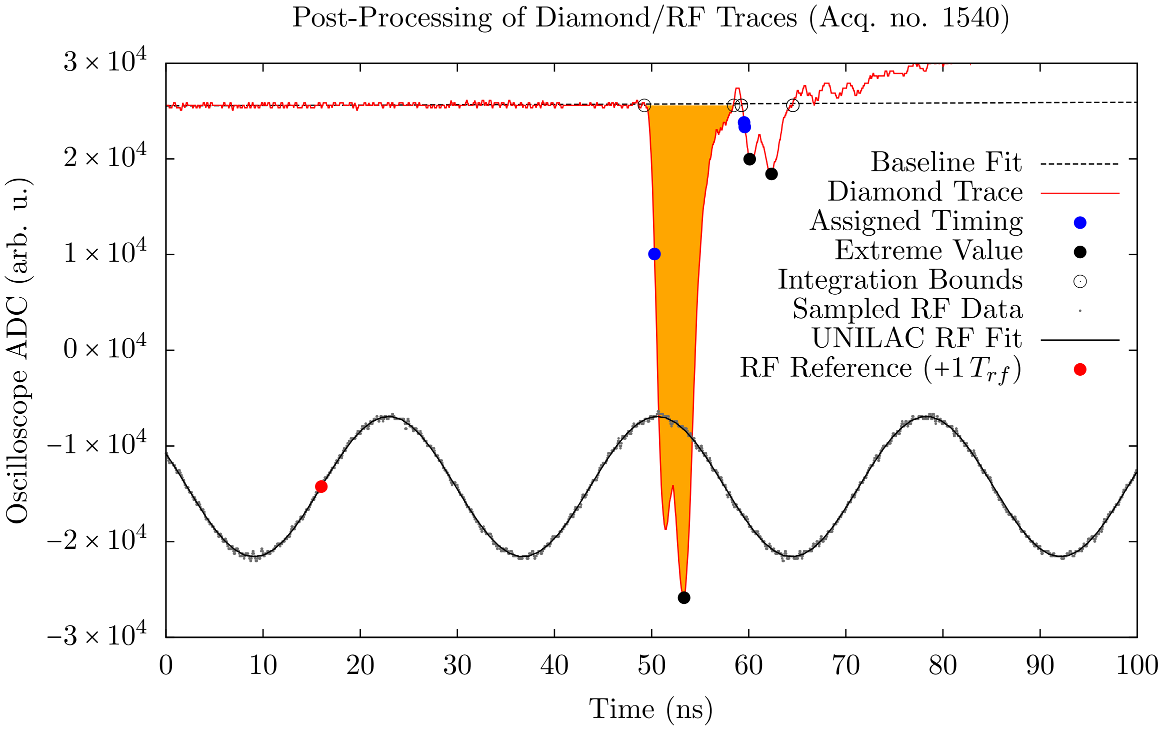

Fig. 4.9: Exemplary recordings of Ar^{14+} particle hits at the mono-crystalline diamond detector (20 GS/s, 2000 samples per trace). The red trace represents the sampled diamond pulse data. At the lower part of each plot the simultaneously sampled UNILAC RF is shown along with the corresponding fit of a sine. While top plot shows a single particle hit from the centre of phase space, the bottom plot shows one of the rare double-hit events. Determined timing values are given in the legend.

RF Reference. Similar to the TOF setup, the arrival time at the diamond detector, with respect to a defined RF zero-crossing, is a measure of the ion phase. To obtain the RF reference timing, the RF is sampled along with the diamond trace. This allows to perform a fit of the sampled RF data to a general sine parameterisation. Once the fit parameters have been determined the zero-crossing at positive slope can be extracted straightforward. The corresponding, perfectly aligned, fit and assigned timings are plotted in Fig. 4.9 (see legend).

Baseline Restoration. Determination of pulse heights and pulse integrals depend on a well defined baseline. In particular, pick-up of unwanted signals may result in a varying baseline. As it is not always possible to screen those contributions, it is advisable to perform a baseline restoration on each pulse acquisition. A linear fit using the first 45 % of samples of the diamond trace is used to determine the baseline reference. The restored baseline is given by the dashed line in Fig. 4.9. An overview of the fit parameter *offset* and *slope* is presented as a scatter plot in Fig. 4.10.

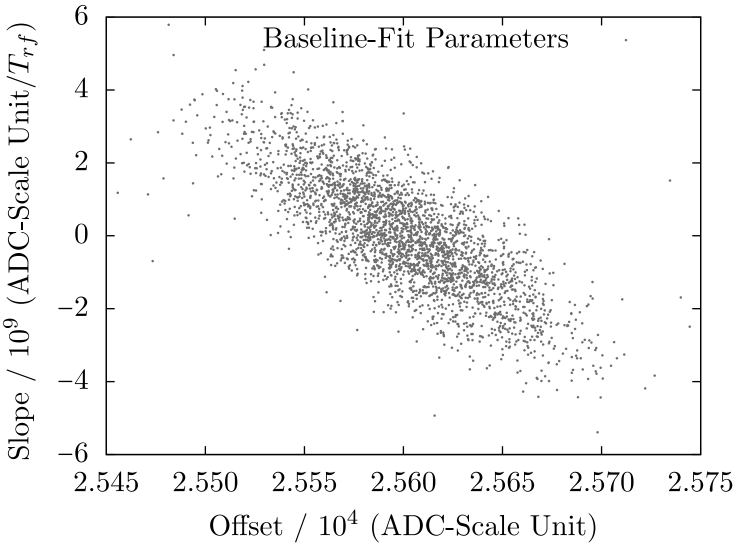

Fig. 4.10: Scatter plot of the Ar^{14+} baseline-fit parameters.

Pulse Properties. With restored baselines, crucial properties of the pulse event can be determined. This includes the extreme-value index (sample index), which provides the pulse height with respect to the baseline. Furthermore, integration bounds are determined by storing the indices of the signal when it crosses the baseline. Subsequently, integration is performed with respect to the restored baseline within these limits. Finally, the pulse timing is extracted at a fixed fraction of the pulse height on the rising slope. A 30 % level has been used throughout all presented data. The determined values, as well as the pulse-integral area, are provided aligned to the data traces in Fig. 4.9. For completeness, the custom program drops all reflected pulses and checks for overlapping pulses. Overlapping pulses are marked *tainted.* This provides the option to automatically exclude double-hit events. Nonetheless, double-hit events turned out to be a good way to judge the linearity of the pulse-integral response.

Pulse-Height/Pulse-Integral Trend. The pulse height of the Ar^{14+} measurement vs. the acquisition index is plotted on the left side in Fig. 4.11. The gap between $\approx -0.5 \times 10^4$ and 0 originates from the trigger threshold, manually set at the oscilloscope. A clear trend towards smaller pulse-heights is apparent. This means that irradiation, at least in this experimental configuration, has an effect on the response of the detector. A linear fit to the core region is used to rescale the measured data. The fit region is marked by the light-blue band, whereas the fit is given by the red line, parameterised by the slope s_h and offset o_h. Assuming a sufficiently linear systematic, correction of the pulse-height data is performed according to the linear fit parameters[8]

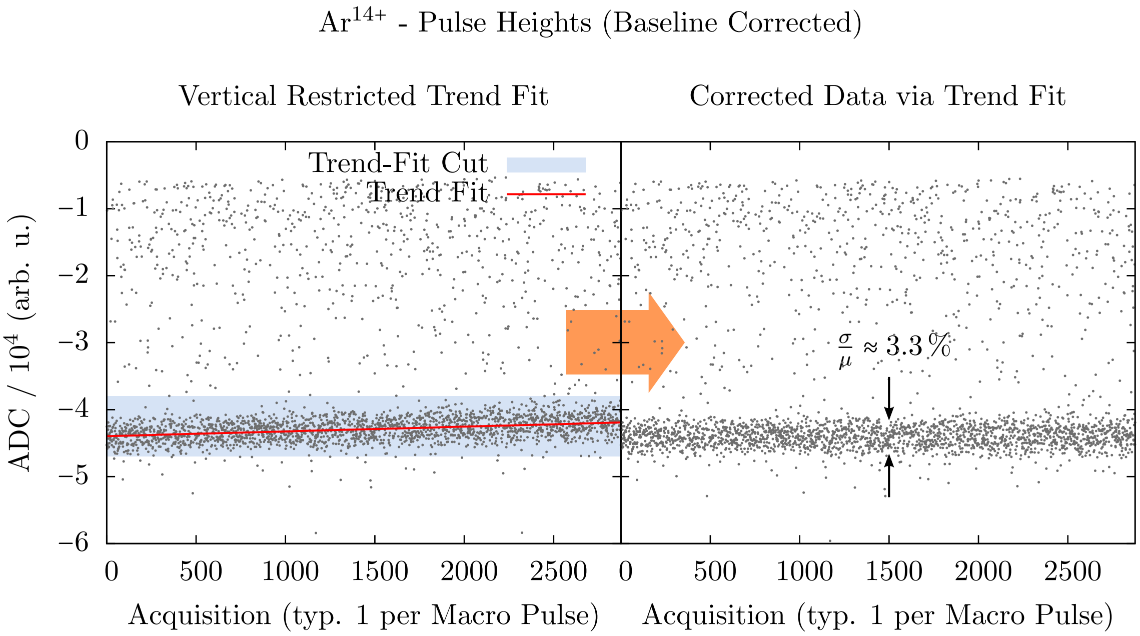

Fig. 4.11: Left: Baseline-corrected pulse-height vs. progressional acquisition number of an Ar^{14+} beam. Additionally, the linear trend fit of the phase-space core region is given by the read line together with the light-blue region which denotes the particles included in the linear fit. **Right:** Data corrected by rescaling with respect to the corresponding trend fit.

$$t_h(n) = s_h \cdot n + o_h, \tag{4.11}$$

with n being the continuous acquisition number. Hence, the rescaling factor $c_h(c)$ of pulse-height n is trivially given by

$$c_h(n) = \frac{o_h}{t_h(n)}. \tag{4.12}$$

---

[8] Index "h" references the pulse **height**.

The rescaled data is plotted on the right side of Fig. 4.11. A gain loss of ≈ 4.9 % of the last event (acq. 2876) emphasize the impact of the irradiation on the pulse height. Above the densely populated band at $\approx -4.4 \times 10^4$, which marks the core region of the phase space and is connected with the expected mean energy ≈ 1.4 AMeV, many events of smaller pulse height are apparent. These events will be discussed in Chapter 5. The core region, using the baseline and trend corrected pulse-height information, features a relative width of $\sigma/\mu \approx 3.3\,\%$ as denoted in Fig. 4.11. The fraction of the standard deviation σ with respect to the mean value μ provides a qualitative measure of the energy resolution.

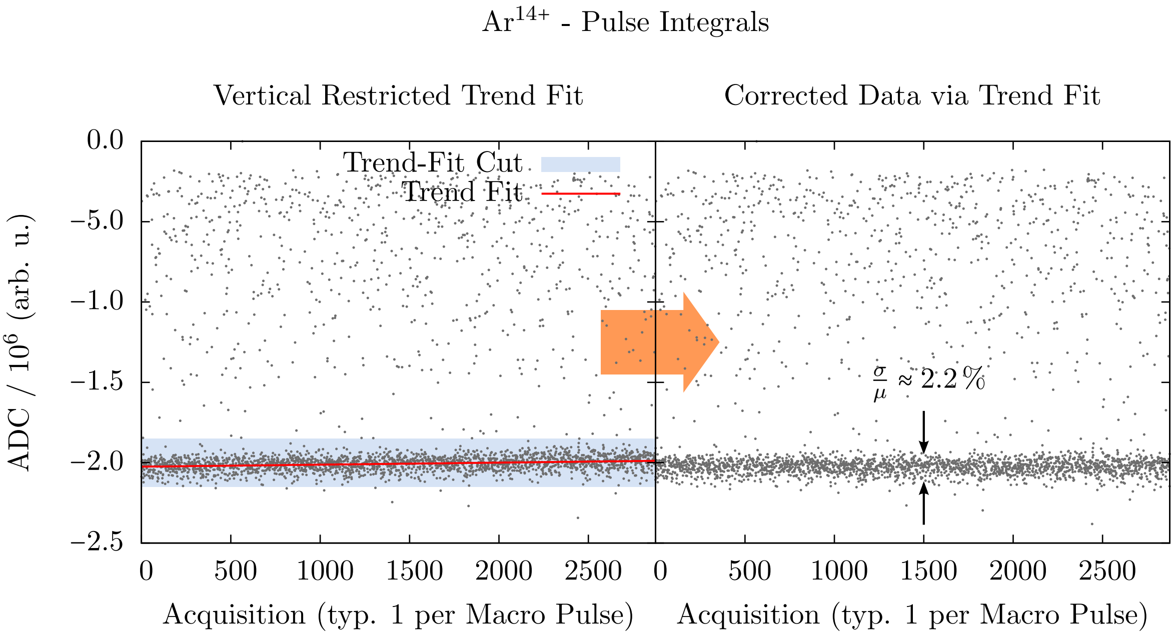

Fig. 4.12: Left: Pulse integral vs. progressional acquisition number of an Ar^{14+} beam including the linear trend fit. **Right:** Data corrected by rescaling with respect to the corresponding trend fit.

In contrast, the left side of Fig. 4.12 shows the pulse-integral data plotted versus the acquisition number. Similar to the pulse-height values, the trend of the pulse-integral values is determined by a linear fit within a narrow band around the core region. Rescaling of the data is provided by the same scheme according to Eq. 4.12. It is evident that the pulse-integral response is also affected by the irradiation of the diamond material in this experimental configuration but at a lower impact. The effect is significantly smaller compared to the pulse-height behaviour at irradiation, with a gain-loss of only 1.8 % at the last recorded event. On the right side of Fig. 4.12, the trend corrected data is shown. Comparison of the pulse-height data clearly shows a smaller relative width of the core band for the integral approach with ≈ 2.2 %. This suggests a higher energy resolution for the pulse-integral measurement.

Phase-Space Equivalent Representation. Using the trend-corrected integral values of the pulses, it is possible to plot the longitudinal phase space. The left side of Fig. 4.13 shows the trend-corrected integral values with respect to the progressional acquisition number, also including the rare double hits. On the right side, events are reordered with respect to the arrival time. The double-hit events give rise to integral values of about twice as big as those from the phase-space centre. This supports a linear calibration scale for this experimental configuration. It should be noted that this is not necessarily a general characteristic. The double-hit event marked by the arrow is associated with the traces in the lower plot of Fig. 4.9.

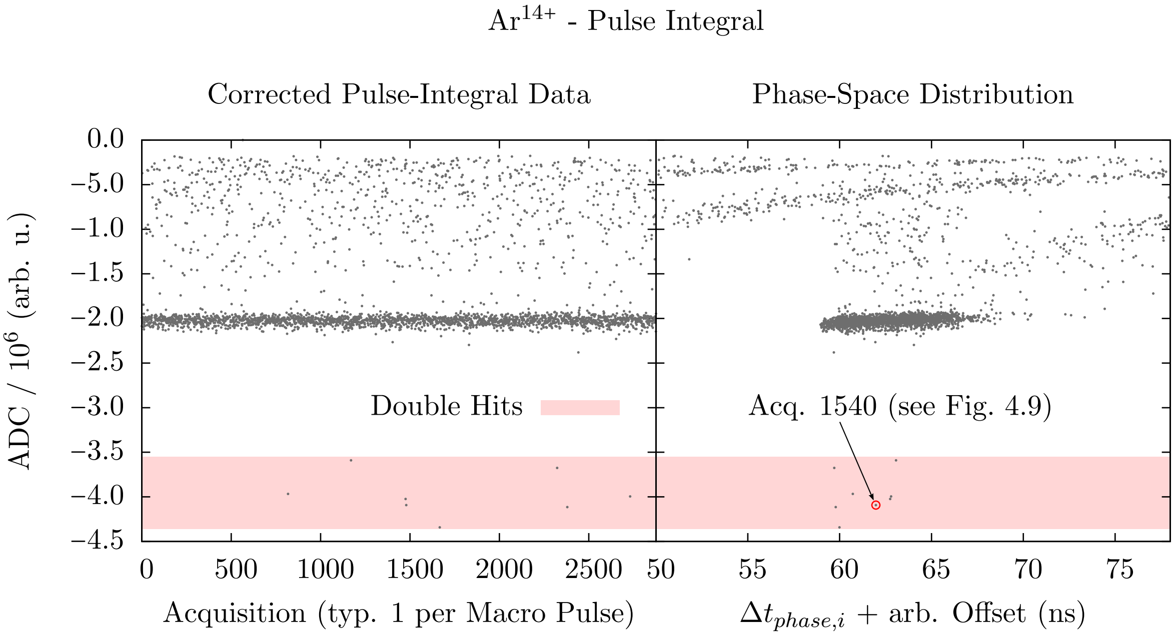

Fig. 4.13: Left: Trend-corrected pulse integral vs. progressional acquisition number. Double particle hits occur inside the light-red band. **Right:** Events ordered with respect to the arrival time as a phase-space equivalent representation.

4.3 Data Analysis

The preceding sections dealt with the electronic DAQ setups and off-line reconstruction of the recorded longitudinal phase-space events. This section presents the data analysis in detail. The data analysis has been developed using the ROOT C++ framework [60].

Characterisation of the measured phase-space is typically provided by the determination of the covariance matrix, from which, as described in Sec. 2.3, the RMS emittance is derived. Thereby the most important statistical parameters, such as location, spread and covariance are extracted.

Determination of covariance matrices can be challenging for different reasons:

- Low event count
- Contaminated data

- Systematic contributions
- Low robustness of estimators

Incomplete sampling of distributions is inherently connected to statistical uncertainties of derived values by means of so-called estimators. This is also true in case of an idealistic system where the underlying distribution can be sampled without background or systematically disturbing contributions. For example, the estimator of the univariate mean

$$\langle x \rangle = \frac{1}{n} \sum_{i=1}^{n} x_i \tag{4.13}$$

has a well-known statistical uncertainty (1-sigma) of

$$\Delta \langle x \rangle = \frac{\sigma_x}{\sqrt{n}}, \tag{4.14}$$

depending on sample standard deviation σ_x and sample size n. The estimator for the standard deviation

$$\sigma_x = \frac{1}{n-1} \sum_{i=1}^{n} (x_i - \langle x \rangle)^2, \tag{4.15}$$

in contrast, is connected with a statistical uncertainty (1-sigma) of

$$\Delta \sigma_x \approx \frac{\sigma_x}{\sqrt{2(n-1)}} \tag{4.16}$$

in good approximation [61] (p. 133). Hence, in this idealistic case, confidence intervals can be contracted by increasing the number of recorded events.

Practically, it may not be possible to record a large number of events as is the case with the setup at hand (typically about 10^4 events). While this already imposes an increased uncertainty of the estimated statistical moments, the situation is more difficult considering the influence of disturbing effects as listed above. Recordings can be contaminated with data that does not reflect real phase-space events. For example, in very rare cases ($\ll 1\%$), uncorrelated events are considered coincident, using the TOF setup, resulting from detector efficiencies or missed trigger thresholds. Most of these artificial events can be discarded. Trivially, events which would be faster than light are easy to filter, while for other coincidences it is difficult to impossible to differentiate between sane data and artifacts. Still, the majority of the unwanted overlaying distributions are of physical systematic origin which will be covered in Chapter 7. The differentiation between contamination and general systematic effects is made to highlight the different characteristics of superimposed distributions and systematic contributions from which all events are affected. An example for the latter are the foils mounted in the setup. All recorded ions are passing the tantalum and aluminum foil. Hence, dissipative contributions are unavoidable and give rise to an energy spread which affects all particles. In contrast, systematic contributions which lead to contamination affect only a fraction of the recorded events. For example scattering at the high-current slits or collimator apertures can be classified as contaminating effects as only a fraction of the bunch is affected. Nevertheless, while contamination is of systematic origin, not all systematic effects are considered contamination.

Classical estimators, as mentioned above, are extremely sensitive to even individual “bad” events. The sensitivity of estimators is usually determined by the *(empirical) influence function* (E)IF, whereas the *breakdown point* [62] defines the fraction of bad observations which are sufficient to result in estimations which can potentially rise beyond all limits. In particular, the classical estimators for the mean and standard deviation, Eq. (4.13) and Eq. (4.15), provide a breakdown point of 0, i.e. a single bad event can significantly distort the estimation of the respective statistical moment. It is therefore evident, that recorded data must be prepared before use of a classical estimator can provide meaningful results. A common approach is trimming data points, either manually or by defining cuts, usually judged by “experience”. When data points can be unambiguously identified as *outliers*, manual trimming is straightforward. Obviously, this is only consistently possible if contaminations are disjoint sets from the phase-space region of interest. Otherwise, manually defined cuts, and consequently estimated values in case of non-robust estimators, can vary significantly between different persons evaluating the raw data.

A defined set of rules is crucial when analysing the recorded data. Objectivity is of major concern when it comes to a consistent approach of data evaluation. This is a precondition to warrant reproducibility, in particular, given low event counts, contamination and systematic effects as stated above.

Well-established methods for consistent evaluation of phase-space scatter data are rare. Common scenarios deal with systematic background models assuming a flat bias and noise figure, typically originating from current amplifiers present in various types of (transverse) phase-space diagnostics. Such data sets are often treated by successively subtracting a constant amount from all bins, setting resulting negative values to zero, while monitoring, for example, the emittance value. A good approximation to the “real” values is considered when corresponding gradients change significantly, as a feedback on when actual signal is affected by the flat subtraction. This defines the %-intensity level with respect to the total, accumulated amount of content which has been subtracted. In contrast, an advanced and widely accepted approach for such scenarios is called SCUBEEx [63]. This method accounts for the fact that noise contributions average out when integrating regions with no signal by variation of exclusion ellipses which eventually define a consistent core region. Since neither the TOF setup nor the setup using a mono-crystalline diamond detector features a bias/noise floor, the previously mentioned methods, in especially SCUBEEx, to analyse the recorded data are ill-suited.

An exemplary histogram of $^{40}\mathrm{Ar}^{10+}$ events is shown in Fig. 4.14. The data, recorded using the TOF setup, contains an exceptionally high amount of $\approx 6 \times 10^4$ events and allows to highlight the main characteristics. It is apparent that the data features no flat noise floor. Instead, prominent contamination in terms of trails need to be taken care of. The actual phase-space region of interest, i.e. the longitudinal phase-space when the ions enter the setup, is located where the elliptical shapes are plotted. While the residual events are, effectively, real phase-space events at the setup, they are introduced by the measurement process. Hence, they must be excluded from entering in the covariance matrix in a consistent way to keep contamination of the covariance matrix by spurious events as low as possible. Such an approach is the robust Minimum Covariance Determinant estimator.

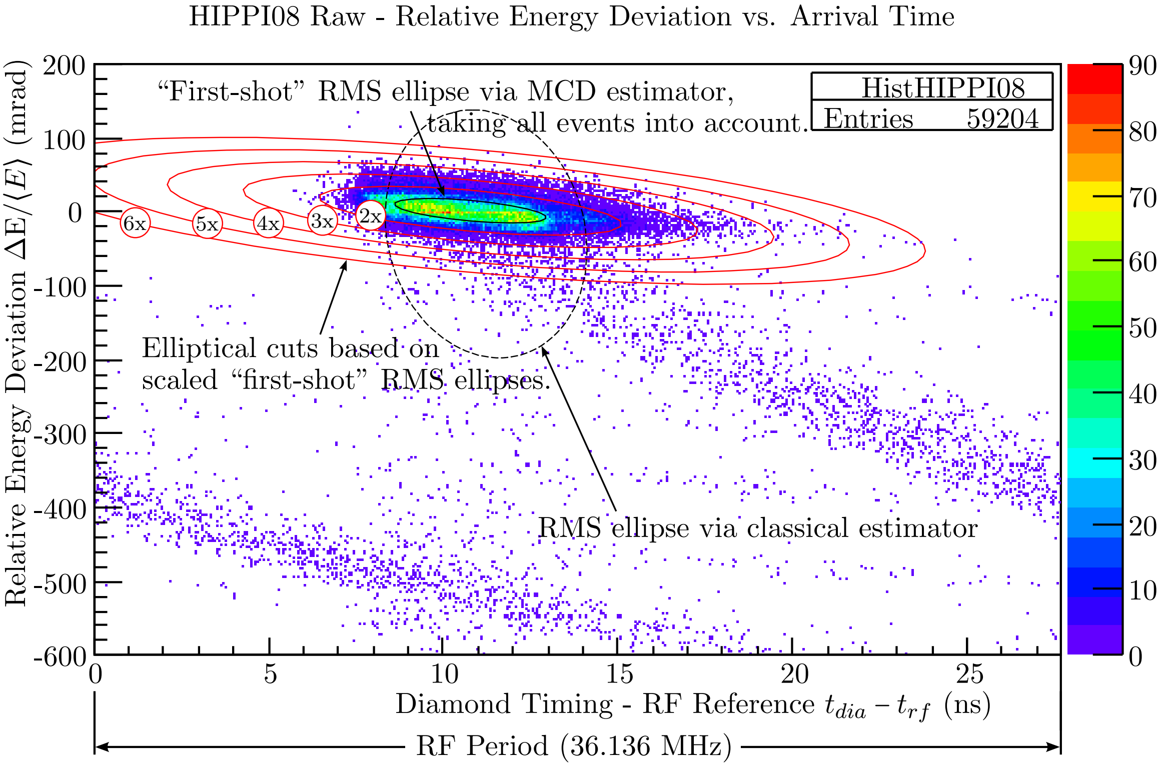

Fig. 4.14: Exemplary $^{40}\mathrm{Ar}^{10+}$ phase-space data recorded during the HIPPI [58] campaign 2008. The phase-space region of interest is located where the red ellipses are plotted.

4.3.1 Minimum Covariance Determinant Estimator

As mentioned above, using the classical covariance and location estimators would require a biased preparation of the raw data by means of manually set cuts to exclude spurious data. Evaluation of measured data, such as shown in Fig. 4.14, can only be consistently accomplished if an estimator with a high breakdown point is used. An alternative quantitative approach used in this work is the so-called *Minimum Covariance Determinant* (MCD) robust estimator for multivariate data, which was first proposed in 1985 by Rousseeuw [64]. MCD is a variant of the *Minimum Volume Ellipsoid* (MVE) concept proposed in the same report. Both concepts are based on the idea to only take into account a fractional subsample size α_{mcd}[9] of the original data containing n points, with $1/2 \leq \alpha_{mcd} < 1$. By minimizing either the smallest ellipsoid covering all data points (MVE) or the variance-covariance matrix determinant (MCD) over all possible subsamples for a given fraction α_{mcd}, a robust estimate of the location and scatter is provided. To ensure consistency in case of multivariate normality, the covariance matrix is multiplied by an correction factor depending on α_{mcd}. For bivariate cases, in particular the longitudinal subspace, the determinant of the

---

[9] If the subsample size equals the size of the original data, i.e. $\alpha_{mcd} = 1$, the MCD approach delivers the values of the classical estimators. Depending on the implementation this is not always true due to partitioning of sizes of initial data above a certain threshold (typically 600 points).

variance-covariance matrix C writes

$$|C| = \begin{vmatrix} \sigma_{xx} & \sigma_{xy} \\ \sigma_{xy} & \sigma_{yy} \end{vmatrix} = \begin{vmatrix} \sigma_x^2 & \sigma_{xy} \\ \sigma_{xy} & \sigma_y^2 \end{vmatrix} = \sigma_x^2 \sigma_y^2 - \sigma_{xy}^2 \overset{!}{=} \varepsilon_{rms}^2 \,, \tag{4.17}$$

and thus equals the square of the RMS emittance ε_{rms}. Since the square function is a strictly monotonic function, the MCD algorithm effectively minimizes the estimated RMS emittance.

Roderich Keller et al. used a method similar to MVE, in 1985 [65], to successfully analyse transverse phase-space data of small size. Calculation of the MVE and MCD, even for bivariate data, is combinatorially expensive which practically limits the reasonable size of the data. According to Rousseeuw [64], MCD is favourable over MVE, due to its higher statistical efficiency and higher accuracy. In case of MCD, a more efficient algorithmic approach exists, proposed by Rousseeuw et. al [66] in 1999, often referred to as FAST-MCD. It allows to calculate MCD multivariate location and variance-covariance matrices even for large data sets.

Data analysis of this thesis is based on the ROOT C++ framework [60] that includes an implementation of the FAST-MCD algorithm [67]. Unfortunately, benchmarks based on known bivariate Gaussian distributions revealed a significant mismatch between the variance-covariance matrix compared to the known parameterisation, which is not expected. While the variances and covariances are flat for different values of α_{mcd}, which is favourable, they are smaller by $\approx 10\,\%$. This behaviour is unexpected and not in agreement with the goal of the MCD method. Consequently, this lead to the decision to not use the *TRobustEstimator* implementation. Instead, this work uses the R (*The R Project for Statistical Computing*) [68] implementation of FAST-MCD which directly interfaces the FORTRAN routine [69, 70] by the original authors P. J. Rousseeuw et al.[10] Additionally, the most recent correction factors for multivariate normality [72] are included in the R calling routines. Contrary to the ROOT implementation, the covariance matrices are reproduced as expected.

MCD on Actual Data. In the following, the values of the MCD estimator are compared to those of the classical estimator using the phase-space data shown in Fig. 4.14. Elliptical cuts are systematically generated to monitor the impact of event exclusion on the MCD and classical estimator. A “first-shot” ellipse is acquired from the MCD estimator with $\alpha_{mcd} = 0.75$. Typically, this provides a good estimation of the covariance matrix and its location of the phase-space region of interest where most events agglomerate. Table 4.1 lists the scatter values computed via the classical estimator and those of the “first-shot” variance-covariance matrix ($\alpha_{mcd} = 0.75$). Apart from the phase location $\langle x \rangle$ all other values in Tab. 4.1 differ significantly between the classical and robust estimator. While the classical estimator for the bunch length σ_x is larger by about 30%, the measure for the energy spread σ_y is larger by more than a factor of five in case of the classical estimator. The magnitude of the covariance σ_{xy} is larger using the classical estimator due to the long-ranged trails. For the same reason, the location of the energy centre and the RMS emittance differ significantly between the classical and robust estimator. The classical estimator of

---

[10] The R framework is interfaced by C++ using RInside [71] by D. Eddelbuettel et al.

Tab. 4.1: Comparison of MCD ($\alpha_{mcd} = 0.75$) and classical estimator without event exclusion on the HIPPI [58] 2008 data, as seen in Fig. 4.14. The MCD values of location and scatter are referred to as "first-shot" RMS ellipse. For a better readability $x = t_{dia}$ and $y = \frac{\Delta E}{\langle E \rangle}$ has been substituted.

Estimator "first-shot"	σ_x (ns)	σ_y (mrad)	σ_{xy}	$\langle x \rangle$ (ns)	$\langle y \rangle$ (mrad)	ε_{rms} (mrad·ns)
MCD	2.08	17.08	-17.84	10.80	0.48	30.72
Classical	2.71	91.39	-66.01	11.09	-19.48	238.70

the RMS emittance is larger by more than a factor of seven. This clearly shows that even with a pronounced fraction of contamination the MCD estimator provides a reliable, robust estimate of location, size and orientation, as can be seen from Fig. 4.14. The "first-shot" ellipse is well-aligned in the core phase-space region, although only one parameter, α_{mcd}, has been specified.

Estimators under Different Cuts. Study of the influence of different cuts on the estimators has been performed in a consistent way. The cuts used to compare estimator values belong to a certain class of cuts. It is sensible to use elliptical cuts which are generated from scaled entities of the "first-shot" covariance matrix with a common centre location. The core phase space of interest is automatically located well by the MCD algorithm. Furthermore, scaling of the covariance matrix makes it easy to define a reasonable region of interest (ROI). Linear scaling of both semi axes by a factor of n equals scaling of the covariance matrix by n. At the same time the emittance scales by a factor n^2. The first six ellipses, the black "first-shot" ellipse and the red ellipses with scaling factors 2 to 6 (see labels), are plotted in Fig. 4.14.[11] Classical and robust MCD[12] estimator values $\sigma_{\frac{\Delta E}{\langle E \rangle}}$ corresponding to cut ellipses of different size are plotted in Fig. 4.15 with respect to the scaling factor n. Additionally, the fraction of total events inside the cuts is represented by the grey line. The fraction grows fast until it reaches a quasi plateau of lower gradient at a cut-scaling factor of ≈ 5. For this cut ellipse, the area is 25 times the size of the "first-shot" ellipse and includes $\approx 90\,\%$ of all events. In other words, as denoted in Fig. 4.15, $f_{cont} \approx 10\,\%$ of all recorded events contribute to the contamination located in the long-ranged trails in this measurement. This assumption agrees with the elliptical cuts plotted in Fig. 4.14, i.e. at a scaling factor of 4-5, the cut region encloses the phase-space distribution of interest. Further scaling to larger cut regions mostly accumulate events from pure contamination by means of the prominent trails. As expected, the classical estimator (red line) has a strong dependency on the cut size with no obvious cut scaling that makes for a meaningful evaluation.[13] In contrast, the robust MCD estimator data shows a significantly lower dynamics above cut scalings ≈ 5. Only estimations which exclude less than the fraction of contamination, i.e. $\alpha_{mcd} \gtrsim 0.9$ in this

---

[11] Given scaling factors in this section refer to the linear axis scaling.

[12] MCD estimators are evaluated for α_{mcd} in the range $0.5 \le \alpha_{mcd} \le 1$ at a step size of 0.025.

[13] The intermediate plateau of lower gradient at cut scalings between 25-30 is an artifact which is due to the wrapped phase information with respect to the RF period as seen by the trails in Fig. 4.14.

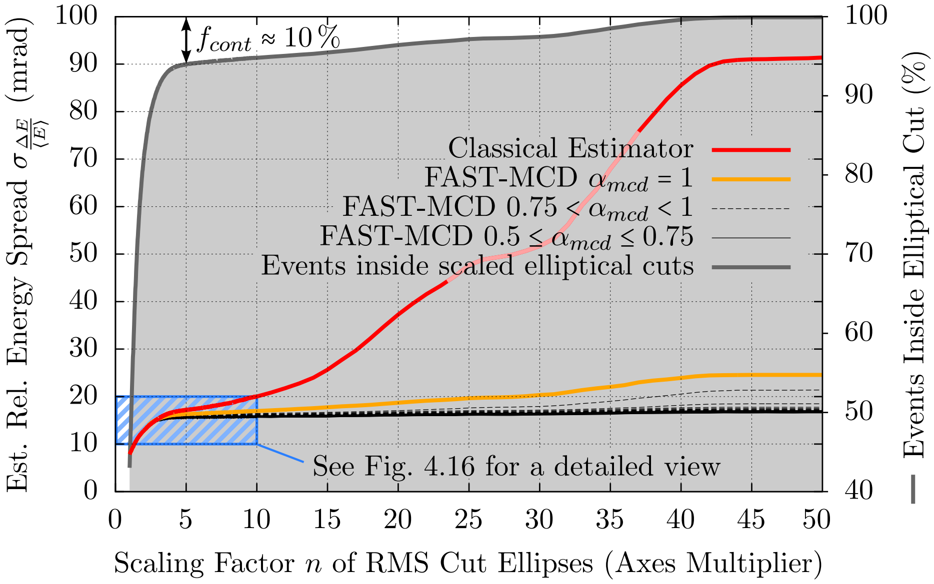

Fig. 4.15: The plot shows the classical estimator (red line) and robust MCD estimators (black dashed and solid lines) for the standard deviation of the relative energy deviation acting on real data (HIPPI [58] 2008). The horizontal axis denotes the scaling factor of the “first-shot” covariance matrix used to define automated cuts.

measurement, are prone to deviate from the otherwise stable band at larger cut scalings.

A magnified plot, as marked by the blue rectangle in Fig. 4.15, is shown in Fig. 4.16. Compared to the classical estimator, a band of MCD estimators using different α_{mcd} displays a very low gradient for cut scalings of $n \gtrsim 4$. Additionally, the blue line represents the fraction of events inside the scaled “first-shot” ellipse, assuming a bivariate Gaussian density distribution. The corresponding functional relation between the fraction f of events inside the scaled “first-shot” ellipse only depends on the determinant of the variance-covariance matrix and, thus, the RMS emittance ε_{rms}. By means of the associated scaled emittance $\varepsilon(f)$ this relation is given in [73] (p. 68)

$$\varepsilon(f) = -2\,\ln(1 - f)\,\varepsilon_{rms}\,. \tag{4.18}$$

If the scaling is parameterised by $\varepsilon(f) = n^2_{(f)}\varepsilon_{rms}$, Eq. (4.18) yields the fraction f in terms of the scaling multiplier n

$$f = 1 - \mathrm{e}^{-\frac{n^2}{2}}\,, \tag{4.19}$$

which is represented by the blue line in Fig. 4.16. Effectively all events ($\approx 99.96\,\%$) are enclosed at a cut scaling by a factor of $n = 4$ under the assumption of a bivariate distributed phase-space region of interest. Although this assumption is only a rough model to realistic phase-space distributions, it agrees with the cut scaling $n \gtrsim 4$ where the band of MCD estimator reaches a low-gradient quasi plateau. This suggests, with a small margin, evaluation

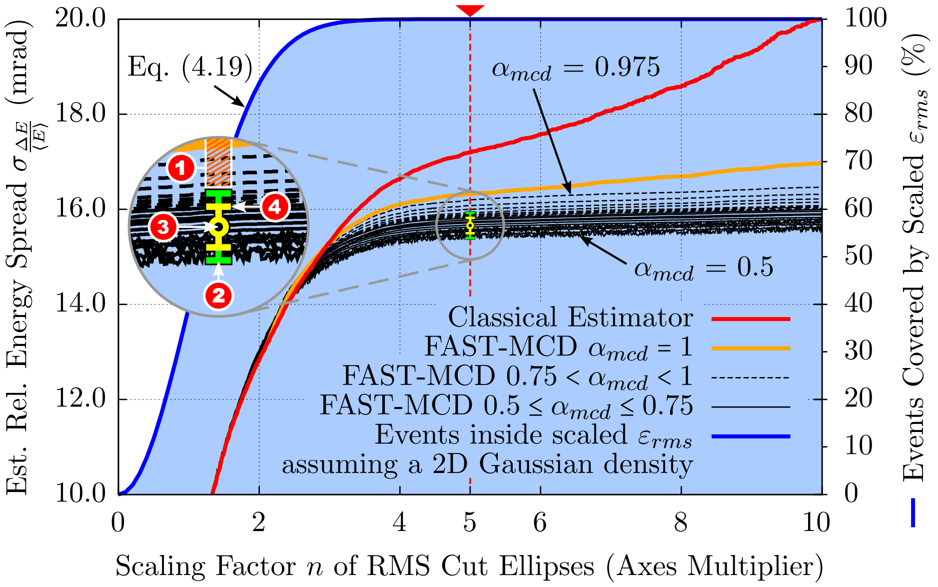

Fig. 4.16: This plot refers to the same data of the estimators as Fig. 4.15 at a different viewport. The blue line represents the *theoretical* fraction of particles inside the scaled elliptical cuts, by taking a 2-dimensional Gaussian distribution as reference which is parameterised by the “first-shot” covariance matrix. Values provided by the robust estimators are drawn dashed for subsample fractions $0.75 < \alpha_{mcd} < 1$ and solid from $0.5 \leq \alpha_{mcd} \leq 0.75$. Evaluation is carried out at a cut scaling of 5. A magnified view of the evaluation region is provided on the left and is explained in the text.

and comparison of the estimators at a cut-scaling factor $n = 5$ as a consistent rule.

Evaluation and Error Bounds. The FAST-MCD estimator routine has been evaluated for subsample fractions $0.5 \leq \alpha_{mcd} < 1$ at a step size of 0.025. For non-Gaussian distribution this leads to an unavoidable spread of the calculated values which is clearly visible by the resulting band. In this example, values increase with increasing α_{mcd}. A magnified view of the point of evaluation at $n = 5$ is shown on the left of Fig. 4.16. The hatched interval ❶ defines the range of α_{mcd} which is excluded from the final evaluation. According to Rousseeuw et al. [66], choosing $\alpha_{mcd} = 0.75$ is a good compromise between breakdown value and statistical efficiency if contamination f_{cont} is lower than 25 %. However, even when contamination is lower than 10 %, as it is the case at the discussed cut scaling $n = 5$, α_{mcd} should not exceed 0.9. For subsample sizes close to 1, the break down value drops significantly, which effectively means the estimator loses on robustness. As a general rule, setting $\alpha_{mcd}^{max} \leq 1 - f_{cont}$ is reasonable. The green bounds ❷ mark the range of included α_{mcd} values of subsample sizes. In good approximation, the corresponding estimator values v are uniformly distributed for constant step sizes of α_{mcd}.[14] This allows to determine the

---

[14] The estimator v is a placeholder for any location and scatter parameter accessible by the MCD routine.

centre of the evaluated range ③ by taking the arithmetic mean of the bounds ②

$$\langle v \rangle_{uni} = \frac{v_{min} + v_{max}}{2} \, . \tag{4.20}$$

The spread is interpreted as the statistical uncertainty and consequently the standard deviation ④ is extracted via the standard deviation of uniform distributions

$$\sigma_v^{uni} = \frac{v_{max} - v_{min}}{\sqrt{12}} = \frac{v_{max} - \langle v \rangle_{uni}}{\sqrt{3}} \, . \tag{4.21}$$

This approach allows to extract a target value $v \pm \sigma_v$ based on a defined set of rules and statistical uncertainty σ_v. Exemplary values for the phase-space data in Fig. 4.14 are listed in Tab. 4.2. The table lists the classical and MCD estimator values at a cut scaling of $n = 5$, including both, the variance-covariance matrix elements, location estimates and the derived RMS emittance. As it is possible to define a measure for the statistical uncertainties in case of the MCD method, as described above, those are also listed together with the corresponding relative uncertainty where meaningful. Estimator values evaluated according to Eq. (4.20) deviate by less than 1 % compared to the approach of taking all estimators into account within the bounds ② and evaluating the arithmetic mean. Standard deviations, according to Eq. (4.21), deviate by less than 10 %. All MCD estimator values provided in this work incorporate the full set of estimators within the evaluation bounds. Nevertheless, Eq. (4.20) and Eq. (4.21) are typically very good approximations which could be used likewise.

Tab. 4.2: MCD estimator values for the data shown in Figs. 4.14 - 4.16. For a better readability x refers to the arrival time t_{dia} (ns) and y refers to the relative energy deviation $\frac{\Delta E}{\langle E \rangle}$ (mrad).

Cut Scaling	**Classical**	**MCD**		
$n = 5$	**Estimator**	**Estimator**	**Std. Dev.**	**Uncertainty**
σ_x (ns)	1.88	2.00	3.5×10^{-2}	1.8 %
σ_y (mrad)	17.19	15.67	0.14	0.9 %
σ_{xy}	−14.16	−16.57	0.70	4.2 %
ε_{rms} (mrad·ns)	29.04	26.60	0.13	0.5 %
$\langle x \rangle$ (ns)	10.880	10.804	1.7×10^{-3}	-
$\langle y \rangle$ (mrad)	1.13	0.21	0.20	-

At the given cut scaling, comparison of both estimators features no distinct outlier. While all values are close, the energy spread σ_y is smaller in case of the MCD, as can be also seen from Fig. 4.16. This shows a typical and appreciated behaviour since the influence of the contamination, in particular the trails, is damped using the MCD over the classical approach. At the same time, the covariance σ_{xy} is higher for the same reason. The standard deviations of the scatter estimators are in the order of only few %. The more the region of interest deviates from a bivariate normal distribution, the larger the relative width of the bands and, thus, the uncertainty will be. In case of ideal bivariate Gaussian distributions and disjoint contamination, the relative spread between estimators using different α_{mcd} effectively completely contracts.

Calculation of Robust Estimator Values. It is now possible to define a procedure for the determination of estimator values. This procedure will be consistently applied to measured data presented in this work.

- The MCD algorithm is used to determine the "first-shot" ellipse at $\alpha_{mcd} = 0.75$. [15]
- This ellipse is scaled by $n = 5$ and used as geometric cut parameterisation.
- The MCD algorithm is applied again on the data contained in the scaled ellipse.
- This is done by sampling robust estimator covariance matrices and centre locations with α_{mcd}-values of $0.75 \leq \alpha_{mcd} \leq 0.9$ at a step size of 0.05.
- As described in the previous paragraph, average values and error bounds of the covariance matrix ensemble and centre locations are calculated as well as RMS emittance and Twiss parameters.

Final Remarks. When comparing the classical and MCD estimator applied to contaminated data, the advantage of robust estimators, such as the MCD estimator, is evident. Table 4.1 highlights the expected deviation from the classical and robust estimator. The RMS emittance is larger in case of the classical estimator by more than a factor of seven. On the other hand, location, size and orientation of the robust estimate does not significantly change under various cut conditions, as long as the core phase-space distribution is included entirely. This provides an improved procedure compared to the usage of the classical estimator which requires manual, biased exclusion of events. While Fig. 4.16 may suggest to apply the classical estimator under a defined cut scaling, for example $n = 5$, and discard the MCP approach, this is not possible. The "first-shot" ellipse already strictly relies on the robust MCD routine.

4.4 Additional Information Provided by the TOF Setup

As outlined in Sec. 4.1.2, the TOF setup DAQ also records the macro-pulse start timing provided by the VME-timing module. The overflow corrected timing is known precisely relative to the macro-pulse start timing which allows to access further information beyond the plain longitudinal phase-space.

---

[15] In case of very high contamination, larger than 25 %, manual discarding of most outlying events may be required until the contamination is reduced below this threshold. Alternatively, the value of α_{mcd} can be lowered down to $\alpha_{mcd} = 0.5$ for the first-shot ellipse. Since the first-shot ellipse only defines a cut region.

4.4.1 High-Resolution Macro-Pulse Structure

The high-resolution macro-pulse structure information provides further information about the state of the ion source and the real macro-pulse duration. This is achieved by histogramming the bunch number at which an event occurs, with respect to the start of the macro-pulse timing and can be considered to provide similar information than a high-resolution beam-current transformer. Two exemplary macro pulses are shown in Fig. 4.17.

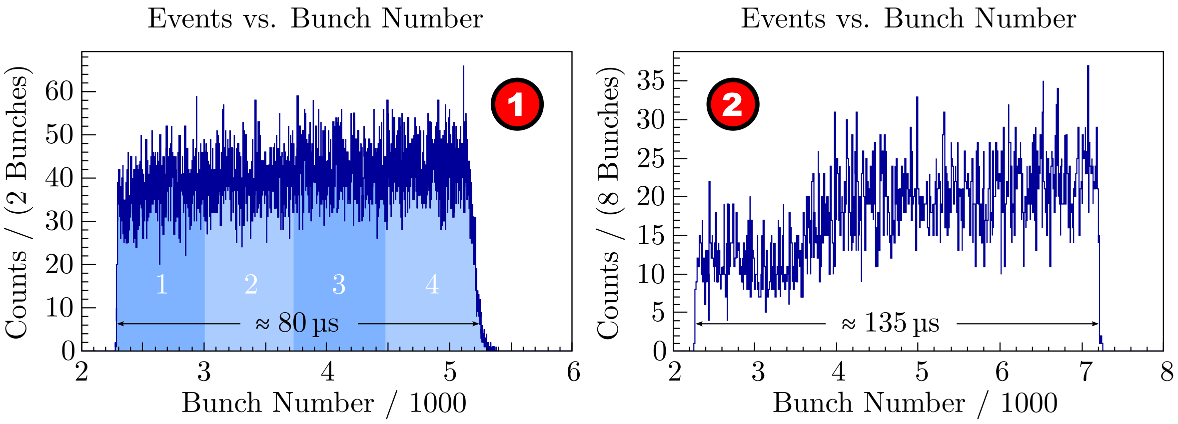

Fig. 4.17: Exemplary macro-pulse structures extracted from different TOF recordings.

Both macro pulses belong to different argon measurements. Despite from the shorter macro-pulse duration, recording ① shows a more regular macro-pulse shape compared to recording ②. This information may hint a performance degradation of the ion source through aging or, less likely, unoptimised settings of the UNILAC RF.

4.4.2 Time-Sliced Phase Spaces

The data analysis of the TOF setup allows to select events inside a custom micro-pulse range. For example, the macro pulse ① in Fig. 4.17 features four sections, labeled 1 to 4. Each micro-pulse range cut represents a subset of the total phase-space distribution. The phase spaces can be evaluated separately and compared to each other. This requires a sufficiently large number of total events, depending on the range of the cuts.

The macro pulse ① corresponds to the argon data recorded during the HIPPI campaign in December 2008 as shown in Fig. 4.14. In a later section (see Sec. 5.2.4) these time slices will be analysed as the data set contains a relatively high amount of events ($\approx 6 \times 10^4$ events).

4.4.3 Event-Separation Statistics

The event statistics discussed in Sec. 3.4.5 can be verified by histogramming the separating time intervals between adjacent events recorded within a macro pulses. A typical histogram is shown in Fig. 4.18 together with a fit of to the expect distribution Eq. (3.14). The fit is in agreement with the data. At low time separations a “hole” is apparent, which is excluded from the fit range. The reason for the missing information is either the double-hit resolution

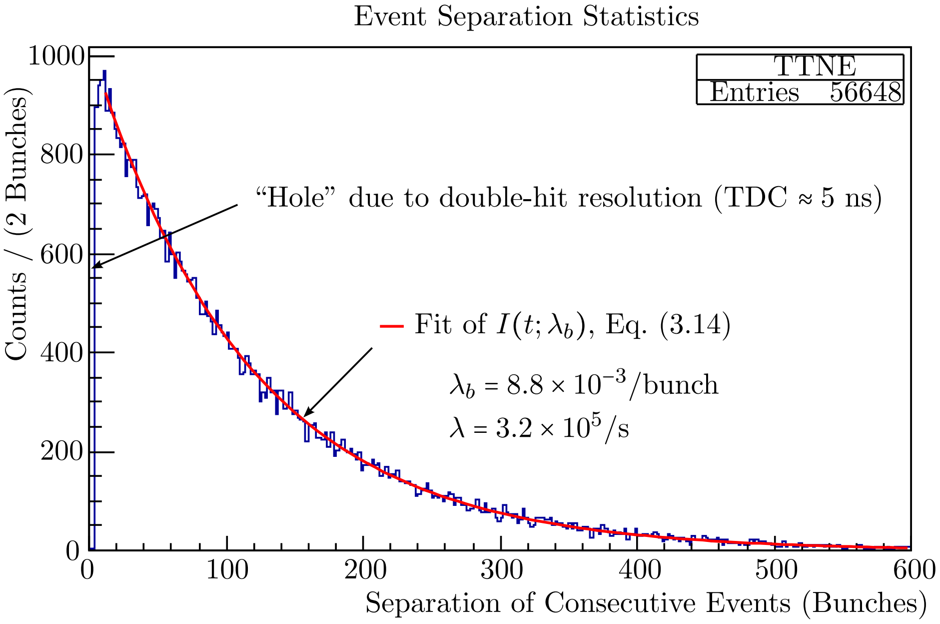

Fig. 4.18: Exemplary event separation histogram for the HIPPI 2008 data. The red line is a fit to Eq. (3.14).

of the TDC and the size of the time window used to determine coincidence events at the MCP and diamond detector. Any multiple events occurring within the time span of the coincidence window are considered ambiguous and are discarded.

Chapter 5

System Tests and Measurements

The experimental setup described in this work cannot perform measurements simultaneously with other experiments which request beam from the high-current injector. Settings of the gas pressure and high-current slits at the stripper section, to attenuate the primary high-current beam, do not allow for selective adjustment of individual virtual accelerator targets. Hence, the global nature of the attenuation settings turn the experimental setup into an exclusive measurement. In the following, the measurement procedure, and in particular the attenuation settings, will be outlined. The chapter continues with a discussion of selected data sets recorded using the TOF setup and closes with the first recorded data using the mono-crystalline-diamond detector setup.

5.1 Measurement Procedure

Typically[1] a measurement comprises three parts.

- Find appropriate attenuation settings of the beam.
- Set parameters of measurement setup (TOF or MC diamond).
- Run data acquisition.

The TOF setup relies upon well-defined threshold settings for the MCP discriminator and to a lesser extent the threshold settings of the PC diamond discriminator. Furthermore, the supply voltages of the PC diamond detector and the MCP module are set via the DAQ

---

[1] In case of machine experiments the first step is to prepare a beam if required.

frontend (see Sec. 4.1.3). In contrast, the SC diamond setup relies upon the supply voltage of the detector and appropriate vertical and horizontal range settings of the oscilloscope.

After the attenuation of the beam is accomplished and parameters are set, the modules are exposed to the beam via pneumatic feed-throughs and the data acquisition is started. Depending on the beam configuration, the targeted event count and measurement method, measurement times typically range between 15 minutes to several hours per phase-space recording.

Because of their importance, the attenuation procedures are covered, as well as the determination of the MCP discriminator values.

5.1.1 Attenuation Settings

As discussed in Section 3.4, reconstruction of the longitudinal phase space distribution requires unambiguous single-particle coincidences in case of the TOF measurement. With the beam containing about up to 10^9 particles per bunch, a mechanism to attenuate the particle flux entering the device is strictly necessary. Otherwise, without a sufficiently diluted particle rate on the bunch time scale, most of the timing signals of the two detectors cannot be unambiguously connected to a certain event.

Furthermore, the heating power of the beam scales with the nuclear charge of the ion beam, the particles per unit time, the macro-pulse length and the thickness of the foils. Since fabrication processes do not allow for significantly thinner foil targets than those installed in the experimental setup, beam attenuation is strictly necessary to prevent the tantalum foil from melting. A common beam of several milliamperes at typical macro-pulse lengths would immediately destroy the thin foil.

Low-Current Beams. When measuring low beam currents, much smaller than 1 mA, space-charge effects during acceleration and transport of the ion beam, leading to emittance blow-up, are negligible. In this case it is feasible to attenuate the beam in front of the RFQ entrance (see Fig. 2.9) by using a transverse defocusing configuration at the quadrupole magnets. The imposed extended transverse beam spread leads to a reduced transmission due to the limiting transverse acceptance of the RFQ structure. This is a typical setting to provide a test environment for the measurement setup.

Intermediate- to High-Current Beams. At high-intensity beam currents of several milliamperes, space-charge effects play a major role. Non-linear space-charge forces result in an increasing emittance after a drift. Attenuation must therefore accomplished as close to the entrance of the measurement setup as possible.

Several methods are used in combination to achieve a well-adjusted incoming beam. The gas stripper (see Sec. 2.8 and Fig. 2.10), for generation of higher charge states, and the following chicane, for charge-state separation preceding the Alvarez structures, are leveraged to reduce the number of particles impinging on the tantalum foil down to several tens of microamperes. For a detailed technical drawing of the stripper/chicane section, see Fig. 3.4.

Depending on the ion species and beam intensity, individual settings are necessary for a well adapted bunch entrance current is required. Viable parameters, in case of high-intensity measurements, are the pressure of the gas jet (US2VK1), selection of a certain charge state via dipole adjustment (US3MK1) and slit settings (US3DS4/5). The pressure of the gas stripper affects the charge distribution after stripping, whereas the slits are used to geometrically shadow large parts of the beam close to the device entrance. Section 5.2.2 and 5.2.3 investigate the effect of the attenuation on the measured phase-space distribution.

5.1.2 MCP - Voltage and Discrimination Threshold

A crucial component of the achievable time resolution is the correct setting of discrimination thresholds which assigns timings to detector pulses. MCP signal shapes inherently feature a broad pulse-height distribution (see Sec. 3.3.1). Additionally, distorted rising edges have been experienced and will be discussed in 7.4.1. In order to decide on reasonable settings for MCP front voltage and discriminator thresholds, a measurement varying both parameters has been performed.

A stable low-current $^{40}\mathrm{Ar}^{10+}$ beam served as test distribution. Under variation of discriminator thresholds and applied voltages to the MCP front side, the spread in TOF has been evaluated. Extraction of the covariance and mean values has been performed using the robust MCD estimator, according to Sec. 4.3.1. The evaluated data is shown in Fig. 5.1. Error bars reflect the statistical uncertainty of the robust estimator. A general trend towards measuring smaller TOF spreads at higher MCP front voltages is evident. The lowest three threshold configurations agree within the statistical uncertainty. Larger thresholds result in significantly larger measured energy spreads. Hence, it is reasonable to apply a MCP front voltage of 2 kV and keep thresholds below -100 mV/-200 mV (upper/lower threshold). These settings define a stable operating region.

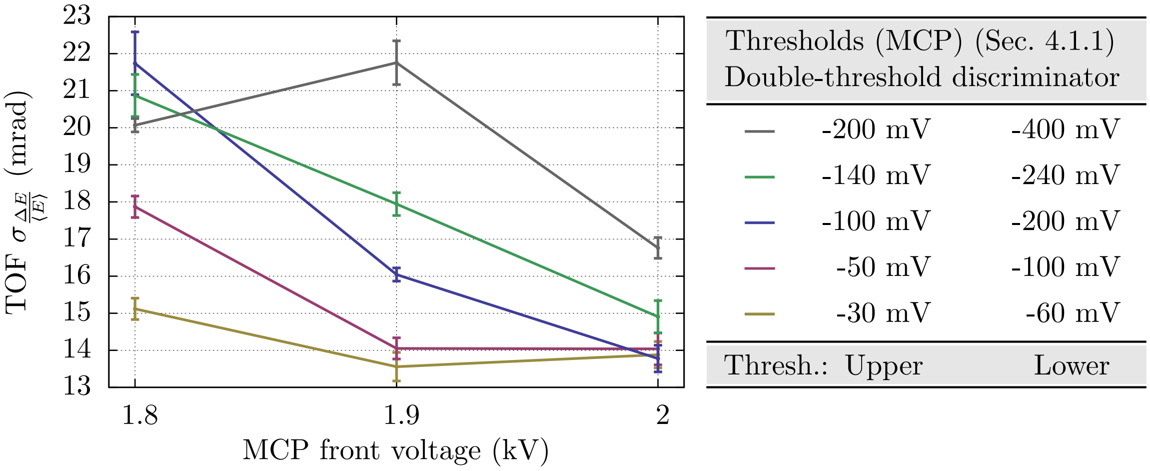

Fig. 5.1: MCP discrimination performance at different MCP front voltages and discriminator thresholds. The measurement is based on a low-current $^{40}\mathrm{Ar}^{10+}$ beam.

The poly-crystalline diamond detector, in contrast, features a significantly smaller pulse-height distribution, where a low threshold level above noise floor is reasonable.

5.2 Time-of-Flight

5.2.1 Sensitivity on Different Phase-Space Distributions

This section investigates the sensitivity of the TOF setup on different phase-space distributions. A straightforward way to prepare significantly different phase-space distributions is detuning of the synchronous phase ϕ_s at the IH cavities. The test beam was a low-current $^{40}\mathrm{Ar}^{1\rightarrow 10+}$ beam. Appropriate attenuation has been performed at the RFQ entrance using a defocusing setting of the quadrupole doublet. This resulted in an entrance current of about 20 µA. Furthermore, the gas pressure of the stripper was set to 2.8 bar, high-current slits have been open at ±15 mm (DS4) and ±5 mm (DS5).

Reference phase settings for the IH cavities are calculated as a function of the ion mass to charge state ratio A/q. In case of argon, references phases are set to 189° IH1 and 199° at IH2. Detuning of the last IH stage was performed in steps of 5° from 199° to 219°. As described in Sec. 2.5.3 and Sec. 2.6, KONUS beam dynamics is sensitive to the adjustment of the synchronous phase ϕ_s. By detuning the synchronous phase, significantly different phase-spaces are to be expected, in particular, an increase of the emittance.

The longitudinal phase spaces have been recorded with the TOF setup. Figure 5.2 shows the two-dimensional distributions and the corresponding projected bunch structures. To be visually comparable, the axes ranges are identical. The phase spaces are spanned by the relative energy deviation $\Delta E/\langle E\rangle$, with $\beta = 5.5\%$, versus the time arrival of the ion at the diamond detector t_{dia} with respect to the UNILAC RF t_{rf}. An orange symbol ● marks the calculated centre location of the reference phase space for comparison. Other phase-space centre locations are denoted by a white symbol ○. The arrival time of has been consistently shifted so that the reference phase space is centred at zero. Hence, other phase spaces indicate the relative arrival time.

Ellipses plotted on top of the phase space represent either cut regions ① or covariance ellipses ②-③. This nomenclature will be kept in the following sections.

- Red dashed ellipses ① represent the scaled first-shot RMS ellipse of the robust MCD estimator as discussed in Sec. 4.3.1.
- The red solid ellipse ② is the covariance ellipse calculated from the robust estimator and is considered the relevant estimation of the location and covariance matrix.
- As particles exist in trailings, not included in the displayed range, a plain classical estimator, acting on the full data set, provides much larger covariance ellipses. Those ellipses are drawn with a black dashed line ③.

Important values calculated using the MCD estimator are listed in Tab. 5.1. When moving away from the synchronous phase towards larger phases, the populated phase space increases. This can be clearly seen from the distributions in Fig. 5.2 and matches the steadily increasing emittance values in Tab. 5.1. Also, for larger deviations from the synchronous phase, the mean energy drops. In case of $\phi_s = 219°$ the mean energy drops about about 2% as listed in Tab. 5.1 with $\frac{\Delta E}{\langle E\rangle}$=-17.92 mrad. At the same time, the bunch arrives later. The drift of the bunch after leaving the IH section to the diamond detector is about 10 m (see Fig. 3.3). Without further accelerating or bunching structures, this requires a qualitative

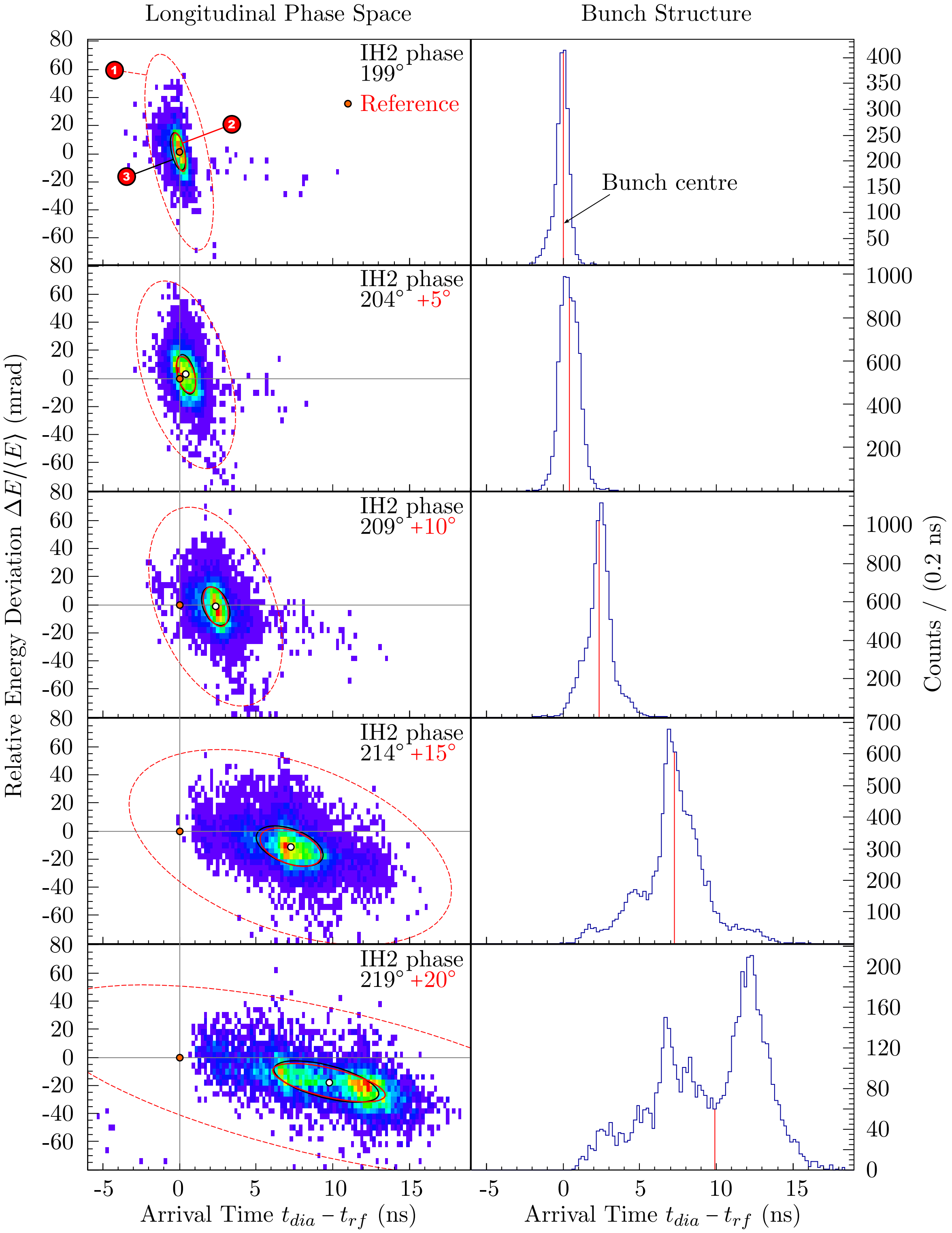

Fig. 5.2: Longitudinal argon phase-space data of detuned IH2 cavities recorded using the TOF setup.

Tab. 5.1: Estimator values (MCD) of phase-space data shown in Fig. 5.2.

ϕ_s (deg)	$\langle t_{arr} \rangle$ (ns)	$\left\langle \frac{\Delta E}{\langle E \rangle} \right\rangle$ (mrad)	$\sigma_{t_{arr}}$ (ns)	$\sigma_{\frac{\Delta E}{\langle E \rangle}}$ (mrad)	cov (mrad·ns)	ε_{rms} (mrad·ns)	α
199	0.0	0.0	0.43	13.69	-3.35	4.84	0.69
204	0.41	2.84	0.63	12.90	-3.50	7.4	0.47
209	2.37	-1.25	0.82	14.10	-4.58	10.52	0.43
214	7.27	-11.48	1.99	13.66	-11.62	24.56	0.47
219	9.78	-17.92	3.67	13.66	-31.87	38.57	0.82
Δ_{mcd}	< 0.19	< 0.42	< 0.12	< 0.59	< 1.6	< 0.60	< 0.05

correlation which is reflected by the measurement. On the other hand, the emittance scales about linearly with the bunch length, whereas the energy spread stays about constant. This is noteworthy, as one could expect a larger energy spread to be responsible for a larger bunch length after a drift. Most noticeable is the deformation of the bunch structure. Initially, at $\phi_s = 199°$, the bunch has an almost Gaussian, but slightly asymmetric, longitudinal density distribution. By deviating from the reference synchronous phase a multi-peak forms structure for $\phi_s = 214°, 219°$. To this point, sensitivity on the centre phase and centre energy is evident. While the bunch structure can be resolved the constant energy spread does not hint a fine energy resolution beyond the centre energy.

5.2.2 Variation of Stripper Pressure

In this section, the influence of the stripper pressure on the measurement is studied. As test beam an argon beam (US2DT5=4.3 mA) has been used. The pressure of the gas stripper, see Sec. 3.2.1, has been varied from 2000 mbar to 1000 mbar in steps of 200 mbar and additionally at 500 mbar to fill the gap to lower pressures. To account for different count rates of the measurements, the macro-pulse duration has been adjusted from 50 µs to 300 µs at a constant macro-pulse repetition rate of 1 Hz, which is considered to have no significant influence on the bunch phase-space distribution. Other parameters are kept constant among the different measurements. The high-current slits have been set fixed at typical UNILAC operation settings ±15 mm (DS4) and ±6 mm (DS5).

At high currents it is difficult to attenuate the beam without using a very small slit opening. If the charge-state distribution features a suppressed charge state with an appropriate current entering the measurement device, this one can be used as an attenuation approach. An appropriate charge state should also provide a current which is high enough to produce a practicable count rate. Otherwise, slits must be adjusted also. The given beam configuration fortunately provided a good candidate of a suppressed charge state with $^{40}\mathrm{Ar}^{14+}$ at a equilibrium charge-state of 10+, the most prominent peak in the charge-state distribution.

Recorded longitudinal phase spaces are depicted in Fig. 5.3. The gas pressure has been varied from 2000 mbar to lower pressures from to top to bottom. Horizontal axes represent the arrival time of the ions at the diamond detector with respect to the UNILAC RF. The vertical phase-space axis represents the energy by means of the relative energy deviation and a reference energy corresponding to $\beta = 5.5\%$. Recorded timings have been consistently shifted, so that the reference phase space at 2000 mbar is centred at (0,0). On the right column, the bunch structure is featured which includes all events contained in the scaled first-shot covariance ellipse on the left side. Additionally, the profile of the 2000 mbar reference is plotted as a grey profile, rescaled to match the event count of the respective histogram. This allows easy comparison of the bunch structures with the reference histogram. Estimator and derived values are listed in Tab. 5.2.

The reference phase space at 2000 mbar features an asymmetric bunch structure with an RMS width of about 2 ns. As the gas pressure is lowered to 1760 mbar, a two-peak bunch structure evolves. This structure remains for lower pressures until the high-energy peak merges with the low-energetic peak at about 970 mbar. At 470 mbar only one peak exists along with a pronounced low-energetic tail of late arrival times. As the gas pressure is lowered, the mean energy rises and the bunch arrives earlier. Also, the energy spread through straggling at the gas jet gets smaller and, consequently, the bunch length decreases which in turn results in a smaller emittance. This behaviour is expected and is reflected by the extracted estimator data as listed in Tab. 5.2. However, at around 1170 mbar and below this trend is reversed. Covariances and Twiss-α values also follow this trend with a minimum around a stripper pressure of about 1400 mbar. The estimator values are significantly affected by the trailing particles being more pronounced towards lower pressures in this configuration. The trailings are not considered to be a direct result of the stripper pressure. Instead, it is to assume that the horizontal radii of the bunch trajectories at the dipole section, resulting from the pressure-dependent energy losses inside the gas jet, may give rise to an enhanced interaction of bunch ions with the high-current slits. This motivates dedicated measurements to study the effect of the high-current slits on the longitudinal phase-space distribution of the next section.

Tab. 5.2: Estimator values (MCD) of phase-space data shown in Fig. 5.3.

Pressure (mbar)	$\langle t_{arr} \rangle$ (ns)	$\left\langle \frac{\Delta E}{\langle E \rangle} \right\rangle$ (mrad)	$\sigma_{t_{arr}}$ (ns)	$\sigma_{\frac{\Delta E}{\langle E \rangle}}$ (mrad)	cov (mrad·ns)	ε_{rms} (mrad·ns)	α
2000	0.0	0.0	2.04	14.22	-18.78	22.22	0.85
1760	-0.15	1.58	1.81	13.78	-15.31	19.69	0.78
1560	-0.12	2.50	1.78	13.48	-14.38	19.13	0.75
1400	-0.14	3.20	1.72	13.13	-12.91	18.50	0.70
1170	-0.34	2.66	1.80	13.73	-14.81	19.73	0.75
970	-0.36	2.97	1.71	13.68	-13.31	19.20	0.69
470	0.03	0.87	1.90	16.78	-19.98	24.83	0.80
Δ_{mcd}	< 0.02	< 0.4	< 0.04	< 0.16	< 0.65	< 0.26	< 0.03

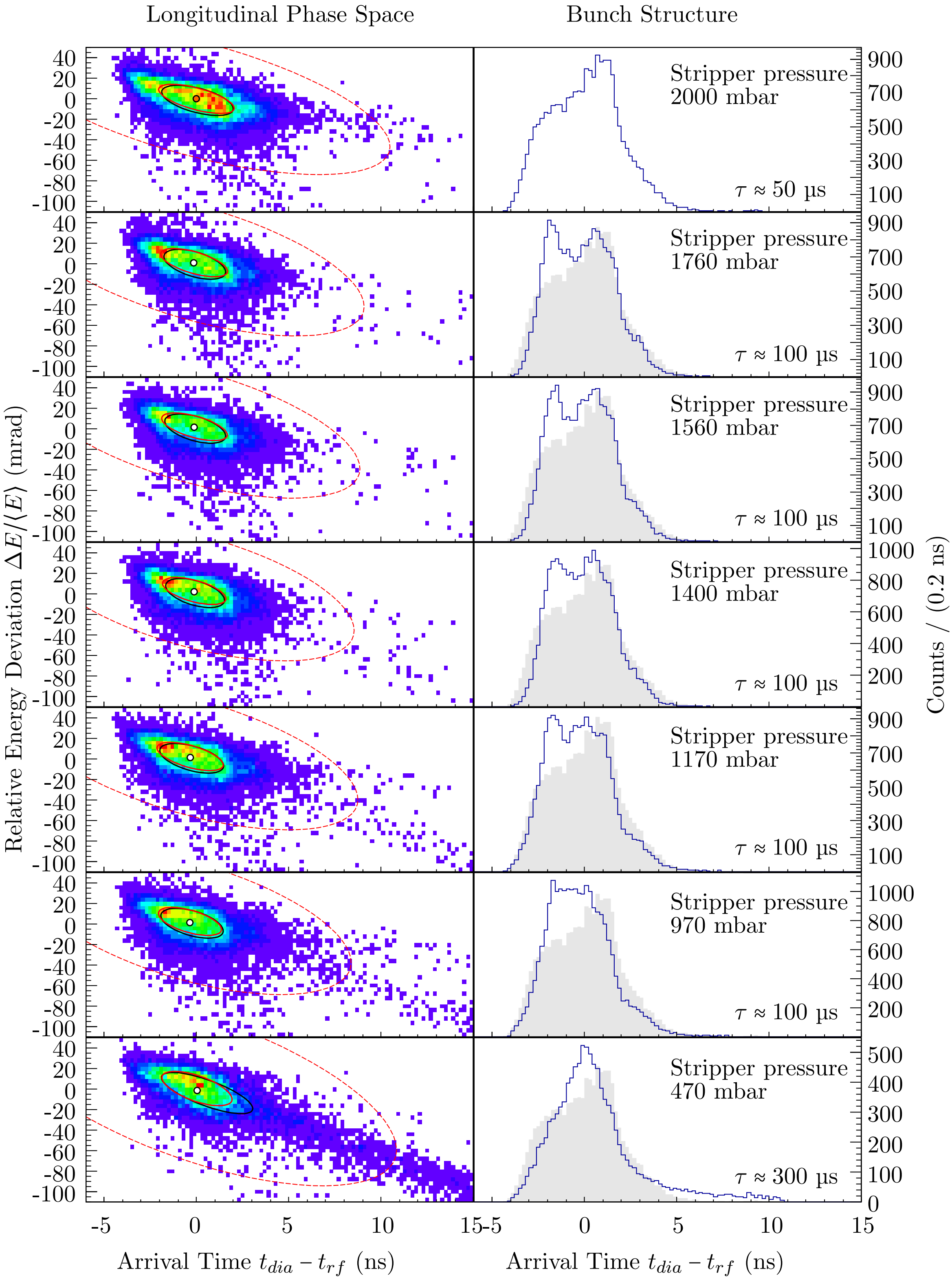

Fig. 5.3: Longitudinal phase-space distributions varying pressures at the gas-stripper nozzle recorded with the TOF setup.

5.2.3 Variation of High-Current Slits

Section 5.2.2 hinted an unexpected influence of the high-current slits on the longitudinal phase-space distribution. Limiting the transverse geometric trajectories of particles is one way to attenuate the beam. By symmetric openings, with respect to the horizontal beam axis, parts of the beam are scraped off the beam distribution. At the given beam energies of about 1.4 *A*MeV ions have a typical range in matter of several micrometers only. Due to the short range in matter, the assumption has been that ions either pass the slit opening unaffected or are absorbed at the slit geometry. A dedicated measurement has been performed with different high-current slit settings. For comparison with the measurements in Sec. 5.2.2, an identical high-current injector setup has been targeted. The high charge-state $^{40}\mathrm{Ar}^{14+}$ served as primary beam attenuation at stripper pressure of 2000 mbar. Of both charge-separating high-current slits US3DS4 and US3DS5, see Sec. 3.2.1, the slit DS5 closer to the measurement has been varied, whereas DS4 is fixed at an open setting ±15 mm.

In the following, longitudinal phase-space measurements with different symmetric slit settings of US3DS5 have been performed using the TOF setup. The slit openings have been ±5 mm to ±1 mm in steps of 1 mm and a slit opening of ±0.5 mm, which is the smallest possible slit setting. To account for the high dynamics in count rate at different slit settings, the macro-pulse length has been adjusted between 50 µs to 250 µs and the macro-pulse repetition rate between 1 Hz and 2 Hz. This procedure is not considered to have an influence on the six-dimensional phase space of the bunches. Longitudinal phase-space distributions and corresponding bunch structure are given in Fig. 5.4. The bunch structures are based on all events contained in the corresponding scaled first-shot ellipse. Axes scalings are kept from the previous section. Horizontal axes represent the arrival time of the ions at the diamond detector with respect to the UNILAC RF. The vertical phase-space axis represents the energy by means of the relative energy deviation and a reference energy corresponding to $\beta = 5.5\%$. Recorded timings are consistently shifted, so that the reference phase space at 2000 mbar is centred at (0,0). The bunch-structure data additionally features a normalised, grey profile of the reference bunch structure for easy comparison.

Comparing the reference phase space to the one in Sec. 5.2.2 shows a good agreement. The corresponding bunch structure also agrees in the characteristic shape. Minor deviations are expected after a readjustment of the accelerator settings. Also estimator values agree to large extent. The larger bunch length correlates with a slightly higher energy spread.

Comparison of the first four measurements with slit openings from ±5 mm to ±2 mm reveals no significant deviations of the longitudinal phase-space distribution and the bunch structure. The estimator numbers hint a small increase in energy spread towards a smaller slit opening but this does not noticeably affect the bunch length due to the short drift of about 1.6 m between slits and measurement device. A slit setting of ±1 mm shows a clear distortion of the bunch structure. While the edge of the faster ions matches with the reference distribution, a second peak evolves at the end of the bunch as some ions arrive later compared to the previous slit settings. This is reflected by the data in Tab. 5.4, with a larger bunch length of about 10% accompanied by an increased energy spread. The phase space of the narrowest possible slit setting at ±0.5 mm is shown in the bottom row of Fig. 5.4. This phase space noticeably depletes near the center which results in two pronounced peaks of the bunch structure. Again, the edge of early-arriving ions is sustained for the most part.

The second peak forms around the original edge of the reference bunch structure and the bunch length is significantly enlarged by about 21% over the reference bunch structure.

By closing the high-current slits US3DS5 from ±5 mm to ±0.5 mm the longitudinal energy spread gradually increases. At the time same the bunch structure does not significantly change within the range ±5 mm and ±2 mm. Further closing the slits results in a pronounced two-peak structure of the longitudinal phase projection and a significantly enlarged bunch length. Also, by closing the slits the energy centre is shifted to lower energies which matches the later arrival times of the bunches. The magnitude of the covariance gradually increases from ≈-21 mrad·ns to ≈-31 mrad·ns, whereas the RMS emittance does not vary with a slit setting down to ±2 mm and increases about 20% for smaller slit openings. The Twiss-α gradually increases from 0.8 to 1.0 towards smaller slit settings.

The depleted center of the bunch structure may originate from scattering of a fraction of particle at the slit geometries. Thereby an energy shift to lower energies may occur, which is supported by the increasing energy spread and the trend of the energy centre. Those particle arrive later at the Particles that pass the slit without interaction are Attenuation via high-current slits may significantly influence the longitudinal phase space for very small openings. TODO:Again, energy width is larger than expected and Twiss-α is too low.

Tab. 5.3: Estimator values (MCD) of phase-space data shown in Fig. 5.4.

Slit DS5 (mm)	$\langle t_{arr} \rangle$ (ns)	$\left\langle \frac{\Delta E}{\langle E \rangle} \right\rangle$ (mrad)	$\sigma_{t_{arr}}$ (ns)	$\sigma_{\frac{\Delta E}{\langle E \rangle}}$ (mrad)	cov (mrad·ns)	ε_{rms} (mrad·ns)	α
±5	0.0	0.0	2.25	14.64	-20.82	25.41	0.82
±4	0.06	-0.82	2.22	14.93	-21.07	25.71	0.82
±3	-0.05	-0.77	2.25	14.99	-21.92	25.54	0.86
±2	-0.08	-1.28	2.24	15.23	-22.45	25.74	0.87
±1	0.06	-1.25	2.51	15.61	-27.00	28.48	0.95
±0.5	0.20	-0.90	2.71	15.97	-30.75	30.59	1.00
Δ_{mcd}	< 0.005	< 0.39	< 0.06	< 0.18	< 2.02	< 0.05	< 0.067

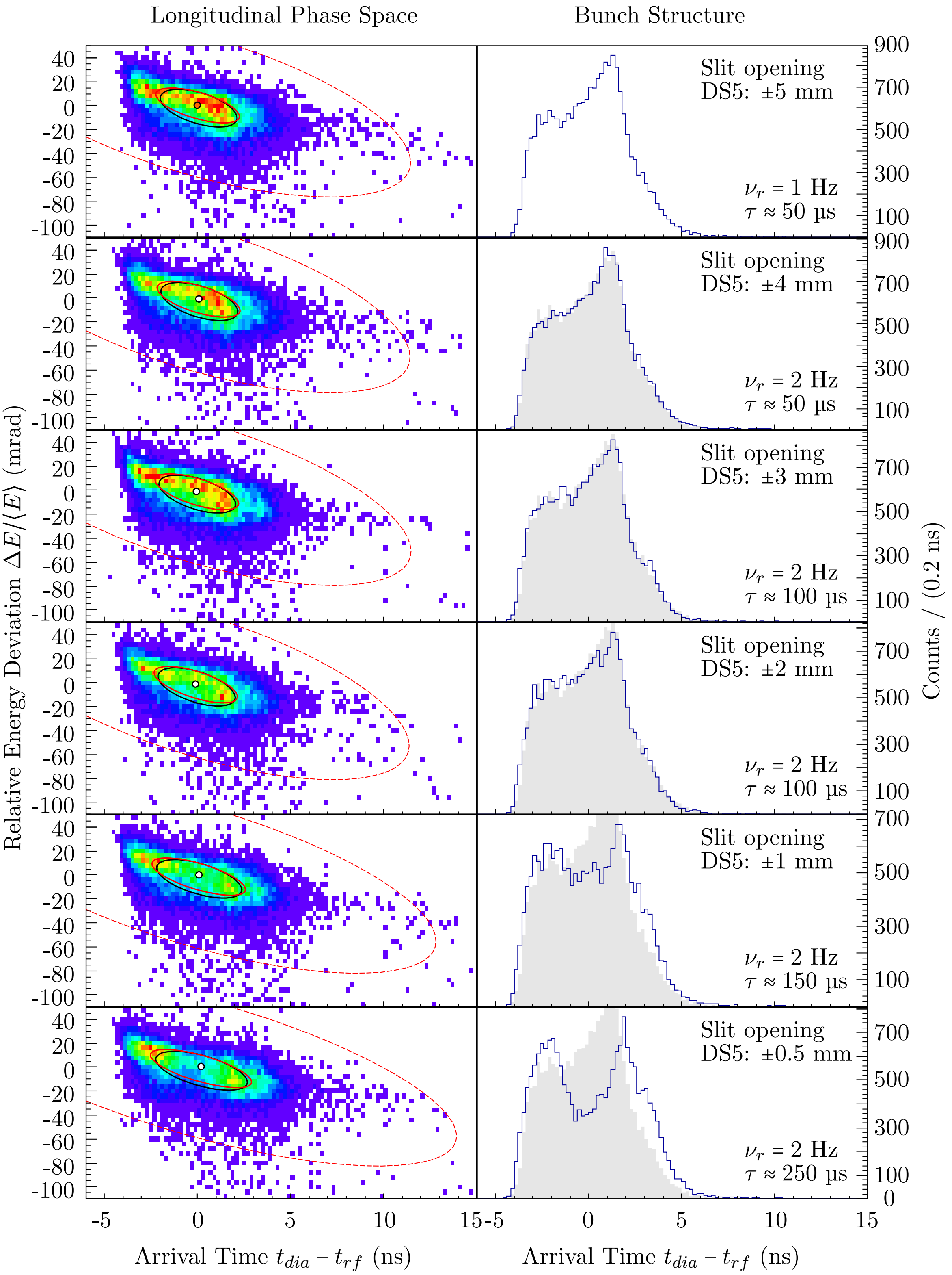

Fig. 5.4: Longitudinal phase-space recordings of different high-current slit (DS5) openings using the TOF setup.

5.2.4 High-Current Argon Data (HIPPI Campaign)

TODO include citation [58]

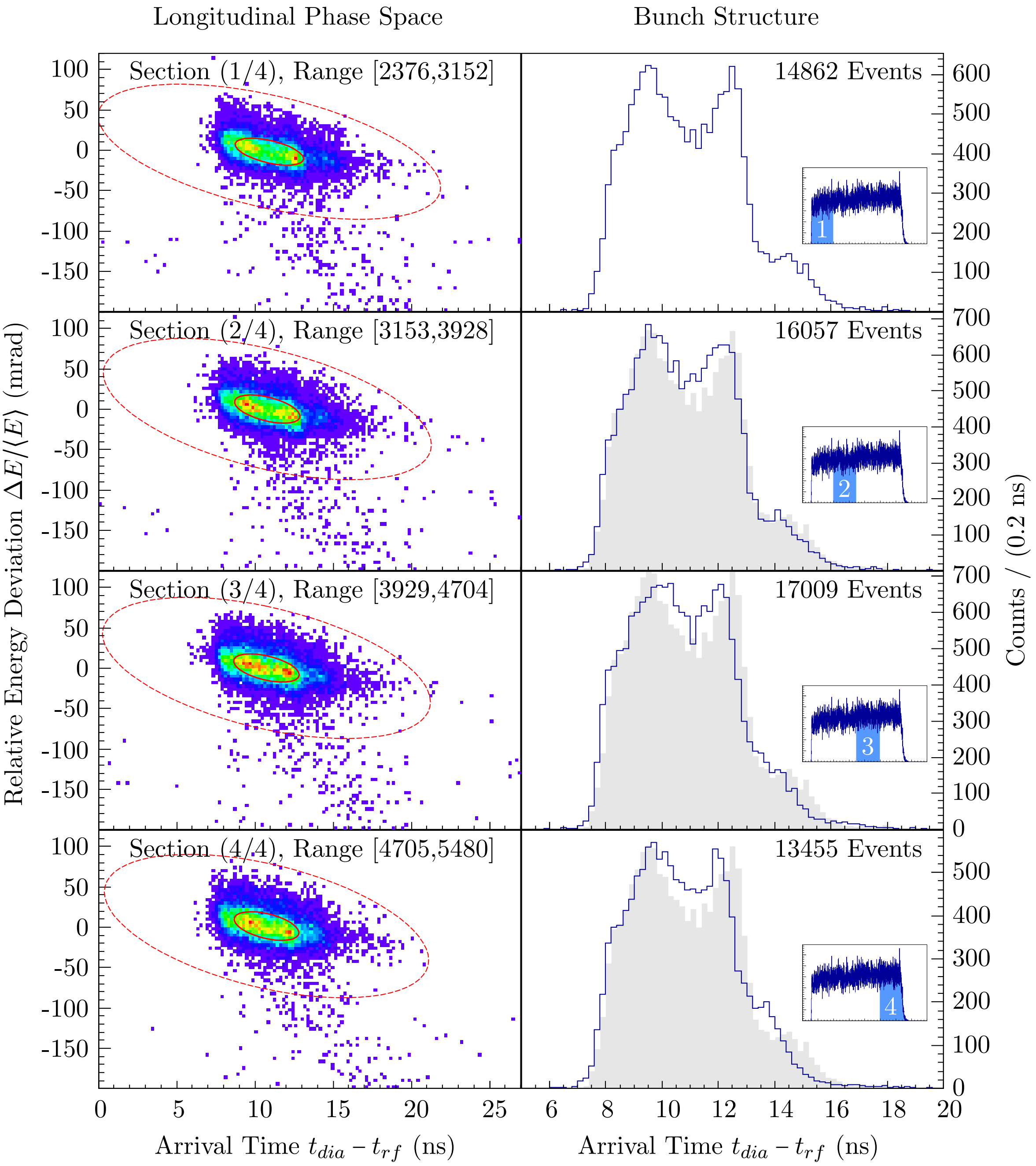

Fig. 5.5: High-current argon measurement for the HIPPI collaboration. A high amount of $\approx 6.0 \times 10^4$ events allowed to evaluate the robust MCD estimator for different macro-pulse sections. The macro-pulse section taken into account is depicted in the event-density histogram right of the bunch structures.

Tab. 5.4: Estimator values (MCD) of the HIPPI phase-space data shown in Fig. 5.5.

Section (Macro-pulse)	$\langle t_{arr} \rangle$ (ns)	$\left\langle \frac{\Delta E}{\langle E \rangle} \right\rangle$ (mrad)	$\sigma_{t_{arr}}$ (ns)	$\sigma_{\frac{\Delta E}{\langle E \rangle}}$ (mrad)	cov (mrad·ns)	ε_{rms} (mrad·ns)	α
(1/4)	10.89	-1.70	2.05	15.16	-17.42	25.81	0.67
(2/4)	10.81	-0.66	1.97	15.70	-16.64	26.08	0.64
(3/4)	10.72	0.42	1.98	15.79	-15.96	26.89	0.59
(4/4)	10.72	0.92	1.95	16.16	-15.95	27.32	0.58
Δ_{mcd}	< 0.01	< 0.23	< 0.04	< 0.19	< 0.87	< 0.17	< 0.04

5.3 Calorimetric Measurements with Mono-Crystalline Diamond

The preceding sections covered time-of-flight measurements using a MCP detector and a poly-crystalline diamond detector. This section discusses the first recorded data with the mono-crystalline diamond detector, described in Sec. 4.2, and comprises a samarium and an argon recording. In particular, a first evaluation of the measurement chain, i. e. detector and DAQ, is targeted.

^{152}Sm^{20+} Measurement. A low-current samarium beam has been attenuated by defocusing quadrupole settings at the RFQ cavity, as described in Sec. 5.1.1. Figure 5.6 shows the recorded $^{152}\mathrm{Sm}^{20+}$ phase-space data. The energy axis is a linear mapping of the pulse-integral information. Determination of the phase-space center via the robust MCD estimator allows for linear calibration of the energy by assigning the expected kinetic energy corresponding to the design machine $\beta \approx 0.055$ to it. The measurement contains 10^4 events which equals a measurement duration of about 3 hours with the current DAQ at a macro-pulse repetition rate of 1 Hz.

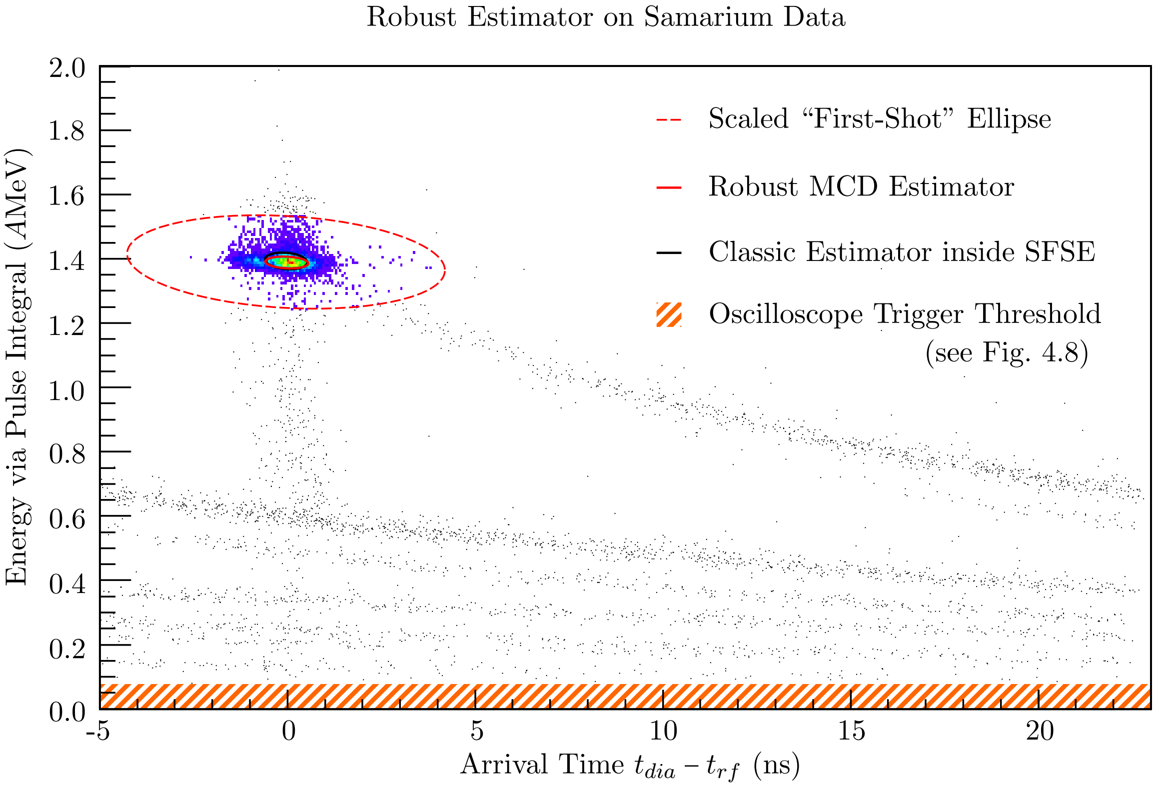

Fig. 5.6: Samarium phase-space data recorded with the mono-crystalline diamond using the pulse-integral information and linear energy calibration. The ellipses are the scaled first-shot ellipse (red dashed), the robust estimator ellipse (red) and the classical estimator (black) applied to events inside scaled first-shot ellipse.

It is evident from the recorded distribution that the core phase space, inside the SFSE,

Tab. 5.5

Tab. 5.5: Robust estimator values (MCD) of the samarium phase-space data shown in Fig. 5.6.

^{152}Sm^{20+} MC Diamond	$\sigma_{t_{arr}}$ (ns)	$\sigma_{\frac{\Delta E}{\langle E \rangle}}$ (mrad)	cov (mrad·ns)	ε_{rms} (mrad·ns)	α
Integration	0.57	13.52	-1.39	7.52	0.18
Pulse Height	0.52	30.18	-1.30	15.45	0.08
Δ_{mcd}	< 0.03	< 1.16	< 0.04	< 0.11	< 0.005

$$E_{kin} = \frac{m_u}{2} \frac{d^2}{\left(t + t_{\langle \beta \rangle}\right)^2} = \frac{m_u}{2} \frac{1}{\left(\frac{t}{d} + \frac{1}{\beta c}\right)^2} \tag{5.1}$$

Tab. 5.6: Robust estimator values (MCD) of the argon phase-space data shown in Fig. 5.11.

^{40}Ar^{10+} MC Diamond	$\sigma_{t_{arr}}$ (ns)	$\sigma_{\frac{\Delta E}{\langle E \rangle}}$ (mrad)	cov (mrad·ns)	ε_{rms} (mrad·ns)	α
Integration	2.26	21.24	-20.16	43.54	0.46
Pulse Height	2.22	36.32	-12.73	79.63	0.16
Δ_{mcd}	< 0.03	< 0.21	< 0.54	< 0.20	< 0.01

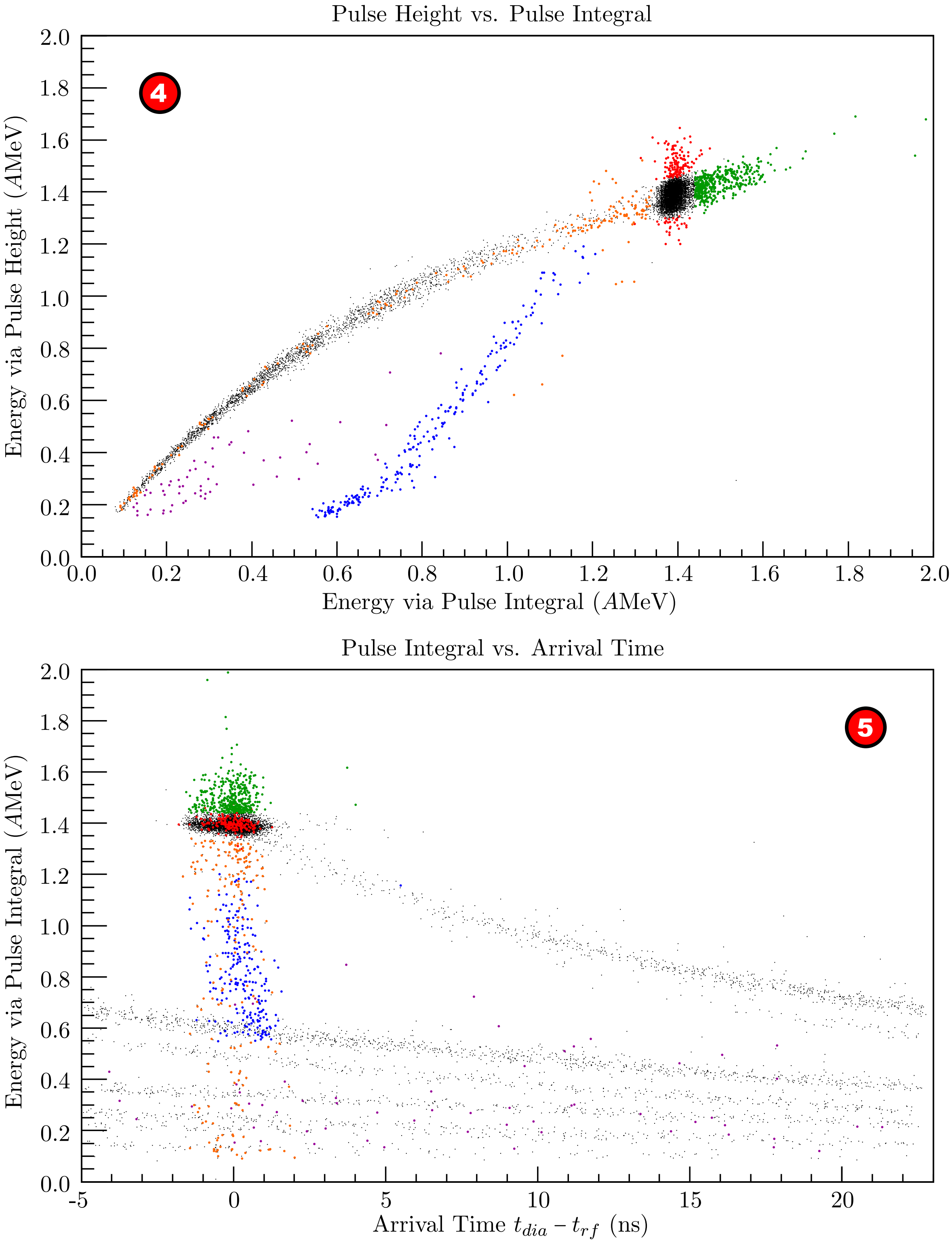

Fig. 5.7: Different representation of the recorded samarium data. Plot ④ shows the pulse height vs. the pulse integral, both in linear energy calibration. Plot ⑤ shows the kinetic energy via the pulse-integral information vs. the arrival time at the mono-crystalline diamond detector. Coloured events of both plots correspond to each other and are defined by certain cuts (see text).

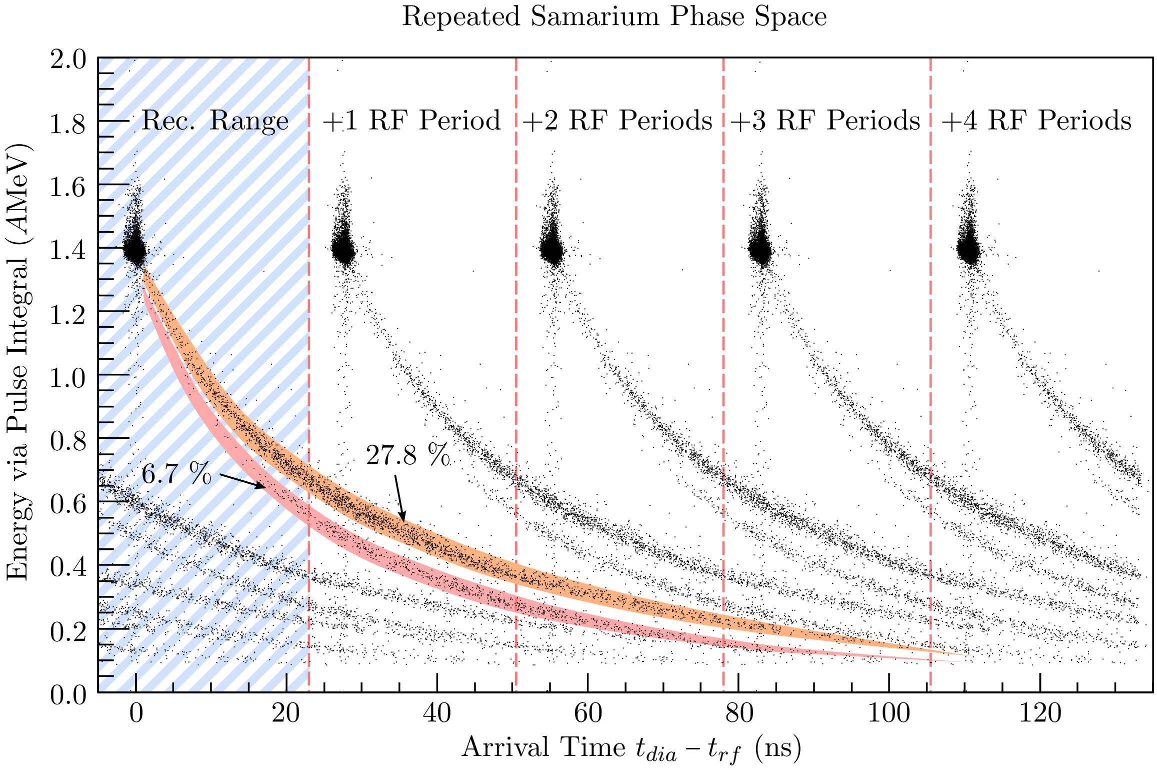

Fig. 5.8: Repeated samarium phase space data by concatenating RF periods. Two trails are visible emerging from the core region and comprise, at least, a third of all registered events for this experimental configuration.

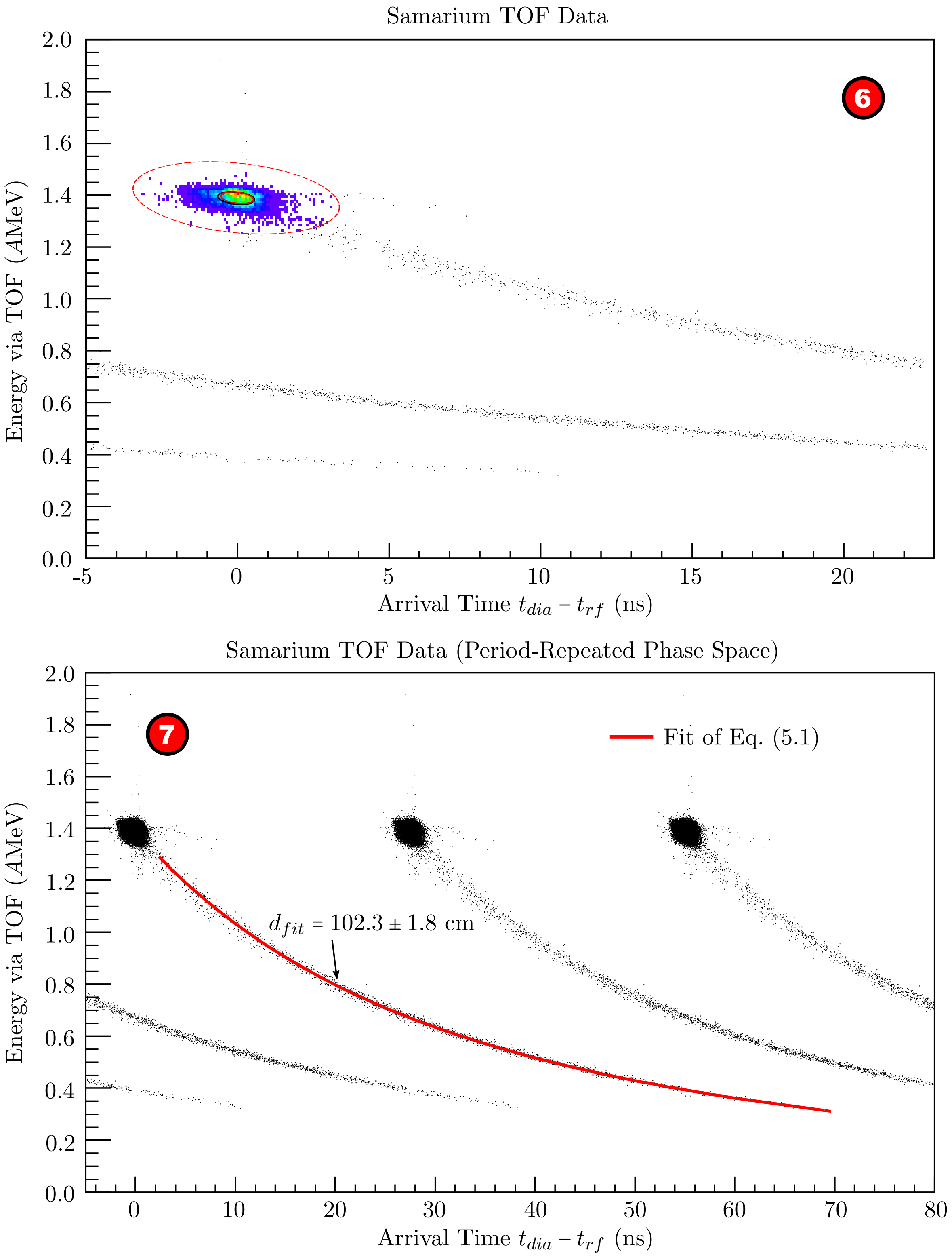

Fig. 5.9: Plot ⑥ shows the longitudinal Samarium phase space recorded with the TOF setup. The meaning of the ellipses corresponds to those in Fig. 5.6. Plot ⑦ concatenates three TOF recordings, which allows fitting of the trail with Eq. (5.1).

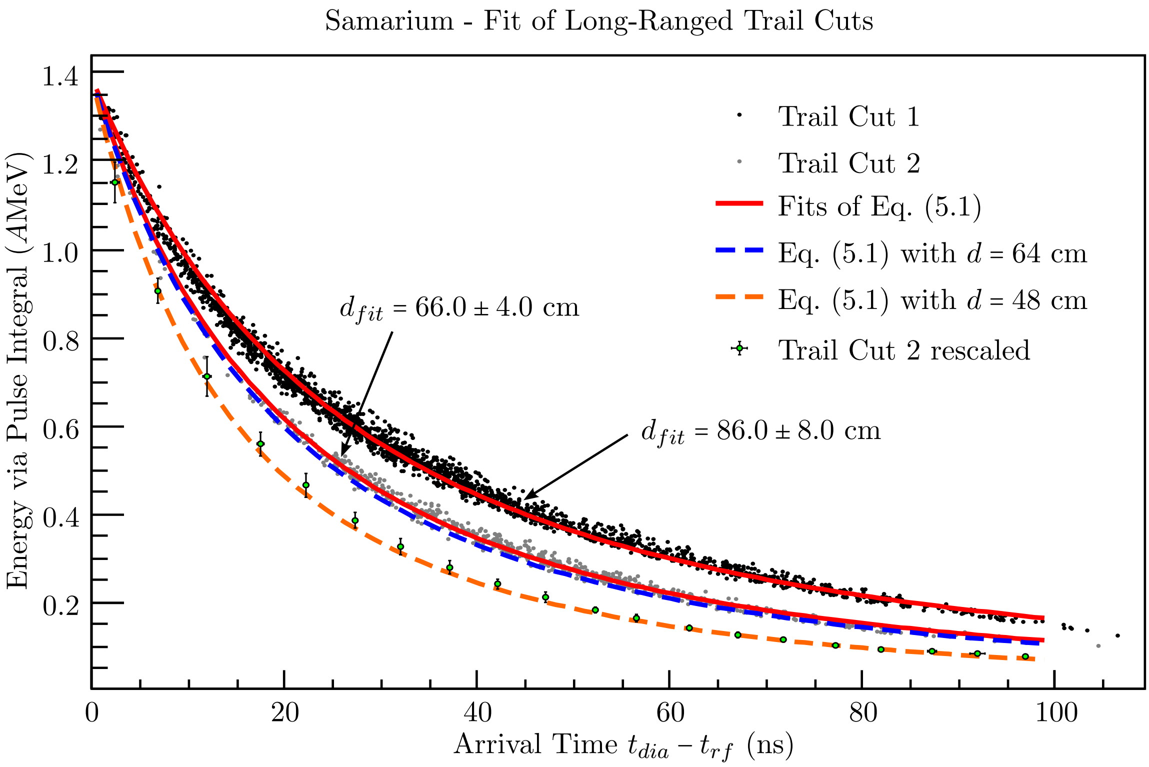

Fig. 5.10: Fit of trails visible in the samarium measurement. The black and grey events are inside the trail cuts highlighted in Fig. 5.8 and labeled "Trail Cut 1/2". A fit of Eq. (5.1) to each trail is given by the red lines. The corresponding fitted vertices, i.e. the distance of the location of interaction and the mono-crystalline diamond determined by the fits, are shown by d_{fit}. Additionally, Eq. (5.1) has been plotted for supposed vertices of d = 64 cm and d = 48 cm by the dashed blue and orange lines, corresponding to the actual separation of the collimator apertures and the mono-crystalline diamond (see Fig. A.1). See text for data points labeled as "Trail Cut 2 rescaled".

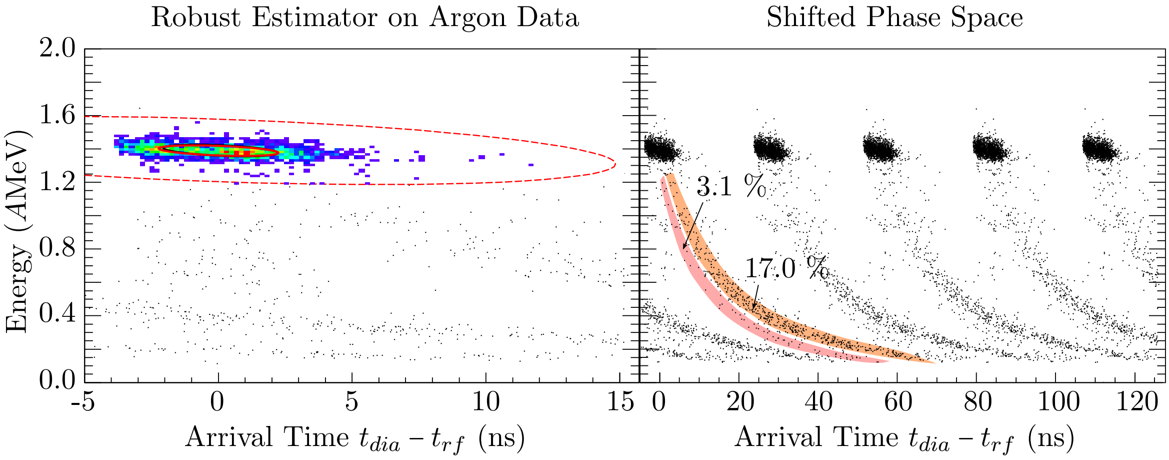

Fig. 5.11: Argon measurement using the mono-crystalline diamond detector and the repeated phase space to visualise the trails.

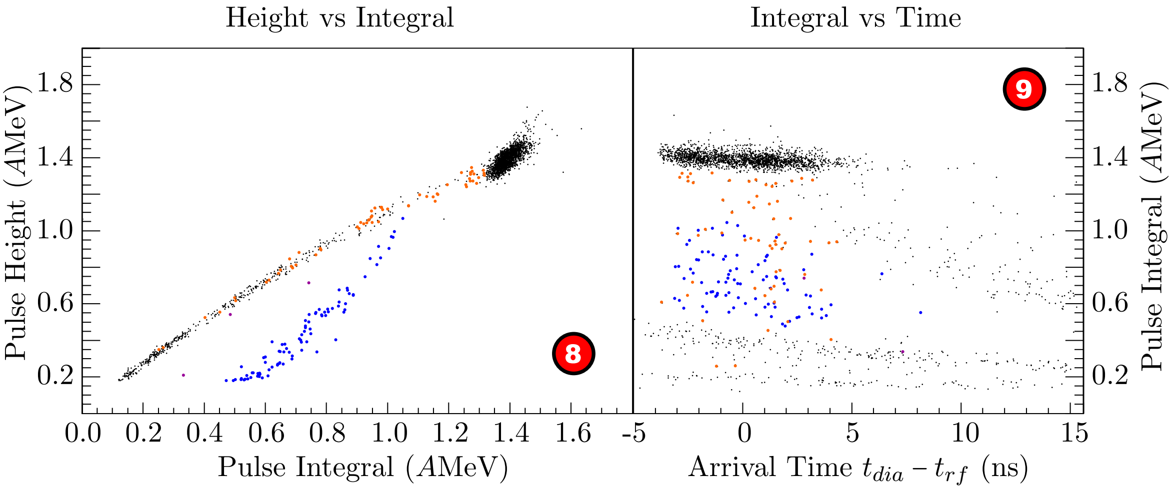

Fig. 5.12: Different representation of the recorded argon data. Plot ⑧ shows the pulse height vs. the pulse integral, both in linear energy calibration. Plot ⑨ shows the kinetic energy via the pulse-integral information vs. the arrival time at the mono-crystalline diamond detector. Coloured events of both plots correspond to each other and are defined by certain cuts (see text).

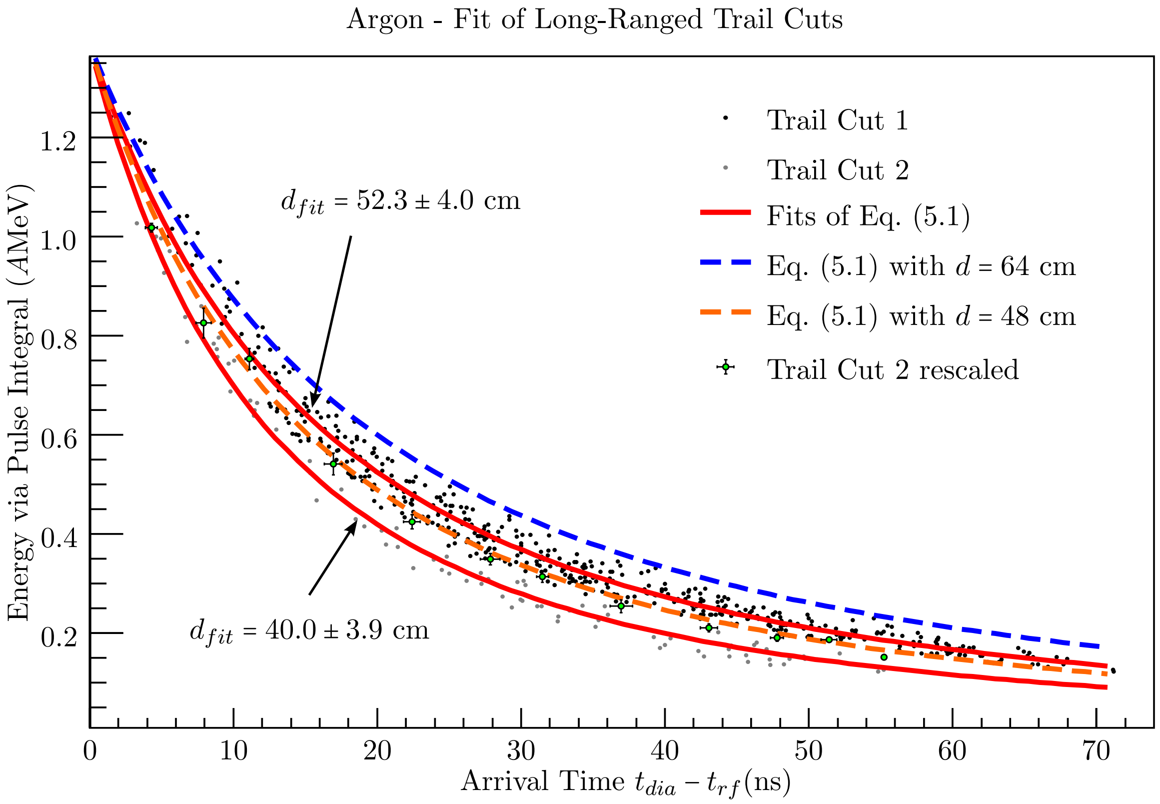

Fig. 5.13: Determination of interaction vertices via fit of trails with Eq. (5.1). For a detailed description see Fig. 5.10.

Chapter 6

Influence of Finite Resolution on Twiss Parameters

6.1 Introduction

Measurements in chapter 5 consistently have a energy spread $\Delta E/\langle E \rangle$ and a significantly lower correlation α as expected. While a reference measurement with another device does not exist, an energy spread close to 1% in case of high-current beam settings. As described in chapter 7, systematic uncertainties lead to a limitation in resolution. With the lack of a monochromatic reference beam, direct access to the response function of the whole setup is not available. In this chapter a Gaussian model space is used for the longitudinal particle density distribution. Together with the response function, which is also considered to be of Gaussian type, this allows an analytic approach to investigate the consequences of the limiting resolution during the measurement process.

6.2 Gaussian Model Space

A common model to describe the phase spaces in transverse and longitudinal degree of freedom in accelerator physics are Gaussian density distributions. The integral parameters used to define those distributions is the RMS emittance ε and the Twiss parameters $\{\alpha, \beta, \gamma\}$ based on central statistical moments as explained in Sec. 2.3. For simplicit, the degrees of freedom will, in the following, be denoted as x and y whereas we have x for the phase or equivalent and y represents the energy or momentum. With this parameterisation, a

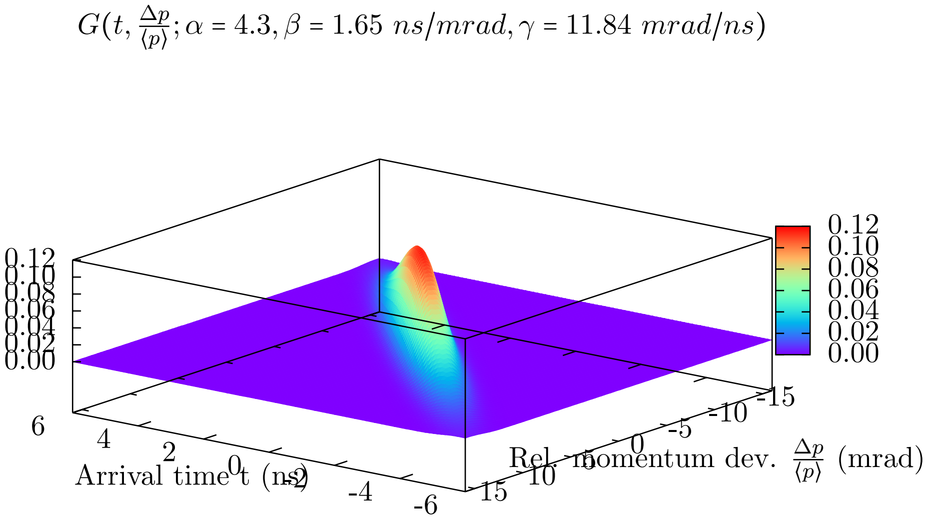

Fig. 6.1: Expected high current density distribution for ^{238}U at the measurement setup as shown in Fig. 7.11 for Twiss parameter $\alpha = 4.3$, $\beta = 1.65$ ns/mrad, $\gamma = 11.84$ mrad/ns and $\varepsilon = 1.36$ ns·mrad in Eq. (6.1).

general Gaussian 2-dimensional probability distribution is given by

$$G(x, y; \alpha, \beta, \gamma, \varepsilon) = \frac{1}{2\pi\varepsilon}\, \mathrm{e}^{-\frac{1}{2\varepsilon}\left(\gamma\, x^2 + 2\,\alpha\, x\, y + \beta\, y^2\right)}\,. \tag{6.1}$$

6.2.1 1-dimensional Convolution

Taking into account the expected beam energy width (RMS) $\frac{\Delta E}{\langle E \rangle}$ of about 1% which corresponds to a Δt_{rms} of about 240 ps TODO:REF and common bunch lengths (RMS) of larger than 1 ns, it is clear that Time-of-flight requires a much more precise measurement compared to the bunch structure for a direct measurement of the 2-dim longitudinal phase space. A limited time resolution in the TOF will therefore have a much larger impact on the phase space representation compared to an equally absolute timing deficiency in the bunch structure measurement. This suggests that we will restrict ourselves to the TOF degree of freedom and convolve the phase space distribution Eq. (6.1) with the Gaussian response function

$$g_y^{res}(y; \sigma_{res,y}, \mu) = \frac{1}{\sqrt{2\pi}\,\sigma_{res,y}}\, \mathrm{e}^{-\frac{(y-\mu)^2}{2\sigma_{res,y}^2}} \tag{6.2}$$

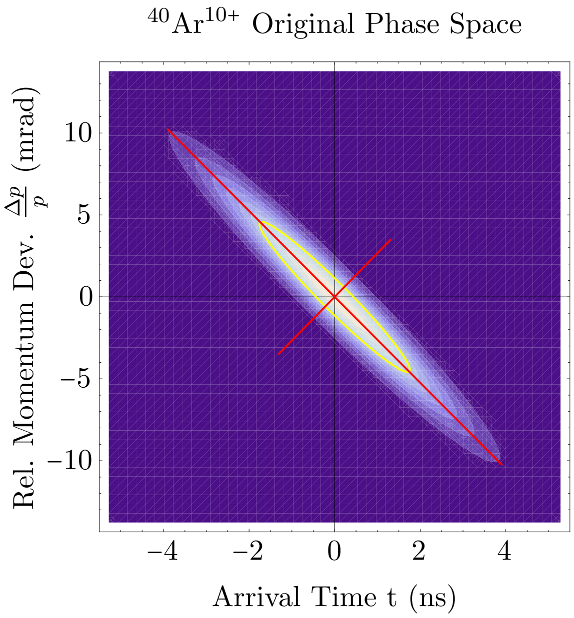

Fig. 6.2: ^{40}Ar^{10+} Phase space density distribution from Fig. 7.11 at 7.1 mA. The yellow ellipse marks the RMS Twiss ellipse.

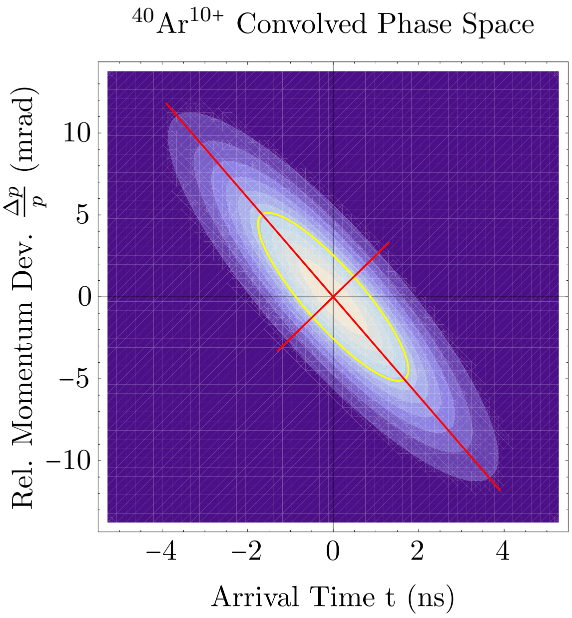

Fig. 6.3: Phase space from Fig. 6.2 convolved in vertical axis with two times the rms width $\sigma_y^{x=0} = \sqrt{\varepsilon/\beta}$ of the original distribution at x=0.

which writes as

$$\left(g_y^{res}\circ G\right)(x,y) = \int_{-\infty}^{+\infty} \mathrm{d}z\, G(x,y;\alpha,\beta,\gamma,\varepsilon)\; g(y-z;\sigma_{res,y},\mu=0) =$$

$$\frac{1}{2\pi\varepsilon\sqrt{2\pi}\sigma_{res,y}}\int_{-\infty}^{+\infty}\mathrm{d}z\;\mathrm{e}^{-\frac{1}{2\varepsilon}\left(\gamma\, x^2+2\,\alpha\, x\, z+\beta\, z^2\right)-\frac{(y-z)^2}{2\,\sigma_{res,y}^2}}\,.$$

Taking the constant factor, with respect to the integration variable z, out of the integral and rearranging the exponent in terms of z and z^2

$$\left(g_y^{res}\circ G\right)(x,y) = \frac{1}{2\pi\varepsilon\sqrt{2\pi}\sigma_{res,y}}\;\mathrm{e}^{-\left(\frac{\gamma x^2}{2\varepsilon}+\frac{y^2}{2\,\sigma_{res,y}^2}\right)}\int_{-\infty}^{+\infty}\mathrm{d}z\;\mathrm{e}^{-\left(\frac{\beta}{2\varepsilon}+\frac{1}{2\,\sigma_{res,y}^2}\right)z^2+\left(\frac{y}{\sigma_{res,y}^2}-\frac{\alpha x}{\varepsilon}\right)z}$$

allows completion of the square of the exponent. The evaluation of the integral becomes

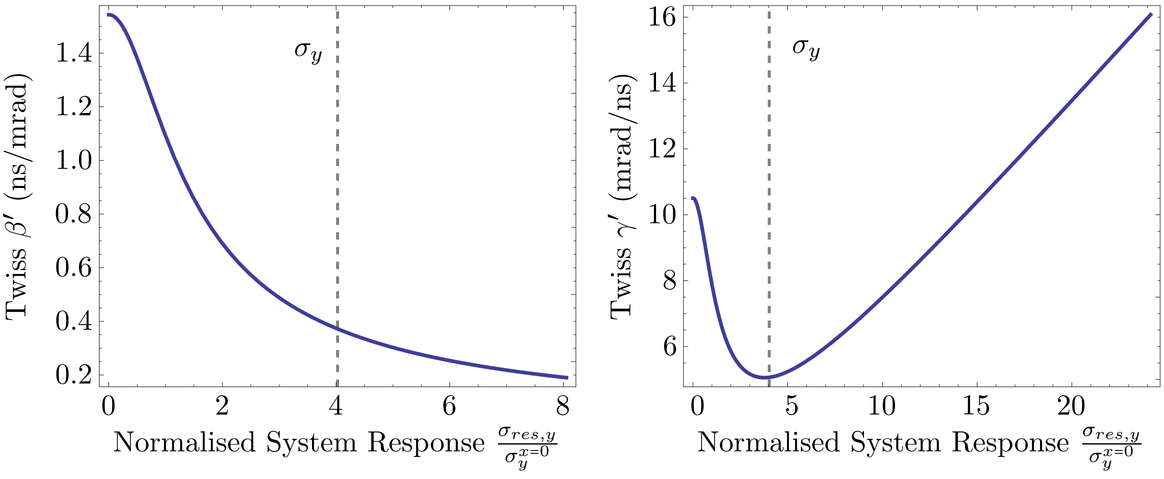

Fig. 6.4: Twiss parameter β' and γ' after 1-dimensional convolution with the Gaussian response function Eq. (6.2), that represents the limited resolution. The transformed Twiss parameters are plotted by means of the width of the response function which is denoted on the abscissa by multiples of the waist $\sigma_y^{x=0}$ of the longitudinal phase space distribution at $x = 0$. The original parameterisation is taken from the uranium start configuration as shown in Fig. 7.11. As a special point, the projected width of the momentum distribution σ_y is marked as dashed vertical line. In this case the width of the response function is as large as the expected beam energy width.

trivial using the well-known Gaussian integral $\int_{-\infty}^{\infty} \mathrm{d}x \, \exp\left(-\alpha x^2\right) = \sqrt{\pi/\alpha}$.

$$\left(g_y^{res}\circ G\right)(x,y) = \frac{1}{2\pi\varepsilon\sqrt{2\pi}\sigma_{res,y}}\,\mathrm{e}^{-\left(\frac{\gamma x^2}{2\varepsilon}+\frac{y^2}{2\sigma_{res,y}^2}\right)+\frac{1}{2}\frac{\left(\frac{y}{\sigma_{res,y}^2}-\frac{\alpha x}{\varepsilon}\right)^2}{\frac{\beta}{\varepsilon}+\frac{1}{\sigma_{res,y}^2}}}$$

$$\times\underbrace{\int_{-\infty}^{+\infty}\mathrm{d}z\,\mathrm{e}^{-\frac{1}{2}\left(\frac{\beta}{\varepsilon}+\frac{1}{\sigma_{res,y}^2}\right)\left(z-\frac{\left(\frac{y}{\sigma_{res,y}^2}-\frac{\alpha x}{\varepsilon}\right)}{\frac{\beta}{\varepsilon}+\frac{1}{\sigma_{res,y}^2}}\right)^2}}_{\sqrt{\frac{2\pi}{\frac{\beta}{\varepsilon}+\frac{1}{\sigma_{res,y}^2}}}}$$

Eventually, the phase space convoluted in y and denoted by $G'(x,y;\alpha',\beta',\gamma',\varepsilon')$ is represented by

$$\left(g_y^{res}\circ G\right)(x,y) = \frac{1}{2\pi\varepsilon\sigma_{res,y}\sqrt{\frac{\beta}{\varepsilon}+\frac{1}{\sigma_{res,y}^2}}}\,\mathrm{e}^{-\left(\frac{\gamma x^2}{2\varepsilon}+\frac{y^2}{2\sigma_{res,y}^2}\right)+\frac{1}{2}\frac{\left(\frac{y}{\sigma_{res,y}^2}-\frac{\alpha x}{\varepsilon}\right)^2}{\frac{\beta}{\varepsilon}+\frac{1}{\sigma_{res,y}^2}}}\,. \tag{6.3}$$

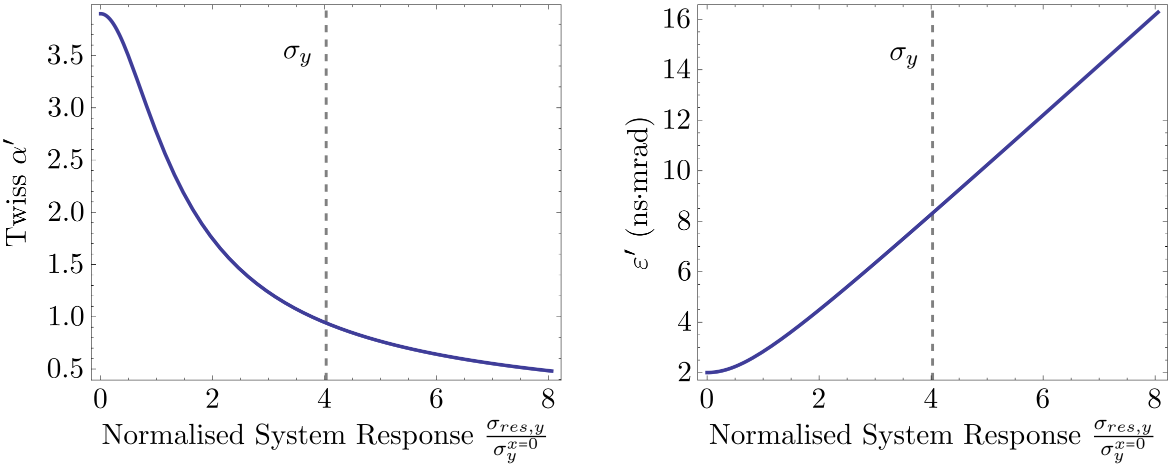

Fig. 6.5: Correlation α' and the emittance ε' after 1-dimensional convolution. As with β' the correlation drops off quickly with a decreasing time resolution. Compared to an ideal measurement setup, a response function with a width that corresponds to the original projected energy width σ_y the measured correlation α' is about four times smaller.

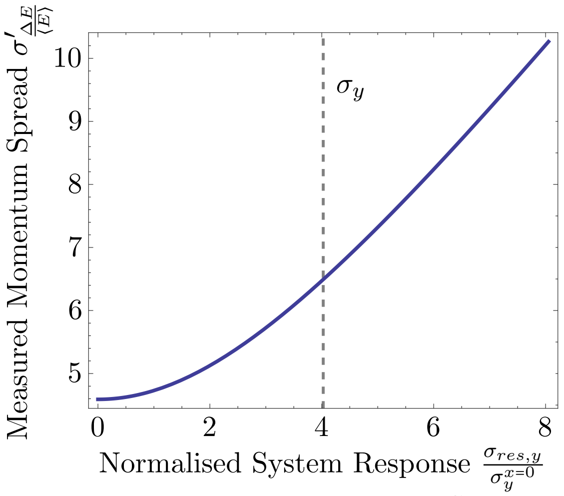

Fig. 6.6: The plot shows the RMS relative momentum width against the width of the response function. At the dashed line the RMS width response function is equal to $\sigma_{\Delta E}$, which results in a measured momentum width that is $\sqrt{2}$ times larger.

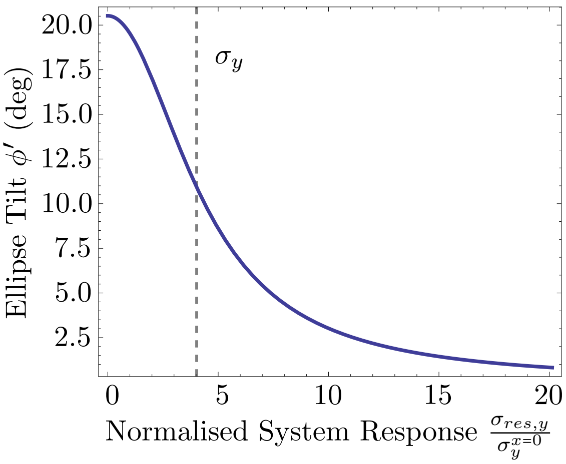

Fig. 6.7: Under a limited time resolution, the orientation of the phase space ellipse is not conserved. The angle ϕ' is given by $\phi' = (1/2)\mathrm{atan}\{-2\alpha'/(\beta'-\gamma')\}$.

We see that the Gaussian phase space parameterisation is form-invariant under convolution with a Gaussian response function and thus, after expansion of the exponent in Eq. (6.3), the transformed Twiss parameters can be extracted via comparison to G':

$$G'(x,y;\alpha',\beta',\gamma',\varepsilon') = \frac{1}{2\pi\varepsilon'}\,\mathrm{e}^{-\frac{1}{2\varepsilon'}\left(\gamma'\,x^2+2\,\alpha'\,x\,y+\beta'\,y^2\right)} \overset{!}{=} \left(g_y^{res}\circ G\right)(x,y). \tag{6.4}$$

Transformed Twiss parameters are listed primed.

$$\varepsilon' = \varepsilon\sqrt{1+\sigma_{res,y}^2\frac{\beta}{\varepsilon}} \tag{6.5}$$

$$\alpha' = \frac{\alpha}{\sqrt{1+\sigma_{res,y}^2\frac{\beta}{\varepsilon}}} = \alpha\left(\frac{\varepsilon}{\varepsilon'}\right) \tag{6.6}$$

$$\beta' = \frac{\beta}{\sqrt{1+\sigma_{res,y}^2\frac{\beta}{\varepsilon}}} = \beta\left(\frac{\varepsilon}{\varepsilon'}\right) \tag{6.7}$$

$$\gamma' = \frac{\gamma+\frac{\sigma_{res,y}^2}{\varepsilon}}{\sqrt{1+\sigma_{res,y}^2\frac{\beta}{\varepsilon}}} = \left(\gamma+\frac{\sigma_{res,y}^2}{\varepsilon}\right)\left(\frac{\varepsilon}{\varepsilon'}\right) \tag{6.8}$$

It is easy to very that

$$1 = \beta'\gamma' - \alpha'^2 \tag{6.9}$$

is still valid[1] To investigate the transformed Twiss parameters Eqs. (6.5)-(6.8), the uranium phase space distribution from (7.11) is taken as a reference. The transformed values of are plotted against multiples of the vertical beam waist standard deviation $\sigma_y^{x=0}$. The corresponding plots are shown in Fig. 6.4 and 6.5. Of major importance to j

$$\gamma' = \gamma\sqrt{1+\sigma_{res,y}^2\frac{\beta}{\varepsilon}} - \frac{\sigma_{res,y}^2}{\varepsilon}\frac{\alpha^2}{\sqrt{1+\sigma_{res,y}^2\frac{\beta}{\varepsilon}}} = \gamma\left(\frac{\varepsilon}{\varepsilon'}\right) - \alpha^2\sigma_{res,y}^2\left(\frac{\varepsilon'}{\varepsilon^2}\right) \tag{6.10}$$

6.2.2 2-dimensional Convolution

For Gaussian error contribution in both longitudinal degrees of freedom the corresponding transformation is provided by the two-dimensional convolution of the undisturbed phase space $G(x,y)$ Eq. (6.1) with the Gaussian distribution $(g_x^{res}\cdot g_y^{res})$ that represents the limited resolution in both degree of freedom.

$$\begin{aligned}\left((g_x^{res}\cdot g_y^{res})\circ G\right)(x,y) &= \frac{1}{(2\pi)^2\varepsilon\,\sigma_{res,x}\sigma_{res,y}}\iint_{-\infty}^{+\infty}\mathrm{d}q\,\mathrm{d}p\,\mathrm{e}^{-\frac{1}{2\varepsilon}\left(\gamma\,q^2+2\,\alpha\,q\,p+\beta\,p^2\right)-\frac{(x-q)^2}{2\,\sigma_{res,x}^2}-\frac{(y-p)^2}{2\,\sigma_{res,y}^2}} = \\ &\frac{1}{2\pi\varepsilon''}\,\mathrm{e}^{-\frac{1}{2\varepsilon''}\left(\gamma''\,x^2+2\,\alpha''\,x\,y+\beta''\,y^2\right)} = G''(x,y;\alpha'',\beta'',\gamma'',\varepsilon'')\end{aligned} \tag{6.11}$$

The integration of (6.11) and equating the coefficients with respect to $G(x,y)$ provides the Twiss parameters (double primed) after taking account a limited resolution in either degree

---

[1] Which is a requirement if $\{\alpha',\beta',\gamma'\}$ are Twiss parametes.

of freedom. Non-primed Twiss parameters are associated with the undisturbed phase space.

$$\varepsilon'' = \varepsilon\sqrt{\left(1+\sigma_{res,x}^2\frac{\gamma}{\varepsilon}\right)\left(1+\sigma_{res,y}^2\frac{\beta}{\varepsilon}\right)-\left(\sigma_{res,x}\sigma_{res,y}\frac{\alpha}{\varepsilon}\right)^2} \tag{6.12}$$

$$\alpha'' = \frac{\alpha}{\sqrt{\left(1+\sigma_{res,x}^2\frac{\gamma}{\varepsilon}\right)\left(1+\sigma_{res,y}^2\frac{\beta}{\varepsilon}\right)-\left(\sigma_{res,x}\sigma_{res,y}\frac{\alpha}{\varepsilon}\right)^2}} = \alpha\left(\frac{\varepsilon}{\varepsilon''}\right) \tag{6.13}$$

$$\beta'' = \frac{\beta+\frac{\sigma_{res,x}^2}{\varepsilon}}{\sqrt{\left(1+\sigma_{res,x}^2\frac{\gamma}{\varepsilon}\right)\left(1+\sigma_{res,y}^2\frac{\beta}{\varepsilon}\right)-\left(\sigma_{res,x}\sigma_{res,y}\frac{\alpha}{\varepsilon}\right)^2}} = \left(\beta+\frac{\sigma_{res,x}^2}{\varepsilon}\right)\left(\frac{\varepsilon}{\varepsilon''}\right) \tag{6.14}$$

$$\gamma'' = \frac{\gamma+\frac{\sigma_{res,y}^2}{\varepsilon}}{\sqrt{\left(1+\sigma_{res,x}^2\frac{\gamma}{\varepsilon}\right)\left(1+\sigma_{res,y}^2\frac{\beta}{\varepsilon}\right)-\left(\sigma_{res,x}\sigma_{res,y}\frac{\alpha}{\varepsilon}\right)^2}} = \left(\gamma+\frac{\sigma_{res,y}^2}{\varepsilon}\right)\left(\frac{\varepsilon}{\varepsilon''}\right) \tag{6.15}$$

$$\tag{6.16}$$

It is easy to verify that $\beta''\gamma'' - \alpha''^2 = 1$ is still valid as required.

$$\varepsilon = \varepsilon'\sqrt{1-\sigma_{res,y}^2\frac{\beta'}{\varepsilon'}} \tag{6.17}$$

$$\alpha = \frac{\alpha'}{\sqrt{1-\sigma_{res,y}^2\frac{\beta'}{\varepsilon'}}} \tag{6.18}$$

$$\beta = \frac{\beta'}{\sqrt{1-\sigma_{res,y}^2\frac{\beta'}{\varepsilon'}}} \tag{6.19}$$

$$\gamma = \frac{\gamma'-\frac{\sigma_{res,y}^2}{\varepsilon'}}{\sqrt{1-\sigma_{res,y}^2\frac{\beta'}{\varepsilon'}}} \tag{6.20}$$

To fulfill the backward transformation between the primed and non-primed parametrisation

$$\sqrt{1+\sigma_{res,y}^2\frac{\beta}{\varepsilon}}\cdot\sqrt{1-\sigma_{res,y}^2\frac{\beta'}{\varepsilon'}} \overset{!}{=} 1 \tag{6.21}$$

is strictly required and can be verified easily.

$$\varepsilon = \varepsilon''\sqrt{\left(1-\sigma^2_{res,x}\frac{\gamma''}{\varepsilon''}\right)\left(1-\sigma^2_{res,y}\frac{\beta''}{\varepsilon''}\right)-\left(\sigma_{res,x}\sigma_{res,y}\frac{\alpha''}{\varepsilon''}\right)^2} \tag{6.22}$$

$$\alpha = \alpha''\left(\frac{\varepsilon''}{\varepsilon}\right) = \frac{\alpha''}{\sqrt{\left(1-\sigma^2_{res,x}\frac{\gamma''}{\varepsilon''}\right)\left(1-\sigma^2_{res,y}\frac{\beta''}{\varepsilon''}\right)-\left(\sigma_{res,x}\sigma_{res,y}\frac{\alpha''}{\varepsilon''}\right)^2}} \tag{6.23}$$

$$\beta = \left(\beta''-\frac{\sigma^2_{res,x}}{\varepsilon''}\right)\left(\frac{\varepsilon''}{\varepsilon}\right) = \frac{\beta''-\frac{\sigma^2_{res,x}}{\varepsilon''}}{\sqrt{\left(1-\sigma^2_{res,x}\frac{\gamma''}{\varepsilon''}\right)\left(1-\sigma^2_{res,y}\frac{\beta''}{\varepsilon''}\right)-\left(\sigma_{res,x}\sigma_{res,y}\frac{\alpha''}{\varepsilon''}\right)^2}} \tag{6.24}$$

$$\gamma = \left(\gamma''-\frac{\sigma^2_{res,y}}{\varepsilon''}\right)\left(\frac{\varepsilon''}{\varepsilon}\right) = \frac{\gamma''-\frac{\sigma^2_{res,y}}{\varepsilon''}}{\sqrt{\left(1-\sigma^2_{res,x}\frac{\gamma''}{\varepsilon''}\right)\left(1-\sigma^2_{res,y}\frac{\beta''}{\varepsilon''}\right)-\left(\sigma_{res,x}\sigma_{res,y}\frac{\alpha''}{\varepsilon''}\right)^2}} \tag{6.25}$$

$$\tag{6.26}$$

$$\begin{aligned}&\sqrt{\left(1+\sigma^2_{res,x}\frac{\gamma}{\varepsilon}\right)\left(1+\sigma^2_{res,y}\frac{\beta}{\varepsilon}\right)-\left(\sigma_{res,x}\sigma_{res,y}\frac{\alpha}{\varepsilon}\right)^2}\\ &\qquad\times\sqrt{\left(1-\sigma^2_{res,x}\frac{\gamma''}{\varepsilon''}\right)\left(1-\sigma^2_{res,y}\frac{\beta''}{\varepsilon''}\right)-\left(\sigma_{res,x}\sigma_{res,y}\frac{\alpha''}{\varepsilon''}\right)^2} \overset{!}{=} 1\end{aligned} \tag{6.27}$$

Chapter 7

Systematic Effects on Resolution

TODO.ELEMENTS.WITH.ENTRANCE.ORDER. A reliable measurement setup requires reasonable access to sources of intrinsic uncertainties and systematic error contributions to get a quantified measure of the achievable resolution. While this holds true for all experimental setups and measurement instrumentation in general, it is most important if at least one component of the setup has a maximum resolution performance close to the minimum resolution required. This is not necessarily based on bad design decisions, but often represents a challenge due to available hardware.

To estimate the required resolution of the momentum/energy measurement via time-of-flight (TOF), it is helpful to take a closer look at the expected beam parameters in question. Longitudinal phase space distributions downstream from the *High Current Injector* (HSI, see Fig. 2.9) right after the first stripper section (Fig. 3.3) are expected to have an RMS energy spread σ_E of about 1% with respect to the mean particle energy $\langle E \rangle$ of about 1.4 AMeV [74]. Since the setup is based on timing measurements, the accuracy depends on the timing performance of detectors and readout electronics. A particle of mean energy $\langle E \rangle$ compared to a particle with energy of $\langle E \rangle + \sigma_E$ has an arrival time delay σ_t of

$$\sigma_t = t_{\langle E \rangle} - t_{\langle E \rangle + \sigma_E} \overset{\frac{\sigma_E}{\langle E \rangle} \ll 1}{\approx} \frac{\sigma_E}{\langle E \rangle} \cdot \frac{l_{tof}}{2c \langle \beta \rangle} . \qquad \text{(see Sec. 4.1.5)} \qquad (7.1)$$

Due to the limited space at the UNILAC site, the detector separation for the TOF measurement is about 800 mm which results in $\sigma_t \approx 240$ ps. Figure 7.1 shows the relation of σ_t with respect to the drift length l_{tof} under the conditions stated above. Assuming a Gaussian energy distribution and a Gaussian function of the system response, an estimate on the impact of a resolution on the measurement can be made. In the following, the real width

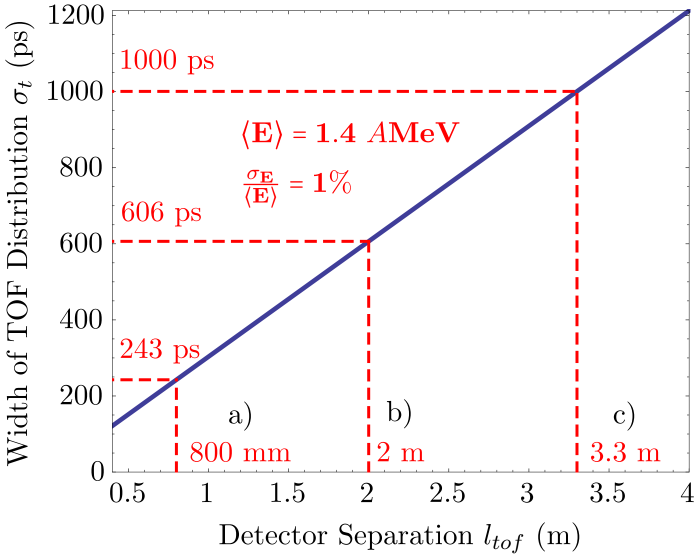

Fig. 7.1: The RMS difference in TOF σ_t between a particle of mean energy $\langle E\rangle = 1.4$ *A*MeV and a particle with an energy of $\langle E\rangle + \sigma_E$ is plotted versus the drift length l_{tof}. A longitudinal energy distribution with an RMS energy spread of 1% is assumed. The dashed lines mark the current TOF detector separation of a) 800 mm, a hypothetical drift length of b) 2 m with σ_t^{2m} and a drift length of c) about 3.3 m which would correspond to a much more relaxed $\sigma_t^{3.3m}$ of 1 ns.

of the arrival time distribution is denoted by σ_t, whereas the width of the system response function is denoted by σ_{res}[1]. Consequently, the measured width σ_m is given by

$$\sigma_m^2 = \sigma_t^2 + \sigma_{res}^2 , \tag{7.2}$$

using the fact that convolving of Gaussian distributions effectively means to add their variances. A relative error f_{err} can be defined as

$$f_{err} = \frac{\Delta\sigma}{\sigma_t} = \frac{\sigma_m - \sigma_t}{\sigma_t} = \frac{\sqrt{\sigma_t^2 + \sigma_{res}^2} - \sigma_t}{\sigma_t} . \tag{7.3}$$

Generally, the allowed width of the system response σ_{res}, that corresponds to a certain relative error f_{err}, is given by

$$\frac{\sigma_{res}}{\sigma_t} = \sqrt{(f_{err} + 1)^2 - 1} \tag{7.4}$$

and plotted in Fig. 7.2 as the fraction of σ_t. For the present experimental setup, a width of $\sigma_{res}^{1\%} \leq 34$ ps, representing the systems response, is required to reproduce the expected

---

[1] The subscript *res* and its meaning is kept in the following. It should be strengthened that it relates to the system *response* and **not** to the *resolution*.

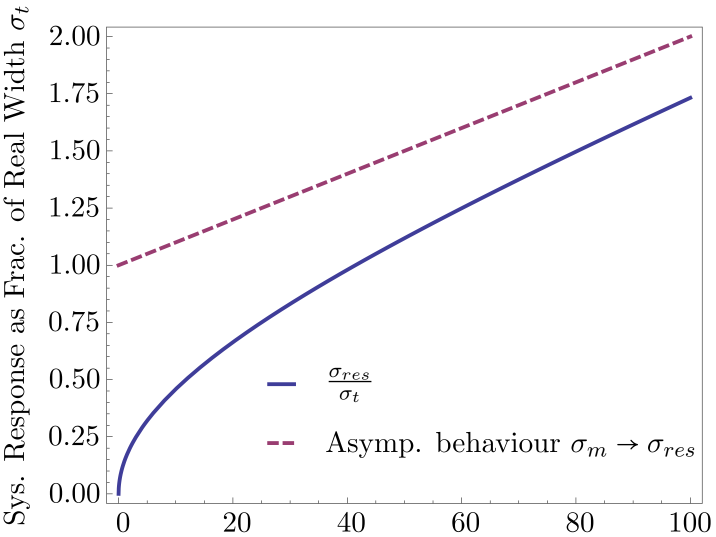

Fig. 7.2: The continuous line shows the maximum width allowed for the system response σ_{res} to provide a relative error f_{err}, generalised by the fraction with respect to the real width σ_t. For increasing f_{err} the actual energy distribution becomes irrelevant and the measurement only represents the response of the detector and readout electronics, such that $\sigma_m = \sigma_{res}$, given by the dashed asymptote.

energy spread ΔE in a direct measurement within a relative resolution f_{err} of 1%. On the other hand, aiming for an accuracy of 10% would allow a system response of up to $\sigma_{res}^{10\%} \approx 110$ ps. It should be noted that this considers only the precision of how well the second momenta are represented by the measurement. Any details of the distribution of smaller scale than σ_{res} cannot be resolved.

The measurement setup is an intercepting device, which means by definition that major interaction between the particle distribution and the setup occurs. Since a significant amount of the particle-device interaction is contributed by the attenuation mechanism, dissipative effects are present prior to the actual measurement process between the two detectors. Hence, meeting the time resolution of the detector and readout electronics alone is not sufficient to provide a precise measurement. Moreover, all effects, i. e. interactions on the beam and thus parameters of interest must be small compared to typical values of beam parameters. This includes the accelerator setup necessary for the measurement procedure.

For the setup, we can coarsely differentiate between two classes of error contributions that may lead to distortions of the original (unaffected) phase space distribution:

- Effects on real physical phase space distribution: $\{\Delta E_{diss,i}\}$
- Timing precision of electronic and detector components: $\{\Delta t_i\}$

The effective uncertainty is given by means of RMS timing uncertainties Δt_i, where possible, originating from different components of the measurement setup which in turn can be expressed as resulting uncertainties in energy observation ΔE_i in the classical limit

$$\Delta E_i \approx \frac{\mathrm{d}}{\mathrm{d}t} E(t)\bigg|_{t=t_{\langle E\rangle}} \cdot \Delta t_i = -2\,\frac{E(t_{\langle E\rangle})}{t_{\langle E\rangle}} \Delta t_i = -2\,\frac{\langle E\rangle}{t_{\langle E\rangle}} \Delta t_i\,. \tag{7.5}$$

Additionally, direct energy contributions of uncertainties $\Delta E_{diss,i}$ are imposed by dissipative elements, e. g. as given by the energy spread introduced by both foils. Consequently, the net relative uncertainty of a given set of sufficient uncorrelated contributions[2] $\{\Delta E_{diss,i}\}$ and $\{\Delta t_i\}$ is calculated by

$$\frac{\Delta E}{\langle E\rangle} \approx \sqrt{\left(\frac{2}{t_{\langle E\rangle}}\right)^2 \sum_{\{\Delta t_i\}} (\Delta t_i)^2 + \frac{1}{\langle E\rangle^2} \sum_{\{\Delta E_{diss,i}\}} (\Delta E_{diss,i})^2}\,. \tag{7.6}$$

Direct measurement of the net resolution would require a well-known reference beam and sufficient small longitudinal energy spread. A perfect reference would be a quasi-monochromatic beam with an energy spread of $\Delta E \ll 1\%\,\langle E\rangle$, which provides direct access to the response function and, thus, represents a measure of the net resolution. For the present situation this option is not available. An α-source is not a feasible approach to simulate quasi-monochromatic beam conditions due to the small solid angle of the setup.

In the following, components of the setup will be investigated in detail, focusing on a measure of uncertainty contribution. Finally, the total uncertainty will be compared to the measurement characteristics.

7.1 Tantalum Foil

Single-particle detection is accomplished by deflecting primary particles into the detector acceptance. This is done by Coulomb scattering at a thin tantalum foil of 210 µg/cm^2, which corresponds to a thickness of $\approx$ 126 nm, mounted behind a cylindrical aperture with a diameter of 2 mm (see Fig. A.1). Subsequently, scattered particles are selected by a collimator under a small solid angle which provides an attenuation factor on the order of 10^8. For a detailed description, see Sec. 3.4.

This section covers several aspects concerning the impact of the tantalum foil on the measurement precision. It includes the discussion of energy straggling of heavy-ion projectiles in perfect foils and the more realistic assumption of variation of thickness TODO.EFF.CHARGE.EXCHANGE. The section closes with a discussion of the possible impact of the transversal phase-space distribution on the total scattering angle and, thus, different momentum transfers to the target nucleus is covered.

---

[2] Slight but non-dominating correlated effects are for example the separation jitter due to the tilted aluminium foil inside the MCP module (Sec. 7.3.4) and the signal propagation time jitter on the diamond electrode (Sec. 7.4.2.2).

7.1.1 Electronic Stopping and Straggling

In addition to the specific mean energy shift of the incident beam particles when passing through the tantalum foil, the statistical transfer of momentum to the electrons introduces a broadening of the energy distribution. Electronic stopping in matter and the resulting *mean* energy loss can be described by the well known Bethe-Bloch formula [75]

$$-\frac{\mathrm{d}E}{\mathrm{d}x} = \frac{4\pi n z^2}{m_e c^2 \beta^2} \left(\frac{e^2}{4\pi\epsilon_0} \right)^2 \left[\ln\left(\frac{2\, m_e\, c^2\, \beta^2}{I\,(1-\beta^2)} \right) - \beta^2 \right]. \tag{7.7}$$

The specific parameters are the *projectile charge* z, the *electron number density* n of the target medium and the *mean ionisation potential* I. The mean ionisation potential I for a certain target can be approximated [48] by

$$I \approx (11 \pm 3)\, Z \text{ eV}, \tag{7.8}$$

where Z is the target atomic charge number.

The *mean* energy shift is not a critical issue for the determination of the phase space and will be covered in Sec. 7.7.1. Still, as a statistical process, fluctuations occur usually referenced as *(energy) straggling*, sometimes called *collisional straggling*, which is not described by the Bethe-Bloch equation. Such dissipative contributions affect the real phase and contribute a component $\Delta E_{diss,i}$ to Eq. (7.6). Quantitative estimations of collisional straggling can be received by Monte-Carlo simulation programs such as SRIM [49].

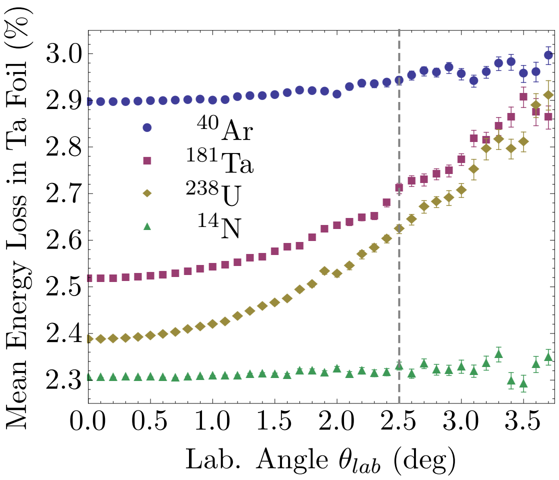

Fig. 7.3: SRIM: Total energy loss of transmitted particles after transmission through the Ta foil, given in % with respect to the mean energy $\langle E \rangle$ as a function of the laboratory angle.

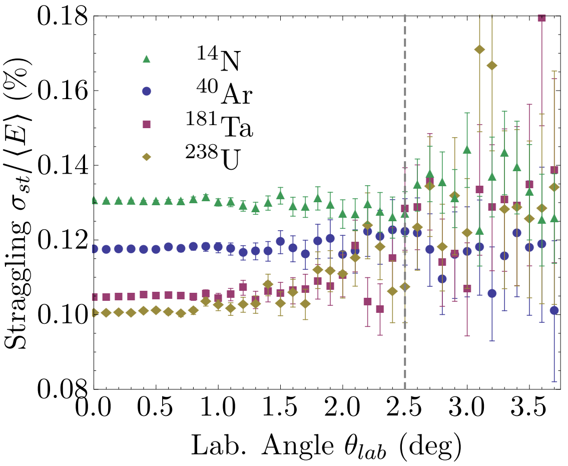

Fig. 7.4: SRIM: Energy broadening RMS after transmission through the Ta foil. Values are given in % with respect to the mean energy $\langle E \rangle$. Error bars are connected to the highly damped statistics, see text.

A SRIM calculation for nitrogen, argon, tantalum and uranium projectiles with 10^7 particles each has been carried out to estimate the dissipative straggling contribution. The projectiles were transmitted through a tantalum foil of 210 µg/cm^2 which corresponds approximately to a thickness of 126 nm or roughly about 1300 atomic layers. The incident angle of the projectiles was set to 1.25° to match the real configuration. Only those particles were taken into account which have been scattered into the given solid angle of 7.7×10^{-6} sr, sampled on scattering angles θ from 0° to 3.7° in the laboratory frame. A laboratory angle of $\theta = 2.5°$ represents the configuration of the measurement setup. Figure 7.3 shows the energy loss in % with respect to the mean energy $\langle E \rangle$ for different angles of particle emission. The dashed vertical line marks the measurement setup with an emission angle of 2.5°. The stopping power $-\frac{\mathrm{d}E}{\mathrm{d}x}$, i. e. the energy loss per unit distance, for uranium is larger than that of argon and tantalum due to its higher charge z. Nevertheless, the overall energy loss is smaller since the total energy of 333.2 MeV for uranium is much higher in comparison to that of argon with 56 MeV. As seen from the data, the relative mean energy loss is estimated in the range between 2.3% and 3%. Apart from the statistical error, represented by the error bars, the semi-empirical SRIM code, as of 2010, claims to provide an overall model based accuracy of about 5% (1-sigma) concerning the calculation of the stopping power [76].

For an estimate on the straggling contribution, it is useful to extract the transmitted particle energy RMS value from the SRIM output. Fig. 7.4 shows the RMS values of nitrogen, argon, tantalum and uranium projectiles with respect to the mean energy in % versus the emission angle θ. The configuration of the setup is, again, marked by the dashed vertical line. Since the particle data is evaluated by considering the geometry of the setup, and thus a very small solid angle, the statistical error increases significantly with $\theta > 1.5°$ For the statistic error contribution, the number of events N is considered via $\frac{\sigma_{st}}{\langle E \rangle} / \sqrt{2(N-1)}$, according to the statistical uncertainty of the classical estimator of the standard deviation [61] (p. 133). The spread between the four ion species used in the simulation are confined within a relative deviation of 30%. If the obtained values are related to the *expected* RMS energy spread of $1\% \langle E \rangle$, it seems legitimate to consider the straggling contribution of about 13%. The histograms of uranium and argon for an angle of $\theta = 1°$ are shown in Fig. 7.5.

It should be noted that the simulation requires a very large number of primary particles since the fraction of particles scattered into θ and solid angle $\Delta\omega = 7.7 \times 10^{-6}$ sr is connected with a very small yield factor as shown in Fig. 3.15 and 3.17. As a result, significant fluctuations for the RMS value of the electronic stopping occur above $\approx 1.5°$ net emission angle where statistics is low. At a scattering angle of 2.5°, at the given solid angle $\Delta\omega$, only about 150 particles are available of the initial 10^7 particles. Hence, in favour for the better statistics, the data of Fig. 7.5 shows the energy distributions for a scattering angle $\theta = 1°$.

7.1.2 Inhomogeneity in Thickness and Texture

The tantalum foil of (210±10) µg/cm^2 thickness installed in the collimator setup has been manufactured at the GSI target laboratory by a rolling process. This thickness is considered the lower limit which can be achieved by the process without disrupting the material. Rolled foils posses a much higher durability at beam radiation than those produced by evaporation onto a substrate. On the other hand, the homogeneity in thickness is lower in case of rolled foils. The determination of the thickness variation in thickness or roughness of thin films proves to be difficult and is still an ongoing topic of research.

A variation in thickness implies a statistical variation in mean energy shift of the particles

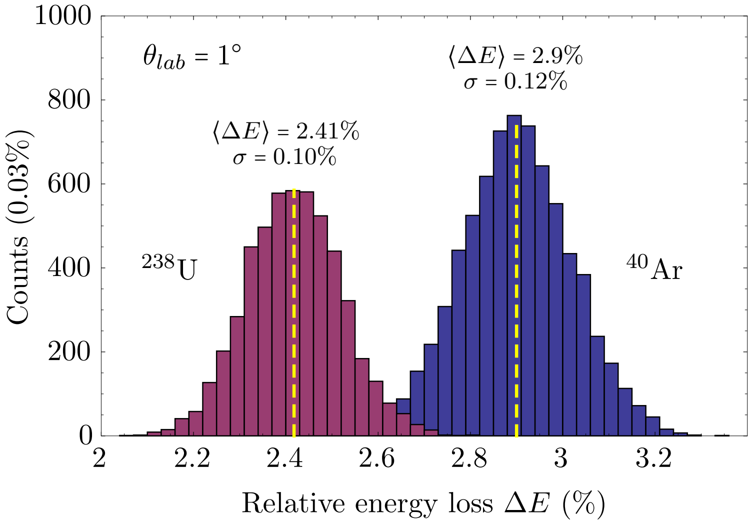

Fig. 7.5: Energy distribution of exemplary ^{40}Ar and ^{238}U ions after crossing of the tantalum foil at a net laboratory angle of $\theta = 1°$ and a solid angle of $\Delta\omega \approx 7.7 \times 10^{-6}$. The data sets have been calculated using SRIM with an input energy of 1.4 *A*MeV.

transmitted through the Ta foil on top of the collisional straggling contribution. When the mean energy loss $\langle \Delta E \rangle$ in a thin target of thickness $\langle x \rangle$ is small compared to the total energy $\langle E \rangle$, the energy loss is approximately given by Eq. (7.7) with

$$\langle \Delta E \rangle \approx \frac{\mathrm{d}E}{\mathrm{d}x} \langle x \rangle. \tag{7.9}$$

Albeit difficult to measure, the RMS variation in foil thickness σ_x^h leads to an energy spread contribution[3] due to the different distances the particles travel inside the foil material and can be approximated by

$$\sigma_E^h \approx \frac{\mathrm{d}E}{\mathrm{d}x} \sigma_x^h. \tag{7.10}$$

Since the expected RMS energy width of the beam is about 1%, $\sigma_E^h / \langle E \rangle \ll 10^{-2}$ should be fulfilled to warrant a meaningful measurement of the longitudinal energy distribution.

Also the texture, i. e. the nature of the inhomogeneities, mainly the granularity of the pattern, plays an important role. Issues concerning the inhomogeneities have been raised for example in [77], where thin carbon foils were investigated for the characteristic electron capture using U^{91+} ions at 46 *A*MeV. The conclusion has been that for all tested manufacturers characteristic differences exist. Measured yields became significantly higher than predicted towards thinner foils and were attributed to their texture and inhomogeneity. This is supported by experiment runs with two foils stacked, which matched a single thicker foil of the same manufacture. The stacked setup provided significantly higher electron capture yields

---

[3] Superscript "*h*" denotes the contribution due to the inhomogeneity of the foil.

compared to the stacked configuration of two thinner foils.

An indirect method to access the inhomogeneities of the foil for Gaussian-like straggling profiles was suggested by Besenbacher et al. [78]. The authors assume the total straggling Ω to be described by the variances given by the *true* collisional straggling Ω_{ls} for a perfectly homogeneous material of constant width and a term Ω_h that depends on the texture and variation in thickness

$$\Omega^2 = \Omega_{ls}^2 + \Omega_h^2 \,. \tag{7.11}$$

The contribution from the variation in thickness Eq. (7.10) varies to good approximation with the nuclear charge squared of the projectile accounted to the stopping power. Hence, a set of measurements with different projectile energies and ion species provides a way to isolate Ω_h^2. A similar method has been used in [79] where, amongst others, a rolled tantalum foil of 367 µg/cm^2 thickness was tested for homogeneity. According to this data, the inhomogeneity is large with a relative deviation in thickness of $\sigma_x^h / \langle x \rangle \approx 0.34$. This supports the tendency given in experimental data presented by Besenbacher et al. [78] and would cause a major effect on the energy resolution required for the present setup at hand. A relative mean energy loss $\langle \Delta E \rangle / \langle E \rangle \approx 3\,\%$ can be assumed, as given in Fig. 7.3. Together with Eq. 7.9 and 7.10

$$\frac{\sigma_E^h}{\langle E \rangle} \approx \frac{\sigma_x^h}{\langle x \rangle} \frac{\langle \Delta E \rangle}{\langle E \rangle} \,, \tag{7.12}$$

the mean energy loss and relative deviation in thickness gives rise to a dissipative relative energy contribution $\sigma_E^h / \langle E \rangle \approx 1\,\%$.

Nevertheless, the impact of foil inhomogeneities on the performance of the setup presented in this work is an open question. The circular apertures of the collimator configuration close behind the tantalum foil are small with diameters of 0.5 mm (see Sec. 3.4) and are assumed to partly suppress the contributions of the thickness variation. While the same argumentation is also provided in [80] this effect is not considered negligible and still has to be studied in detail.

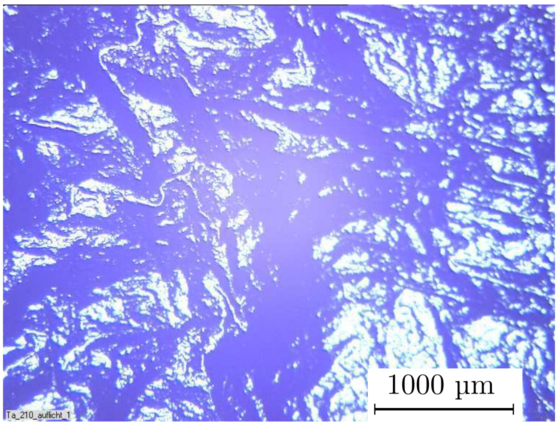

Fig. 7.6: Ta 210 µg/cm^2, rolled Scale 1000 µm, reflected light.

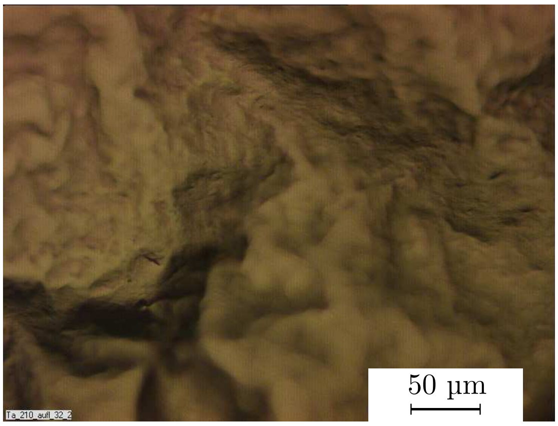

Fig. 7.7: Ta 210 µg/cm^2, rolled Scale 50 µm, reflected light.

Figures 7.6-7.9 show a set of images (optical microscopy) of a *new* tantalum foil from the same delivery and the same rolling pass as the one currently installed. In Fig. 7.6 the tantalum foil is photographed using reflected light (scale 1000 µm). The surface features clear wrinkling which is unavoidable in the manufacturing process at the given thickness. Any stress on the material would lead to instant destruction. Thus, the material is fixed on the mount without tension. Obviously the wrinkling structure is present on that scale and affects the energy spread by the *effective thickness* which scales approximately with $(\cos\theta_n)^{-1}$, where θ_n is the angle with respect to the normal of the foil at the impact location. Figure 7.7 shows the same foil on a smaller scale (50 µm) also using reflected light. The different angles imposed by the wrinkles are obvious from the structural shadows. By using transmitted light it is possible to get a qualitative picture of the thickness variation. A typical area of the tantalum foil has been photographed accordingly and is shown in Fig. 7.8 at a scale of 1000 µm.

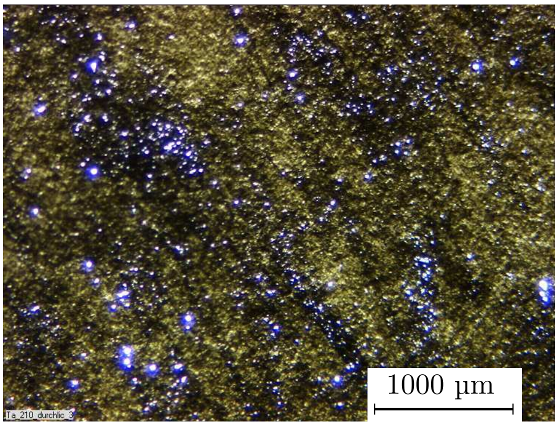

Fig. 7.8: Ta 210 µg/cm^2, rolled
Scale 1000 µm, transmitted light.

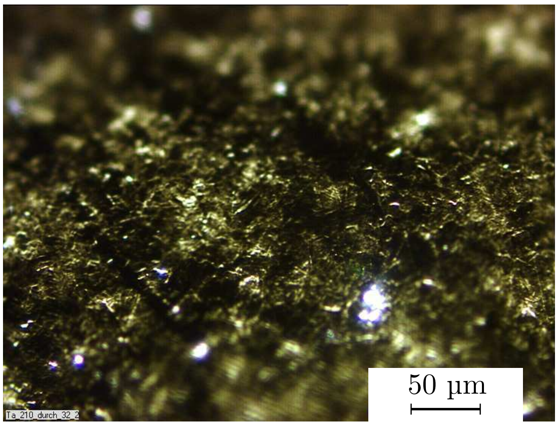

Fig. 7.9: Ta 210 µg/cm^2, rolled
Scale 50 µm, transmitted light.

An inherent texture and variation in homogeneity is evident. Even a significant amount of holes appear to be scattered over the surface in clusters where light is transmitted with a sharp high contrast. This leads to the assumption that these regions actually are real holes or at least singular areas covered by much less material than the average thickness suggests. Due to diffraction, holes are represented by their airy disc and are actually smaller than they appear on the photograph. Nevertheless, considering the circular collimator apertures of 0.5 mm it is to apprehend that the thickness of the foil varies within the location of the aperture. A higher magnification of the tantalum foil is shown in Fig. 7.9.

7.1.3 Dependence of Energy Transfer on Transverse Parameters

In Section 3.4.2, the momentum transfer from a projectile to the target nucleus depending on the net scattering angle θ has been determined using classical Coulomb Scattering. This assumes elastic scattering on the target nuclei only. A corresponding SRIM calculation, with the electronic stopping subtracted, indicates a good agreement within better than 5%. Figure 3.16 and 3.18, respectively, show the net angle dependency of the momentum transfer to the target nucleus.

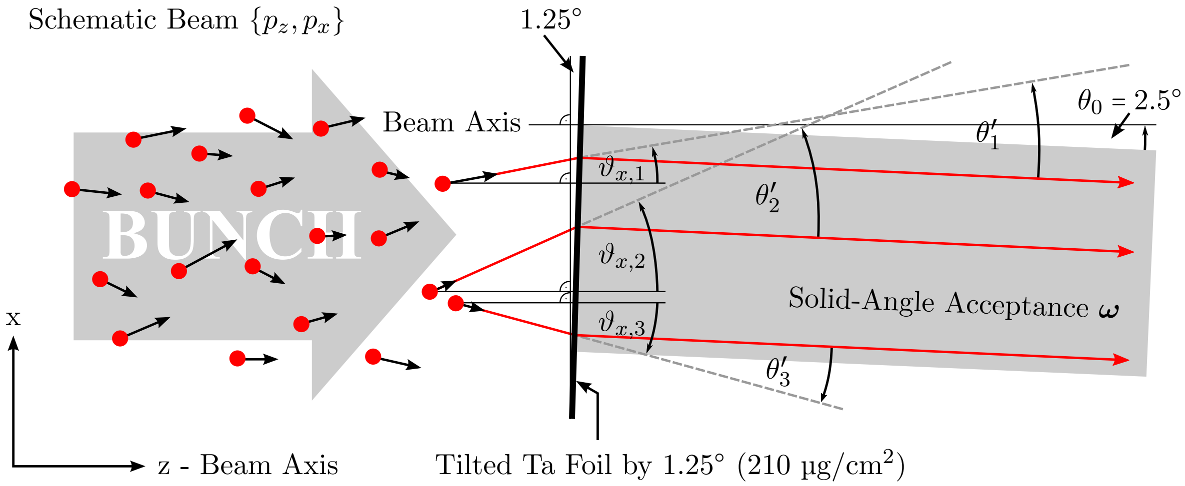

Fig. 7.10: Beam particles are schematically depicted by red dots with momentum vectors in the x-z plane only for simplicity. The resulting net scattering angle θ'_i, required for the particle to pass the collimator, depends on the transverse angle $\vartheta_{x,i}$. Consequently, an energy spread is imposed by the energy transfer to the target nucleus which depends on the net scattering angle θ'_i.

So far, the incoming bunch is approximately treated as a strictly parallel stream of particles, neglecting the transverse degree of freedom. More precisely, the net scattering angle θ' required for a certain particle to be scattered into the solid-angle acceptance ω of the collimator configuration depends on the transverse momentum as they contribute to a divergence angle $\{\vartheta_x, \vartheta_y\}$. On the other hand, the energy transfer to the target nuclei depends on the net scattering angle as given in Eq. (3.9). Figure 7.10 schematically depicts the dependence of the net scattering angle on the transverse momentum distribution, projected onto the x-z plane for simplicity. The particles arrive from the left and approach the tilted foil with different momenta marked by the arrows. Only particles scattered into the solid-angle acceptance, the grey area behind the foil, will be registered in the measurement setup. A beam suffers an additional longitudinal energy spread by the transverse momentum distribution and the geometrical constraint of the collimator acceptance. The different effective angles θ'_i required for particle i to scatter into the collimator acceptance are connected with a specific energy transfer to the target nucleus. If, for simplicity, we restrict ourselves to the x-z plane at first, the resulting net angle is given by $\theta' = \theta_{2.5°} + \vartheta_x$, where the transverse divergence angle ϑ_x depends on the transverse and longitudinal momenta by $\vartheta_x = \mathrm{atan}(p_x/p_z)$ of the particles. Including the vertical degree of freedom y, the net angle θ' to fulfill the condition of matching the acceptance of the setup is a function of ϑ_x and ϑ_y, while the undisturbed angle is denoted by $\theta_0 (= 2.5°)$.

The net scattering angle $\theta'(\vartheta_x, \vartheta_y; \theta_0)$ can be derived from the unit vectors along the orientation of the solid-angle acceptance $\vec{e}_0$, given by θ_0, and the transverse degrees of freedom

$\vec{e}_{x'}(\vartheta_x)$ and $\vec{e}_{x'}(\vartheta_x)$, respectively

$$\vec{e}_0 = \begin{pmatrix} -\sin\theta_0 \\ 0 \\ \cos\theta_0 \end{pmatrix}, \quad \vec{e}_{x'}(\vartheta_x) = \begin{pmatrix} \sin\vartheta_x \\ 0 \\ \cos\vartheta_x \end{pmatrix}, \quad \vec{e}_{y'}(\vartheta_y) = \begin{pmatrix} 0 \\ \sin\vartheta_y \\ \cos\vartheta_y \end{pmatrix}. \tag{7.13}$$

The net angle θ' is therefore given by the scalar product

$$\theta'(\vartheta_x, \vartheta_y; \theta_0) = \arccos\left(\frac{\vec{e}_0 \cdot (\vec{e}_{x'} + \vec{e}_{y'})}{|\vec{e}_0| \cdot |\vec{e}_{x'} + \vec{e}_{y'}|} \right) \tag{7.14}$$

and thus

$$\theta'(\vartheta_x, \vartheta_y; \theta_0) = \arccos\left(\frac{\cos\theta_0\,(\cos\vartheta_x + \cos\vartheta_y) - \sin\theta_0\,\sin\vartheta_x}{\sqrt{2\,(1 + \cos\vartheta_x\,\cos\vartheta_y)}} \right). \tag{7.15}$$

To evaluate the contribution of the transverse angle distribution to the TOF uncertainty, the bunch is considered centred on the beam axis. Due to the small aperture of the collimator configuration, only a small region around $x \approx 0$ and $y \approx 0$ is selected by the setup. This allows the angle distribution $\rho_{\vartheta_x,\vartheta_y}(x, y, \vartheta_x, \vartheta_y)$ to be written as a product $\rho_{\vartheta_x}(\vartheta_x) \cdot \rho_{\vartheta_y}(\vartheta_y)$. The corresponding response function is given by

$$\begin{aligned} R(\Delta E; \theta_0, \omega) = \int_{-\infty}^{+\infty} \mathrm{d}\vartheta_x\, \rho_{\vartheta_x}(\vartheta_x) \int_{-\infty}^{+\infty} \mathrm{d}\vartheta_y\, \rho_{\vartheta_y}(\vartheta_y) \\ \cdot P_{sc}\left(\theta'(\Delta E), \omega\right)\, \delta(\theta'(\Delta E) - \theta'(\vartheta_x, \vartheta_y; \theta_0)). \end{aligned} \tag{7.16}$$

Integration is performed including both transverse angle distributions, ρ_{ϑ_x} and $\rho_{\vartheta y}$, thereby only taking into account net angles that contribute to a specific energy transfer ΔE. This selection is provided by the Dirac delta function and further weighted by the probability $P_{sc}\left(\theta'(\Delta E), \omega\right)$ of θ' to occur as given in Eq. (3.3). Alternatively, the effect can be calculated by a Monte-Carlo simulation. The angle distributions $\rho_{\vartheta_x}(x)$ and $\rho_{\vartheta_y}(y)$ are parameterised by Gaussian distributions, and a set of angles $\{\vartheta_x, \vartheta_y\}$ is sampled accordingly and weighted by the probability $P_{sc}\left(\theta'(\Delta E), \omega\right)$. Evaluating the standard deviation of the corresponding histogram allows to extract the system response.

High-current phase space distributions of Ar^{10+} and U^{27+} are plotted in Fig. 7.11. These 6-dimensional phase-space distributions are considered realistic configurations at the TOF setup location by the GSI injector division [81]. They are used as boundary conditions for tracking simulations through the post-stripper section. It is therefore considered the best reference configuration for the transverse plane which is of importance in this case.

For completeness, it should be noted that the longitudinal phase-space configurations shown in Fig. 7.11 have been constructed by measurements of the longitudinal phase space using the TOF setup presented in this work. A detailed explanation of the procedure is given in [82]. The bunch length as well as the momentum spread has been adopted from the TOF measurement while the correlation α was empirically set to the expected values around

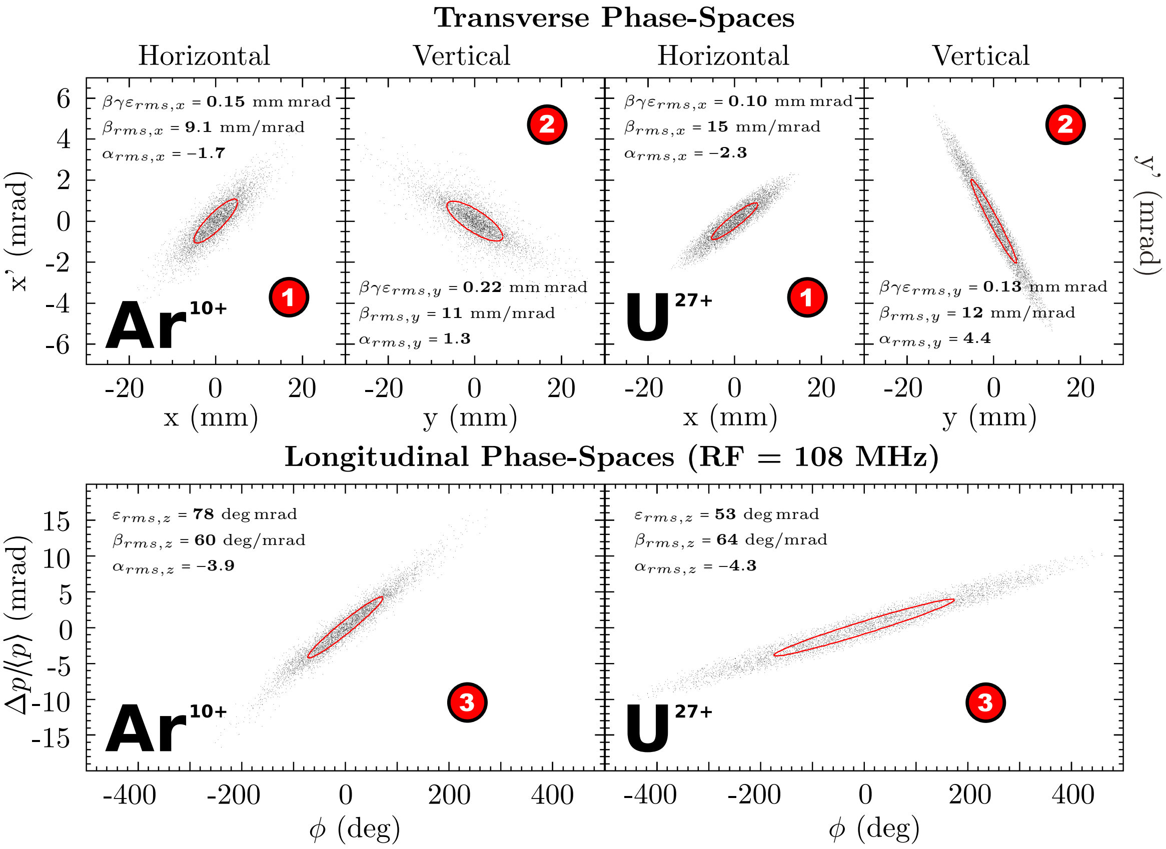

Fig. 7.11: 6-dimensional phase space start distributions for Ar^{10+} and U^{27+} used for high current tracking simulation along the UNILAC post-stripper (L. Groening [81]). The distributions represent the *expected* situation at the location of the TOF setup. For a detailed explanation of the procedure which yields the start distributions see [82]. **Left**: Ar^{10+} phase space at 7.1 mA and a gas pressure inside the stripper section of about 2 bar. **Right**: Corresponding U^{27+} phase space distribution. For both ion species, ① and ② depict the transverse horizontal and vertical phase-space distributions at the setup location, whereas ③ shows the longitudinal degree of freedom. Both longitudinal phase-space distribution represent divergent beams. The horizontal orientation is flipped if the arrival time is used instead of the phase (see Sec 2.2). Worth noting are both absolute longitudinal correlation values of $\alpha \approx 4$.

$|\alpha| \approx 4$. Hence, the emittance is consequently calculated as

$$\varepsilon = \sqrt{\frac{\sigma_p \sigma_\phi}{\alpha^2 + 1}}. \tag{7.17}$$

A simulation has been carried out with the Ar^{10+} and U^{27+} phase-space distributions with the relevant data listed in Tab. 7.1. The relative error $\frac{\sigma_{tr}}{\langle E \rangle}$ is less than 2×10^{-5}. In relation to the expected energy width $\sigma_E^{1\%}$, listed as $\frac{\sigma_{tr}}{\sigma_E^{1\%}}$ in Tab. 7.1, this clearly shows that transverse momentum components have a negligible effect on the total resolution.

Tab. 7.1: Simulated effect of transverse momentum on energy resolution.

	$\sigma_{\vartheta x}$ (mrad)	$\sigma_{\vartheta y}$ (mrad)	$\langle\Delta E\rangle / \langle E\rangle$	$\sigma_{tr} / \langle E\rangle$	$\sigma_{tr} / \sigma_E^{1\%}$ (%)
Ar^{10+}	0.55	0.60	4.2×10^{-4}	5.3×10^{-6}	5.3×10^{-2}
U^{27+}	0.35	0.45	2.5×10^{-3}	2×10^{-5}	0.2

7.2 Energy Spread by Finite Solid Angle

The finite solid angle of the collimator setup imposes an energy spread σ_E^θ as the transferred energy depends on the net scattering angle θ. The variation of Eq. (3.9) with respect to the net scattering angle θ in the laboratory frame is given by

$$\sigma_E^\theta = \frac{\mathrm{d}E}{\mathrm{d}\Theta} \frac{\mathrm{d}\Theta}{\mathrm{d}\theta} \sigma_\theta \tag{7.18}$$

with

$$\frac{\mathrm{d}E}{\mathrm{d}\Theta} = -8\, E_0 \sin\Theta \frac{A_{red}}{A_p + A_t} \tag{7.19}$$

and the reciprocal derivative of Eq. (3.6)

$$\frac{\mathrm{d}\Theta}{\mathrm{d}\theta} = \left(\frac{\mathrm{d}\theta}{\mathrm{d}\Theta}\right)^{-1} = \frac{1 + \left(\frac{A_p}{A_t}\right)^2 + 2\,\frac{A_p}{A_t}\cos\Theta}{\frac{A_p}{A_t}\cos\Theta + 1}. \tag{7.20}$$

Hence, the imposed energy spread is given by the knowledge of σ_θ. Assuming, in good approximation, a homogeneous probability density within the very small solid angle ω, allows the variance of the net scattering angle σ_θ^2 to be extracted

$$\sigma_\theta^2 = \left\langle \Delta\theta^2 \right\rangle = \frac{2}{\pi r_{ap}^2 d_{sep}^2} \int_{-r_{ap}}^{r_{ap}} \mathrm{d}r\, r^2 \sqrt{r_{ap}^2 - r^2} = \frac{r_{ap}^2}{4 d_{sep}^2} \approx \frac{\omega}{4\pi}\,. \tag{7.21}$$

Another simplification has been made by neglecting the azimuthal component, which is suppressed by more than one order of magnitude. An estimate of the uncertainty can now be deduced using Eqs. (7.18) - (7.20). For the given configuration a value $\sigma_\theta = 8.3 \times 10^{-4}$ rad has been calculated. Figure 7.12 shows the energy spread according to Eq. (7.18) for different projectiles using the calculated value of σ_θ. From the dashed, vertical line (at $\theta = 2.5°$) a maximum contribution to the energy spread of 0.017 % in case of uranium shows a minor effect and can be safely neglected compared to other contributions of energy spread.

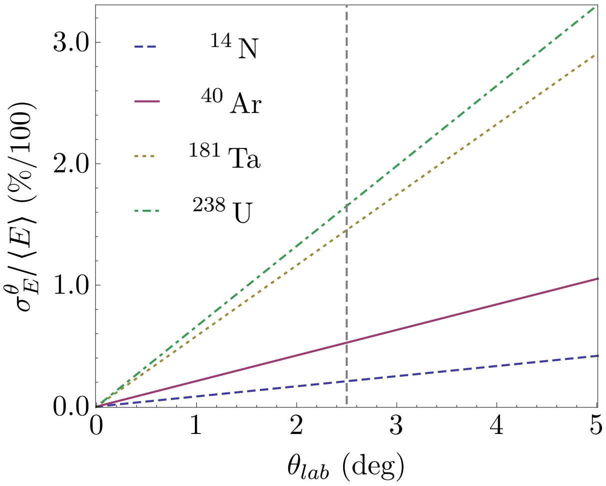

Fig. 7.12: Maximum energy spread imposed by the finite solid angle ω of the collimator.

7.3 Aluminium Foil

The TOF measurement relies on two timing signals at a well-defined separation. Since the first timing signal has to be created by a minimum interaction of the particle under consideration, to prevent a major negative impact on the TOF, a thin aluminium foil of about 10 µg/cm^2 is mounted in front of the MCP, tilted by an angle of $(42.5 \pm 0.5)°$. When a heavy-ion projectile passes the foil, electrons are liberated and accelerated towards the MCP front at a voltage of 2 kV. An avalanche of electrons is generated inside the MCP stack with an applied voltage applied of 1.9 kV. Eventually, the avalanches of electrons leaving the MCP are collected at an anode and the pulse is extracted via a Bias tee. For details see Sec. 3.3.1.

7.3.1 Electronic Stopping and Straggling

In contrast to the tantalum foil used in the particle-attenuation setup, the aluminium foil has been manufactured in an evaporating process at the GSI target laboratory. Table 7.2 lists values calculated with the ATIMA programme [83] for typical projectiles at $\langle E\rangle = 1.4\ A$MeV. Due to the very thin foil, the mean energy as well as the collisional straggling contribution is much lower compared to the tantalum foil. Using the ATIMA code, the largest contribution has been 0.033 % with respect to the mean energy $\langle E\rangle$. This is very small compared to the expected energy width of 1% but the value is based on the assumption of a perfectly homogeneous foil.

7.3.2 Inhomogeneity in Thickness and Texture

As mentioned beforehand, the aluminium foil has been manufactured by evaporating the material onto a substrate. While this provides a more homogeneous thickness than the rolling process and allows thinner foils, the material is not as resistive. Moreover, the surface

Tab. 7.2: ATIMA calculation for straggling contribution (at ideal thickness) for the MCP aluminium foil of about 370 Å at an incident angle of 42.5°.

	$\langle \Delta E \rangle / \langle E \rangle$ (%)	σ_{st} (AMeV)	$\sigma_{st} / \langle E \rangle$ (%)
N	0.35	4.6×10^{-4}	3.3×10^{-2}
Ar	0.46	3.1×10^{-4}	2.2×10^{-2}
Ta	0.38	1.5×10^{-3}	1.1×10^{-2}
U	0.34	1.3×10^{-3}	9.2×10^{-3}

structure of the solvable substrate manifests as the negative relief on the foil material. On the other side, this is a structure of absolute scale and thus becomes more relevant the thinner the foils are.

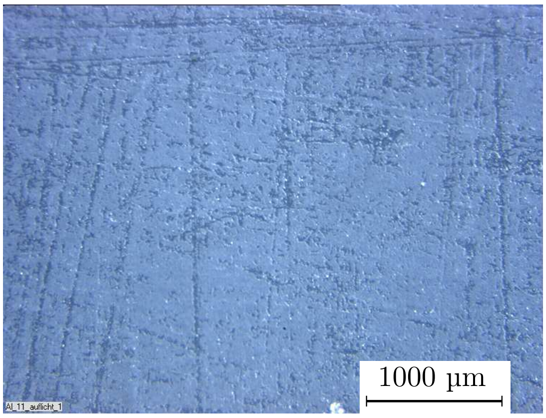

Fig. 7.13: Al 11 µg/cm^2, evaporated Scale 1000 µm, reflected light.

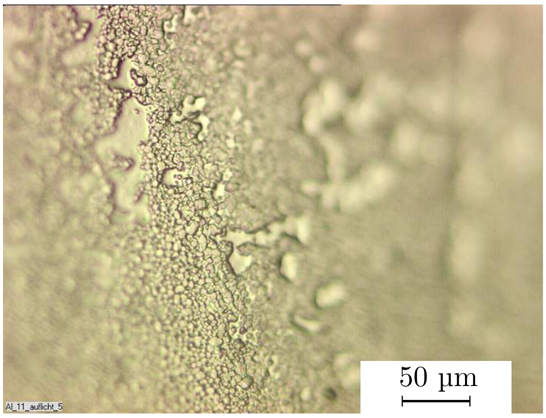

Fig. 7.14: Al 11 µg/cm^2, evaporated Scale 50 µm, reflected light.

For a qualitative measure of the surface characteristics, optical microscopy was used as in the case of the rolled tantalum foil (see Sec. 7.1.2). Figures 7.13-7.14 show two photographs of an aluminium 11 µg/cm^2 foil at different magnification. The foil stems from the same delivery as the foil currently installed in the TOF measurement setup. Only photographs using reflected light were possible due to the low contrast in case of transmitted light. In Fig. 7.13, at the scale of 1000 µm, the imprint of the substrate is visible. Nevertheless, apart from the scratch-like structure, regions of an even surface are present on a scale of about a quarter millimeter. Holes are scarcely featured although a big clustered disruption can be seen at the lower border next to the scale. Figure 7.14 shows the foil using reflected light at a scale of 50 µm and reveals a granular structure with a small grain size of about 3-5 µm. Other regions which correspond to the scratch-like shapes on the lower magnification appear embossed but with a very even and smooth surface area. It appears that the surface can

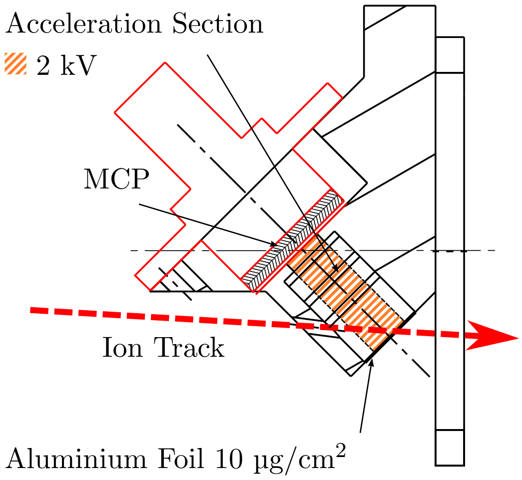

Fig. 7.15: Cut through the PEEK mounting of the MCP, the aluminium foil and the MCP module.

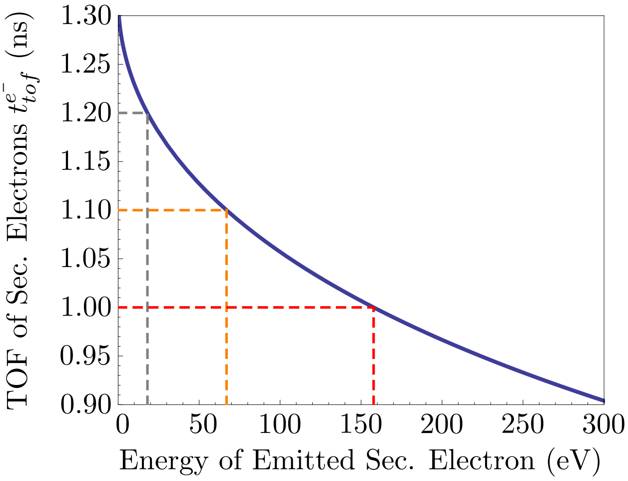

Fig. 7.16: TOF (Al-foil→MCP) of secondary electrons vs. kinetic energy (projection on MCP axis) at emission.

be characterised by mainly two thickness levels, the emboss and the granular level. This is different from the rolled tantalum foil, with a rather continuous thickness distribution (see Fig. 7.8).

Although quantitative data concerning the thickness variation is not available, some upper limits on the uncertainty can be derived from the thickness variation of the tantalum foil and the given mean energy loss at the aluminium foil for projectiles of energy $\langle E \rangle = 1.4\ A\text{MeV}$. It is known that evaporated foils are less prone to thickness variation than rolled foils. Taking the variation in thickness given in [79] for the rolled tantalum foil, we assume the evaporated aluminium foil to be of higher homogeneity, thus, $\sigma_x / \langle x \rangle < 0.34$. According to Eq. (7.10) this would contribute an uncertainty $\sigma^h_{al} < 0.15\%$ with respect to $\langle E \rangle$.

7.3.3 Secondary Electron Emission Spectra

The first generated timing in the TOF setup is realised as an indirect measurement by the secondary electrons liberated from the aluminium foil. Backwards emitted electrons are accelerated through 2 kV as depicted in Fig. 7.15, after which they have a velocity of about 9% of the speed of light. This considers a low initial kinetic energy at emission from the aluminium foil with an order of magnitude of a few electronvolts. To provide a homogeneous electric field, three guide rings have been included and are connected to an appropriate voltage divider circuit. For a corresponding CST Microwave Studio® simulation of the geometry [39] see Appendix Fig. A.2.

Ideally, the TOF of the secondary electrons between the aluminium foil and the MCP is constant. The TOF $t^{e^-}_{tof}$ of the electrons depends on the separation d between the aluminium foil and the MCP, the voltage U applied and the initial velocity component $v^{\perp}_0$ along the

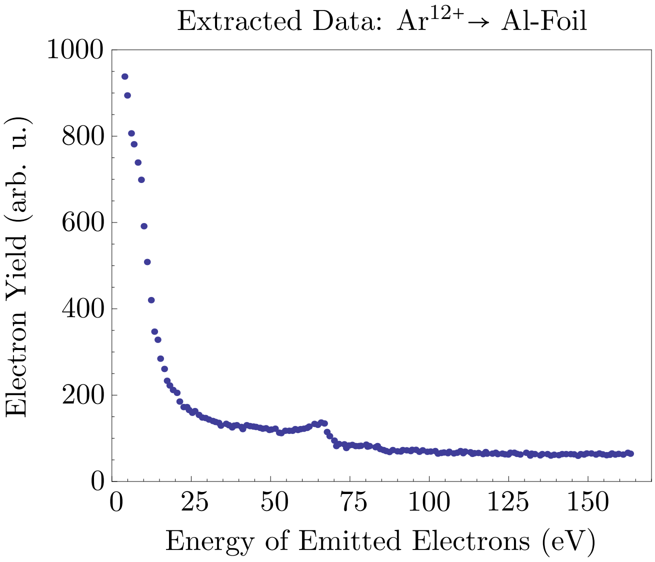

Fig. 7.17: Energies of backward scattered secondary electrons as measured in [85] for Ar^{12+} ions at 1.1 *A*MeV. Although no angles are resolved, the total solid angle of the detector has been only 1 sr, which is small enough to consider all electrons being within the acceptance of the MPC/foil setup. The original data provides no information about statistical and systematic errors.

symmetry axis, thus, in the classical limit

$$t_{tof}^{e^-} = \sqrt{\frac{2d}{\xi} + \left(\frac{v_0^\perp}{\xi}\right)^2} - \frac{v_0^\perp}{\xi} \qquad \text{with} \qquad \xi = \frac{U}{m_{el} \cdot d} . \tag{7.22}$$

Figure 7.16 shows the TOF $t^{e^-_{tof}}$ vs. the initial kinetic energy of the electrons for the configuration of the setup with $d = 17.5$ mm and $U = 2$ kV and under the assumption that the energy of the electrons are attributed to $v_0^\perp$ alone. The difference in TOF between an electron with initially 0 eV kinetic energy and 18 eV is about 100 ps, while an electron of 68 eV and 0 eV will have a difference in TOF of about 200 ps. Therefore, we cannot preclude that the electron spectra do not affect the accuracy of the first timing signal. On the other hand, multiple electrons will be liberated per ion passage of the aluminium foil. The Sternglass formula [84] allows to estimate the amount of liberated secondary electrons with several electron volts of kinetic energy. According to Sternglass, the electron yield for the given configuration is about 150 electrons in case of argon and about 600 electrons in case of uranium. Hence, for narrow energy spectra one could conclude that a large number of liberated electrons per ion would result in a more or less identical distribution on each passage of an ion. In other words, the ensemble of electrons from a single ion event would already be a good representation of the energy distribution itself. Consequently, the response of the MCP could be expected to consist of very similar pulse shapes.

Nevertheless, the actual spectra of the secondary electrons are unknown. Experimental data up to 163 eV of the electron spectra can be extracted from [85] for the argon case and are shown in Fig. 7.17. The configuration of the experimental setup which has been used is very similar to the situation present in the TOF setup at hand. Although no angle information is included, we can safely assume all electrons to be inside the acceptance of the foil-MCP detector setup since Koyama et al. specify the solid-angle acceptance of their setup to be 1 sr which is equal to a polar angle of 32.8°. From this data, a very long high energetic tail is apparent and cannot be considered a narrow distribution. Since the MCP is sensitive to single electrons, those electrons reaching the MCP front at first are most relevant to the leading edge of the pulse. A large high energy tail can negatively influence the timing accuracy as the highest energy occurring in each ion event could fluctuate on a large scale. Even with several hundreds of electrons per ion, these fluctuations may be prominent. Taking the energy spectra of Fig. 7.17 as reference, the most likely energies to occur are those of low energy below 20 eV. At the same time those are the least relevant for leading edge of the pulse. It may even be, that the fluctuations connected to the electron with the highest energy is responsible for the random distortions of the leading edge which is discussed in Sec. 7.4.1.1.

7.3.4 Tilted Foil Geometry

As explained in Sec. 3.3.1, the aluminium foil is tilted at a certain angle with respect to the plane orthogonal to the beam axis z. This is a strict requirement as the MCP front must be installed centric parallel with respect to the foil and assure a homogeneous, symmetric electric field. Additionally, the ion must transit the foil only and bypass the MCP at the same time. Thus, the angle also depends on the geometry of the MCP module (Sec. 3.3.1). A tilt angle of $\varphi = 42.5°$ represents a minimum for the current distance between the foil and the MCP front. The finite solid angle of the beam together with the tilted foil geometry introduces a geometric jitter $\Delta l_{tof}(x)$ in total drift space which is schematically depicted in Fig. 7.18. In the following, the particles are considered to follow parallel trajectories which significantly simplifies the evaluation of uncertainty without major tampering, since lateral contribution are suppressed by at least one order of magnitude. Furthermore, the diamond electrode is assumed to be illuminated uniformly.

The first moment $\langle \Delta l \rangle$ vanishes which reduces the uncertainty estimation of the rms drift jitter to the evaluation of

$$\sigma_{\Delta l} = \sqrt{\langle \Delta l^2 \rangle}\,. \tag{7.23}$$

As can be seen from Fig. 7.18, the dependence of Δl on x is given by

$$\Delta l(x) = x \tan\varphi\,. \tag{7.24}$$

Depending on either the solid angle ω given by the collimator configuration or the distance of the diamond detector electrode, the illuminated area on the aluminium foil is different. The maximum effective solid angle is given by the size of the diamond detector electrode and its distance to the tantalum foil. This is taken into account by limiting the integration

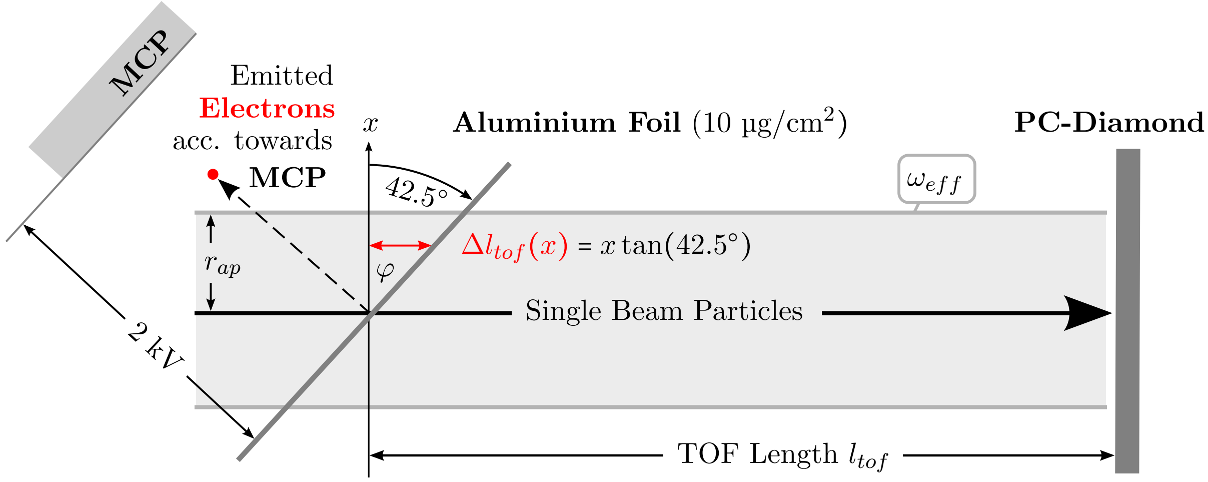

Fig. 7.18: The MCP module is shown including the aluminium foil. All ions are uniformly distributed within the range of the *effective aperture* given by the radius r_{ap}. Due to the inevitable tilted placement of the foil, the TOF length depends on the lateral offset from the centre.

within the projected circular boundary that matches the *effective aperture* r_{ap}

$$\langle \Delta l^2 \rangle_\varphi = \frac{1}{\pi r_{ap}^2} \int_{-r_{ap}}^{r_{ap}} \mathrm{d}x \, x^2 \tan^2\varphi \int_{-\sqrt{r_{ap}^2 - x^2}}^{\sqrt{r_{ap}^2 - x^2}} \mathrm{d}y = \frac{\tan^2\varphi}{4} r_{ap}^2 \,. \tag{7.25}$$

The aperture can be treated as an effective value depending on the solid angle spanned by the circular area of the diamond, given by means of r_{dia} and its separation to the primary (Ta) foil squared. In the following, l_{mcp} is the separation of the MCP to the primary foil, l_{dia} marks the separation of the diamond detector to the primary foil and $l_{tof} = l_{dia} - l_{mcp}$ is the drift distance relevant for the TOF. The technical drawing Fig. A.1 provides an overview. Starting with the *effective solid angle* ω_{eff} given by the separation l_{dia} of the poly-crystalline detector

$$\omega_{eff} = \frac{A_{dia}}{l_{dia}^2} = \frac{\pi r_{dia}^2}{(l_{mcp} + l_{tof})^2} \tag{7.26}$$

the effective aperture r_{ap} is given accordingly by

$$r_{ap} = \sqrt{\frac{A_{dia}}{\pi}} \frac{l_{mcp}}{l_{mcp} + l_{tof}} = \frac{r_{dia}}{1 + \frac{l_{tof}}{l_{mcp}}} \,. \tag{7.27}$$

Together with Eq. (7.25), the jitter in detector separation writes as

$$\sigma_{\Delta l} = \sqrt{\langle \Delta L^2 \rangle_\varphi} = \frac{\tan\varphi}{2} \frac{r_{dia}}{1 + \frac{l_{tof}}{l_{mcp}}} \tag{7.28}$$

and is trivially transformed into the corresponding time jitter by taking the mean velocity $\langle\beta\rangle\, c$ of the particles into account

$$\sigma_t = \frac{\sigma_{\Delta l}}{\langle\beta\rangle\, c} \,. \tag{7.29}$$

For the current configuration of the setup and the typical velocity of $\beta = 0.055$ this results in an absolute RMS time jitter of about 25 ps.

7.4 Detectors

7.4.1 Microchannel Plate

Time measurements with the TDC requires NIM pulses as input. Those logical pulses are delivered using the *double-threshold discriminators* [54] described in Sec. 4.1.1. Typically, the MCP pulses at the 50 Ω anode readout deliver a pulse-height distribution from ≈ 150 mV to 1.2 V.

7.4.1.1 Pulse Shapes and Discrimination

As it turned out, evaluation of precise timings is falsified by distorted pulse shapes at the falling edge, as can be seen in Fig. 7.19. The left trace shows a “normal” pulse shape, while the right picture shows the leading-edge distortions of frequent occurrence. To estimate the resulting timing jitter, the recorded pulse has been complemented by dashed lines to reconstruct the expected leading edge. Based on this method, typical pulse shapes are shown with a timing jitter of ≈ 150 ps and ≈ 400 ps. Pile-ups caused by multiple ions as the reason for the bump can be eliminated. The multiple-hit occurrence can be deduced from the bunch separation distribution Eq. (3.14) which has been experimentally verified.

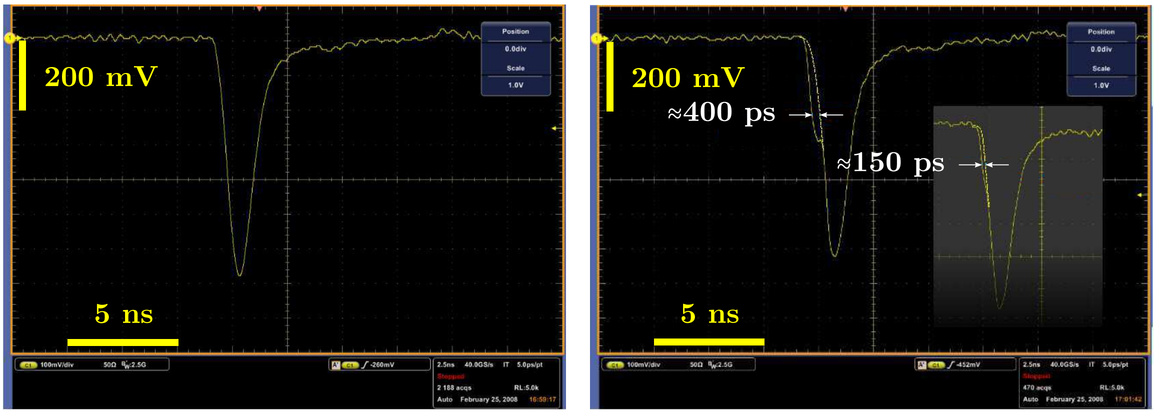

Fig. 7.19: Left: Normal MCP pulse shapes with a well defined rising slope with a rise-time of about 850 ps. **Right:** Distorted MCP pulse shapes which randomly feature an additional bump on the falling edge with different time offsets. The dashed yellow curve has been added manually representing the expected shape that allows the estimation of the corresponding error contribution.

Consultation of the manufacturer confirmed that the mechanical and electrical installation is in compliance with the companies' guidelines. Ion feedback is equally unlikely the cause of the distortions, given the low pressure of 1×10^{-6} to 1×10^{-7} mbar and the Chevron configuration, in particular with the frequent occurrence. Since the MCP is sensitive to single electrons, this effect might be correlated with the electron emission spectra at the aluminium foil. Isolated fast electrons may reach the MCP earlier by several 100 picoseconds as depicted in Fig. 7.16. As a safe estimate on the RMS timing contribution 150 ps seems legitimate.

7.4.2 Poly-Crystalline Diamond Detector

7.4.2.1 Pulse Shapes and Discrimination

The diamond detector does not suffer from significant distortions of the leading edge. Based on the characteristics of the double-threshold discriminator and the amplifier stage, an RMS uncertainty of 50 ps is considered.

7.4.2.2 Signal Propagation on Diamond Electrode

Particles scattered into the solid-angle acceptance of the collimator are detected directly at a diamond detector on an circular electrode area with a radius of 4 mm. Signals are collected at the connector as depicted schematically in Fig. 7.20. Depending on the location of impact, the distance to the connector differs. We can assume a uniform illumination of the electrode area since the scattering statistics does not change significantly inside the very small solid angle. According to Fig. 7.20, a given impact location can be parameterised by

$$\vec{r}(r,\varphi) = r(\cos\varphi\,\vec{e}_x + \sin\varphi\,\vec{e}_y) \qquad \text{and} \qquad \vec{R} = -R\,\vec{e}_y\,. \tag{7.30}$$

Therefore, the square of the distance from location of impact to the electrode connector writes as

$$\left|\vec{r}(r,\varphi) - \vec{R}\right|^2 = r^2\cos^2\varphi + (r\,\sin\varphi + R)^2\ . \tag{7.31}$$

Consequently, the mean signal transport distance on the detector is evaluated by the following integral

$$\langle|\vec{r}-\vec{R}|\rangle = \frac{\int_0^R r^2\mathrm{d}r\int_0^{2\pi}\mathrm{d}\varphi\sqrt{\cos^2\varphi + \left(\sin\,\varphi + \frac{R}{r}\right)^2}}{\int_0^R r\mathrm{d}r\int_0^{2\pi}\mathrm{d}\varphi}\,. \tag{7.32}$$

As the integral is of elliptical type, no analytical solution exists. A numerical calculation for electrode radius $R = 4$ mm delivers a mean distance $\langle|\vec{r}-\vec{R}|\rangle \approx$4.5 mm. The RMS value $\sigma_{|\vec{r}-\vec{R}|}$ of 3.3 mm has been also evaluated numerically by

$$\sigma_{|\vec{r}-\vec{R}|} = \frac{\int_0^R r\mathrm{d}r\int_0^{2\pi}\mathrm{d}\varphi\left(\langle|\vec{r}-\vec{R}|\rangle - r\sqrt{\cos^2\varphi + \left(\sin\varphi + \frac{R}{r}\right)^2}\right)^2}{\int_0^R r\mathrm{d}r\int_0^{2\pi}\mathrm{d}\varphi}\,. \tag{7.33}$$

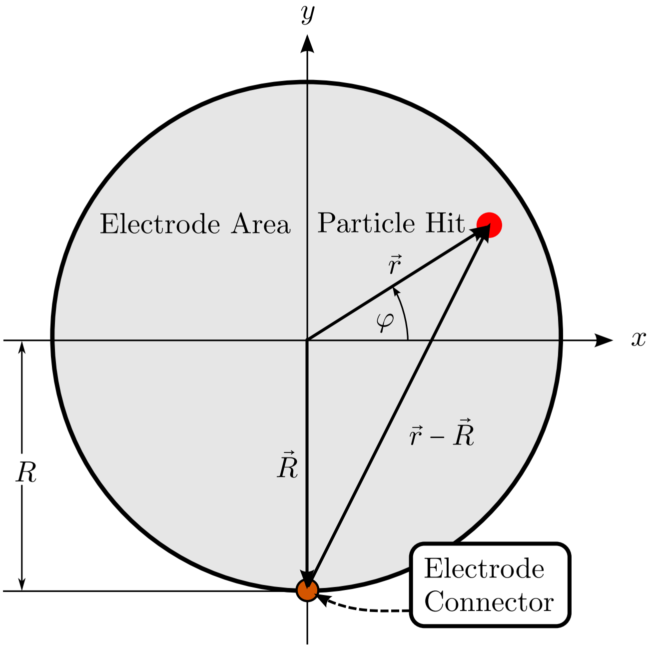

Fig. 7.20: Depending on the point of impact, a different propagation time to the electrode connector has to be considered. This results in an uncertainty concerning the timing precision.

Even in a very optimistic scenario where signals propagate with speed of light this contributes an RMS time jitter of 11 ps.

7.5 Influence of Accelerator Settings

7.5.1 Impact of Gas Pressure at the Stripper Section

TODO: Nur qualitativ. Verweis auf Messungen (Variation Gasdruck) und Effekte.

7.5.2 Coupling of Transverse and Longitudinal Phase Space

The measurement is installed inside a dipole chicane used for charge state selection (see Fig. 3.3). As the dispersion after the first dipole magnet (US3MK1) is fully uncompensated, it is important to investigate the effects related to the coupling of the transverse and longitudinal phase space planes. In standard operation of the beam line, the beam is further deflected by two dipole kicker magnets which accomplish partial compensation of the net dispersion before the bunch is prepared to be injected into the first Alvarez cavity. While the transverse and longitudinal phase space planes along the prestripper section are considered to be decoupled in good approximation, this is not necessarily the case within the dispersive dipole section. If the transverse and longitudinal phase space planes are uncorrelated, the corresponding six dimensional density ρ can be written as a direct product of the transverse and longitudinal densities

$$\rho(x, p_x; y, p_y; \phi, p_z) = \rho_t(x, p_x; y, p_y) \cdot \rho_l(\phi, p_z)\,. \tag{7.34}$$

In this case, measurement of the longitudinal phase space would be independent of the location (x, y).

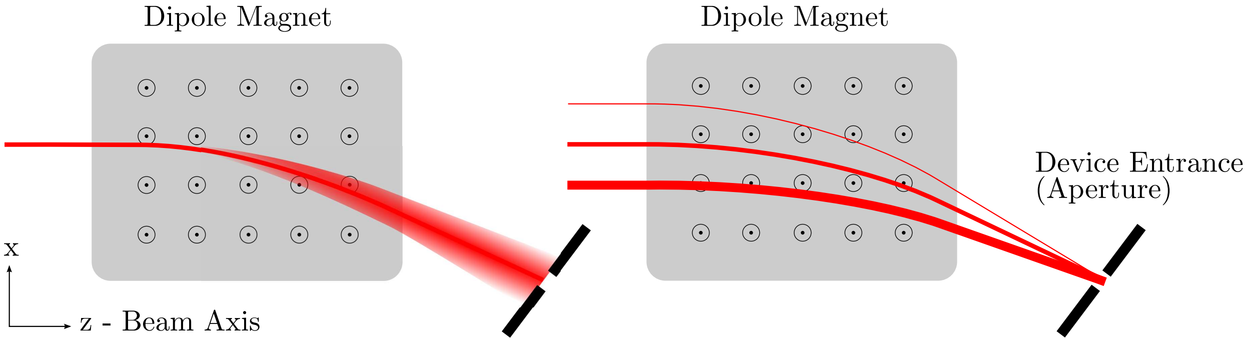

Fig. 7.21: Schematic effect of transverse and longitudinal coupling along a dispersive dipole section (neglecting the interaction of the particles and transverse momenta). Particle trajectories are depicted by red lines. Considering the narrow aperture, two systematic contributions can be distinguished. On the **left** figure, a beam section of small transverse extension enters the dipole. The longitudinal momentum spectra give rise to different radii of the particle trajectories. Thus, the aperture selects a certain range of energies from the incoming particle stream. The **right** figure shows particle sections with different transverse offsets. The magnitude of the longitudinal momenta is schematically denoted by the thickness of the trajectories.

The present setup relies on a narrow aperture at the entrance. Hence, the measurement only reflects the longitudinal phase space connected to a certain transverse offset (x, y) if the transverse and longitudinal planes are strongly correlated. The duration required for a measurement does not allow for a sampling at several offsets x. Data is therefore taken at the centre of the transverse distribution only. Moreover, the count rate drops fast for a larger offset from the beam centre.

Schematically, the coupling of the horizontal degree of freedom is depicted in Fig. 7.21. On the left figure, the dispersion leads to a horizontal beam spread depending on the initial longitudinal momentum distribution and the strength of the dipole field. This means for a narrow aperture that the spatial point-to-point mapping from a transverse position before entering the dipole and the location of the aperture is connected with a small longitudinal momentum range (neglecting the transverse momenta for simplicity). On the right figure, different initial transverse offsets are mapped to aperture with the matching momenta.

To estimate the influence of the dispersive section, a DYNAMION [18] tracking simulation has been used for the typical case of an Ar^{1+} beam of 10 mA entering the gas stripper. The particles were tracked [86] through the gas stripper and the consecutive dipole section to the location of the setup. The simulation was restricted to the charge-state equilibrium 1+ → 10+ at 1.4 AMeV. Due to the symmetry of the charge state spectrum, a current of 100 mA can be assumed. Figure 7.22 shows the longitudinal phase ϕ and relative momentum

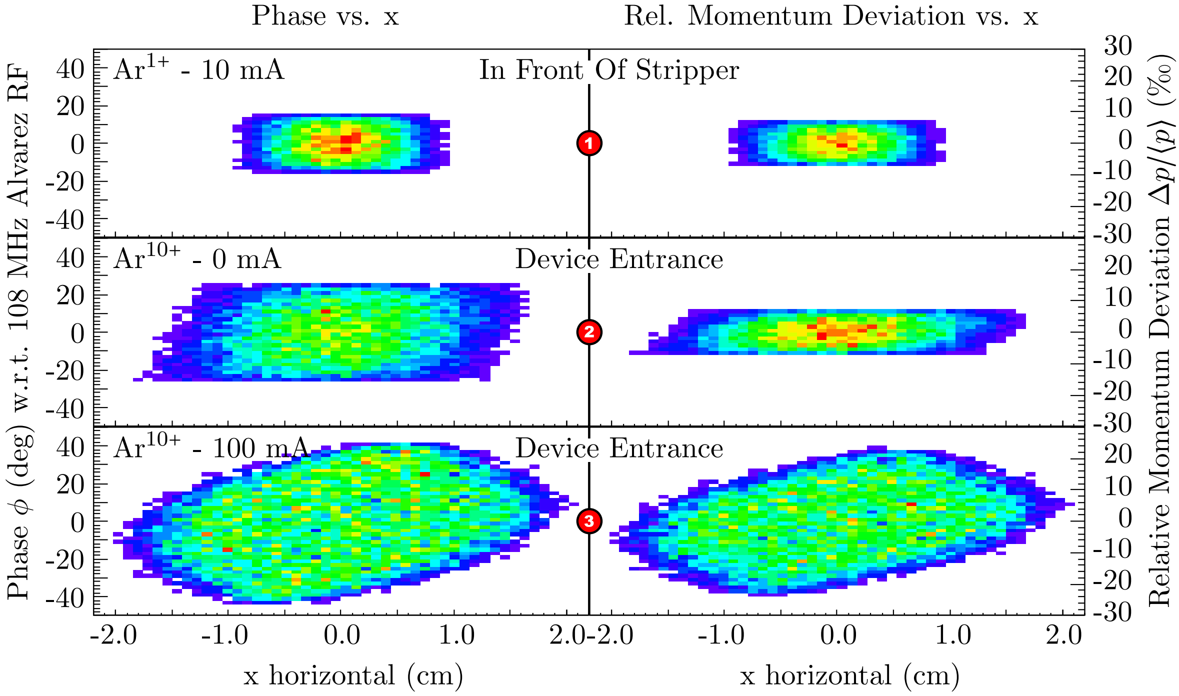

Fig. 7.22: Subspaces (ϕ vs. x and $\frac{\Delta p}{p}$ vs. x) of DYNAMION tracking data calculated by S. Yaramishev [86]. To investigate the effect of the transverse and longitudinal coupling at the dispersive dipole section, a start distribution of Ar^{1+} (10 mA), (top row ①) has been tracked through the gas stripper to the measurement setup. After stripping (1+ → 10+) the distribution has been further tracked without considering particle interaction (middle row ②) and considering full space-charge (bottom row ③).

deviation $\Delta p/p$ versus the transverse horizontal offset x, at which the top row corresponds to the start configuration before entering the gas stripper. The middle row represents the beam at the measurement setup tracked without taking space-charge effects into account, i. e. the beam has been treated as an ensemble of non-interacting particles. The bottom row considers realistic values of the space-charge. For completeness the associated longitudinal phase spaces are given in the appendix (see Fig. A.4).

From the tracked phase spaces it is apparent, that under low space-charge influence the phase space undergoes shear mapping in the $(\phi \otimes x)$ and $(\frac{\Delta p}{p} \otimes x)$ plane. Hence, an uncorrelated phase space at the entrance of the gas stripper remains largely uncorrelated at the measurement setup. A realistic picture requires the consideration of the strong inter-particle effects, mainly the space-charge. Then, as can be seen from the bottom row subspaces of Fig. 7.22, a prominent correlation is present. Nevertheless, a range of ±0.5 cm from the centre obviously provides about the same particle distribution, but at a strongly correlated mean value. This can be seen from Fig. 7.23 where cuts at equidistant locations $x \pm 0.25$ cm have been evaluated for their mean value and sample standard deviation. While the coupling of the transverse and longitudinal phase-space planes may lead to a strong correlation of the mean values for the realistic space-charge simulation, the sample means vary by a smaller margin within $[-1.25\ \mathrm{cm}, 1.25\ \mathrm{cm}]$ of less than 5% for a fraction of the total particles

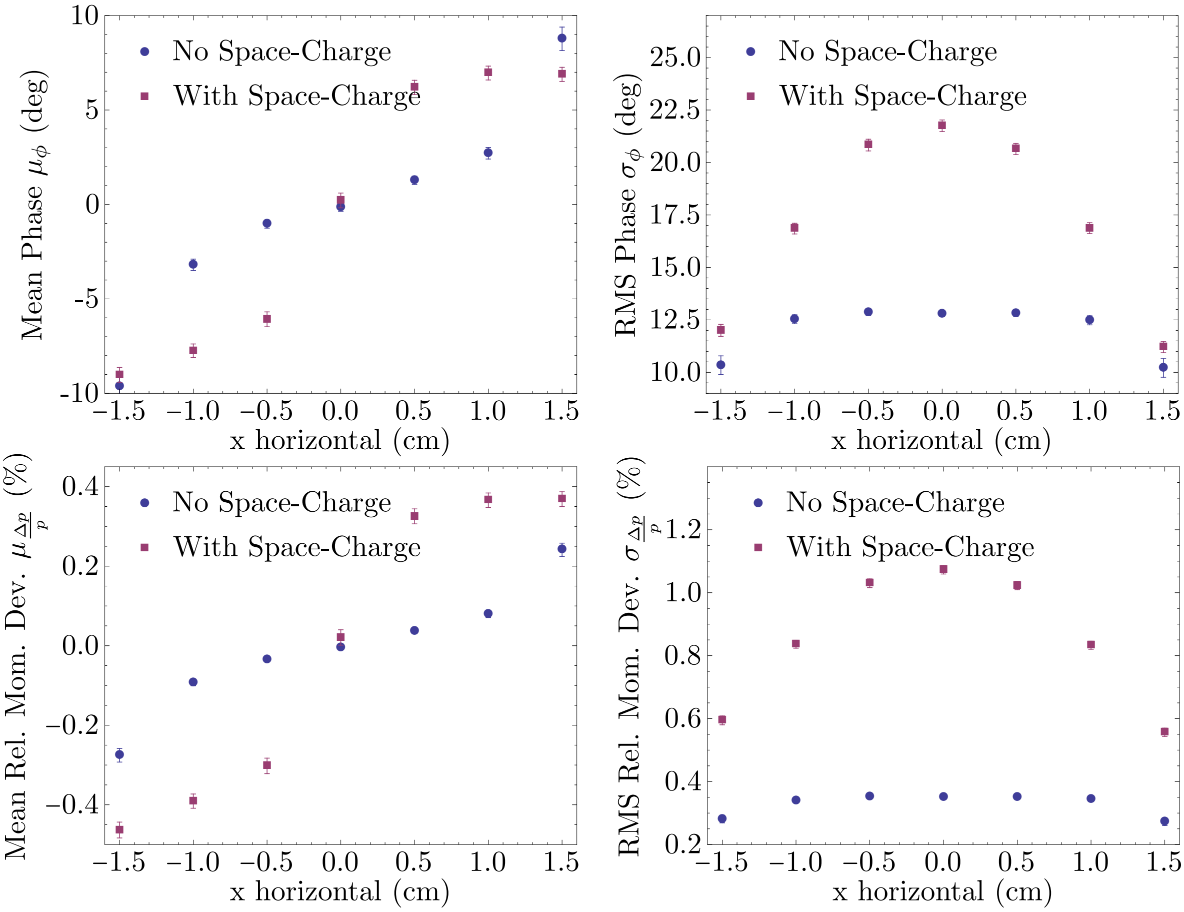

Fig. 7.23: Mean and standard variation for different cuts (horizontal location ±0.25 cm) at horizontal degree of freedom x based on the data shown in Fig. 7.22 (device entrance).

of about 60%. Nevertheless, neglecting any dissipative effects as well as timing limitations, a measurement at the transverse centre may underestimate the total bunch length and momentum distribution. This is obvious, since the mean values vary about 10° (0.8 ns) concerning the phase and about 0.8% for the relative momentum distribution. Thus, the total projection is affected.

On the other hand, these effects are less significant compared to the sample simulation during a measurement for two reasons: At first, the stripping efficiency for the equilibrium charge state is far below the 100% taken as an extreme case. Therefore, the blow-up effects due to the lower charge density after a short distance inside the dipole are much lower. Furthermore, the measurement requires the primary beam current to be attenuated to several microamperes before hitting the Ta-foil (see Sec. 5.1.1). Usually this is accomplished by appropriate settings of the high-current slits (DS4/5) and therefore more than 1 m drift is taken into account with only minor space-charge effects. Hence, the actual properties of coupling between the transverse and longitudinal phase space lie in between the non-interacting and space-charge case shown in Fig. 7.23. The required extensive DYNAMION calculations are beyond the scope of this work.

7.5.3 Impact of High Current Slits

TODO: Nur qualitativ moeglich. Verweis auf Messungen (Variation Schlitze) und Effekte.

7.5.4 Impact of the Collimator Apertures

TODO: Nur qualitativ moeglich. Hinweise durch Single-Crystal Daten. Verweis auf evtl. zukuenftige Untersuchungen. Moeglicherweise aehnliche Effekte bei Pepperpot Emittanz (Emittanz deutlich ueberschaetzt)

7.6 DAQ Electronics

Testing of the TOF DAQ electronics has been performed with a Berkeley DB-2 random pulse generator. It serves as an idealistic monochromatic source by splitting the signals and feeding them instead of the diamond and MCP signals. While this approach would help to reveal severe systematic limitations of the electronics and the TDC, it does not reflect the real pulse shape situation as described in Sec. 7.4.1.1 and 7.4.2.1. Figure 7.24 shows the recorded histogram with a standard deviation of ≈ 0.934 channels, which corresponds to ≈ 22.8 ps. The RF RMS deviation turns out to be about the same value as determined from the linear fit (see Fig. 4.6). This suggests that the resolution of the DAQ electronics, in this idealistic approach with deterministic pulse shapes from the random-pulse generator, is dominated by the TDC and not by the NIM chain. Inami [87] determined a RMS timing

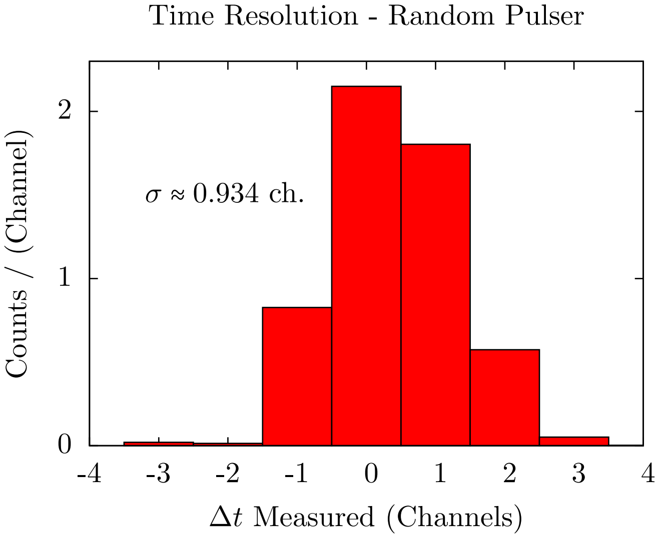

Fig. 7.24: A signal from a random pulser is splitted and feeds the DAQ chain of the diamond and MCP detector simultaneously as an idealised monochromatic source. The full NIM chain is explained in Sec. 4.1.2.

7-9 ps for a similar NIM/CAMAC configurations fed by a random pulser, which supports a RMS timing resolution of better than 10 ps for the NIM chain. We can therefore, for simplicity, assign the total measured jitter to the TDC input channels. Since two of them are involved to measure the timing separation the input jitter for a single input is smaller by a factor of $1/\sqrt{2}$. Hence, we can account for an RMS jitter per TDC input of ≈ 17 ps.

7.7 Linear Approximation at Phase-Space Reconstruction

An absolute determination of the TOF requires both detectors to be synchronised, i. e. the knowledge of the relative offset of both timing signals. Not only relative cable delays are involved in the total time delay but also delays of relevant scale inside the detectors itself as the TOF of the emitted secondary electrons at the foil mounted in front of the MCP module. A synchronisation has not been accomplished in the present setup which focuses on relative evaluation of momentum and energy with respect to their mean values. As was described in Sec. 4.1.5 the phase-space mapping of the relative momentum and energy deviation follows a linear approximation in TOF for particle i,

$$\frac{\Delta p_i}{\langle p \rangle} \approx -\frac{\Delta t_i}{t_{\langle p \rangle}} \tag{7.35}$$

$$\frac{\Delta E_i}{\langle E \rangle} \approx -2\frac{\Delta t_i}{t_{\langle E \rangle}} \tag{7.36}$$

with $\Delta p_i = p_i - \langle p \rangle$, $\Delta E_i = E_i - \langle E \rangle$ and $\Delta t_i = t_i - t_{\langle p \rangle}$ or $\Delta t_i = t_i - t_{\langle E \rangle}$, respectively. In the following $t_{\langle p \rangle}$ denotes the TOF of the mean particle velocity (which is not necessarily the synchronous particle) along the detector separation l_{tof} with

$$t_{\langle p \rangle} = \frac{l_{tof}}{\langle \beta \rangle \, c}, \tag{7.37}$$

thus that

$$p(t = t_{\langle p \rangle}) = \langle p \rangle \ . \tag{7.38}$$

In the same way, $t_{\langle E \rangle}$ denotes the TOF of the mean kinetic energy particle with

$$E(t = t_{\langle E \rangle} \approx t_{\langle p \rangle}) = \langle E \rangle \ . \tag{7.39}$$

Both, momentum and kinetic energy are considered in non-relativistic limit since the setup is located at a section that is traversed by a reference particle at about $\langle \beta \rangle \approx 5.5\%$. Thus, with the atomic mass unit m_u and TOF t_i between the MCP and diamond detectors at separation l_{tof}, the equations for the momentum p_i and kinetic energy E_i per nucleon of particle i are given by

$$p_i = p(t_i) = m_u \, l_{tof} \frac{1}{t_i} \tag{7.40}$$

and

$$E_i = E(t_i) = \frac{m_u\, l_{tof}^2}{2}\,\frac{1}{t_i^2}\,. \tag{7.41}$$

As the kinetic energy E_i in Eq. (7.41) is not a linear function in p_i, the TOF of the mean momentum particle and the particle mean energy is not identical in the general case, i. e. $t_{\langle p\rangle} \neq t_{\langle E\rangle}$. In other words, a particle of mean momentum is not necessarily a particle of mean energy. Evaluating the average of momentum and energy with the corresponding TOF distribution $\{t_i\}$ using Eq. (7.38) and (7.39) allows comparison of $t_{\langle p\rangle}$ and $t_{\langle E\rangle}$.

$$\langle p\rangle = m_u\, l_{tof}\left\langle\frac{1}{t}\right\rangle \overset{!}{=} m_u\, l_{tof}\frac{1}{t_{\langle p\rangle}} \qquad \Rightarrow \quad t_{\langle p\rangle} = \left\langle\frac{1}{t}\right\rangle^{-1} \tag{7.42}$$

$$\langle E\rangle = \frac{m_u\, l_{tof}^2}{2}\left\langle\frac{1}{t^2}\right\rangle \overset{!}{=} \frac{m_u\, l_{tof}^2}{2}\frac{1}{t_{\langle E\rangle}^2} \qquad \Rightarrow \quad t_{\langle E\rangle} = \sqrt{\left\langle\frac{1}{t^2}\right\rangle^{-1}} \tag{7.43}$$

Although not identical, treating $t_{\langle p\rangle} \approx t_{\langle E\rangle}$ is feasible if the standard deviation of the momentum distribution σ_p is sufficiently smaller than $\langle p\rangle$, i. e. $\sigma_{\frac{p}{\langle p\rangle}} \ll 1$. This can be seen by expressing the standard deviation of $\{\frac{p_i}{\langle p\rangle}\}$ by means of $\{t_i\}$ using Eq. (7.40) and (7.41)

$$\sigma_{\frac{p}{\langle p\rangle}} = \frac{\sqrt{\left\langle\frac{1}{t^2}\right\rangle - \left\langle\frac{1}{t}\right\rangle^2}}{\left\langle\frac{1}{t}\right\rangle} = \frac{\sqrt{\frac{1}{t_{\langle E\rangle}^2} - \frac{1}{t_{\langle p\rangle}^2}}}{t_{\langle p\rangle}} = \sqrt{\left(\frac{t_{\langle p\rangle}}{t_{\langle E\rangle}}\right)^2 - 1}, \tag{7.44}$$

which shows that $t_{\langle p\rangle}$ and $t_{\langle E\rangle}$ differ by a factor of $\sqrt{\sigma_{\frac{p}{\langle p\rangle}}^2 + 1}$. Therefore, with the typical relative momentum spread $\sigma_{p/\langle p\rangle}$ of less than 1%, $t_{\langle p\rangle}$ and $t_{\langle E\rangle}$ are used synonymously for this setup, as $\sqrt{(0.01)^2 + 1} \approx 1.00005$.

Furthermore, with Δt_i denoting the time deviation of an arbitrary particle i with respect to $t_{\langle p\rangle}$ or $t_{\langle E\rangle}$ respectively

$$\Delta t_i = t_i - t_{\langle p\rangle} \approx t_i - t_{\langle E\rangle}\,, \tag{7.45}$$

the absolute longitudinal momentum deviation per nucleon writes as

$$\begin{aligned}\Delta p_i = p(t_i) - \langle p\rangle = m_u\, l_{tof}\left\{\frac{1}{t_{\langle p\rangle} + \Delta t_i} - \frac{1}{t_{\langle p\rangle}}\right\} = \\ = -m_u\, l_{tof}\frac{\Delta t_i}{t_{\langle p\rangle}(t_{\langle p\rangle} + \Delta t_i)} = -\underbrace{m_u\, l_{tof}\frac{1}{t_{\langle p\rangle}}}_{m_u v_{\langle p\rangle} \overset{!}{=} \langle p\rangle}\,\frac{\frac{\Delta t_i}{t_{\langle p\rangle}}}{1 + \frac{\Delta t_i}{t_{\langle p\rangle}}}\,,\end{aligned} \tag{7.46}$$

which finally delivers the exact relative momentum deviation in the classical limit

$$\left.\frac{\Delta p_i}{\langle p\rangle}\right|_{ex} = -\frac{\frac{\Delta t_i}{t_{\langle p\rangle}}}{1+\frac{\Delta t_i}{t_{\langle p\rangle}}} . \tag{7.47}$$

In the same manner the absolute longitudinal energy deviation per nucleon is given by

$$\begin{aligned}\Delta E_i = E(t_i) - \langle E\rangle &= \frac{m_u\, l_{tof}^2}{2}\left\{\frac{1}{\left(t_{\langle E\rangle}+\Delta t_i\right)^2} - \frac{1}{t_{\langle E\rangle}^2}\right\} = \\ &= \frac{m_u\, l_{tof}^2}{2}\frac{t_{\langle E\rangle}^2 - (t_{\langle E\rangle}+\Delta t_i)^2}{\left(t_{\langle E\rangle}(t_{\langle E\rangle}+\Delta t_i)\right)^2} = -\underbrace{\frac{m_u\, l_{tof}^2}{2}\frac{1}{t_{\langle E\rangle}^2}}_{\frac{m_u v_{\langle E\rangle}{}^2}{2} \overset{!}{=} \langle E\rangle}\frac{2\frac{\Delta t_i}{t_{\langle E\rangle}} + \left(\frac{\Delta t_i}{t_{\langle E\rangle}}\right)^2}{\left(1+\frac{\Delta t_i}{t_{\langle E\rangle}}\right)^2} .\end{aligned} \tag{7.48}$$

Therefore, in the classical limit, the exact relative kinetic energy deviation per nucleon writes as

$$\left.\frac{\Delta E_i}{\langle E\rangle}\right|_{ex} = -\frac{2\frac{\Delta t_i}{t_{\langle E\rangle}} + \left(\frac{\Delta t_i}{t_{\langle E\rangle}}\right)^2}{\left(1+\frac{\Delta t_i}{t_{\langle E\rangle}}\right)^2} . \tag{7.49}$$

Comparison of the exact relative deviations of momentum Eq. (7.47) and kinetic energy Eq. (7.49) to their linear approximations Eq. (7.35) and (7.36) as a function of $\frac{\Delta t_i}{t_{\langle p\rangle}}$ are visualised in Fig. 7.25. The deviations from the exact values have a trivial asymmetric characteristic, being smaller than the classical exact values for faster particles, while slower particles overestimate the relative momentum and energy deviation. For a particle with an exemplary difference in TOF of $\Delta t_i = \pm 1$ ns with respect to a particle of mean velocity (red guide lines), corresponding to $\frac{\Delta t}{t_{\langle p\rangle}} \approx 2\%$, the linear approximation is still very close to the exact values as listed in Tab. 7.3. As this represents four times the expected standard deviation of the kinetic energy to either side, this correction can be neglected.

7.7.1 Deviations from the Expected Mean Energy

Timing signals recorded at the MCP and diamond detector exhibit a constant offset, turning it into a relative measurement (see Sec. 4.1.5). Due to the nonlinearity in Δt_i of the exact equations Eq. (7.47) and (7.49) for the relative momentum and energy deviation, those are not form-invariant under translations with a constant offset c_{off} in time

$$\Delta t_i \quad \longrightarrow \quad \Delta t_i + c_{off}, \tag{7.50}$$

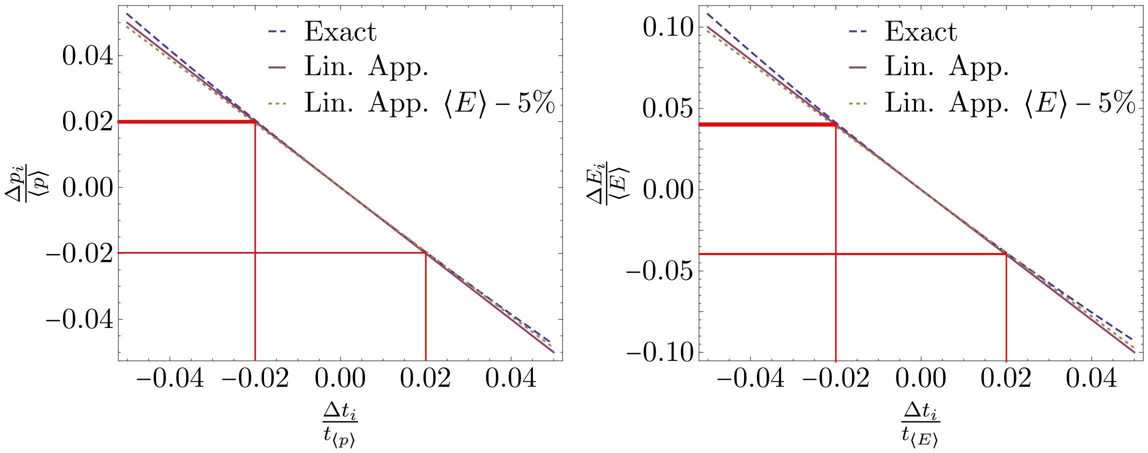

Fig. 7.25: *Relative momentum deviation* $\Delta p_i / \langle p\rangle$ and *relative energy deviation* $\Delta E_i / \langle E\rangle$ in linear approximation (solid lines) and classical exact representation (dashed lines) in terms of the *relative time deviation* $\Delta t_i / t_{\langle p\rangle}$ and $\Delta t_i / t_{\langle E\rangle}$, respectively. Additionally, the linear approximations are plotted with a different evaluation point $t_{\langle E\rangle}$ of the Taylor series (see Sec. 4.1.5), shifted to a lower kinetic energy by 5 %. The effect of a mismatched evaluation point is discussed in Sec. 7.7.1. To visualise the minor impact from the exact classical description, the width of the red lines corresponds to the deviation of $\Delta p_i / \langle p\rangle$ and $\Delta E_i / \langle E\rangle$, respectively, at a deviation from the mean energy ±4 standard deviations of the expected energy distribution.

except for a constant shift, which is irrelevant using central moments, and hence do not conserve the shape of the phase space:

$$\left.\frac{\Delta p_i}{\langle p\rangle}\right|_{ex} = -\frac{\frac{\Delta t_i}{t_{\langle p\rangle}}}{1+\frac{\Delta t_i}{t_{\langle p\rangle}}} \longrightarrow -\frac{\frac{\Delta t_i+c_{off}}{t_{\langle p\rangle}}}{1+\frac{\Delta t_i+c_{off}}{t_{\langle p\rangle}}} \neq \left.\frac{\Delta p_i}{\langle p\rangle}\right|_{ex} + const\,, \tag{7.51}$$

$$\left.\frac{\Delta E_i}{\langle E\rangle}\right|_{ex} = -\frac{2\,\frac{\Delta t_i}{t_{\langle E\rangle}} + \left(\frac{\Delta t_i}{t_{\langle E\rangle}}\right)^2}{\left(1+\frac{\Delta t_i}{t_{\langle E\rangle}}\right)^2} \longrightarrow -\frac{2\,\frac{\Delta t_i+c_{off}}{t_{\langle E\rangle}} + \left(\frac{\Delta t_i+c_{off}}{t_{\langle E\rangle}}\right)^2}{\left(1+\frac{\Delta t_i+c_{off}}{t_{\langle E\rangle}}\right)^2} \neq \left.\frac{\Delta E_i}{\langle E\rangle}\right|_{ex} + const\,. \tag{7.52}$$

Consequently, the determination of the Twiss parameters (Sec. 2.4) is not independent from c_{off}, when using the exact equations. On the other hand, we can exploit the fact that by the linear approximations the Twiss parameters are intrinsically invariant under translations with respect to Δt_i. Fortunately, as seen in Fig. 7.25 and the corresponding values in Tab. 7.3, the error through the linear approximation is negligible compared to other experimental uncertainties.

Nevertheless, the validity of this procedure obviously depends on the evaluation point of the series expansion, which is the TOF of a mean-momentum particle $t_{\langle p\rangle}$ or a mean-energy particle $t_{\langle E\rangle}$ in case of the relative momentum deviation or relative energy deviation. With a design energy of the accelerator chain at the stripper section of about 1.4 MeV per nucleon,

Tab. 7.3: Exemplary values of the exact relative momentum $\Delta p_i / \langle p \rangle |_{ex}$ Eq. (7.47) and relative kinetic energy $\Delta E_i / \langle E \rangle |_{ex}$ Eq. (7.49) and their linear approximation Eq. (7.35) and (7.36) for a particle that is separated four standard deviations of the expected relative momentum and energy deviation ($\frac{\Delta t_i}{t_{\langle p \rangle}} \approx \pm 0.02$). The third column additionally considers the effect of a mean energy shift $\Delta \langle E \rangle$ due to the gas stripper and foils of 5% and thus for an evaluation point being slightly off.

	Exact	**Lin. approx.**	**Lin. approx., $\boldsymbol{\Delta\langle E\rangle}$**
$\boldsymbol{\frac{\Delta p_i}{\langle p \rangle} \times 10^2}$	2.04, −1.96	2.00, −2.00	1.95, −1.95
$\boldsymbol{\frac{\Delta E_i}{\langle E \rangle} \times 10^2}$	4.12, −3.88	4.00, −4.00	3.89, −3.89

we can investigate the influence of an exemplary mean energy loss to account for a shifted evaluation point using the linear approximation. As a conservative margin of 5%, mean energy loss on passage of the gas stripper is reasonable. This includes dissipative effects at the tantalum and aluminum foils and the jitter in output energy for different ion species given by the nature of the IH structures.

According to Eq. (7.36), a mean energy shift $\Delta \langle E \rangle$ of 5% with respect to the design energy can be mapped to the timing data by

$$\frac{\Delta t_{\langle p \rangle}}{t_{\langle p \rangle}} \approx \frac{\Delta t_{\langle E \rangle}}{t_{\langle E \rangle}} \approx -\frac{\Delta \langle E \rangle}{2 \langle E \rangle} . \tag{7.53}$$

This allows modification of Eq. (7.35) and (7.36) to comprise a shift in mean TOF $\Delta t_{\langle p \rangle}$ using the following approximation since $\frac{\Delta t_{\langle p \rangle}}{t_{\langle p \rangle}} \ll 1$:

$$\frac{\Delta t_i}{\left(t_{\langle p \rangle} + \Delta t_{\langle p \rangle}\right)} = \frac{\Delta t_i}{t_{\langle p \rangle}\left(1 + \frac{\Delta t_{\langle p \rangle}}{t_{\langle p \rangle}}\right)} \overset{\frac{\Delta t_{\langle p \rangle}}{t_{\langle p \rangle}} \ll 1}{\approx} \frac{\Delta t_i}{t_{\langle p \rangle}}\left(1 - \frac{\Delta t_{\langle p \rangle}}{t_{\langle p \rangle}}\right) \approx \frac{\Delta t_i}{t_{\langle p \rangle}}\left(1 - \frac{\Delta \langle E \rangle}{2 \langle E \rangle}\right) . \tag{7.54}$$

Fig. 7.25 includes the corresponding approximations with a mean energy shift of 5%. Within a *four sigma range*, with respect to the expected standard deviation of the kinetic energy, there are no significant deviations from the classical exact formulae, and thus these discrepancies are also negligible.

7.8 Summary to TOF Uncertainties

The uncertainties which have been accounted for in this chapter are of different quality and significance when it comes to the effect on the measurement of the longitudinal phase space. Most timing uncertainties and dissipative effects can be attributed to uncertainties in the Gaussian sense. The overall effect of Gaussian contributions on an two-dimensional Gaussian model space will be investigated in chapter 6. Effects that cannot be treated as

Gaussian contributions occurred during the variation of the gas pressure at the stripper section, the variation of the position of the high current slits (DS4/5) and the interaction of particles with the collimator configuration responsible for particle number attenuation. All uncertainties taken into account are listed in Tab. 7.4.

The tantalum foil at the entrance of the collimator configuration, which serves as a thin target to provide Coulomb scattering, is inherently connected to the particle number attenuation and is an essential concept of the measurement setup. From the consideration of uncertainties, a major impact on the capabilities of the method is apparent. While the contribution from the collisional straggling, i. e. by assuming a perfect and homogeneous foil thickness, is already about 10-15% of the expected energy width, the texture of the rolled foils represents an even larger impact. Other authors, such as Bitao et al. [79], claim a significant contribution of the texture to the effective straggling. Their measurements with a rolled tantalum foil of 367 µg/cm^2, compared to 210 µg/cm^2 installed in the present setup, hinted an effective thickness variation of about 34%. Optical microscopy of the tantalum foil supports the experimental results by revealing prominent inhomogeneities on a small scale that does not allow to consider the foil sufficiently homogeneous within the aperture dimensions. The mean energy loss together with an assumed thickness variation of 34% alone contributes about 1% of energy spread which is the expected energy spread of the bunch. Thus, it represents a very strong limitation on the capabilities of the setup. Evaporated foils, on the other hand, are expected to feature a more homogeneous thickness of about 10% but are known to be not as resistant to the particle beam and thus are not feasible for particle number attenuation.

Compared to the straggling contribution of the first foil, the thin aluminium foil mounted in front of the MCP is negligible. The collisional straggling is about four times smaller magnitude than the corresponding contribution from the tantalum foil. More importantly, the evaporated aluminium foil is expected to be more homogeneous compared to the rolled tantalum foil. Nevertheless, even assuming a comparable inhomogeneity to the tantalum foil, the effective straggling is about six times smaller due to the lower mean energy loss. Hence, the tantalum foil clearly dominates the limiting overall dissipative contribution originating from straggling.

Another minor effect connected to the aluminium foil is the unavoidable geometric alignment which comes with an uncertainty of the detector separation. This contribution scales inversely with the separation and is about 25 ps for the setup at hand.

No quantitative value of timing jitter can be provided for the spectra of the liberated secondary electrons. Although more than 100 electrons per ion will be emitted it is not clear if this results in a sufficiently low jitter timing characteristic. In fact, since the TOF between the aluminium foil and the MCP front is very sensitive to the initial energy of the electrons, at the same time the MCP is sensitive to single electrons. Fluctuations of the fastest electrons may contribute a major jitter in the generation of the logic time signal. In particular, distortions of the leading edge of the MCP pulse shape may be connected to them.

The time resolution connected with the discrimination of the particle detector signals was estimated by the plain pulse shapes recorded with a fast oscilloscope. Additionally, using the logic signal from the discriminator as external trigger in persistence mode, provides rough information about the timing jitter. While the poly-crystalline diamond material shows a pulse-height distribution with a dynamic range within about a factor of 2, the leading edge does not feature any significant distortions. Together with the design properties of the double threshold discriminator, a time jitter of 50 ps is considered a realistic value. Due to the extension of the electrode and the finite propagation of the signal, an additional (but minor) time jitter of about 10 ps is taken into account. The MCP pulse shapes have a higher dynamic range of pulse height than the poly-crystalline diamond detector and do feature shoulders of fluctuating duration (see Fig. 7.19) which makes an estimate of the effect problematic. Nevertheless, taking into account a time jitter of 150 ps appears to be an appropriate choice without overestimating the effect.

It is important to distinguish absolute timing effects, such as the trigger accuracy, from dissipative effects. While all absolute timing contributions will get less significant with a (theoretical) larger separation of the detectors, the later ones affect the phase space itself and thus represent an asymptotic limitation to the measurement capability that cannot be overcome by extending the separation of the detectors. Figure 7.26 shows the systematic relative error according to Eq. (7.6) with respect to the detector separation. It incorporates

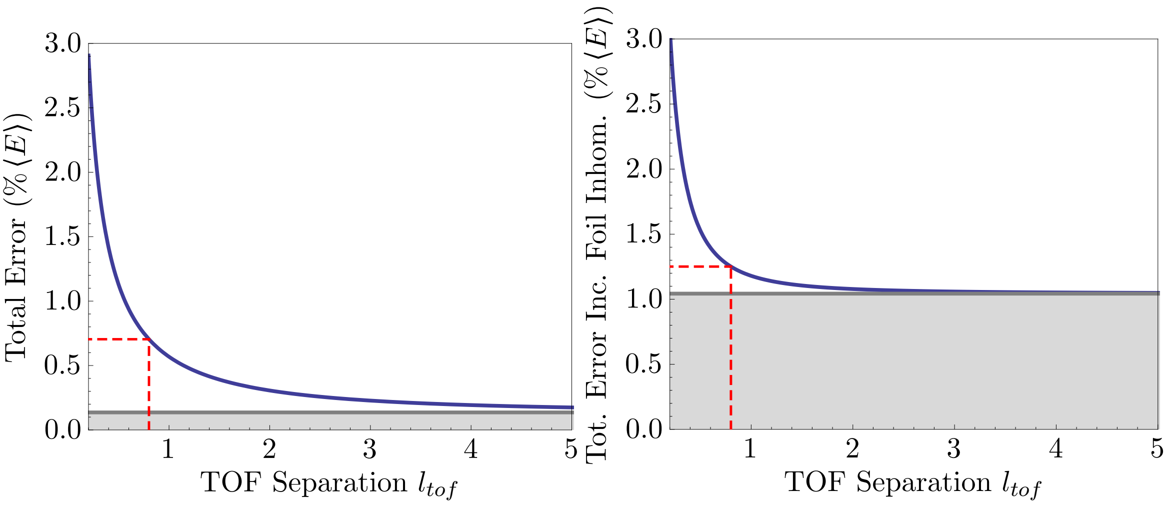

Fig. 7.26: Both plots show the accumulated relative error contribution $\sigma_E^{tot}/\langle E\rangle$ versus the detector separation l_{tof} used in the TOF section. The left plot includes the error components listed in Tab. 7.4 omitting the major impact of the foil inhomogeneities which are included in the right plot. Absolute timing uncertainties can be damped by an extended TOF separation l_{tof}, which is clearly seen by the shown characteristic. Nevertheless, the gray areas at the bottom mark the asymptotic error contribution introduced by all quantified effects on the phase space itself and cannot be overcome by a larger detector separation. In both plots the red dashed line denotes the current detector separation of about 801 mm and the corresponding relative error σ_E^{tot}. Not including the foil inhomogeneities results in an estimate of the total error of $\sigma_E^{tot}/\langle E\rangle$=0.7% whereas by taking the foil structure into account the error is $\sigma_E^{tot}/\langle E\rangle$=1.25%.

all systematic contributions described in this chapter and listed in Tab. 7.4 which can be treated in the Gaussian sense. This excludes the influences of the gas stripper, the high current slits and the collimator. The reference to the detector separation of the measurement is provided by the red dashed line. As mentioned before, for larger separations of the detectors the relative error asymptotically approaches the dissipative offset represented by the gray area. The left figure does not include the contribution of the foil inhomogeneities in order to visualise the major impact on the total resolution of the measurement setup, which is evident from the right figure. Referring again to the expected energy width of 1% a direct measurement of the total phase space is not possible. Even if an extended separation of the detectors was possible, the dissipative effects alone would be on the order of the expected energy spread itself. Since both, the true energy spread of the bunch as well as the limited resolution, are of about the same order of magnitude it is obvious that a certain sensitivity to the energy distribution is available, but a reliable direct measurement is not possible. The effect of a limited resolution assuming Gaussian error contributions on the phase-space measurement will be discussed in Chapter 6 by means of a Gaussian model phase space.

Tab. 7.4: Systematic contribution for the various components ordered according to the beam direction. Absolute time contributions σ_t are given at the current TOF separation of about 801 mm, in case the value depends on the detector separation.

	$\frac{\sigma_E}{\langle E\rangle}$ (%)	σ_t (ps)	section
Gas pressure at stripper section	n/a	n/a	7.5.1
Coupling of transverse and longitudinal phase space	n/a	n/a	7.5.2
High current slits (US3DS4/5)	n/a	n/a	7.5.3
Ta foil (part. atten.) - Collisional straggling	0.13		7.1.1
Ta foil (part. atten.) - Texture/variation of thickness	≈ 1.0		7.1.2
Ta foil (part. atten.) - Transversal momentum contrib.	0.001		7.1.3
Ta foil (part. atten.) - Finite solid angle	0.015		7.2
Interaction with collimator apertures	n/a	n/a	7.5.4
Al foil (sec. e^-) - Collisional straggling	0.033		7.3.1
Al foil (sec. e^-) - Texture/variation of thickness	≈ 0.17		7.3.2
Al foil (sec. e^-) - Energy spectra/TOF $e^- \rightarrow$ MCP	?	?	7.3.3
Al foil (sec. e^-) - Tilt/variation of TOF length		25	7.3.4
MCP pulse shape distortion/discrimination		150	7.4.1.1
Poly-crystalline diamond detector - discrimination		50	7.4.2.1
Poly-crystalline diamond detector - propagation time		10	7.4.2.2
TDC input jitter per channel incl. NIM setup		17	7.6
Linear Approximation: phase space reconstruction	n/c	n/c	7.7.1

n/a - qualitative analysis/qualitative analysis not available

n/c - not considered/not an error in the Gaussian sense

(see referred section)

Chapter 8

Conclusion & Outlook

- Trend pulse height and pulse integral. For Argon measurement drop of 4.9% in gain (pulse height) within 2876 hits. Drop of 1.8% in integral. It's a lot but ions are fully stopped, thus implanting!
- Long measurement time through single-particle coincidences
- No online measurement
- Exclusive measurement for HSI
- Test measurement sho
- Measurement relies on beam attenuation

Chapter A

Appendix

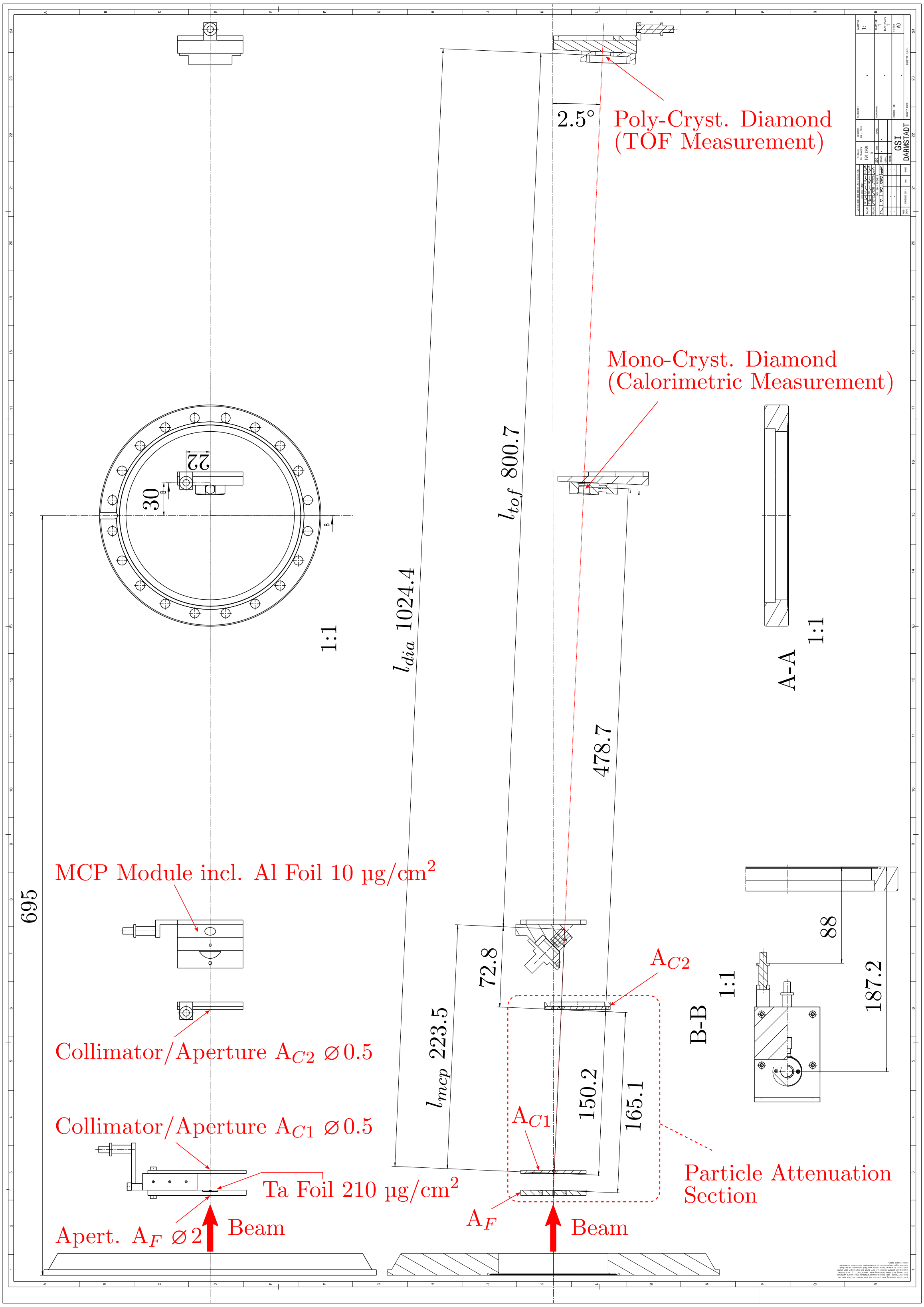

Fig. A.1: Technical drawing of the diagnostics chamber. **Left:** Side view. **Right:** Top view.

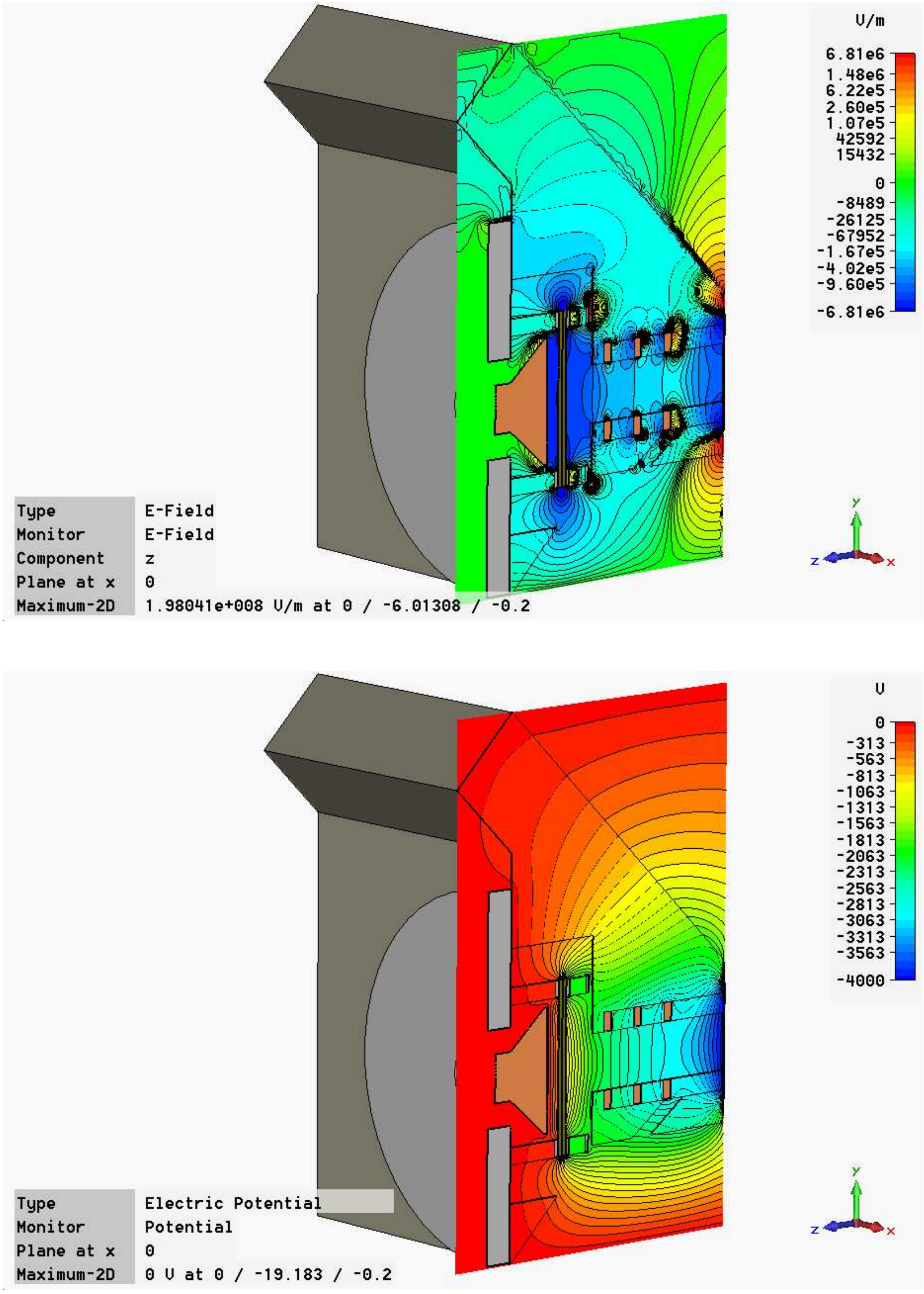

Fig. A.2: Simulation by P. Kowina [39]. CST Microwave Studio simulation of the PEEK mounting, MCP Hamamatsu F4655-13 module (Sec. 3.3.1) and the guide rings. The electric field distribution is depicted in the top figure while the corresponding equipotential lines are given at the bottom figure.

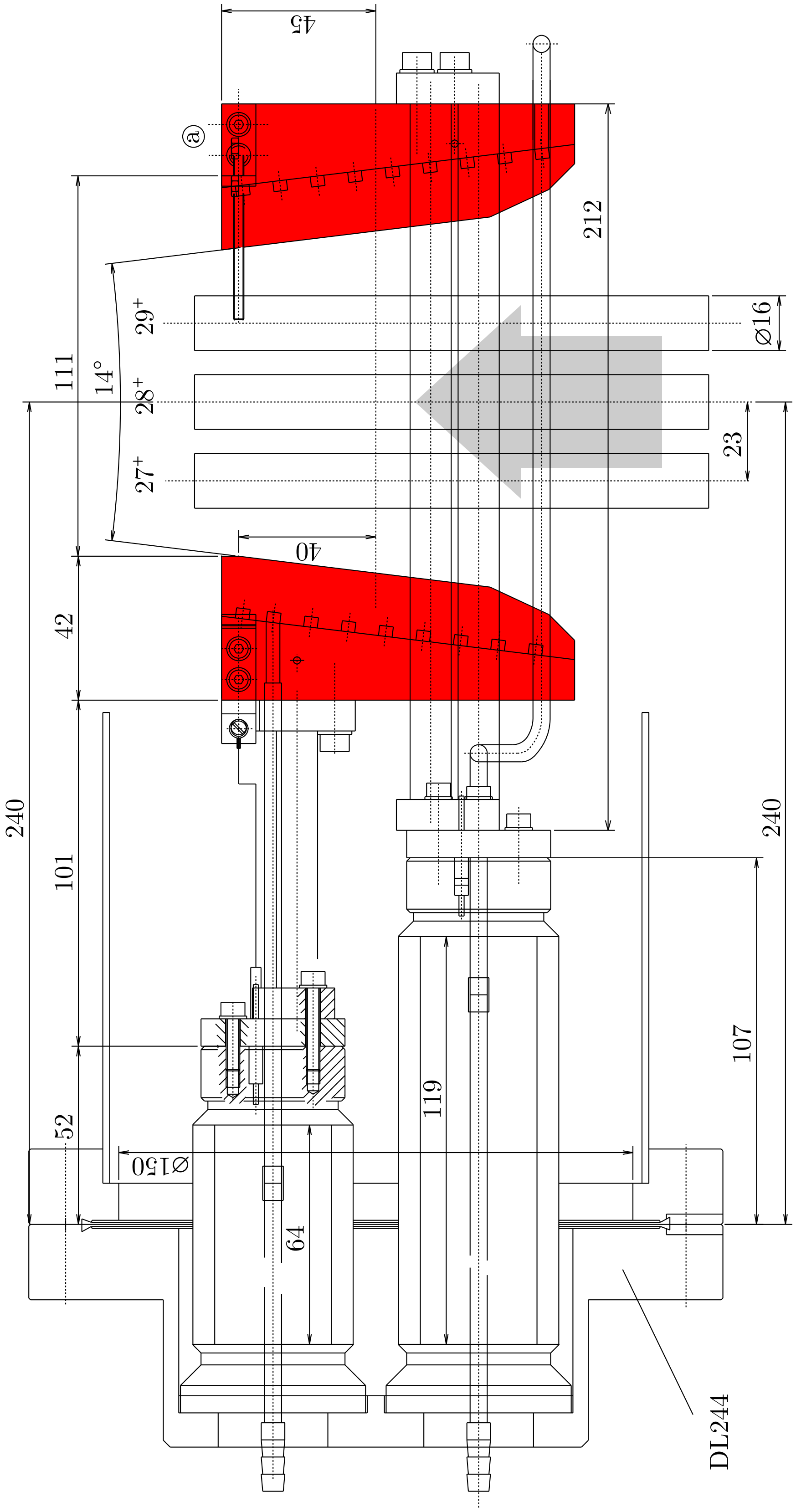

Fig. A.3: High-current slits (cooled) used for charge separation and late attenuation of the beam during high-current measurements of the longitudinal phase space [32].

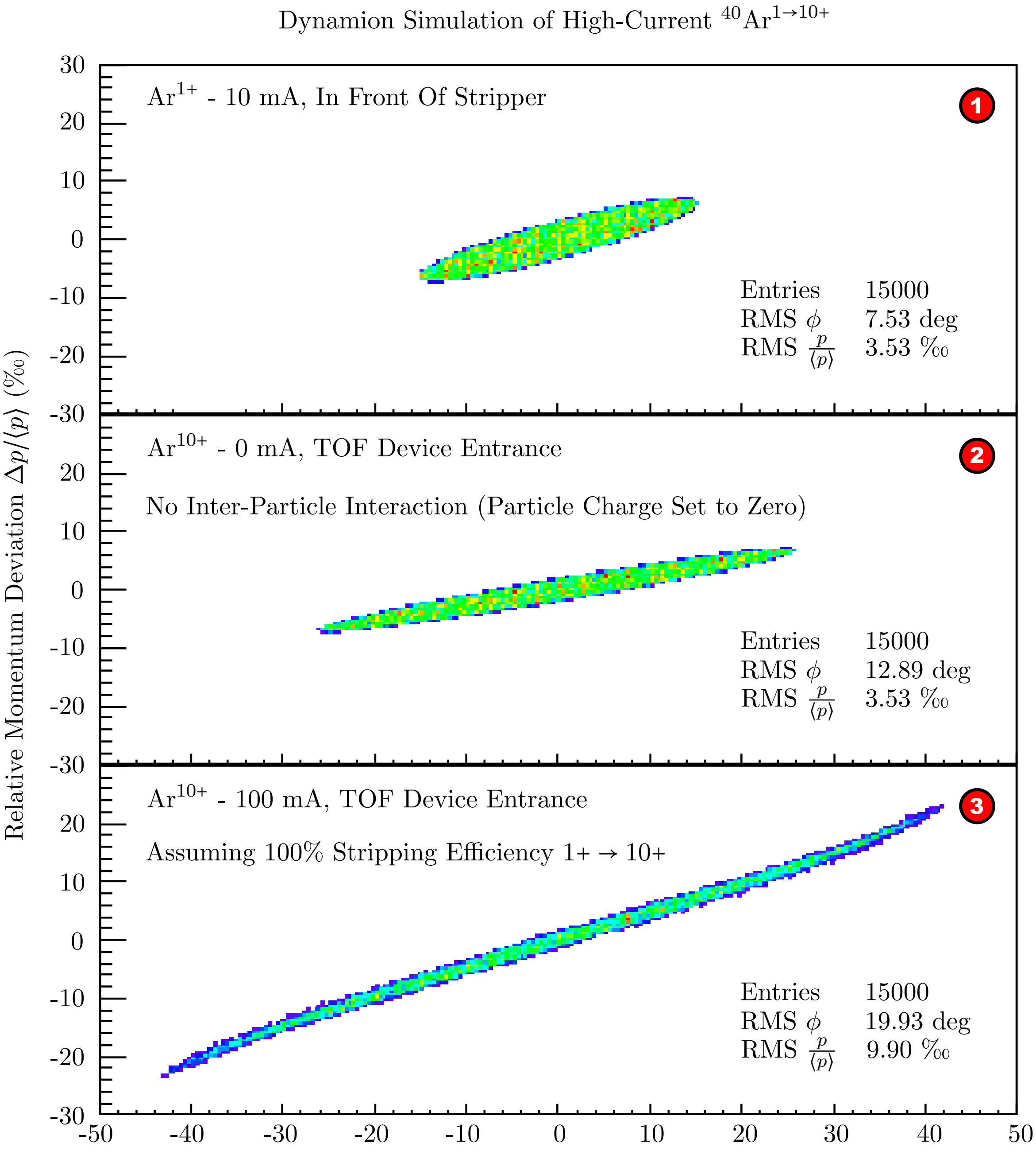

Fig. A.4: Figure ❶ shows the longitudinal phase space which is used as *start distribution* in a DYNAMION calculation [86] to estimate the influence of the dispersive dipole section (US3MK1) and space-charge. The start distribution is located right in front of the UNILAC gas stripper. For simplicity, a homogeneous test distribution with a sharp elliptic bound is assumed to be a sufficiently good representation for the 10 mA Ar^{1+} beam. The particle distribution is tracked to the TOF device entrance using two different assumptions. Figure ❷ shows the tracked longitudinal phase space at the height of the device when particle interaction is not considered. Figure ❸ shows the complementary tracking with the particle interaction included at a stripping efficiency of 100%.

Bibliography

[1] G. Riehl, J. Pozimski, W. Barth, and H. Klein. A Multifunctional Profile and Emittance Measurement System. In *Proceedings of the "European Particle Accelerator Conference"*, page 756, Nice, France, 1990.

[2] A. Reiter, C. Kleffner, and B. Schlitt. Improved Signal Treatment for Capacitive Linac Pickups. In *Proceedings of the "DIPAC" (in print)*, page (in print), Hamburg, Germany, 2011.

[3] S. Richter, W. Barth, L. Dahl, J. Glatz, L. Groening, and S. Yaramyshev. High current beam transport to sis18. page 45, 2004.

[4] P. Forck, F. Heymach, U. Meyer, P. Moritz, and P. Strehl. Aspects of Bunch Shape Measurements for Slow, Intense Ion Beams. In *Proceedings of the "DIPAC"*, page 186, Chester, UK, 1999.

[5] P. Forck, F. Heymach, T. Hoffmann, A. Peters, and P. Strehl. Measurements of the six Dimensional Phase Space at the New GSI High Current Linac. In *Proceedings of the "International Linac Conference"*, page 166, Monterey, California, 2000.

[6] R. Hollinger, M. Galonska, B. Gutermuth, F. Heymach, H. Krichbaum, K.-D. Leible, K. Ochs, P. Schäffer, P. Spädkte, M. Stork, A. Wesp, and R. Mayr. Status of high current ion source operation at the GSI accelerator facility. *Rev. Sci. Intrum.*, 79:523, 2008.

[7] T. Hoffmann, W. Barth, P. Forck, A. Peters, P. Strehl, and D. A. Liakin. Emittance Measurements of High Current Heavy Ion Beams Using a Single Shot System. In *Proceedings of the "Beam Instrumentation Workshop"*, page 432, Cambridge, Massachusetts, 2000.

[8] F. Becker. *Zerstörungsfreie Profilmessung intensiver Schwerionenstrahlen.* PhD thesis, Technische Universität, Darmstadt, 2010.

[9] P. M. Lapostolle. Possible Emittance Increase through Filamentation Due to Space Charge in Continuous Beams. *IEEE Trans. Nucl. Sci. NS-18*, 3:1101, 1971.

[10] Stanley Humphries Jr. *Charged Particle Beams.* Wiley-Intersience, 1990.

[11] J. D. Lawson, P. M. Lapostolle, and R. L. Gluckstern. Emittance, Entropy and Information. *Particle Accelerators*, 5:61, 1973.

[12] R. Wideröe. Über ein neues Prinzip zur Herstellung hoher Spannungen. *Archiv für Elektrotechnik*, 21:387, 1928.

[13] W. Barth, P. Forck, J. Glatz, W. Gutowski, G. Hutter, J. Klabunde, R. Schwedhelm, P. Strehl, W. Vinzenz, D. Wilms, and U. Ratzinger. Commissioning of IH-RFQ and IH-DTL for the GSI High Current Linac. In *Proceedings of the "International Linac Conference"*, page 1033, Monterey, California, 2000.

[14] L. W. Alvarez. The design of a proton accelerator. *Phys. Rev.*, 70:799, 1946.

[15] U. Ratzinger. H-type LINAC Structures. In *Proceedings of the "CERN Accelerator School for Radio Frequency Engineering", CAS*, page 351, Seeheim, Germany, 2000.

[16] R. Tiede, U. Ratzinger, H. Podlech, C. Zhang, and G. Clemente. KONUS Beam Dynamics Designs using H-Mode Cavities. In *Proceedings of "Hadron Beam"*, page 223, Nashville, Tennessee, USA, 2008.

[17] R. Tiede. *Simulationswerkzeuge für die Berechnung hochintensiver Ionenbeschleuniger.* PhD thesis, Johann Wolfgang Goethe Universität, Frankfurt am Main, 2009.

[18] S. Yaramyshev, W. Barth, L. Groening, A. Kolomiets, and T. Tretyakova. Development of the versatile multi-particle code DYNAMION. *NIM, Nuclear Instruments and Methods in Physics Research A*, 558:90, 2006.

[19] J. H. Billen and H. Takeda. PARMILA Manual. *Los Alamos National Laboratory report*, page 90, 1998 (Rev. 2004).

[20] Edwin M. McMillan. The Relation between Phase Stability and First-Order Focusing in Linear Accelerators. *Phys. Rev.*, 80:493, 1950.

[21] T. P. Wangler. *RF Linear Accelerators.* John Wiley and Sons, New York, 1998.

[22] S. Hofmann. Approaching the superheavy elements. *Nuc. Phys. News*, 6:26, 1996.

[23] J. Dilling, D. Ackermann, J. Bernhard, F.P. Hessberger, S. Hofmann, W. Hornung, H.-J. Kluge, E. Lamour, M. Maier, R. Mann, G. Marx, R.B. Moore, G. Münzenberg, W. Quint, D. Rodriguez, M. Schädel, J. Schönfelder, G. Sikler, C. Toader, L. Vermeeren, C. Weber, G. Bollen, O. Engels, D. Habs, P. Thirolf, H. Backe, A. Dretzke, W. Lauth, W. Ludolphs, M. Sewtz, and the SHIPTRAP Collaboration. The SHIPTRAP project: A capture and storage facility at GSI for heavy radionuclides from SHIP. *Hyperfine Interactions*, 127:491, 2000.

[24] C.E. Düllmann. Physical separators for the heaviest elements. *NIM, Nuclear Instruments and Methods in Physics Research B - Beam Interactions with Material & Atoms*, 266:4123, 2008.

[25] U. Ratzinger. The New High Current Ion Accelerator at GSI and Perspectives for LINAC Design Based on H-Mode Cavities. In *Proceedings of the "EPAC"*, page 98, Vienna, Austria, 2000.

[26] W. Barth and P. Forck. The New Gas Stripper and Charge State Separator of the GSI High Current Injector. In *Proceedings of the "International Linac Conference"*, page 235, Monterey, California, 2000.

[27] W. Barth, W. Bayer, L. Dahl, L. Groening, S. Richter, and S. Yaramyshev. Upgrade program of the high current heavy ion UNILAC as an injector for FAIR. *NIM, Nuclear Instruments and Methods in Physics Research Section A*, 557:211, 2007.

[28] W. Barth, L. Dahl, L. Groening, S. Richter, and S. Yaramyshev. Application of Beam Diagnostics for Intense Heavy Ion Beams at the GSI UNILAC. In *Proceedings of the "DIPAC"*, page 161, Mainz, Germany, 2003.

[29] U. Raich. The Longitudinal Emittance Measurement Line at CERN's Proton Linac. In *Proceedings of "Workshop on Transverse and Longitudinal Emittance Measurement in Hadron-(Pre-)Accelerators"*, page 107, Bad Kreuznach, Germany, 2008.

[30] D. Liakin. GSI Generic VME Timing Board. priv. comm., 2007.

[31] E. Berdermann, M. Pomorski, W. de Boer, M. Ciobanu, S. Dunst, C. Grah, M. Kiš, W. Koenig, W. Lange, W. Lohmann, R. Lovrinčić, P. Moritz, J. Morse, S. Mueller, A. Pucci, M. Schreck, S. Rahman, and M. Träger. Diamond detectors for hadron physics research. *Diamond & Related Materials*, 19:258, 2010.

[32] O. Zurkan. Konstruktive und thermische Auslegung eines Hochstrom-Schlitzsystems. Diploma thesis, Fachhochschule Heidelberg, 1996.

[33] J.-C. Denard. Beam Current Monitors. In *Proceedings of "CERN Accelerator School: Course on Beam Diagnostics", CAS*, page 141, Dourdan, France, 2008.

[34] J. W. Wiza. Microchannel plate detectors. *Nucl. Inst. Meth.*, 162:587, 1979.

[35] Krasimir Milchev Kosev. *A High-Resolution Time-of-Flight Spectrometer for Fission Fragments and Ion Beams.* PhD thesis, Technische Universität - Institut für Kern und Teilchenphysik, Dresden, 2007.

[36] P. Forck, A. Bank, T. Giacomini, and A. Peters. Profile Monitors Based on Residual Gas Interaction. In *Proceedings of the "DIPAC"*, page 223, Lyon, France, 2005.

[37] Hamamatsu Photonics K.K. Specification sheet of the MCP compound module F4655-13 used in the Time-of-Flight setup. `http://sales.hamamatsu.com/assets/pdf/parts_F/F4655-13_TMCP1021E05.pdf`.

[38] Hamamatsu Photonics K.K. MCP Selection & MCP Assembly Guide. `http://sales.hamamatsu.com/assets/pdf/catsandguides/MCPassy_TMCP0001E08.pdf`.

[39] P. Kowina. Simulation of the electric field distribution via CST Microwave Studio®. priv. comm., 2009.

[40] E. Berdermann, K. Blasche, P. Moritz, and B. Voss. The use of CVD-diamond for heavy-ion detection. *Diamond & Related Materials*, 10:1770, 2001.

[41] E. Berdermann, K. Blasche, P. Moritz, H. Stelzer, and F. Zeytouni. Diamond detectors for heavy ion measurements. In *Proceedings of the "XXXVI International Winter Meeting on Nuclear Physics"*, page 589, Bormio, Italy, 1998.

[42] J. Isberg, J. Hammersberg, E. Johansson, T. Wikstr"om, D. J. Twitchen, A. J. Whitehead, S. E. Coe, and G. A. Scarsbrook. High Carrier Mobility in Single-Crystal Plasma-Deposited Diamond. *Science*, 297:1670, 2002.

[43] A. Galbiati, S. Lynn, K. Oliver, F. Schirru, T. Nowak, B. Marczewska, J.A. Dueas, R. Berjillos, I. Martel, and L. Lavergne. Performance of Monocrystalline Diamond Radiation Detectors Fabricated Using TiW, Cr/Au and a Novel Ohmic DLC/Pt/Au Electrical Contact. *IEEE Transactions on Nuclear Science*, 56:1863, 2009.

[44] M. Pomorski, E. Berdermann, M. Ciobanu, A. Martemyianov, P. Moritz, M. Rebisz, and B. Marczewska. Characterisation of single crystal CVD diamond particle detectors for hadron physics experiments. *phys. stat. sol. (a)*, 202(11):2199, 2005.

[45] M. Pomorski, E. Berdermann, W. de Boer, A. Furgeri, C. Sander, J. Morse, and for the NoRHDia Collaboration. Charge transport properties of single crystal CVD-diamond particle detectors. *Diamond and Related Materials*, 16:1066, 2007.

[46] P. Strehl. *Beam Instrumentation and Diagnostics.* Springer-Verlag Berlin Heidelberg, 2006.

[47] P. Sigmund. *Particle Penetration and Radiation Effects.* Springer Berlin Heidelberg New York, 2008.

[48] R. D. Evans. *The Atomic Nucleus.* McGraw-Hill Book Company, 1955.

[49] J. F. Ziegler, J. P. Biersack, and M. D. Ziegler. *SRIM - The Stopping and Range of Ions in Matter.* SRIM Co., 2008.

[50] G. F. Knoll. *Radiation Detection and Measurement (3rd Ed.).* John Wiley & Sons, Inc., 2000.

[51] W. R. Leo. *Techniques for Nuclear and Particle Physics Experiments, 2nd Ed.* Springer-Verlag, Berlin Heidelberg, 1994.

[52] A. R. Folov, T. V. Oslopova, and Yu. N. Pestov. Double threshold discriminator for timing measurements. *Nucl. Inst. Meth.*, 356(5):447, 1994.

[53] C. Neyer. A Discriminator Chip for Time of Flight Measurements in ALICE. In *Proceedings of the "3rd Workshop on Electronics for LHC Experiments"*, page 238, London, UK, 1997.

[54] GSI Helmholtzzentrum für Schwerionenforschung GmbH Experiment Electronics Department. Fast Time-Walk Suppressing Double Threshold Discriminator ASIC. `http://www.gsi.de/informationen/tt/Double-Threshold-1_e.html`.

[55] U. Krause and P. Kainberger. UNILAC-event-timing documentation (german) "PZU - Unilac-Pulsezentrale", 6 December 2007. `http://bel.gsi.de/mk/hfu/gm_hfu.pdf`.

[56] CAEN S.p.A. Homepage of the manufacturer of the VME TDC module V1290N. Manuals and specifications are available online. `http://www.caen.it`.

[57] Struck Innovative Systeme GmbH. Homepage of the manufacturer of the USB 2.0 to VME interface SIS3150. Manuals and specifications are available online. `http://www.struck.de`.

[58] HIPPI "High Intensity Pulsed Proton Injectors" collaboration part of the CARE framework: JRA3 in the CARE proposal. `http://care.lal.in2p3.fr/Joint/JRA3/HIPPI-modif-26-09-03.doc`, 2003.

[59] Inc. Tektronix. Homepage of the manufacturer of the oscilloscope DPO 7254. Manuals and specifications are available online. `http://www.tek.com`.

[60] ROOT - A Data Analysis Framework. `http://root.cern.ch`.

[61] E. Lohrmann V. Blobel. *Statistische und numerische Methoden der Datenanalyse.* B. G. Teubner Stuttgart, 1998.

[62] R. Maronna P. Filzmoser, S. Serneels. Robust multivariate methods in chemometrics. *Comprehensive Chemometrics*, page 681, 2009.

[63] M. P. Stockli, R. F. Welton, and R. Keller. Self-consistent, unbiased root-mean-square emittance analysis. *Rev. Sci. Intrum.*, 75:1646, 2004.

[64] P. J. Rousseeuw. Multivariate Estimation with High Breakdown Point. *Mathematical Statistics and Applications*, B:283, 1985.

[65] P. Allison R. Keller, J. D. Sherman. Use of a Minimum-Ellipse Criterion in the Study of Ion-Beam Extraction Systems. *IEEE Transactions on Nuclear Science*, NS-32:2579, 1985.

[66] K. v. Driessen P. J. Rousseeuw. A fast algorithm for the minimum covariance determinant estimator. *Technometrics*, 41(3):212, 1999.

[67] TRobustEstimator - ROOT implementation of the FAST-MCD concept proposed by P. J. Rousseeuw et al. `http://root.cern.ch/root/html/TRobustEstimator.html`.

[68] R, The R Project for Statistical Computing'. `http://www.r-project.org/`.

[69] V. Todorov. robustbase - R package which includes an implementation of FAST-MCD (covMcd). `http://cran.r-project.org/web/packages/robustbase/index.html`.

[70] P. J. Rousseeuw et al. Fast-mcd, fortran implementation including improved correction factors. `http://agoras.ua.ac.be/Robustn.htm`.

[71] D. Eddelbuettel and R. Francois. Rcpp/RInside, Easier embedding of R in C++ application. `http://dirk.eddelbuettel.com/code/rinside.html`.

[72] G. Pison, S. Van Aelst G., and Willems. Small sample corrections for lts and mcd. *Metrika, International Journal for Theoretical and Applied Statistics*, 55:111, 2002.

[73] P. Forck. Joint University Accelerator School - Lecture Notes on Beam Instrumentation and Diagnostics. `http://indico.cern.ch/getFile.py/access?contribId=172&resId=22&materialId=slides&confId=162969`, 2012.

[74] L. Groening and W. Barth. Expected energy width at GSI stripper section. priv. comm., 2007.

[75] H. A. Bethe. Zur Theorie des Durchgangs schneller Korpuskularstrahlen durch Materie. *Ann. Phys.*, 5:325, 1930.

[76] J. F. Ziegler, J. P. Biersack, and M. D. Ziegle. SRIM - The Stopping and Range of Ions in Matter. *NIM, Nuclear Instruments and Methods in Physics Research B - Beam Interactions with Material & Atoms*, 11:325, 2010.

[77] H. Bräuning, A. Bräuning-Demian, G. Bednarz, F. Bosch, X. Cai, C. Cohen, D. Dauvergne, A. Gumberidze, R. Kirsch, C. Kozhuharov, D. Liesen, P. H. Mokler, J.-P. Rozet, Z. Stachura, Th. Stölker, M. Terasawa, S. Toleikis, and A. Warczak. Multiple electron capture from thin C-foils into 46 MeV/u U^{91+}. *NIM, Nuclear Instruments and Methods in Physics Research Section B*, 205:826, 2003.

[78] F. Besenbacher, J. U. Andersen, and E. Bonderup. Straggling in Energy Loss of Energetic Hydrogen and Helium Ions. *Nuclear Instruments and Methods*, 168:1, 1980.

[79] Hu Bitao, Li Yuhong, Cheng Ximen, Liu Zhengmin, and Liu Zhaoyuan. Energy-loss straggling of low energetic ^{16}O ion in Co, Ni and Lu. *Journal of Radioanalytical and Nuclear Chemistry*, 262:489, 2004.

[80] N. Nankov, E. Grosse, A. Hartmann, A. R. Junghans, K. Kosev, K. D. Schilling, M. Sobiella, and A. Wagner. A High-Resolution Time-of-Flight Spectrometer with Tracking Capabilities for Fission Fragments and Beams of Exotic Nuclei. In *GSI Scientific Report*, page 266, Darmstadt, Germany, 2005.

[81] L. Groening. High current Argon (10+) and Uranium (27+) start distributions at TOF device location used for tracking simulation runs through the post-stripper section. priv. comm., 2010.

[82] L. Groening et. al. Benchmarking with UNILAC Experiment. `http://indico.cern.ch/contributionDisplay.py?contribId=23&confId=39839`, 2008. Presentation at "HIPPI 2008 Annual Meeting".

[83] H. Geissel, C. Scheidenberger, P. Malzacher, and J. Kunzendorf. ATIMA - ATomic Interaction with MAtter. `http://www-linux.gsi.de/~weick/atima/`.

[84] E. J. Sternglass. Theory of Secondary Electron Emission by High-Speed Ions. *Phys. Rev.*, 108:1, 1957.

[85] A. Koyama, O. Benka, Y. Sasa, and M. Uda. Energy spectra of secondary electrons from Al induced by heavy-ion impact. *Phys. Rev. B*, 34:8150, 1986.

[86] S. Yaramyshev. DYNAMION tracking simulations through gas stripper and dispersive dipole section for estimation of transverse and longitudinal coupling. priv. comm., 2011.

[87] K. Inami. Time-of-Flight Measurement with MCP-PMT. In *Proceedings of the "SNIC Symposium"*, Stanford, California, 2006. PSN 044.

Acknowledgements

Erklärung

Hiermit erkläre ich, dass ich die vorliegende Dissertation selbständig verfasst, keine anderen als die angegebenen Hilfsmittel verwendet und bisher noch keinen Promotionsversuch unternommen habe.

Darmstadt, November 14, 2012 *Timo Milosic*